

**Affinity Gradient of Chimeric Antigen Receptor T-Cells  
Against Low-Antigen Density Target**

**Evangelia K Kokalaki**

Cancer Institute  
University College London

A thesis submitted for the degree of Doctor of Philosophy

2017

## **DECLARATION**

I, Evangelia K Kokalaki, confirm that the work presented in this thesis is my own. Where information has been derived from other sources, I confirm that this has been indicated in the thesis.

## **ACKNOWLEDGEMENTS**

First of all, I would like to thank Dr Martin Pule for giving me many opportunities over the years, as well as providing guidance, support, and advice throughout my PhD. I would like to thank Dr Sergio Quezada for providing *in vivo* model guidance, and a great amount of morale support. A special thank you to Dr Shaun Cordoba and Dr Shimobi Onuoha from Autolus for invaluable input and help in my PhD project.

I would like to thank Mathieu Ferrari and Alex Kinna not only for their guidance, but actual hands-on help with the protein work.

The four years of my PhD have been an amazing experience, which is mainly due to the amazing people that populate the Pule lab at 306. A special thank you to Brian Philip, Pati Wawrzyniecka, Paul Maciocia, Gordon Cheung, Leila Mekkaoui, Cassie Stowe, Farhaan Parekh, Francesco Nannini, Claire Roddie, Sara Gharashian, and Lydia Lee for making this experience unique, for providing lots of cake, sharing a lot of ice-cream, instigating a lot of laugh, and building the world's most accurate seesaw. It has been a pleasure meeting and working with all of you.

Finally, the biggest thank you to family. To my parents Antonis and Loukia for the infinite support to all my endeavours, for always being there in any way possible; and my fiancée Greg for being present in my life for the last four years, for being very patient and understanding, and tolerating me during the writing of my thesis.

## **ABSTRACT**

Adoptive Cell Therapy (ACT) is a novel approach to cancer treatment, which implements the use of the patient T-cells redirected to eradicate tumour cells. The T-cells are engineered to express a Chimeric Antigen Receptor (CAR) that bestows specificity for an arbitrary antigen. CAR-T cell clinical trials have shown tumour eradication of leukaemia, but modest results against solid tumours. There is an ongoing debate regarding the correlation of CAR affinity and antigen-density recognition threshold, which we sought to investigate.

Although the TCRs sensitivity against low antigen targets is superior at low-affinity, the effect of affinity in CAR efficacy and sensitivity is controversial. In order to examine the correlation between CAR efficacy and affinity, we designed a CAR against an intracellular protein in melanoma. Tyrosinase-Related Protein 1 (Tyrp1) resides in the surface of the organelles called melanosomes. However, Tyrp1 is also trafficked to the surface at a low density. We mutated an anti-Tyrp1 single-chain Variable Fragment (scFv) to acquire eight mutants of various affinities. The affinity range was 0.74nM-54.3nM. Including the wild-type scFv, these nine affinity gradient CARs were challenged with a cell line expressing low, medium and high densities of cell-surface Tyrp1. Three mutant scFv CARs were superior to the wild-type scFv. However, the affinities of those superior CARs was variant. There was no pattern observed to suggest a direct correlation between the affinity and the CAR efficacy.

In contrast to previous publications, this study shows that affinity does not play a key role in determining the CAR efficacy. We hypothesise that the difference in CAR efficacy depends on a combination of factors, such as scFv stability and affinity, CAR density, and antigen density. However, the complex interaction of these parameters, as well as further confounding factors, renders the deduction of a pattern challenging. In order overcome this complexity, a multivariate analysis of all the parameters together is necessary.

## TABLE OF CONTENTS

Declaration.....	2
Acknowledgements .....	3
Abstract .....	4
Table of Contents .....	5
List of Figures .....	11
List of Tables .....	13
Abbreviations.....	14
<b>CHAPTER 1: INTRODUCTION .....</b>	<b>18</b>
<b>1.1 Melanoma .....</b>	<b>18</b>
<b>1.2 Systematic therapies and clinical trials.....</b>	<b>18</b>
<b>1.3 Melanosome development and melanin synthesis.....</b>	<b>20</b>
<b>1.4 Tyrosinase-related protein 1 As a potential target for CAR therapy.....</b>	<b>22</b>
<b>1.5 Targeting TYRP1 using TA99 Antibody.....</b>	<b>25</b>
<b>1.6 Tyrp1 trafficking.....</b>	<b>26</b>
<b>1.7 Chimeric antigen receptors .....</b>	<b>29</b>
1.7.1 The Structure of the T-Cell Receptor .....	29
1.7.2 The Structure of the Chimeric Antigen Receptor .....	31
1.7.3 Activation of TCR .....	33
1.7.4 Optimal TCR/CAR and Antigen Density .....	35
1.7.5 CAR T-Cell Clinical Trials.....	37
1.7.6 Advantages and Challenges of CAR Technology .....	39
<b>1.8 Antigen sensitivity in relation to affinity .....</b>	<b>40</b>
1.8.1 Binding Kinetics .....	40
1.8.2 Effect of Affinity on T-Cell Receptors.....	41
1.8.3 Effect of Affinity on Chimeric Antigen Receptors .....	44
<b>1.9 Hypotheses .....</b>	<b>50</b>
<b>1.10 Project aims .....</b>	<b>50</b>
<b>CHAPTER 2: Materials and Methods.....</b>	<b>53</b>
<b>2.1 Molecular Biology .....</b>	<b>53</b>

2.1.1	Molecular Cloning.....	53
2.1.1.1	Phusion PCR .....	53
2.1.1.2	DNA Construction by Oligo Assembly .....	54
2.1.1.3	Alanine Scanning.....	56
2.1.1.4	Restriction Endonuclease Digestion.....	56
2.1.1.5	DNA Ligation and Transformation .....	56
2.1.1.6	Small and Large Scale DNA Preparation.....	57
2.1.1.7	Gel Electrophoresis .....	57
2.1.1.8	Gel Extraction.....	57
<b>2.2</b>	<b>Protein Work .....</b>	<b>58</b>
2.2.1	Protein Isolation .....	58
2.2.1.1	Column A Protein Purification .....	58
2.2.1.2	Calculating Protein Concentration with Nanodrop.....	58
2.2.1.3	Protein Dialysis.....	59
2.2.1.4	Sodium Dodecyl Sulphate Polyacrylamide Gel Electrophoresis.....	59
2.2.1.5	Coomasie Staining.....	59
2.2.2	Surface Plasmon Resonance (SPR).....	60
2.2.3	Differential Scanning Fluorimetry (DSF) .....	60
<b>2.3</b>	<b>Tissue Culture .....</b>	<b>61</b>
2.3.1	Cell Lines .....	61
2.3.2	Basic Cell Culture Techniques .....	61
2.3.2.1	Cryopreservation and recovery of Cell Lines .....	61
2.3.2.2	Cellular Recovery from Cryopreservation .....	62
2.3.2.3	Transient Transfection of 293T Cells for Protein Production.....	62
2.3.3	Primary Cell Culture.....	62
2.3.3.1	Isolation of PBMCs .....	62
2.3.3.2	Murine Splenocyte Isolation .....	63
2.3.4	Retroviral Supernatant Production.....	63
2.3.4.1	Retroviral Supernatant Production for Transduction of PBMCs .....	63
2.3.4.2	Retroviral Supernatant Production for Transduction of Splenocytes .....	64
2.3.4.3	Coating of Tissue Culture Plates with Retronectin.....	64
2.3.4.4	Retroviral Transduction of PBMCs .....	65
2.3.4.5	Retroviral Transduction of Splenocytes .....	65
2.3.5	Primary Melanoma Samples.....	65
<b>2.4</b>	<b>Flow Cytometry .....</b>	<b>67</b>
2.4.1	General Labelling Protocol .....	67
2.4.2	Labelling for Extracellular Antigens .....	67

2.4.3	Labelling for Intracellular Antigens.....	67
2.4.4	Preparation of Counting Beads.....	67
2.4.5	Signal Enhancement with Miltenyi FASER Kit PE .....	68
2.4.6	Antigen Quantification with QIFIKIT Beads .....	68
2.4.7	Antigen Quantification with QuantiBrite-PE.....	68
<b>2.5</b>	<b><i>In Vitro Assays</i></b> .....	<b>68</b>
2.5.1	CD56 Magnetic Bead Negative Selection .....	68
2.5.2	<sup>51</sup> Cr Release Assay.....	69
2.5.3	Co-Culture Assays .....	69
2.5.3.1	Preparation of Co-Culture .....	69
2.5.3.2	Flow-Cytometry Based Killing Assay (FBK) .....	70
2.5.3.3	T-Cell Differentiation Panel.....	70
2.5.3.4	T-Cell Exhaustion Panel.....	71
2.5.3.5	ELISA for IFN- $\gamma$ and IL2 .....	71
2.5.4	Microscopy .....	72
2.5.4.1	Confocal Imaging of Acetone Fixated Tissue .....	72
2.5.4.2	Live-Cell Imaging .....	73
<b>2.6</b>	<b><i>In Vivo Procedures</i></b> .....	<b>73</b>
2.6.1	Experimental Overview .....	73
2.6.2	Intravenous Injection of Mice.....	73
2.6.3	Organ Harvest and Preparation .....	74
2.6.3.1	Blood Harvest and Preparation.....	74
2.6.3.2	Tumour Sample Preparation.....	74
2.6.3.3	Spleen Harvest and Preparation .....	75
2.6.3.4	Bone Marrow Harvest and Preparation .....	75
<b>CHAPTER 3: Results: Validating Tyrp1 as a Target on Melanoma Cells .....</b>		<b>77</b>
<b>3.1</b>	<b>INTRODUCTION.....</b>	<b>77</b>
3.1.1	Tyrosinase-Related Protein 1.....	77
3.1.2	TA99.....	77
3.1.3	Live-Cell Imaging: Eos .....	77
3.1.4	Antigen Density Quantification .....	78
<b>3.2</b>	<b>Aims .....</b>	<b>80</b>
<b>3.3</b>	<b>Results .....</b>	<b>81</b>
3.3.1	Cloning of constructs .....	81
3.3.1.1	Generation of TA99 scFV.....	81

3.3.1.2	Generation of TA99 Constructs.....	82
3.3.1.3	Generation of Tyrp1 Constructs.....	83
3.3.2	TA99 Recognises Tyrp1 on the Cell Surface.....	85
3.3.2.1	Identification of Surface Tyrp1 with Flow Cytometry.....	85
3.3.2.2	Detection of Tyrp1 in Mouse metastatic Melanoma.....	88
3.3.2.3	Live-Cell Imaging of Tyrp1-mMEos.....	89
3.3.2.4	Determination of Tyrp1 Expression Profile on Melanoma Cell Lines.....	92
3.3.2.5	Conclusion.....	95
3.3.3	Labelling Optimisation for Flow Cytometry.....	96
3.3.3.1	Tyrp1 Signal Enhancement.....	96
3.3.3.2	Protocol for Tyrp1 Density Quantification.....	99
3.3.3.3	Conclusion.....	101
3.3.4	Density of Surface Tyrp1.....	102
3.3.4.1	Tyrp1 Density on Melanoma Cell Lines.....	102
3.3.4.2	Tyrp1 Density on Primary Melanoma.....	105
3.3.4.3	Conclusion.....	109
<b>3.4</b>	<b>Discussion.....</b>	<b>110</b>
<b>CHAPTER 4: Results: Testing and Optimising the TA99-CAR.....</b>		<b>115</b>
<b>4.1</b>	<b>Introduction.....</b>	<b>115</b>
4.1.1	The Importance of CAR Spacers.....	115
<b>4.2</b>	<b>Aims.....</b>	<b>116</b>
<b>4.3</b>	<b>Results.....</b>	<b>117</b>
4.3.1	Validation of TA99-CAR <i>In Vitro</i> .....	117
4.3.1.1	Engineering of the Human and Murine TA99-CAR.....	117
4.3.1.2	Labelling Optimisation for CAR Detection.....	118
4.3.1.3	Transduction Efficiency of TA99-CAR PBMCs.....	120
4.3.1.4	Cytotoxicity Assay for <i>In Vitro</i> TA99-CAR Validation.....	121
4.3.1.5	Interferon- $\gamma$ Production by TA99-CAR T- cells.....	123
4.3.1.6	Conclusion.....	125
4.3.2	TA99-CAR Spacer Optimisation.....	125
4.3.2.1	Engineering the TA99-CAR with Four Distinct Spacers.....	125
4.3.2.2	Transduction Efficiency of TA99-CAR Spacer Variants.....	126
4.3.2.3	Cytotoxic Capacity Comparison of TA99-CAR Spacers.....	127
4.3.2.4	Interferon- $\gamma$ Production Comparison of TA99-CAR Spacers.....	129
4.3.2.5	Conclusion.....	130
4.3.3	<i>In vitro</i> Validation of the Murine TA99-CAR Efficacy.....	131

4.3.3.1	Splenocyte Transduction Efficiency .....	131
4.3.3.2	Cytotoxic Capacity of Murine TA99-CAR.....	132
4.3.3.3	Conclusion.....	133
4.3.4	B16 Melanoma Tumour Model .....	133
4.3.4.1	Experimental Set up for <i>In Vivo</i> Model .....	134
4.3.4.2	Transduction Efficiency of CAR-Bearing Splenocytes.....	135
4.3.4.3	CAR T-cell Engraftment .....	136
4.3.4.4	<i>In Vivo</i> Model Tumour Volumes .....	137
4.3.4.5	Conclusion.....	140
4.3.5	B16 Transduced with Tyrp1 for Tumour Model .....	141
4.3.5.1	Experimental Set up for <i>In Vivo</i> Model .....	141
4.3.5.2	Transduction Efficiency of CAR-Bearing Splenocytes.....	142
4.3.5.3	CAR-T-cell Engraftment.....	142
4.3.5.4	<i>In Vivo</i> Mouse Model Tumour Volumes.....	143
4.3.5.5	Conclusion.....	145
<b>4.4</b>	<b>Discussion .....</b>	<b>146</b>

## **CHAPTER 5: Results: Manipulating the Affinity of the TA99-CAR to Increase Sensitivity 150**

<b>5.1</b>	<b>Introduction.....</b>	<b>150</b>
5.1.1	Relation of CAR Affinity to Density Sensitivity.....	150
5.1.2	Differentiation and Exhaustion Markers in T-Cells .....	151
5.1.3	Alanine Scanning for Engineering TA99 Mutants .....	152
5.1.4	Surface Plasmon Resonance (SPR) for Kinetic Analysis .....	152
5.1.5	Differential Scanning Fluorimetry (DSF) for Protein Stability Analysis .....	153
<b>5.2</b>	<b>Aims .....</b>	<b>154</b>
<b>5.3</b>	<b>Results .....</b>	<b>155</b>
5.3.1	Production of CDR3 Heavy and Light TA99 Mutants .....	155
5.3.1.1	Alanine Scanning.....	155
5.3.1.2	Crystallographic Structure of TA99 mutants.....	155
5.3.2	Binding Kinetics and Protein Characterisation of TA99 Mutants.....	156
5.3.2.1	Kinetic Profiling of TA99 Mutants .....	156
5.3.2.2	Stability of TA99 Mutants .....	159
5.3.2.3	Conclusion.....	160
5.3.3	Functional Characterisation of TA99-CAR Affinity Gradient.....	161
5.3.3.1	Transduction Efficiency of TA99-CAR Affinity Gradient .....	161
5.3.3.2	Cytotoxic Capacity of TA99-CAR Affinity Gradient .....	162

5.3.3.3	Cytokine Production of TA99-CAR Affinity Variants.....	166
5.3.3.4	Conclusion.....	168
5.3.4	Determining the Differentiation and Exhaustion Status of the Mutant TA99-CAR T-Cells.....	170
5.3.4.1	Differentiation Profile of Mutant TA99-CAR Expressing T-Cells.....	170
5.3.4.2	Exhaustion Profile of Mutant TA99-CAR Expressing T-Cells.....	171
5.3.4.3	Conclusion.....	174
5.3.5	Correlation Between Affinity and Mutant TA99-CAR Efficacy.....	174
5.3.5.1	Analysis of Correlation Between Affinity and CAR Efficacy.....	174
5.3.5.2	Conclusion.....	176
<b>5.4</b>	<b>Discussion .....</b>	<b>178</b>
<b>CHAPTER 6:</b>	<b>Final Discussion .....</b>	<b>183</b>
<b>6.1</b>	<b>Summary of Results on the Tyrp1 Antigen.....</b>	<b>183</b>
<b>6.2</b>	<b>Significance of Results on the Tyrp1 Antigen .....</b>	<b>186</b>
<b>6.3</b>	<b>Summary of Results on the Affinity Correlation to CAR Efficacy .....</b>	<b>188</b>
<b>6.4</b>	<b>Significance of Results on the Affinity Correlation to CAR Efficacy .....</b>	<b>193</b>
<b>6.5</b>	<b>Future Perspectives.....</b>	<b>195</b>
<b>References</b>	<b>.....</b>	<b>197</b>

## LIST OF FIGURES

FIGURE 1: STAGES OF MELANOSOMAL FORMATION. ....	21
FIGURE 2: THE PATHWAY OF MELANIN SYNTHESIS. ....	22
FIGURE 3: THE STRUCTURE OF TYROSINASE RELATED PROTEIN-1 (TYRP1). ....	23
FIGURE 4: MECHANISMS THAT LEAD TO SURFACE LOCALISATION OF TYRP1. ....	28
FIGURE 5: THE STRUCTURE OF THE CHIMERIC ANTIGEN RECEPTOR. ....	32
FIGURE 6: THE KINETIC SEGREGATION MODEL. ....	35
FIGURE 7: AFFINITY RANGE OF PUBLISHED DATA INVESTIGATING THE CORRELATION BETWEEN AFFINITY AND CAR EFFICACY. ....	48
FIGURE 8: REACTION OF PHUSION PCR. ....	53
FIGURE 9: OLIGO ASSEMBLY OF TA99. ....	55
FIGURE 10: GREEN-TO-RED PHOTOCONVERSION OF MEOS. ....	78
FIGURE 11: SEQUENCE OF TA99 HEAVY AND LIGHT CHAINS. ....	82
FIGURE 12: SECRETED TA99-RABBIT Fc. ....	83
FIGURE 13: TYRP1 CONSTRUCTS. ....	84
FIGURE 14: TESTING TA99 BINDING ON TRANSDUCED SUP T1 CELLS WITH INTRACELLULAR LABELLING. ....	86
FIGURE 15: EXTRACELLULAR LABELLING OF SUP T1 CELLS WITH THE TA99 scFv. ....	87
FIGURE 16: COMPARISON OF EXTRACELLULAR ABUNDANCE OF TYRP1 VARIANTS IN SUP T1 CELLS. ....	88
FIGURE 17: CONFOCAL IMAGING OF TYRP1 IN MOUSE METASTATIC MELANOMA CRYOSECTIONS. ....	89
FIGURE 18: LIVE-CELL IMAGING OF T618A CELLS TRANSDUCED WITH PROXIMAL FUSED TO MEOS. ....	91
FIGURE 19: ILLUSTRATION OF TYRP1 VESICLE TRAFFICKING IN ACCORDANCE TO MEMBRANE PROXIMITY. ....	92
FIGURE 20: LABELLING HUMAN MELANOMA CELL LINES FOR SURFACE TYRP1. ....	94
FIGURE 21: OVERLAY FOR THE EXTRACELLULAR LABELLING OF MELANOMA CELL LINES. ....	95
FIGURE 22: HISTOGRAM OVERLAY OF CELLS LABELLED WITH TA99-RABBIT AND TA99-MOUSE IGG2A AMPLIFIED FOR TYRP1 SIGNAL. ....	98
FIGURE 23: ENHANCEMENT OF TYRP1 SIGNAL WITH THE FRASER-PE KIT. ....	99
FIGURE 24: BEAD POPULATIONS BEFORE AND AFTER SIGNAL AMPLIFICATION. ....	101
FIGURE 25: STANDARD CURVE OF DAKO QIFIKIT BEADS FOLLOWING TWO ROUNDS OF FRASER KIT SIGNAL ENHANCEMENT. ....	101
FIGURE 26: SUP T1 AND MELANOMA CELL LINES ENHANCED TWICE WITH FRASER-PE KIT. ....	103
FIGURE 27: TYRP1 DENSITY ON THE CELL SURFACE OF TARGET CELL LINES. ....	105
FIGURE 28: PRIMARY MELANOMA SAMPLES INTERROGATED FOR INTRACELLULAR AND SURFACE EXPRESSION OF TYRP1. ....	108
FIGURE 29: GRAPH ILLUSTRATION OF PRIMARY MELANOMA TYRP1 ANTIGEN DENSITY ON THE CELL SURFACE. ....	109
FIGURE 30: THE Fc SPACER DOMAIN IS DERIVED FROM THE ANTIBODY CONSTANT HEAVY REGION CH2-CH3. ....	118
FIGURE 31: THE STRUCTURE OF THE HUMAN AND MOUSE TA99 CAR. ....	118
FIGURE 32: OPTIMISATION PROTOCOL FOR LABELLING THE TA99-CAR POSITIVE CELLS. ....	120
FIGURE 33: LEVEL OF CAR EXPRESSION IN CELLS TRANSDUCED WITH A CAR TRANSGENE. ....	121

FIGURE 34: <sup>51</sup> CR RELEASE ASSAY WITH TA99-HUMANCAR T-CELLS.....	123
FIGURE 35: IFN- $\gamma$ CYTOKINE PRODUCTION AFTER 24-HOUR CO-CULTURE.....	125
FIGURE 36: FOUR SPACERS WERE ANALYSED FOR IDENTIFICATION OF OPTIMAL TA99-CAR STRUCTURE.....	126
FIGURE 37: TRANSDUCTION LEVELS OF TA99-CAR CELLS BEARING DIFFERENT SPACERS.....	127
FIGURE 38: COMPARISON OF CYTOTOXIC CAPACITY BETWEEN TA99-CARS WITH DIFFERENT SPACER VARIANTS.....	129
FIGURE 39: COMPARISON OF IFN- $\gamma$ PRODUCTION INDUCED BY TA99-CAR SPACER VARIANTS.....	130
FIGURE 40: SPLENOCYTE $\mu$ CAR EXPRESSION LEVELS.....	132
FIGURE 41: CYTOTOXIC CAPACITY OF TA99- $\mu$ CAR T-CELLS.....	133
FIGURE 42: B16 <i>IN VIVO</i> MELANOMA MODEL OUTLINE.....	135
FIGURE 43: CAR EXPRESSION LEVEL IN TRANSDUCED SPLENOCYTES.....	136
FIGURE 44: T-CELL ENGRAFTMENT SEVEN DAYS POST T-CELL INOCULATION.....	137
FIGURE 45: TUMOUR VOLUME AND SURVIVAL OF B16 MELANOMA TUMOUR MICE TREATED WITH CAR-TRANSDUCED SPLENOCYTES.....	138
FIGURE 46: CD8 <sup>+</sup> CAR T-CELL TUMOUR INFILTRATING LYMPHOCYTES.....	139
FIGURE 47: GRANZYME B EXPRESSION IN CD8 <sup>+</sup> CAR T-CELLS.....	140
FIGURE 48: OUTLINE FOR B16 TRUNC <i>IN VIVO</i> MELANOMA MODEL.....	141
FIGURE 49: TA99- $\mu$ CAR EXPRESSION LEVEL IN TRANSDUCED SPLENOCYTES.....	142
FIGURE 50: CD4 AND CD8 CAR-BEARING T-CELLS IN THE CIRCULATING BLOOD OF B16 MELANOMA MOUSE MODEL ANIMALS.....	143
FIGURE 51: TUMOUR VOLUME AND SURVIVAL CURVE FOR THE B16 TRUNC <i>IN VIVO</i> MOUSE MODEL.....	144
FIGURE 52: CD8 CAR T-CELL TUMOUR INFILTRATING LYMPHOCYTES IN TUMOUR MICROENVIRONMENT.....	145
FIGURE 53: THE PRINCIPLE OF SURFACE PLASMON RESONANCE.....	153
FIGURE 54: THE SEQUENCE OF THE HEAVY AND LIGHT CDR3 MUTANTS OF TA99 scFv.....	155
FIGURE 55: STRUCTURAL HOMOLOGY MODEL OF THE TA99 MUTANTS.....	156
FIGURE 56: SENSOGRAMS ILLUSTRATING THE BINDING KINETICS OF THE TA99 WT AND MUTANT scFvs.....	157
FIGURE 57: KINETIC CHARECTERISATION OF THE BINDING OF WT AND MUTANT TA99 scFvs.....	158
FIGURE 58: DENATURATION TEMPERATURE OF TA99 VARIANTS.....	160
FIGURE 59: TRANSDUCTION EFFICIENCY OF T-CELLS BEARING THE TA99 AFFINITY VARIANTS.....	162
FIGURE 60: CYTOTOXIC CAPACITY OF THE TA99-CAR AFFINITY GRADIENT AT D1.....	164
FIGURE 61: CYTOTOXIC CAPACITY OF THE TA99-CAR AFFINITY GRADIENT AT D7.....	165
FIGURE 62: IFN- $\gamma$ PRODUCTION OF THE TA99-CAR AFFINITY GRADIENT.....	167
FIGURE 63: IL2 PRODUCTION OF THE TA99-CAR AFFINITY GRADIENT.....	168
FIGURE 64: DIFFERENTIATION PROFILE OF MUTANT TA99-CAR EXPRESSING T-CELLS.....	171
FIGURE 65: EXHAUSTION PROFILE OF MUTANT TA99-CAR EXPRESSING T-CELLS.....	173
FIGURE 66: CORRELATION BETWEEN AFFINITY AND EFFICACY OF THE TA99-CAR MUTANTS.....	176

## LIST OF TABLES

TABLE 1: SUMMARY OF STUDIES DESCRIBING TYRP1 EXPRESSION IN MELANOMA. ....	25
TABLE 2: AFFINITY OF CAR scFV IN CLINICAL TRIALS. ....	45
TABLE 3: STUDIES ON AFFINITY CORRELATION TO CAR EFFICACY. ....	49
TABLE 4: PRIMARY PCR (PHUSION PCR). ....	54
TABLE 5: PHUSION PCR (PHUSION PCR). ....	54
TABLE 6: PRIMARY PCR (OLIGO ASSEMBLY). ....	55
TABLE 7: SECONDARY PCR (OLIGO ASSEMBLY). ....	56
TABLE 8: BUFFER REQUIRED FOR PROTEIN PURIFICATION. ....	58
TABLE 9: TRANSFECTING 293T FOR ANTIBODY SECRETION ....	62
TABLE 10: TRIPLE TRANSFECTION OF 293T FOR RETROVIRAL PRODUCTION. ....	64
TABLE 11: TRANSFECTING PHOENIX ECO CELLS FOR PRODUCTION OF ECOTROPIC RETROVIRUS. ....	64
TABLE 12: ANTIBODIES USED FOR PRIMARY MELANOMA CELL LABELLING: PANEL NO1. ....	66
TABLE 13: ANTIBODIES USED FOR PRIMARY MELANOMA CELL LABELLING: PANEL NO2. ....	66
TABLE 14: PANEL FOR FLOW-CYTOMETRY BASED KILLING ASSAY. ....	70
TABLE 15: PANEL FOR T-CELL DIFFERENTIATION PROFILE. ....	71
TABLE 16: PANEL FOR T-CELL EXHAUSTION PROFILE. ....	71
TABLE 17: ANTIBODIES FOR IN VIVO T CELL ENGRAFTMENT SCREENING. ....	74
TABLE 18: MEAN INTENSITY VALUES OF VESICLES IN CORRELATION TO MEMBRANE PROXIMITY OVER TIME. ....	92
TABLE 19: DENSITY OF SURFACE TYRP1 DENSITY ON MELANOMA CELL LINES. ....	104
TABLE 20: TYRP1 DENSITY OF PRIMARY MELANOMA SAMPLES. ....	108
TABLE 21: EXPRESSION PATTERN OF DIFFERENTIATION MARKERS. ....	151
TABLE 22: KINETIC PROFILING OF TA99 MUTANTS AND WT. ....	159

## ABBREVIATIONS

ABC	Antibody Binding Capacity
ACT	Adoptive Cell Therapy
AICD	Antigen-Induced Cell Death
ALL	Acute Lymphoblastic Leukaemia
AP	Adaptor Protein
BCMA	B-Cell Maturation Antigen
BCR	B-Cell Receptor
BiTE	Bispecific T-cell Engagers
BLOC	Biogenesis of Lysosome-Related Organelles Complex
BSA	Bovine Serum Albumin
CAR	Chimeric Antigen Receptor
CCR7	C-C chemokine receptor 7
CD	Cluster of Differentiation
CDR	Complementary Determining Region
CLL	Chronic Lymphocytic Leukaemia
Cr	Chromium
D	Day
DAPI	4',6-diamidino-2-phenylindole
DLS	Dynamic Light Scattering
DMSO	Dimethyl sulfoxide
DSF	Differential Scanning Fluorimetry
Eco	Ecotropic
eGFP	Enhanced Green Fluorescent Protein
EGFR	Epidermal Growth Factor Receptor
ELISA	Enzyme Linked Immunosorbent Assay
Fab	Fragment Antigen Binding
FBK	Flow-cytometry Based Killing
Fc	Fragment Crystallisable
FCS	Foetal Calf Serum
GzmB	Granzyme B
HER2	Human Epidermal Growth Factor Receptor 2
HLA	Human Leukocyte Antigen
ICOS	Inducible T-cell COStimulator
IFN- $\gamma$	Interferon- $\gamma$
IL2	Interleucin 2
ITAM	Immunoreceptor Tyrosine Activation Motif
L	Linker
LAT	Linker of Activated T-Cells
LB	Luria Bertani broth

Lck	Lymphoid-specific Cytosolic protein tyrosine Kinase
LN	Lymph Node
MCAM	Melanoma Cell Adhesion Molecule
MCSP	Melanoma-associated Chondroitin Sulfate Proteoglycan
MHC	Major Histocompatibility Complex
MITF	Microphthalmia-associated transcription
MM	Metastatic Melanoma
muCAR	Murine CAR
Nck	Non-Catalytic Tyrosine Kinase
NK	Natural Killer
NT	Non-Transduced
PAGE	PolyAcrylamide Gel Electrophoresis
PBMCs	Peripheral Blood Mononuclear Cells
PBS	Phosphate-Buffered Saline
PCR	Polymerase Chain Reaction
PD-1	Programmed Cell Death Protein 1
PD-L1	Programmed Cell Death Protein Ligand 1
PFA	Paraformaldehyde
Pmel17	Pro-MELanosome Protein 17
Rab	Ras superfamily of monomeric G proteins
RFU	Relative Fluorescence Units
RT	Room Temperature
SB	Super Block
scFv	Single Chain Variable Fragment
SDS	Sodium Dodecyl Sulphate
SG	Serine-Glycine
SPR	Surface Plasmon Resonance
TB	Terrific Broth
TBE	Tris, Boric acid, EDTA
Tcm	Central Memory T-Cell
TCR	T-Cell Receptor
Tem	Effector Memory T-cell
TIL	Tumour Infiltrating Lymphocyte
Tim3	T cell immunoglobulin and mucin-domain-containing molecule 3
Tnaive	Naïve T-cell
TNFR	Tumour Necrosis Factor Receptor
Trunc	Truncated
Tscm	Stem-Cell Memory T-Cell
Tyrp1	Tyrosinase-Related Protein 1
WT	Wild-Type

Zap-70

ζ-Chain Associated Protein Tyrosine Kinase 70

# **CHAPTER 1:**

## **Introduction**

## **CHAPTER 1: INTRODUCTION**

### **1.1 MELANOMA**

According to NHS, 13,000 people are diagnosed with melanoma annually, leading to 2,000 deaths per year. Melanoma has been characterized as a chemo-resistant malignancy (Soengas and Lowe, 2003), rendering therapy challenging. The 5-year survival percentage depends on the tumour stage at the time of diagnosis. Patients diagnosed and submitted to surgery at stage I, have 90-100% probability of 5-year survival. However, the 5-year survival rates for patients with stage III metastatic disease is approximately 30% (Balch et al., 2009).

Melanoma is caused by the uncontrolled proliferation of melanocytes. Melanocytes are the cells specialised in producing melanin, and they are present in the epidermis, in the iris, and also in stria vascularis of the ear (Bertolotto, 2013). The role of melanin is to prevent damage imposed by UV irradiation (Kollias et al., 1991), and to mitigate the oxidative stress caused by reactive oxygen species (Rózanowska et al., 1999).

### **1.2 SYSTEMATIC THERAPIES AND CLINICAL TRIALS**

Surgery constitutes the main melanoma treatment. The stage of the disease determines the therapeutic strategy to be followed. Different therapeutic categories are surgery, immunotherapy, and chemotherapy (Bertolotto, 2013)(Berrocal et al., 2014).

Excision of stage I or II melanomas leads to a 10-year survival of 93% of the patients (Balch et al., 2009). In more advanced disease stages, patients undergo additional therapies such as chemotherapy and immunotherapy. Chemotherapy agents are usually combined for increased efficacy. Dacarbazine is an alkylating agent approved by FDA for melanoma treatment. However, only 2% of patients experience a complete remission (Hill et al., 1984). A combination regimen includes dacarbazine, cisplatin and vinblastine. Cisplatin is a platinum-based drug, which cross-links to DNA, and vinblastine is an anti-microtubule drug. The combination therapy leads to median survival rate of average 9 months (Legha, 1997). To enhance the anti-tumour effect, Interferon- $\alpha$  (IFN $\alpha$ ) and Interleucin-2 (IL2) were incorporated into the above

combination treatment for a phase II clinical trial. However, the combination of these five therapeutic regimens did not increase the overall survival of the patients (Legha et al., 1996).

Small molecule inhibitors constitute an expanding field for melanoma treatment, mainly targeting the RAS/RAF/MEK pathway. It has been reported that 48% of melanoma patients bear a V600E BRAF mutation (Long et al., 2011). Vemurafenib is a small molecule inhibitor, which specifically recognises a BRAF point mutation (Tsai et al., 2008). A phase II clinical trial of patients bearing this point mutation treated with vemurafenib showed an overall survival of 16 months (Sosman et al., 2012), compared to patients treated with systemic therapies that have an overall survival of 6-10 months (Falkson et al., 1998)(Chapman et al., 1999)(Atkins et al., 2008). The response rate in this cohort of patients was 50% (Chapman et al., 2011). Trametinib is a MEK inhibitor, and its benefit has been investigated in clinical trials for melanoma patients. Although trametinib treatment led to 40% partial response in patients bearing BRAF mutations, the partial response for the BRAF-wild type patients was only 10% (Falchook et al., 2012). In contrast, a different small molecule inhibitor, YM155, that targets survivin, a protein that suppresses apoptosis (Ambrosini et al., 1997) was unsuccessful with only 1 patient responding among the 34 recruited in a phase II clinical trial (Lewis et al., 2011). Elesclomol, which is also a small molecule drug, induces formation of reactive oxygen species (Foley et al., 2007). In a phase II trial, it was showed that the response rate for the cohort that received elesclomol plus chemotherapy was 15.1%, versus a 3.6% response rate for the cohort that only received chemotherapy (O'Day et al., 2009).

Apart from small molecules, Immunotherapeutic strategies that block immune checkpoints have been tested. Immune checkpoints are pathways that inhibit T-cell proliferation and cytotoxicity (Pardoll, 2012). Ipilimumab is a monoclonal antibody that constitutes a blockade for such checkpoints, and is approved for melanoma therapy. Ipilimumab blocks Cytotoxic T-lymphocyte-associated antigen 4 (CTLA-4), a receptor expressed on T-cells that upon engagement acts as a negative regulator (Schwartz, 1992). A phase III clinical trial for Ipilimumab showed the overall survival was approximately 4 months longer than that of the control group (Hodi et al., 2010).

The mechanism of function is similar for Pembrolizumab, an anti-PD-1 antibody. This monoclonal antibody binds the PD-1 receptor on T-cells (Okazaki and Honjo, 2007). The T-cell inactivation caused by PD-1 to PD-L1 interaction expressed on tumour cells is hindered in patients treated with Pembrolizumab. The overall response rate with Pembrolizumab was 26% for Ipilimumab refractory patients in a phase I clinical trial (Robert et al., 2014). The above therapies increase the overall survival for the patients, but do not constitute disease treatment. A few of the adverse effects are fatigue, rash, alopecia, nausea and vomiting (Palathinkal et al., 2014).

Although it is not part of the systemic therapy for melanoma, Adoptive Cell Therapy (ACT) has been tested for anti-tumour effects. The first approach implemented the *in vitro* expansion of Tumour Infiltrating Lymphocytes (TIL) and administration of the TILs back to the patients (Rosenberg et al., 1994). Despite the promising results, the invasiveness of the procedure and the small success rate of isolating TILs prevents the procedure from becoming a large-scale systemic therapy. This can be circumvented by administrating T-cells that have been *in vitro* transduced to express a T-cell Receptor (TCR) or a Chimeric Antigen Receptor (CAR). Anti-NY-ESO-1 TCR expressing T-cells led to a response in 50% of melanoma patients (Robbins et al., 2011). Multiple anti-melanoma CAR T-cell therapies are being developed, but haven't been tested in a clinical trial yet (Burns et al., 2010, Yvon et al., 2009, Lo et al., 2010, Schmidt et al., 2011).

Several approaches have been developed for treating melanoma including chemotherapy, immunotherapy, and ACT. Recent advances increase the survival rate for a span of a few months, nevertheless they fail to induce complete response. This demonstrates that a new, targeted and efficient strategy to target melanoma is necessary. Since melanoma derives from melanocytes, focusing on melanocytes provides insight into potential targets for melanoma specific therapies.

### **1.3 MELANOSOME DEVELOPMENT AND MELANIN SYNTHESIS**

Adoptive TCR or CAR therapy for the treatment of melanoma requires a specific protein target. Here we discuss some of the key proteins involved in melanosome development and melanin synthesis. Melanocytes produce a plethora of melanocyte-

specific proteins. These proteins are components of the melanosomes, organelles specialized in producing melanin. Melanosomes are derived from the membrane of the endoplasmic reticulum (Maul, 1969), and develop in four stages Figure 1 (Seiji et al., 1963) (Marks and Seabra, 2001). Stages I and II mark the beginning and completion of protein fibrils formation, upon which melanin is stored. Melanin production and deposition commences at stage III, and by stage IV the fibrils are masked due to the abundance of melanin.

Key components of the melanosome are the proteins responsible for the fibril formation, and the enzymes employed in melanin production. The fibril striations are formed by polymerization of the Pro-MELanosome Protein 17 (Pmel17) or gp100 M $\alpha$  subunit (Berson et al., 2001). Pmel17 is enriched in melanosome stages I and II. On the other hand, the melanosomal enzymes accumulate in melanosomes at stages III and IV. The enzymes are tyrosinase, Tyrosinase Related Protein-1 (Tyrp1), and Tyrosinase Related Protein-2 (Tyrp2) also known as DOPAchrome tautomerase (Raposo et al., 2001). All three enzymes are transmembrane type I proteins residing on the melanosomal membrane, and contain a cysteine-rich domain, EGF-like, present on cell membrane proteins (Jackson et al., 1992).

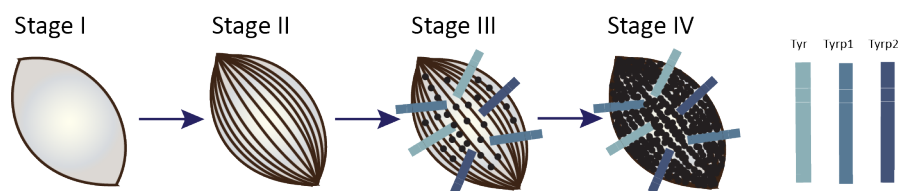


**Figure 1: Stages of melanosomal formation.** Melanosomes are the organelles producing melanin. The organelle formation occurs in four distinct stages. In stages I and II the fibril striations are created by the polymerisation of Pmel M $\alpha$  subunit. Once these striations have been successfully formed, the enzymes Tyrosinase, Tyrp1 and Tyrp2 are delivered to the melanosome. The production of melanin commences at stage III. Melanin is stored upon the fibril striations. Based on (Seiji et al., 1963).

Tyrosinase is the key enzyme for melanin synthesis (Raper, 1927), which converts tyrosine to 3,4-dihydroxyphenylalanine (DOPA), and subsequently to DOPAquinine (Mason, 1948). The substrate for Tyrp2 is DOPAchrome (Aroca et al., 1991). Tyrp2 catalyses the isomerization of DOPAchrome to 5,6-dihydroxyindole-2-carboxylic acid (DHICA) (Tsukamoto et al., 1992). The function of Tyrp1 is the least understood. It has been reported that Tyrp1 plays a role in oxidizing DHICA to the indole-5,6-quinone carboxylic acid intermediate (Kobayashi et al., 1994a, Kobayashi et al., 1994b).

Additionally, Tyrp1 mutations influence the degradation rate of tyrosinase, revealing the role of Tyrp1 in tyrosinase stabilization (Kobayashi et al., 1998). The same research group confirmed this finding, by demonstrating the formation of tyrosinase-Tyrp1 heterodimers (Kobayashi and Hearing, 2007).

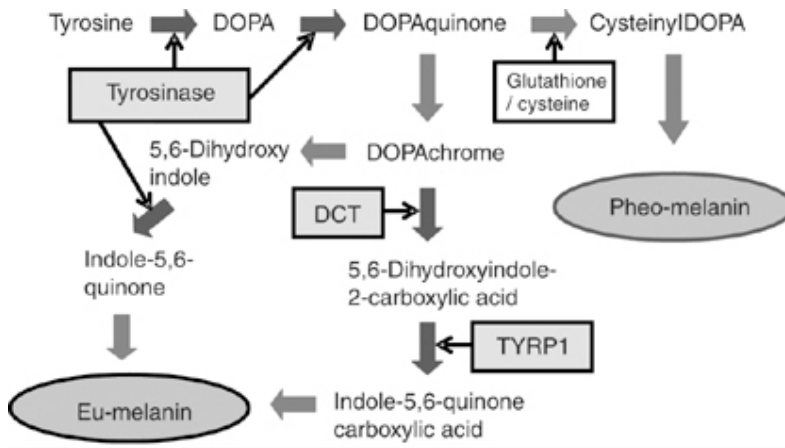


**Figure 2: The pathway of Melanin Synthesis.** Melanin is produced through a reaction cascade. Tyrosinase is the key enzyme, which catalyses the initial substrate. It initially hydroxylates tyrosine to DOPA, and then oxidizes DOPA to DOPAquinone. Melanin synthesis diverges after DOPAquinone for production of either eu-melanin or pheo-melanin. DOPAquinone is converted to DOPAchrome. Tyrp2 isomerizes the latter to the intermediate DHICA (5,6-dihydroxyindole-2-carboxylic acid). Subsequently, Tyrp1 catalyses DHICA to a melanin precursor, and finally the precursor is converted to eu-melanin (Ando et al., 2007).

#### 1.4 TYROSINASE-RELATED PROTEIN 1 AS A POTENTIAL TARGET FOR CAR THERAPY

Attempts to identify the genomic locus of tyrosinase led to the identification of a novel tyrosinase-related protein, named tyrosinase-related protein 1 (Jackson, 1988). Despite Tyrp1 being an intracellular antigen, anti-Tyrp1 antibodies were detected in the serum of melanoma patients (Mattes et al., 1983). Approximately 6% of vitiligo patients also develop auto-antibodies against Tyrp1 (Kemp et al., 1998).

Tyrp1 is a 537aa type I transmembrane protein residing on the membrane of mature melanosomes. The amino acid terminus (1-477aa) consists of a signal peptide and the luminal domain, which mediates the enzymatic activity (Figure 3). The amino acids 478-501 form the transmembrane domain, and the cytoplasmic domain is constituted by the amino acids 502-537 (Vijayasradhi et al., 1995). According to Vijayasradhi's studies, the cytoplasmic domain contains a di-leucine signal that mediates the intracellular retention and sorting of Tyrp1. Ablation of this signal (NQPLLTD) results in impaired Tyrp1 trafficking, which leads to the presence of the

protein on the cell surface. When the melanosome fuses with the cell surface the luminal domain becomes extracellular, and similarly the cytoplasmic domain becomes intracellular (Yiqing Xu et al., 1997). There is also a secreted form of Tyrp1, which lacks cytoplasmic and transmembrane domain, as well 11aa of the luminal domain (Yiqing Xu et al., 1997). Secreted Tyrp1 could constitute a hurdle for anti-Tyrp1 CAR therapy, since the secreted protein could bind to the CAR and hinder its binding to the Tyrp1 expressing cells. The concentration of Tyrp1 in the bloodstream is unknown.

### Tyrosinase-Related Protein 1

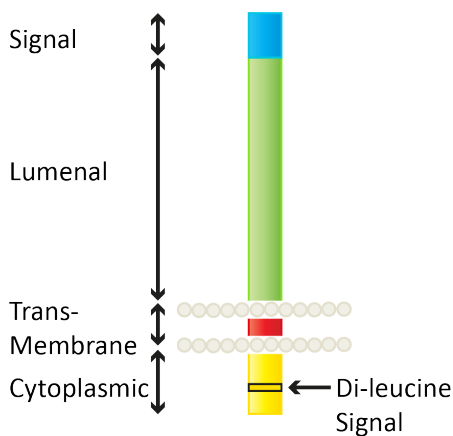


**Figure 3: The structure of Tyrosinase Related Protein-1 (Tyrp1).** Tyrp1 is a type I transmembrane protein, which consists of a cytoplasmic, a transmembrane, and a luminal domain. The cytoplasmic domain protrudes from the melanosome into the cytoplasm, and bears the di-leucine signal that is recognised by carrier proteins for successful delivery of Tyrp1 to the melanosome. The transmembrane domain anchors Tyrp1 to the melanosomal membrane. Finally, the luminal domain resides inside the melanosome, and bears the catalytic activity of Tyrp1. Based on Vijayasaradhi et al., 1995.

The enzymatic activity of Tyrp1 is disputed. Although, it has been reported that Tyrp1 oxidizes DHICA to the indole-5,6-quinone carboxylic acid intermediate (Kobayashi et al., 1994a, Kobayashi et al., 1994b), it also appears to play an important role in the stabilisation of tyrosinase, by binding it and forming heterodimers (Kobayashi et al., 1998, Kobayashi and Hearing, 2007). Tyrp1 mutations lead to retention of tyrosinase in the endoplasmic reticulum and degradation of the protein (Toyofuku et al., 2001). Tyrp1 mutation or down-regulation leads to reduced levels of tyrosinase, thus lack of pigmentation on progressed melanoma metastases (Watabe et al., 2004).

Tyrp1 is the most abundant protein in melanocytes and pigmented melanoma cell lines (Tai et al., 1983). Furthermore, anti-Tyrp1 antibodies provide the most sensitive

and reliable melanocyte identification, as well as delineation of melanoma margins (Bhawan, 1997)(Dean et al., 2002). Staining of frozen healthy skin sections showed that Tyrp1 is the most prominent protein (Virador et al., 2001). Nevertheless, the published data introduce a contradiction regarding the prevalence of Tyrp1 expression in melanoma. For example, another observation of the latter study was the heterogeneous expression pattern of all melanoma markers (tyrosinase, Tyrp2, Pmel17) including Tyrp1 (Virador et al., 2001). Chen and colleagues showed that Tyrp1, tyrosinase and Pmel were expressed on 50%, 69%, and 75% respectively of the 16 melanoma samples analysed (Chen et al., 1995). In agreement to that finding, another study demonstrated that Tyrp1 was highly expressed in 60% of malignant melanoma samples (Bolander et al., 2008). Bolander et al also showed that Tyrp1 is more frequently expressed in progressed primary melanoma. On the contrary, in metastatic melanoma Tyrp1 was higher in earlier stages of the lesion. In detail, of the Tyrp1 positive primary melanomas 24%, 28%, and 36% were grade I, II, and III. Of the Tyrp1 positive metastatic melanomas 42%, 25%, and 19% were grade I, II, and III (Bolander et al., 2008).

Uveal melanomas express higher levels of the melanoma markers including Tyrp1. Sixty-five percent of uveal melanoma samples expressed high levels of Tyrp1 (>75%). Out of 4 metastatic uveal melanoma analysed, two samples showed low, and one showed high Tyrp1 expression (de Vries et al., 1998).

It is unclear whether Tyrp1 plays a role in melanoma progression. According to studies by Bolander, Tyrp1 expression is inversely correlated with cancer progression (Bolander et al., 2008). In agreement to that, Tyrp1 is down-regulated in amelanotic melanoma cell lines (Watabe et al., 2004), and in the amelanotic stages of mouse melanoma models (Orlow et al., 1998). On the other hand, according to a preceding publication, Tyrp1 is positively correlated with tumour stage and progression (Holzmann et al., 1987). Finally, Tyrp1 expression on skin metastases constitutes a poor prognostic marker (Journe et al., 2011). The conclusions on the aforementioned studies are summarised in Table 1.

**Table 1: Summary of studies describing Tyrp1 expression in melanoma.**

Observation	Publication
Tyrp1 most abundant protein in melanocytes and pigmented melanoma cell lines	(Tai et al., 1983)
Tyrp1 best marker for melanoma margin delineation	(Bhawan, 1997) (Dean et al., 2002)
Tyrp1 expressed on 60% of melanoma samples	(Bolander et al., 2008)
Tyrp1 highly expressed on 65% of primary uveal melanomas	(de Vries et al., 1998)
Tyrp1 highly expressed on 50% (2/4) of metastatic uveal melanomas	(de Vries et al., 1998)
Expression pattern of Tyrp1 heterogeneous in melanoma samples	(Virador et al., 2001)
Tyrp1 expressed on 50% of melanoma samples	(Chen et al., 1995)
Inverse correlation between tyrp1 expression and tumour progression	(Bolander et al., 2008)
Positive correlation of Tyrp1 expression and melanoma progression	(Holzmann et al., 1987)

### 1.5 TARGETING TYRP1 USING TA99 ANTIBODY

Tyrp1 is an intracellular protein, thus it is surprising that melanoma patients have been reported to develop auto-antibodies against Tyrp1 (Mattes et al., 1983, Kemp et al., 1998). The role of Tyrp1 trafficking to the surface is unknown. In order to further study the role of Tyrp1 in melanoma, Thomson and colleagues developed the first monoclonal Tyrp1 antibody (Thomson et al., 1985). The antibody was obtained by immunizing mice with the melanoma cell line SK-MEL-23. TA99 was the isolated anti-Tyrp1 IgG2a antibody clone. This antibody recognises both human and murine Tyrp1 (Thomson et al., 1985).

TA99 was radiolabelled, in order to visualise melanoma tumours in Swiss nu/nu mice. The premise was that intracellular antigen would be exposed in necrotic tissue. In order to explore the theory, the TA99 antibody was labelled with iodine-125, the half-life of which is 60 days (True, 2001). Although the imaging was originally obscured by circulating antibody, by day 13, it showed clear localization of <sup>125</sup>I-TA99 at the tumour site (Welt et al., 1987).

A subsequent study showed that TA99 could eradicate tumours in mouse models (Hara et al., 1995). TA99 administration caused rejection of B16F10 subcutaneous and lung-metastatic tumours in C57BL/6 mice. TA99 tumour lysis is complement independent (Hara et al., 1995), and is mediated by innate immune cells expressing

Fcγ receptors (Boross et al., 2012). Since the first demonstration of the TA99 anti-tumour capacity, there have been several studies exploiting TA99 in combination with other regimens in mice. TA99 has been coupled with anti-Vascular Endothelial Growth Factor Receptor (VEGFR) antibody or Pmel17 peptide vaccine (Patel et al., 2008, Ly et al., 2013). It is intriguing that TA99, an antibody recognising the intracellular protein Tyrp1, bears anti-tumour activity. This unexpected result was the first indication of Tyrp1 presence on the cell surface. Additionally, the successful TA99-mediated tumour eradication in these studies shows that Tyrp1 would constitute a promising target for melanoma treatment.

## 1.6 TYRP1 TRAFFICKING

One possible explanation for the observed efficacy of TA99 in tumour rejection is the presence of Tyrp1 on the cell surface. In accordance to this conjecture, B16F10 melanoma cells were positive for surface Tyrp1. However, cells freshly isolated from tumours displayed higher level of surface protein than the ones cultured *in vitro* (Takechi et al., 1996). A following study confirmed that 2% of total Tyrp1 is present on the plasma membrane (Yiqing Xu et al., 1997).

Tyrp1 follows the secretion pathway through the endoplasmic reticulum, and Golgi. Following the exit from the trans-Golgi, Tyrp1 is transferred to early endosomes. From the early endosomes Tyrp1 is delivered to the melanosomes via vesicles. Several carrier proteins that play a role in Tyrp1 trafficking have been characterised. Firstly, Tyrp1 bears a di-leucine signal in its cytoplasmic domain, which facilitates intracellular sequestration and trafficking to the melanosomes. Ablation of the di-leucine signal leads to increased levels of the protein on the cell surface (Vijayasaradhi et al., 1995). This signal is recognised by Adaptor Protein-1 (AP-1) (Theos et al., 2005). Adaptor proteins interact with clathrin-coated vesicles and bind the protein cargo for trafficking (Nakatsu and Ohno, 2003). AP-1 is not exclusive to melanocytes, and has been shown to play a role in recycling receptors to the cell surface (Deneka et al., 2003).

Biogenesis of lysosome-related organelles complex-1 (BLOC-1) is a protein complex crucial for the formation of organelles such as melanosomes (Falcón-Pérez et al.,

2002). Ablation of BLOC-1 subunits affects the trafficking of Tyrp1, with Tyrp1 being trapped on the cell membrane or endosomal vacuoles instead of melanosomes (Setty et al., 2007). BLOC-2 complex deficiency similarly results in mis-localisation of Tyrp1 and tyrosinase, but does not affect Pmel17 (Helip-Wooley et al., 2007).

GTPase Rab proteins are crucial for vesicle transport and protein trafficking (Bhuni and Roy, 1996). In contrast to the carrier proteins mentioned above, which are key components of post-Golgi protein trafficking in a broad spectrum of cell lineages, Rab32 and Rab38 are expressed only in cells with lysosome-related organelles. These organelles are melanosomes, granules of mast cells or platelet cells, lytic granules of T-cells, and lamellar bodies of lung epithelial cells (Cohen-Solal et al., 2003, Zhang et al., 2011). The implication of Rab38 to melanosomal protein trafficking was established by Loftus and colleagues, by showing that mutation of Rab38 impaired Tyrp1 trafficking (Loftus et al., 2002). Rab32/Rab38 are required for transfer of both tyrosinase and Tyrp1 to the melanosomes, however Tyrp2 seems to be dependent only on Rab32 (Wasmeier et al., 2006). The Rab proteins interact with the other components of the trafficking network, such as AP-1, AP-3 and BLOC complexes to fine tune the transfer of the melanosomal proteins to melanosome (Bultema et al., 2012).

The ubiquitous machinery of melanosomal protein sorting works effectively, but individual components affect trafficking of individual proteins differently. Despite the elucidation of trafficking machinery, it is still unknown how and when Tyrp1 escapes to the cell membrane. It has been reported that Pmel17 is transferred to the melanosome directly or indirectly through the cell surface (Valencia et al., 2006), but there are no similar reports explaining the presence of Tyrp1 on the plasma membrane. There are several theories explaining why Tyrp1 is present on the surface, presented on Figure 4. Tyrp1 could have an indirect trafficking path for reaching melanosomes through the membrane, similarly to Pmel17 (Figure 4, Red arrow). Alternatively, high production levels of the protein might saturate the trafficking machinery, leading to Tyrp1 escaping to the cell surface (Figure 4, Purple arrow). Another theory is that Tyrp1 escapes to the cell surface when the melanosome is fusing with the plasma membrane for melanin release (Jimbow et al., 1997) (Figure

4, Blue arrow). A recent study showed that when surface Tyrp1 gets internalized, only a small percentage gets transferred to melanosomes, with the majority being recycled back to the membrane (Truschel et al., 2009) (Figure 4, Red arrow). These findings contradict the first theory of an alternative indirect route of Tyrp1 trafficking.

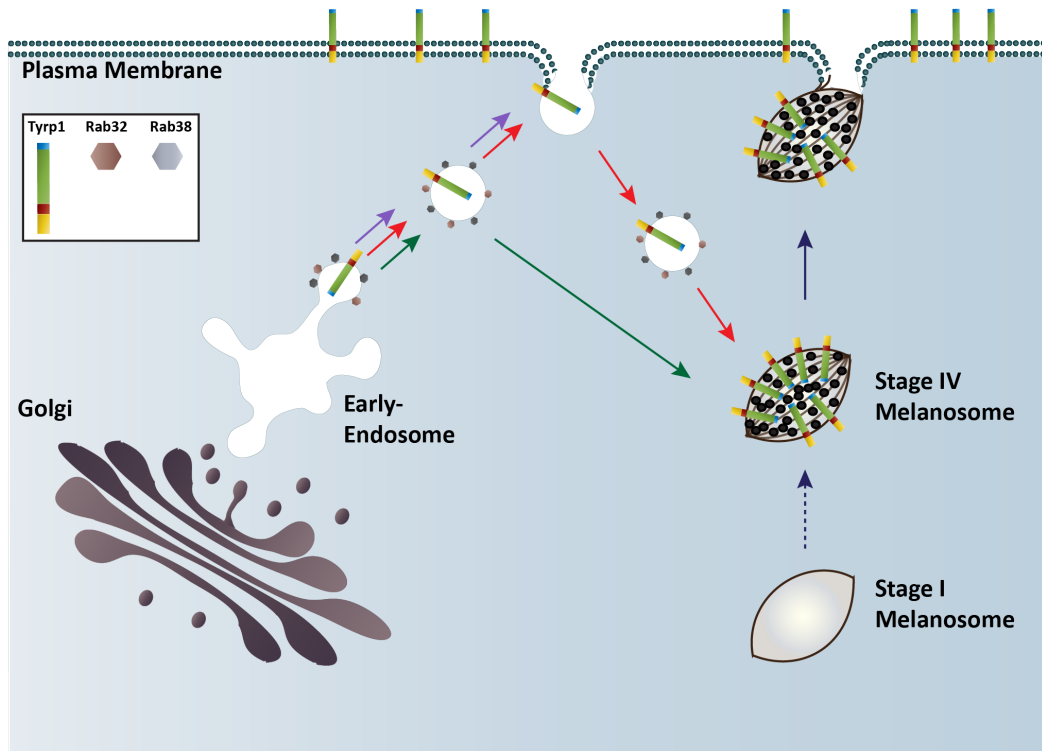


**Figure 4: Mechanisms that lead to surface localisation of Tyrp1.** Based on current research data, Tyrp1 is transferred directly to the melanosomes (Green arrow). Although Tyrp1 has been reported to escape to the cell surface, the mechanism has not been identified. One possibility is an alternative indirect pathway (Red arrow). Saturation of the secretion pathway due to Tyrp1 overexpression can lead to mis-localization of the protein to the cell surface. A third theory includes the fusion of melanosome with the membrane for melanin release (Blue arrow). This way the melanosomal proteins, residing in the melanosomal membrane, become part of the plasma membrane. The luminal domain becomes extracellular, and the cytoplasmic domain becomes the intracellular domain. Finally, the speculation that Tyrp1 is indirectly transferred to melanosomes was rejected by a recent study (Truschel et al., 2009). They showed that a cohort of Tyrp1 is transferred to the membrane instead of the melanosome.

Tyrp1 is expressed on approximately 50% of primary cutaneous melanomas, and 60% of primary uveal melanomas (Chen et al., 1995)(de Vries et al., 1998). However, it is contradictory whether Tyrp1 is inversely or positively correlated to tumour stage and progression (Orlow et al., 1998) (Holzmann et al., 1987). Melanoma and vitiligo patients secrete auto-antibodies against tyrp1, which indicates the presence of cell surface Tyrp1 (Mattes et al., 1983, Kemp et al., 1998). It is intriguing that an anti-Tyrp1 antibody, TA99, caused tumour rejection in B16 melanoma mouse model (Hara et al., 1995). After the Hara and colleagues demonstration of TA99-mediated tumour

eradication, TA99 was successfully used in other studies in combination with other therapies (Patel et al., 2008, Ly et al., 2013). Although, surface Tyrp1 is not exclusive to tumour cells but also present in healthy melanocytes, the toxicity is expected to be limited. This is based on precedent of anti-melanocyte marker (Melan-A) TCR expressing T-cells that were used in a phase I clinical study, with minimum toxicity observed (Mackensen et al., 2006). The presence of Tyrp1 on the plasma membrane, in combination with the anti-Tyrp1 successful melanoma eradication, delineates Tyrp1 as a promising target of adoptive T-cell therapy.

## 1.7 CHIMERIC ANTIGEN RECEPTORS

It is intriguing that the intracellular protein Tyrp1 is present on the cell surface (Yiqing Xu et al., 1997), and that anti-Tyrp1 therapy led to tumour rejection in mice (Hara et al., 1995). Our aim is to exploit the surface-Tyrp1, a marker unique to melanosomes, by using it as a melanoma target for adaptive T-cell therapy.

The adaptive immune system is comprised of B- and T-lymphocytes. The effector function of B-cells can vary between antibody production and antigen presentation (Lesley et al., 1971)(Naradikian et al., 2016). T-cells are the thymus-derived adaptive immune lymphocytes. Thymus aplasia leads to viral infection susceptibility, as it was first reported in 1965 (Cooper et al., 1965). The role of T-cells is to eliminate pathogen infected cells and cancer cells (Williams and Bevan, 2007). CD4 helper T-cells prime the cytotoxic CD8 T-cells, primary through the secretion of cytokines (Ridge et al., 1998)(Shankaran et al., 2001). The T-Cell Receptor (TCR) binds an antigenic peptide presented on Major Histocompatibility Complex (MHC) I or II. The co-receptors CD8 and CD4 bind either the MHC I or II respectively, and thus stabilise the interaction of the TCR to the MHC (Wooldridge et al., 2005).

### 1.7.1 The Structure of the T-Cell Receptor

The TCR bestows the T-cell specificity, and is composed of a heterodimer of either alpha/beta ( $\alpha\beta$ ) or gamma/delta ( $\gamma\delta$ ) chains. The  $\gamma\delta$ TCRs constitute a minor fraction of the T-cell population and their function is outside the scope of this thesis. The  $\alpha\beta$ TCR chains are derived from the somatic rearrangement of the genomic regions: variable (V), diversity (D), joining (J), and constant (C). The rearrangement facilitates

the diversity of the TCR repertoire (Garcia et al., 1996)(Davis and Bjorkman, 1988). Each TCR chain consists of two extracellular domains. Those domains are immunoglobulin-like, and form the variable and constant region. The assembly of the TCR complex relies on an interchain disulphide bond (Bäckström et al., 1996)(Bäckström et al., 1997).

The binding of the TCR to the peptide-MHC complex takes place in two stages: docking and stabilisation. Initially, the contact is dictated by the interaction of the TCR to the MHC independently of the peptide, which leads to the docking. Subsequently, the stabilisation of this contact is dictated by the TCR specificity to the peptide (Wu et al., 2002). The majority of TCR binding interface (75-80%) recognises the MHC. Specifically, Complementary Determining Regions (CDR) 1 and 2 mainly bind to the MHC. On the contrary, CDR3 recognises the antigen peptide (Chothia et al., 1988)(Claverie et al., 1989). Jorgensen and colleagues showed that mutating the CDR3 of either the TCR  $\alpha$ - or  $\beta$ -chain abrogated the antigen interaction (Jorgensen et al., 1992). Both the TCR and the peptide-MHC complex bear flexible interaction surfaces, leading to conformational changes and stabilisation upon binding. The flexibility of the binding surface is a result of the low affinity (Willcox et al., 1999).

The intracellular domains of the  $\alpha\beta$ TCR are short, and bear no catalytic activity. However, TCR is associated with the CD3 complex, which is responsible for the signal triggering (Berkhout et al., 1988). The subunits of delta ( $\delta$ ), gamma ( $\gamma$ ), two epsilon ( $\epsilon$ ), and two zeta ( $\zeta$ ) chains constitute the CD3 complex (Kuhns and Davis, 2012). Each subunit bears a long intracellular domain with Immunoreceptor Tyrosine-based Activation Motifs (ITAMs). The delta, epsilon, and gamma chains bear one ITAM, whereas the zeta chains bear three ITAMs each. Hence, the CD3 complex contains ten ITAMs (Chițu et al., 2001)(Love and Hayes, 2010). The ITAMs are phosphorylated by kinases, and subsequently function as docking sites for the  $\zeta$ -Chain Associated Protein tyrosine kinase 70 (Zap-70). The TCR activation and signalling is discussed later in this chapter.

The co-receptors CD4 or CD8 stabilise the TCR interaction with the MHC (Wooldridge et al., 2005), but also recruit the Lymphoid-specific Cytosolic protein tyrosine Kinase

(Lck) that is crucial for the signal initiation (Artyomov et al., 2010). Lck binds to the CD4 and CD8 co-receptors via a zinc-clasp structure (Kim et al., 2003).

### 1.7.2 The Structure of the Chimeric Antigen Receptor

The TCR recognises the peptide presented by the MHC. As mentioned above, the CDR1 and CDR2 mainly bind the MHC rather than the presented peptide. The peptide binding in the context of MHC constitutes a drawback for TCR adoptive T-cell therapy, due the vast polymorphism of the MHC isoforms (Schreuder et al., 2001). TCR engineered T-cells are restricted to the subpopulation bearing the specific MHC recognised by the engineered TCR.

As an alternative, Eshhar and colleagues designed a chimeric TCR. The Chimeric Antigen Receptors are engineered receptors that render T-cells specific against an arbitrary antigen. The protein is a fusion of functional domains from proteins implicated in TCR recognition and signalling (Eshhar et al., 1993).

The extracellular module of the CAR consists of the Single Chain Variable Fragment (scFv), which grafts the antigen specificity, and a spacer (Figure 5). The spacer provides flexibility for accessing antigens proximal to the cell membrane (Moritz and Groner, 1995)(Guest et al., 2005), while the transmembrane domain is crucial for anchoring the protein on the membrane.

Finally, the intracellular domain facilitates the signal transmission. In order to imitate the function of TCR, CD3 $\zeta$  domain was initially used as the CAR intracellular domain, to facilitate signalling and stimulation (Baniyash et al., 1988). However, in order to avoid T-cell anergy due to co-stimulation absence, the co-stimulatory molecule CD28 was also incorporated (Harding et al., 1992). CD28-CD3 $\zeta$  intracellular domain in CAR T-cells substantially increases the IL2 and IFN- $\gamma$  production, yet they have limited proliferative capacity (Maher et al., 2002). Alternative costimulatory domains have been implemented, such as CD137 (4-1BB), CD134 (OX-40), and ICOS (Milone et al., 2009)(Hombach et al., 2012)(Shen et al., 2013). The inclusion of 4-1BB as a costimulatory domain led to augmented persistence and cytotoxic capacity. OX-40 domain, a member of the Tumour Necrosis Factor Receptor (TNFR) family was also shown to increase the T-cell survival (Akiba et al., 1999). The combination of a

costimulatory domain along the CD3 $\zeta$  constitutes the 2<sup>nd</sup> generation CAR structure. The combinatorial effect of the two costimulatory domains plus the CD3 $\zeta$  domain represent the 3<sup>rd</sup> generation CARs, which demonstrate enhanced proliferation and survival signals (Pulè et al., 2005)(Tamma et al., 2010). The optimal CAR generation and costimulatory-domain combination is an object of an ongoing debate.

The distance between the targeted epitope and the CAR is also crucial. The length of the spacer is pivotal for the engineering of a functional CAR. The optimal distance between the membranes of the CAR T-cell and the target is approximately 15nm, which reflects the distance of the TCR T-cell membrane from its target during the immune synapse (Wild et al., 1999). Therefore, depending on the localisation of the epitope, the optimal spacer length varies between antigens (Guest et al., 2005) (Hudecek et al., 2013). Generally, the spacer length is inversely correlated to the distance of the epitope from the membrane. However other factors are also in play including flexibility, steric hindrance, density and the expression of integrins or co-stimulation receptors. Generally, CARs recognising epitopes that are proximal to the membrane are superior. On the contrary, CARs against membrane-distal epitopes exhibited diminished cytotoxicity (Hombach et al., 2007)(Wilkie et al., 2008)(James et al., 2008).

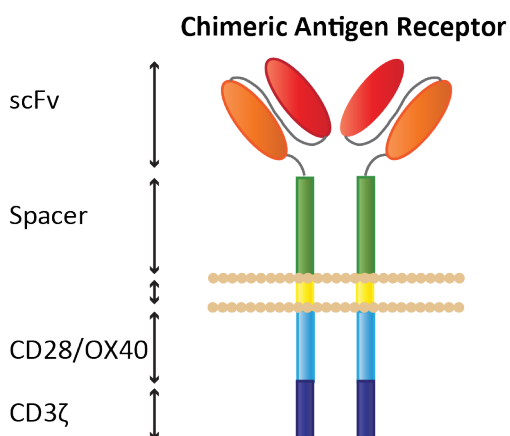


**Figure 5: The structure of the Chimeric Antigen Receptor.** The CAR comprises three domains: the extracellular, intracellular, and transmembrane domain. The extracellular part encompasses two domains, the scFv that bestows the specificity, and the spacer that bestows flexibility and optimised length for the immune synapse. The role of the transmembrane domain is anchoring the molecule in the plasma membrane. Finally, the intracellular domain imitates the TCR signalling bearing the CD3 $\zeta$ , as well as a single or a combination of co-stimulatory domains (such as CD28 or OX40).

### 1.7.3 Activation of TCR

T-cell activation occurs upon TCR binding to a cognate peptide presented on MHC. Consequently, the ITAMs on the cytoplasmic tails of the CD3 complex are phosphorylated by Lck. The phosphorylated ITAMs constitute docking sites for Zap-70, which then phosphorylates substrates, such as Linker of Activated T-Cell (LAT) for downstream signal transmission (Weiss and Littman, 1994).

The mechanism that leads to the initial ITAM phosphorylation after the TCR engagement is undetermined. There have been three models describing the TCR signalling reaction in respect to sensitivity and specificity, and these models are not mutually exclusive. Those are the receptor aggregation, conformational change, and kinetic segregation models. According to the aggregation model, the T-cell triggering requires multimeric MHC, which multimers will consequently induce TCR aggregation. The multimeric TCR clusters can be homologous or not by consisting of TCRs that recognise a cognate peptide, as well as self-peptide MHC complexes (Krogsgaard et al., 2005). These pseudodimers augment the local concentration of components integral to the signal triggering, and thus increase the possibility of phosphorylation for signal triggering (Kuhns and Davis, 2007)(Kumar et al., 2011).

Another model that describes the T-cell activation is the conformational change model. Two distinct but not exclusive changes have been proposed for the conformation of the CD3 $\zeta$  and  $\epsilon$  cytoplasmic domains. The CD3 $\zeta$  cytoplasmic tail is folded and tethered to the inner leaflet of the plasma membrane. Upon TCR binding, the tail is discharged from the membrane, rendering it accessible to phosphorylation (Aivazian and Stern, 2000). Similarly, CD3 $\epsilon$  undergoes a conformational change upon TCR ligation. The exposed proline-rich domain recruits the Non-Catalytic tyrosine kinase (Nck), prior to subsequent phosphorylation (Gil et al., 2002). However, the importance of the Nck recruitment for the T-cell activation is disputed. Controversial studies show that the Nck is either not required for the activation of mature T-cells; or that is required for signal amplification during weak interactions; or finally is required for ITAM phosphorylation inhibition (Szymczak et al., 2005)(Tailor et al., 2008)(Takeuchi et al., 2008). Although conformational changes might play a role in

the induction of signal transmission, the mechanism that provokes the conformation change is still elusive.

Finally, a third model that describes the activation of T-cells upon TCR engagement is kinetic segregation. Approximately 40% of Lck is constitutively active, driving the signal transmission (Nika et al., 2010). It has recently been reported that the early ITAM phosphorylation is mediated by free Lck, and not by Lck associated with the co-receptors (Casas et al., 2014). Since there is no background activation of TCR without antigen engagement, this suggests that phosphatases are constitutively active as well. The main phosphatases implicated in regulating the TCR signalling are CD45 and CD148 (Sieh et al., 1993)(Zhu et al., 2008)(Hermiston et al., 2009). In a resting T-cell, the TCR stochastically gets phosphorylated and de-phosphorylated by diffuse kinases and phosphatases and the resulting equilibrium maintains the T-cell in a non-activated state.

Upon TCR engagement to the peptide-MHC on the surface of another cell, the membrane of the T-cell and target cell form a close contact area approximately 15nm apart from each other. This close contact area constitutes the immune synapse. The complexes within the synapse, such as the TCR-peptide-MHC complex, as well as the complexes formed by adhesion molecules like CD2, have a size of 15nm (van der Merwe et al., 1995). Molecules with ectodomains longer than 15nm are physically excluded from the synapse (Figure 6). The extracellular domain of CD45 is 28-51nm long (McCall et al., 1992). Although the exact structure of CD148 is undetermined, its size has been estimated at 47-55nm based on the 8-10 N-glycosylated fibronectin domains (Ostman et al., 1994). Both CD45 and CD148 bear ectodomains longer than the allowed distance in the synapse, and thus they are segregated. With the exclusion of CD45-CD148 from the synapse, the kinase Lck phosphorylates the ITAMs without the counterbalancing de-phosphorylation by the phosphatases. The increased localised ITAM phosphorylation overcomes the triggering threshold and initiates the signalling cascade.

In support to the kinetic segregation model, truncation of the CD45/CD148 ectodomains hinders T-cell triggering (Irlles et al., 2003)(Lin and Weiss, 2003)(Cordoba et al., 2013). Similarly extension of the peptide-MHC complex

impedes the triggering of TCR signalling cascade (Choudhuri et al., 2005)(Choudhuri et al., 2009). We and others postulate that CAR T-cell triggering depends on kinetic segregation.

An interesting property of the TCR signalling is its sensitivity to low-density targets. The affinity of TCR for the peptide-MHC complex is low (1-100 $\mu$ M), allowing a rapid dissociation after binding. According to the serial triggering theory, a single antigen can rapidly bind and sequentially activate up to 200 TCRs (Valitutti et al., 1995). Serial triggering does not affect the signalling of individual TCRs, but rather ameliorates the combined signal strength in low-density targets, rendering it comparable to their high-density counterparts (Itoh et al., 1999). CARs are based on antibodies having a lower dissociation rate than TCRs (discussed in 1.8.3), and thus CARs do not undergo serial triggering (James et al., 2010).

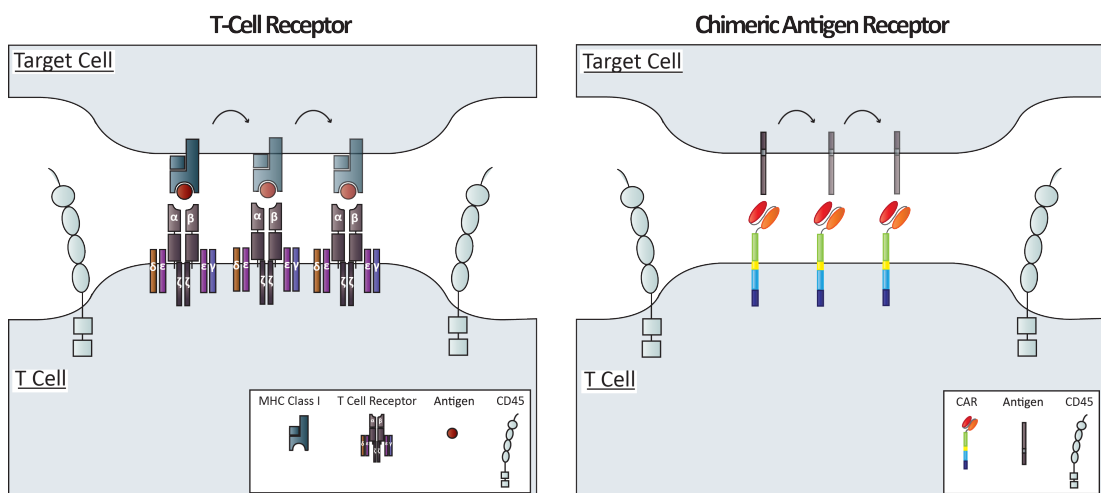


**Figure 6: The kinetic segregation model.** Upon T-cell activation, the membranes of the target and the T-cell form a close contact region of approximately 15nm distance length. The signalling components can diffuse inside the synapse. However, the phosphatases CD45 and CD138 bear ectodomains of 28-51nm and 47-55nm length respectively. Due to the large ectodomains, these phosphatases are physically expelled from the synapse. The lack of phosphatases within the synapse leads to increased phosphorylation of ITAMs and signal triggering. The size exclusion model is called kinetic segregation. Another phenomenon observed for TCRs is the serial triggering. The low affinity of TCR to the peptide-MHC complex leads to fast dissociation from the complex after binding. This way, the peptide-MHC complex can rapidly bind to several TCRs and serially activate them. It was shown that a single peptide-MHC complex can activate up to 200 TCRs. We hypothesise that the activation of T-cells bearing CARs instead of TCRs is also depended on kinetic segregation (right). However, the CARs binding domains are based on scFv of antibodies. Antibodies have higher affinity for the antigen, thus the dissociation rate is slower than that of TCRs. The longer interaction time between CAR and antigen impedes the rapid interaction of the same antigen with multiple CARs, hindering the serial triggering.

#### 1.7.4 Optimal TCR/CAR and Antigen Density

As discussed above T-cell activation is a dynamic process. This process is not binary with only active and inactive states. The quality of the signal depends on a plethora

of parameters, such as affinity, antigen density, and TCR or CAR density. Depending on the quality of the signal, different cytolytic capacity or differentiation profile might be achieved (Sarkar et al., 2007)(Smith-Garvin et al., 2010).

Several studies have been published on the influence of TCR and peptide-MHC density to T-cell activation. There are approximately  $10^5$  TCR molecules on the surface of a T-cell (Christinck et al., 1991). An inverse correlation between TCR density and antigen density was observed. For low-antigen density targets ( $10^4$  epitopes/cell),  $10^5$  TCR epitopes/cell were required to elicit T-cell triggering. Hence, the activation required the full TCR capacity, regardless the TCR affinity. On the contrary, T-cell activation with high-antigen density ( $10^6$  epitopes/cell) was dependent on the TCR affinity. T-cells bearing high-affinity TCR required a density of  $10^3$  TCR epitopes/cell in order to be activated. A 5-fold increase in receptor density was necessary for T-cell triggering in cells bearing a low-affinity TCR (Schodin et al., 1996). Co-receptors also play a crucial role in overcoming the activation threshold. The required TCR density was reduced from  $8 \times 10^3$  epitopes/cell to  $1.5 \times 10^3$  epitopes/cell in the presence of co-stimulatory CD28 (Viola and Lanzavecchia, 1996). The optimal antigen density for CAR targeting is undetermined, since many parameters affect the threshold of activation. The CAR density, affinity, as well as the distance of the epitope from the membrane constitute those parameters. Similarly to TCRs, the CAR and antigen density are also reversely correlated (Alvarez-Vallina and Russell, 1999)(Weijtens et al., 2000). It was shown in a Jurkat T-cell analysis system that the CAR efficacy was enhanced with increasing antigen-density up to a threshold. High CAR density led to activation at low antigen-density levels, and the IL2 production was greater than that of the low-density CAR T-cells. However, density higher than the threshold led to CAR T-cell impairment and Antigen-Induced Cell Death (AICD) (Alvarez-Vallina and Russell, 1999). The minimal amount of CAR epitopes/cell required for maximum cytotoxicity and cytokine production was  $2 \times 10^4$ . Lower CAR density was also efficacious, but the response time was increased by 3-fold. For a CAR density range of  $4.6-70 \times 10^4$  epitopes/cell, the target lysis plateaued above  $10^4$  antigen epitopes/cell independently of the CAR density (James et al., 2010). The CAR sensitivity was initially calculated at approximately 770 antigen

epitopes/cell (Stone et al., 2012). However, a subsequent study demonstrated that the antigen-density threshold for target lysis was approximately 240 epitopes/cell. The threshold for cytokine production was an order of magnitude higher (Watanabe et al., 2015). These values are likely to be dependent on the type of CAR used, and related to its individual characteristics.

In order for a CAR T-cell to engage and serially lyse target cells, an adequate amount of CAR molecules would be required to remain on the cell surface after CAR downmodulation. Although an optimal T-cell activation occurs with a CAR density of  $2 \times 10^4$  epitopes/cell, the downmodulation of the CAR molecules from the surface decreases the capacity for serial target lysis. Based on a mathematical model, a CAR density of  $0.5-1 \times 10^6$  CAR epitopes/cell was predicted to be downmodulation resilient (James et al., 2010). However, high CAR density and prolonged TCR activation cause AICD (Alvarez-Vallina and Russell, 1999)(Iezzi et al., 1998).

Interestingly, the antigenic epitope distance from the membrane of the target cell also influences the CAR cytotoxic capacity. The distance negatively affected the CAR sensitivity, so membrane-distal epitopes were required at a 4-fold higher density in order to elicit a response equivalent to the membrane-proximal epitopes (James et al., 2008).

### **1.7.5 CAR T-Cell Clinical Trials**

CAR T-cell therapies have been efficacious in haematological malignancies. Clinical trials using anti-CD19 CARs have been successful. CD19 is a transmembrane protein expressed in normal and neoplastic B-cells (Wang et al., 2012). Patients with Acute Lymphoblastic Leukaemia (ALL) and Chronic Lymphocytic Leukaemia (CLL) achieved remission after anti-CD19 CAR T-cell administration (Brentjens et al., 2013)(Davila et al., 2014)(Grupp et al., 2015)(Brentjens et al., 2010)(Porter et al., 2011). However, severe neurotoxicity occurred in 50% of the patients treated with anti-CD19 CAR T-cells (Turtle et al., 2016). An additional concern is the antigen escape observed by Sotillo and colleagues (Sotillo et al., 2015). Alternative antigens, such as CD22 or ROR1 are being tested for the treatment of ALL or CLL in phase I clinical trials (NCT02650414 and NCT02706392).

CD19 has also been explored as a potential antigen for targeting multiple myeloma. A therapy using anti-CD19 CAR T-cells has led to complete remission or progression free disease in two separate clinical trials (Garfall et al., 2015)(Ramos et al., 2016). An alternative antigen used for multiple myeloma CAR therapy is B-Cell Maturation Antigen (BCMA), which is solely expressed on plasma cells (Ryan et al., 2007). Partial response was observed in two of the four patients that received high dose of anti-BCMA CAR T-cells (Ali et al., 2016).

It is of great interest to expand the CAR field in solid tumours. To date, results from clinical trials using CAR-T-cell therapy for solid tumours have been modest. An early trial, in which an anti-folate receptor first generation CAR was employed, showed lack of T-cell engraftment to the tumour site (Kershaw et al., 2006). Another promising target is the Human Epidermal Growth Factor 2 (HER2), which is overexpressed in multiple malignancies, and constitutes an attractive target. Three out of sixteen osteosarcoma patients achieved progression free disease (Ahmed et al., 2015). Unfortunately, anti-HER2 CAR therapy was fatal for a colon carcinoma patient, due to on-target off-tumour effect with HER2 present in the lung at low-density (Morgan et al., 2010). More promising results were shown in a different clinical trial for neuroblastoma treatment (Pule et al., 2008). The CAR T-cells were engineered to recognise the diasialoganglioside GD2. Half of the patients experience tumour regression, including a complete remission. An anti-GD2 CAR T-cell clinical trial is currently open in UK (NCT02761915).

More targets are being exploited for CAR T-cell therapy. An ovarian cancer clinical trial has been approved, in which the CAR T-cells will be administered to the patients via an intraperitoneal injection. Additionally, the T-cells are engineered to express and secrete IL-12 (Koneru et al., 2015). CAR T-cells against mesothelin have shown promising results in *in vivo* xenograft models (Carpenito et al., 2009). There are currently two open clinical trials that employ an anti-mesothelin CAR T-cell (Beatty et al., 2014)(NCT02414269 and NCT02465983). Epidermal Growth Factor Receptor variant III (EGFRvIII) is a tumour-specific mutation, which constitutes an optimal target for CAR T-cells. The efficacy of the anti-EGFRvIII CAR was validated *in vitro* and

*in vivo* for glioblastoma treatment, which subsequently led to a phase I clinical trial (Johnson et al., 2015)(NCT02209376).

Two clinical trials are implementing CARs to target melanoma. In the first study, the CAR is against the VEGFR for the treatment of metastatic melanoma and renal cancer (NCT01218867). The clinical trial has been completed, but the results are still unpublished. Another clinical trial aims to target melanoma, neuroblastoma, sarcoma, and osteosarcoma. The CAR in this study targets GD2 (NCT02107963).

### **1.7.6 Advantages and Challenges of CAR Technology**

T-cell receptors recognise an antigen in the context of Major Histocompatibility Complex Class I (MHC I) (Raychaudhuri et al., 1992). However, MHC I (or Human Leukocyte Antigen HLA) protein molecules are highly polymorphic, with 615 reported isoforms among the homologues A, B, and C (Schreuder et al., 2001). TCR recognises the complex of MHC I-antigen, thus it only recognises the antigen in the context of a MHC-I isoform. Hence, only the fraction of the patients that express this isoform is able to receive the TCR T-cells. With 615 MHC I isoforms discovered so far, this mechanism introduces a significant limitation to the TCR development of adoptive T-cell therapy.

Additionally, the engineered  $\alpha$  and  $\beta$  TCR chains introduced into T-cells, can heterodimerize with chains of the endogenous TCRs. This phenomenon introduces two hurdles. First, the presence of the introduced correctly paired TCR is diluted on the surface. This could significantly reduce the sensitivity of the therapy and lead to treatment failure. Second, the function of a mispaired TCR is unpredictable, and there are concerns regarding auto-reactivity of the TCR. However, there are potential strategies to address this issue, either by introducing a cysteine in the  $\alpha$  and  $\beta$  chains to form an extra disulphide bond or by down-regulating the expression of endogenous TCR (Cohen et al., 2007)(Okamoto et al., 2009).

CAR technology bypasses the mispairing and HLA-restriction, and also enables the targeting of non-protein targets. It is important to point out that CARs are engineered receptors containing a combination of individual functional domains. This modularity gives the advantage of flexibility. The rapid development in the field has already

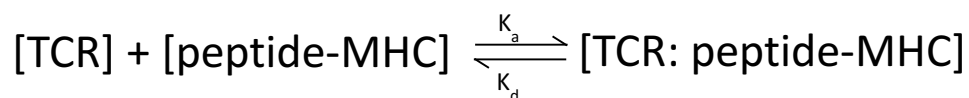
produced three generations of CARs, and the research into developing more advanced receptors is ongoing. The flexibility of CAR design extends to logic gates. A group of cross-talking CARs can be incorporated into a single cell, introducing complexity to the antigenic pattern of recognition.

The serious limitation of CAR technology is the inability to target intracellular antigens. The optimal tumour antigen is elusive. Tumour cells, unlike foreign microorganisms, are derived from the organism itself. As they originate from healthy tissues, tumour antigens might also be present on normal cells. Choosing the antigen for tumour targeting is therefore challenging. The restriction of CAR technology to exclusively surface antigens is significantly limiting the pool of available tumour-antigens.

## 1.8 ANTIGEN SENSITIVITY IN RELATION TO AFFINITY

### 1.8.1 Binding Kinetics

The binding kinetics of a TCR are described by the association and dissociation rate of interaction with the antigen complex. The association rate ( $K_a$ ) portrays how quickly the TCR binds to the peptide-MHC complex. Respectively, the dissociation rate ( $K_d$ ) describes how fast the TCR dissociates from the antigenic complex (Stone et al., 2009). High association rate allows for rapid formation of the complex. High off rate renders the complex unstable and likely to dissociate.



The dissociation constant ( $K_D$ ) describes the affinity of the TCR to MHC complex, and is derived from the quotient of  $K_a$  and  $K_d$ . Affinity expresses how strong the interaction is, and determines the ratio of TCR-MHC-peptide-complex to unbound TCR and MHC-peptide at equilibrium. The higher the affinity, the less unbound proteins are present. The units for the on- and off-rate are  $\text{M}^{-1}\text{s}^{-1}$  and  $\text{s}^{-1}$  respectively. As a result, the unit for  $K_D$  is M.

$$K_D = \frac{K_d}{K_a}$$

As aforementioned, the  $K_d$  describes the dissociation speed. Based on the dissociation rate, we can measure the half-life of interaction between the TCR and the peptide-MHC complex. The measurement unit for the half-life (or  $t_{1/2}$ ) is seconds (s).

$$t_{1/2} = \frac{\ln 2}{K_d}$$

The golden standard technique for measuring binding kinetics is surface plasmon resonance, which is described in chapter 5.1.4.

### 1.8.2 Effect of Affinity on T-Cell Receptors

TCRs have low affinity against cancer antigens, as a result of negative selection of high affinity TCRs against self-antigen (Aleksic et al., 2012). The low-affinity enables the required flexibility, in order for the conformation change to occur in both TCR and peptide-MHC complex during the interaction (Willcox et al., 1999). The TCR affinity range is  $1\mu\text{M}$ - $100\mu\text{M}$ . The association- and dissociation rate range is  $1$ - $3 \times 10^3 \text{ M}^{-1} \text{ s}^{-1}$ , and  $0.3$ - $0.06 \text{ s}^{-1}$  respectively (Matsui et al., 1994). Although the general TCR affinity range is  $1\mu\text{M}$ - $100\mu\text{M}$ , the average affinity of TCRs against foreign antigens is  $10\mu\text{M}$ , whereas the average affinity against cancer antigens is  $100\mu\text{M}$ .

The effect of affinity on TCR efficacy is convoluted. A plethora of studies support the model of optimal dwell time. It was shown that TCRs with half-life shorter than 0.5 min were inactive. On the other hand, half-life longer than 10 min impedes the serial triggering, also rendering the TCR inactive (Kalergis et al., 2001). Therefore, a TCR has to be able to form complexes within a specific range of half-life in order to be functional. In a subsequent study, the optimal dwell time was delineated in accordance to the antigen density. For low-antigen density targets, the serial triggering was crucial in TCR activation. Since the antigen density is the limiting factor, each antigen is required to sequentially bind multiple TCRs. However, when the

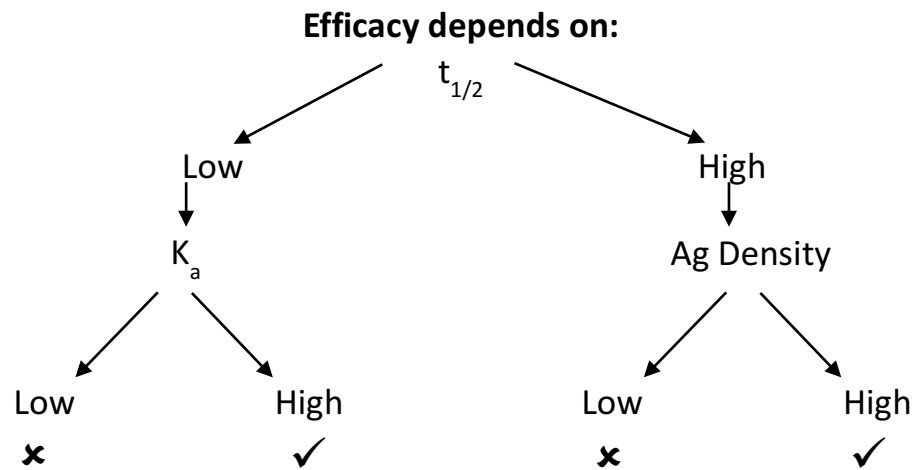
antigen is in abundance, multiple targets will bind multiple TCRs concomitantly. Therefore, the serial triggering is not pivotal in the latter scenario. In accordance to this, for high-antigen targets a half-life of 10min or longer did not thwart the T-cell activation (González et al., 2005). The importance of serial triggering was also underlined by Thomas and colleagues. Their study showed that although high-affinity TCRs achieved faster responses against high density targets, solely low-affinity TCRs recognised low-density targets (Thomas et al., 2011). Interestingly, the optimal dwell time and serial triggering hypothesis is also supported in a study with Bispecific T-cell Engagers (BiTEs). Slow dissociation rate of the BiTE from CD3 decreased the T-cell triggering capacity, due to inefficient serial triggering (Bortoletto et al., 2002).

Compelling evidence suggests that best TCR activity is achieved when it shows an optimal range of association time (dwell time) to the antigen. However, there are studies that show correlation of TCR efficacy to the affinity rather than the off-rate (Tian et al., 2007). Specifically, the TCR efficacy positively correlates with affinity. However, the efficacy reaches a plateau at approximately 5 $\mu$ M, and the T-cell function could not be further enhanced for affinity higher than 5 $\mu$ M (Schmid et al., 2010). Affinity higher than 5nM led to specific TCR antigen recognition only in the absence of CD8, which increases the avidity of the T-cell interaction. TCR in the pM range of affinity altogether lost the antigen specificity (Zhao et al., 2007). The correlation of affinity to the TCR functional capacity, instead of the dissociation rate reflects the effect of the on-rate. According to the optimal dwell time model, TCR with half-life shorter than 30 seconds fails to trigger signal transmission.

Nevertheless, TCR with short half-lives can be active, when their on-rate is rapid (Aleksic et al., 2010). When the association rate is faster than the diffusion rate of the TCR in the membrane, which is less than 100Å in 1ms, the TCR rebinds onto the peptide-MHC complex. The total time of interaction, including the rebindings, is called the aggregate half-life. The probability of 1-3 rebindings is increased for on-rate higher than 10<sup>5</sup>M<sup>-1</sup> s<sup>-1</sup> (Govern et al., 2010). According to the aggregate dwell time model, a TCR with a rapid off-rate, could still be active if the on-rate is also rapid. This would allow for rebinding to the antigen, thus prolonging the interaction time to the aggregate half-life rather than the half-life predicted based on the off-rate.

It is unknown whether the influence of affinity is similar on CAR efficacy. Although, the TCR and CAR signal transmission occurs through the kinetic segregation, the stoichiometry within the synapse is different. The CD4 and CD8 co-receptors independently bind the peptide-MHC complex (Wyer et al., 1999), and stabilise the TCR-MHC complex interaction (Wooldridge et al., 2005). Additionally, the co-receptors recruit the Lck, which is essential for the signal initiation (Artyomov et al., 2010). The affinity of CD8 for MHC-I is  $150\mu\text{M}$ , with a rapid off-rate and a half-life of  $0.04\text{s}$  (Wyer et al., 1999). Despite the low-affinity of CD8 for MHC-I, it was shown that CD8 significantly augments the capacity of low-affinity TCRs ( $3\mu\text{M}$ ). TCRs reach an efficacy plateau at affinities higher than  $1\mu\text{M}$  in the presence of CD8. However, this TCR-efficacy plateau is only attained at  $100\text{nM}$  in the absence of CD8, thus CD8 is pivotal for the TCR function (Holler and Kranz, 2003).

The correlation of kinetics and TCR efficacy can be simplified into a model based on three parameters: half-life, on-rate, and antigen density. It is important to distinguish between TCR's having low or high half-life, because in each case different parameters influence their capacity for signal activation. The efficacy of TCRs characterised by low half-life depends predominantly on their on-rate. Fast on-rate allows rapid rebindings to the target, and thus a functional TCR. Although the interaction between TCR and peptide-MHC complex is rapid, their dynamics result in more complexes being formed in a unit of time. If the on-rate is slow, the interaction time is inadequate to trigger signalling. On the other hand, when the half-life is high, the TCR efficacy depends on the antigen density. For low-antigen density targets the TCR sensitivity, and thus serial triggering, is pivotal. High half-life impairs the serial triggering, and thus undermines the sensitivity.



The function of TCRs in regard to affinity has been widely studied, and the optimal affinity range as well as the optimal half-life has been delineated. The avidity amelioration due to the co-receptor binding is not taken into consideration in these optimal range values for affinity and half-life. However, CARs lack a direct interaction to co-receptors, so no avidity augmentation is observed. Hence, translating the optimal-for-TCR-efficacy values into CAR design would constitute an underestimation of the affinity or half-life required for optimal function. Nevertheless, the influence of kinetics on TCR capacity can be extrapolated as a principle for CAR design.

### 1.8.3 Effect of Affinity on Chimeric Antigen Receptors

The binding moiety of CARs is a scFv derived from an antibody. The antibody kinetics vary significantly from the kinetics of TCRs. The kinetic disparity reflects the difference between antibody maturation and TCR selection. T-cells undergo a positive and negative selection. T-cells bearing TCRs with an affinity below the peptide-MHC recognition levels result in cell death by neglect, as the cells do not receive external growth signals required for their survival. However, T-cells bearing TCR with high affinities are eliminated by apoptosis induction (Sha et al., 1988). Consequently, a narrow window of  $1\mu\text{M}$ - $100\mu\text{M}$  is observed for TCR affinity (Alam et al., 1996)(Williams et al., 1999)(Daniels et al., 2006).

Antibodies are produced by B-cells, after stimulation of the B-Cell Receptor (BCR) and interaction with a helper T-cell. High affinity BCR migrate to the lymph node germinal centre where they undergo somatic hypermutation (Kim et al., 1981). Hence,

antibodies are characterised by higher affinity, faster association rates, and slower dissociation rates than TCRs. Specifically, the range of affinity, on-rate, and off-rate is 1-100nM,  $10^4$ - $10^7$   $M^{-1} s^{-1}$ , and  $10^{-5}$ - $10^{-3}$   $s^{-1}$  respectively (Poulsen et al., 2007)(Poulsen et al., 2011). Table 2 shows the affinity of CAR scFv that have been used in clinical trials. The affinity of those scFv is within the nM range, being approximately an order of magnitude higher than the 1-100 $\mu$ M TCR affinity range (Matsui et al., 1994).

**Table 2: Affinity of CAR scFv in clinical trials.**

Antigen	Clone	Affinity (nM)	Citation
CD19	FMC63	4.2	(Nicholson et al., 1997)
CD19	HD37	0.18	(Ghetie et al., 2004)
CD19	4G7	30	(Kügler et al., 2009)
CD33	MY9-6	0.97	(Hoffee et al., 2012)
CD123	26292	3.5	(Du et al., 2007)
HER2	FRP5	4.2	(Wels et al., 1995)
Mesothelin	SS1	0.7	(Carpenito et al., 2009)

Although the effect of affinity on TCR cytotoxic capacity has been thoroughly studied, the literature on CAR affinity is limited. In the majority of studies, the association rate  $K_a$  values reside within a small range. The difference in function observed is therefore due to the dissociation rate  $K_d$ . The effect of the affinity on the CAR efficacy is still unclear, with a plethora of studies demonstrating that affinity is positively correlated to sensitivity (Chames et al., 2002)(Chmielewski et al., 2004)(Hudecek et al., 2013)(Caruso et al., 2015)(Liu et al., 2015)(Lynn et al., 2016). On the contrary, one study illustrates the superior sensitivity of the low-affinity CAR due to the serial triggering effect (Turatti et al., 2007), which will be discussed below.

In detail, there have been five publications to this date, supporting the increased sensitivity of high-affinity CARs. In 2002, Chames and colleagues analysed the capacity of two CARs based on the same scFv clone, with affinities of 14nM and 250nM. The 14nM CAR exhibited 2-fold higher cytotoxic capacity than the 250nM CAR. However, labelling the target cells with the soluble scFv resulted in a fluorescent

intensity different by two orders of magnitude. This suggests a discrepancy in the scFv stabilities. Hence, the stability, instead of the affinity, could be the cause of the different CAR capacity (Chames et al., 2002). Similarly, two CARs with 1.8nM and 21nM affinities were validated *in vitro*. A disparity in capacity was observed only with an antigen-density below  $3 \times 10^4$  epitopes/cell, which was not mitigated over time (Caruso et al., 2015). However, this study employed CARs with distinct clones of scFv, without addressing potential diversity in stability. Additionally, the difference in affinity in this case reflects the on-rate variation, with the high-affinity CAR having two orders of magnitude faster association than the low-affinity one (Caruso et al., 2015). Two additional CARs with affinities of 0.56nM-32.6nM based on two distinct scFv, were analysed for cytotoxicity and cytokine production. The latter was marginally better for the high-affinity CAR. Nevertheless, the cytotoxic capacity was comparable (Hudecek et al., 2013). The aforementioned studies drew conclusions on the affinity influence on the capacity of CARs based on only two affinity points instead of a range. Therefore, however interesting, the result has to be interpreted with caution and a more reliable measurement is required to support this observation with confidence.

The superiority of the high-affinity CAR was also demonstrated in studies that employed a range of CAR affinities. Firstly, the affinities for the CARs interrogated were 15pM, 0.12nM, 1nM, 16nM, and 320nM. The results were binary, with the affinity between 15pM-16nM leading to equivalently high cytotoxic capacity. On the contrary, the 320nM CAR was not functional. Although these data indicate a plateau of efficacy for affinity higher than 16nM, there are no available data for the affinity gap between 16nM-320nM (Chmielewski et al., 2004). Additionally, Liu and colleagues employed a range of CAR affinities between 0.58nM-3.9 $\mu$ M. The individual affinities for the CARs were 0.58nM, 3.2nM, 1.1 $\mu$ M, and 3.9 $\mu$ M. The two CARs in the  $\mu$ M affinity scale demonstrated reduced capacity against low-antigen targets. Interestingly, the cytokine production of the low-affinity CARs against high-density targets was superior. However, this pattern was reversed with high-affinity CARs producing higher concentration of cytokines against low-density targets. In this study, the affinity gradient of scFv was obtained through antibody humanisation.

Humanisation is achieved by mutating the framework of the antibody structure, not the CDRs (Jorgensen et al., 1992). The framework mutations could introduce discrepancies in the stability of the antibody and scFv. The stability discrepancy has not been investigated or discussed in this study (Liu et al., 2015).

Finally, two CARs with the same clone variants were compared, and their affinities were 1nM and 1.6 $\mu$ M. In this study, the difference in affinity is due to the dissociation, as well as the association rate divergent values. The on-rate and off-rate differed by one and two orders of magnitude respectively. In contrast to the aforementioned studies, this one demonstrated the superiority of the low-affinity CAR against low-density targets (Turatti et al., 2007). This observation is in accordance with the TCR studies, that showed that low-affinity TCRs had a short half-life, and thus underwent serial triggering. Therefore, the low-affinity TCRs were more sensitive to low-density targets (González et al., 2005)(Thomas et al., 2011).

The correlation between affinity and CAR efficacy has not been intensively investigated, with only a limited amount of studies on the subject. Additionally, these studies are very difficult to compare, because they employ different affinity data points, diverse functional assays and time points. The spread of the affinity ranges used in each study are illustrated in Figure 7. The lack of stability data between the scFv variants constitutes one of the major confounding factors in all these studies. Stability divergence could result in a false-positive correlation between affinity and CAR efficacy. CAR affinity-variants based on different clones bind distinct epitopes, and thus constitute an additional confounding factor, since epitopes proximal to the membrane are favourable (Haso et al., 2013). Finally, in each study disparate antigen and CAR densities were used. The collective characteristics and findings of each study are illustrated in Table 3.

The majority of studies show a positive correlation between affinity and CAR potency. This correlation was more pronounced in the suboptimal conditions of low-antigen density. However, these data are inconsistent with Turatti and colleagues, who showed an inverse correlation. An inverse correlation was also shown between affinity and TCR efficacy. TCRs with long interaction time, and thus high affinity exceeded the optimal-dwell time impairing the serial signalling. Taking into

consideration the inconsistencies, as well as the caveats of those studies, reaching a conclusion on the affinity-to-efficacy correlation is challenging. A more thorough study with a plethora of affinity points is essential for establishing the optimal affinity range of CAR T-cells.

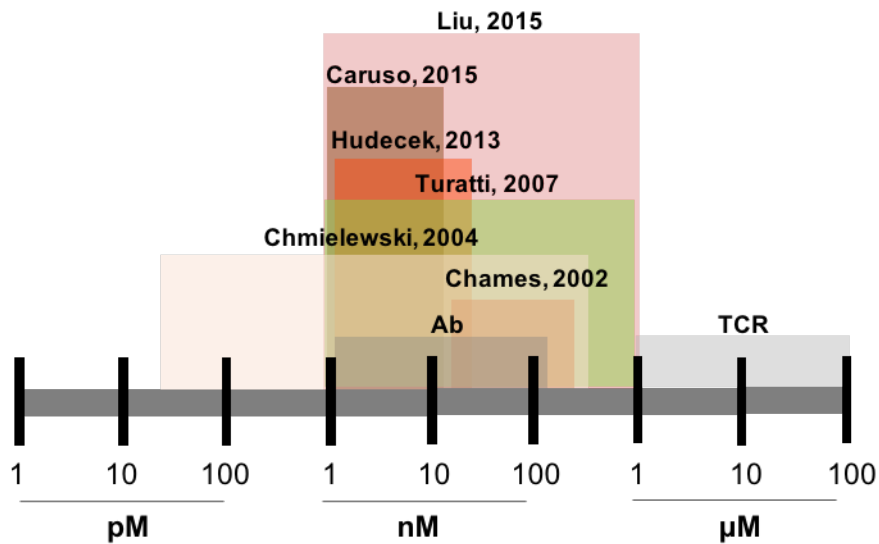


**Figure 7: Affinity range of published data investigating the correlation between affinity and CAR efficacy.** The affinity range of TCRs is 1-100μM (Matsui et al., 1994), in contrast to the antibody affinity range that resides between 1-100nM (Poulsen et al., 2007)(Poulsen et al., 2011). Six studies investigated the influence of affinity and kinetics on CAR cytotoxic capacity. The CAR affinity range employed in each study is illustrated in this figure.

**Table 3: Studies on affinity correlation to CAR efficacy.**

CATEGORY:	Chames, 2002	Chmielewski, 2004	Turatti, 2007	Hudecek, 2013	Carurso, 2015	Liu, 2015
ANTIGEN	MAGE-A1	ErbB2	HER2	ROR1	EGFR	ErbB2
SCFV	G8	C6.5	C6.5	R12 vs 2A2	Cetuximab Nimotuzumab	ErbB2: Humanization EGFR: different clones
AFFINITY RANGE	14nM-250nM	320nM-15pM	1.6uM, 1nM	0.56nM-33nM	0.39nM-45nM	0.3nM-4.4nM
K <sub>a</sub>	Small range	Small range	Small range	Small range	2 log	Unknown
CAR GENERATION	VH-CD4/γ chain VL-CD4/γ chain	1 <sup>st</sup>	1 <sup>st</sup>	2 <sup>nd</sup> (4-1BB, CD28)	2 <sup>nd</sup> (CD28)	2 <sup>nd</sup> (4-1BB)
CAR DENSITY	Similar (Low+)	Similar	Similar (High <sup>++++</sup> , Low <sup>+++</sup> )	Similar (High)	Similar MFI	Similar
TARGET DENSITY	MZ2-MEL2.2- MZ2-MEL3+ MZ2-MEL2.2++ (peptide pulsed)	SK-OV-3+++ Colo201++ MCF-7++ ErbB2 solid phase bound	A341++ A341-HER2+++	Primary CLL++ JeKo-1+ K562- K562_CD19- K562_ROR1++ Raji_ROR1++	A431+ (10 <sup>6</sup> Ag/s) U87 (31 x10 <sup>3</sup> Ag/s) U87 <sup>low</sup> (135 x10 <sup>3</sup> Ag/s) U87 <sup>med</sup> (340 x10 <sup>3</sup> Ag/s) U87 <sup>high</sup> (628 x10 <sup>3</sup> Ag/s) HRCE ( 15 x10 <sup>3</sup> Ag/s)	SK-OV3+++ SK-BR3+++ BT-474+++ EM-Meso+ MCF7+ 293T+ A549+ 624mel+ PC3+
TARGET DENSITY MEASUREMENT	Not measured	MFI (+++ 2log, ++ 1log)	MFI (+++ 2log, ++ 1log)	No measurement	Quantum Simply Cellular polystyrene beads	No measurement
READ-OUT	<sup>51</sup> Cr release (6h) TNF-α (24h)	Cytotoxicity (48h) IFN-gamma (48h)	<sup>51</sup> Cr release assay (18h) Tumour cell growth inhibition (72h)	<sup>51</sup> Cr release (4h) Cytokines Proliferation (72h) NSG animal model	<sup>51</sup> Cr release (4h) Intracellular cytokine Phospho-flow NSG mouse model	Cytotoxicity Cytokine (IL2, IFN-γ) Proliferation CD107a
No OF VARIANTS	2	5	2	2	2	4
CONCLUSIONS	High affinity: Superior	No efficacy gain below 16nM	Low affinity: Superior for low-density targets	Similar cytotoxicity Equivalent <i>in vivo</i>	High affinity: Superior at "low" antigen density	High affinity: Superior at low antigen density

## 1.9 HYPOTHESES

Our hypotheses:

- The low-antigen levels of Tyrp1 on the surface will be sufficient to elicit a T-cell response.
- Since CAR T-cells are not sensitive to low-density targets, optimisation of the anti-Tyrp1 CAR will be paramount.
- Fine tuning of the CAR affinity will enable serial triggering, and will increase the sensitivity.

## 1.10 PROJECT AIMS

In this project we are assessing the feasibility of using an intracellular antigen, which resides on the plasma membrane at low density, as a target for CAR T-cell therapy. The antigen we aim to exploit is the melanosomal protein Tyrp1. Anti-Tyrp1 constitutes the first CAR to exploit the presence of an intracellular antigen on the cell surface, thus indirectly employing an intracellular protein as a target for CAR therapy. This approach can lead to a synergy between the advantages of CAR technology and the exploitation of intracellular proteins for tumour targeting.

Protein trafficking is a complicated machinery, and proteins often have indirect routes to reach a destination. Although, Tyrp1 is present on the cell surface at low antigen density, the exact density and mechanism of reaching the cell surface is unclear. Our first specific aim is the determination of the Tyrp1 density on melanoma cell lines and primary melanoma tissue, as well as the exploration of its trafficking pathway.

Based on the literature, the CAR sensitivity threshold is limited to 240 antigens per cell surface for cytotoxicity, whereas the threshold for IFN- $\gamma$  production lies within the 770-5320 window (Stone et al., 2012)(Watanabe et al., 2015). The Tyrp1 is a very advantageous target due to its expression limited exclusively to melanocytes. However its density could be lower than the CAR sensitivity threshold, since it was estimated that only 2% of Tyrp1 resides on the cell surface (Yiqing Xu et al., 1997).

Therefore, our second aim is the engineering of the anti-Tyrp1 CAR. Consequently, we aim to validate the CAR efficacy against a range of densities for surface Tyrp1, as well as physiological Tyrp1 density on melanoma cell lines.

We expect a limited efficacy of the anti-Tyrp1 CAR against the low-density targets. Thus, our third goal is to optimise the CAR by increasing its sensitivity. In order to achieve this, we have taken into consideration the serial triggering effect (Valitutti et al., 1995). Serial triggering is hypothesised to bestow TCR T-cells sensitivity to low-density targets (Thomas et al., 2011). We aim to examine whether altered binding kinetics of the anti-Tyrp1 CAR lead to enhanced sensitivity.

In summary the specific aims are:

- Quantitation of surface Tyrp1 on melanoma cell lines, and primary melanoma samples.
- Exploration of the Tyrp1 trafficking mechanism, in order to elucidate the pathway that results in a fraction of Tyrp1 being present on the cell surface.
- Engineering and validation of the anti-Tyrp1 CAR.
- Binding kinetic manipulation of anti-Tyrp1 CAR, in order to investigate correlation between affinity and sensitivity.

**CHAPTER 2:**  
**Materials and Methods**

## CHAPTER 2: MATERIALS AND METHODS

### 2.1 MOLECULAR BIOLOGY

#### 2.1.1 Molecular Cloning

##### 2.1.1.1 Phusion PCR

Phusion PCR enables the fusion of two or more DNA fragments at precise junctions. This is achieved in a two-step protocol, the primary Polymerase Chain Reaction (PCR) and the phusion PCR. An arbitrary sequence is inserted in the overhang of the primary PCR primers, which is complementary to another PCR fragment. This overhang is incorporated in the PCR fragment sequence during the primary PCR. These PCR fragments are now complementary, hence during the secondary (phusion PCR) they anneal and extend. The reaction is depicted in Figure 8. The cloning design and analysis was carried out in SnapGene.

The enzyme used for this reaction is phusion polymerase (NEB, F-540L) with the required phusion polymerase HiFid x10 buffer (NEB, F-540L). The reactions are summarized in the tables below.

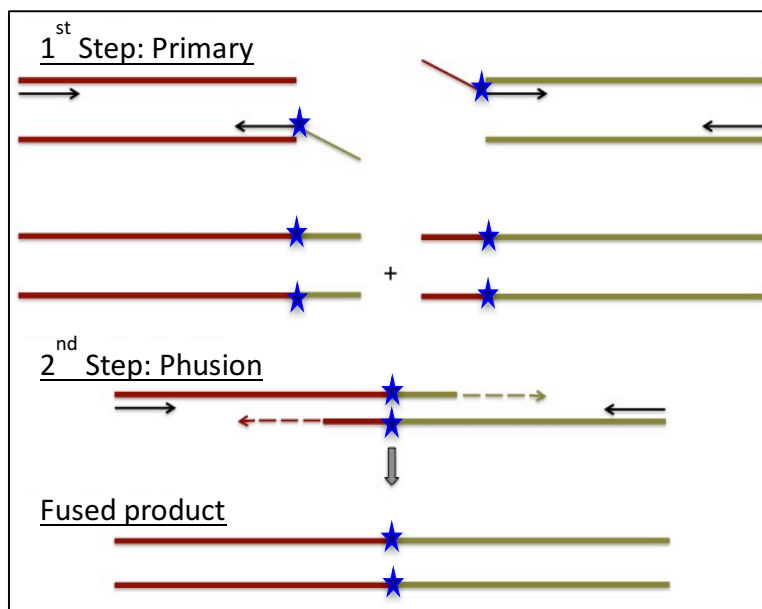


**Figure 8: Reaction of Phusion PCR.** The phusion PCR consists of two separate steps. During the primary PCR the desired mutation or junction sequence is incorporated via the oligo overhangs. The secondary PCR (or phusion) facilitates the fusion of the two PCR fragments that are now complementary.

**Table 4: Primary PCR (Phusion PCR).**

<b>Reagents:</b>	<b>Volume (<math>\mu</math>l):</b>
Nuclease Free H <sub>2</sub> O	35.5
10x High Fidelity Buffer	10
dNTPs	1
Template (200 $\mu$ g/ml)	1
Forward Primer-A (25 $\mu$ M)	1
Reverse Primer-B (25 $\mu$ M)	1
Phusion polymerase	0.5

**Table 5: Phusion PCR (Phusion PCR).**

<b>Reagents:</b>	<b>Volume (<math>\mu</math>l):</b>
Nuclease Free H <sub>2</sub> O	34.5
10x High Fidelity Buffer	10
dNTPs	1
Template (fragment 1)	1
Template (fragment 2)	1
Forward Primer-A1 (100 $\mu$ M)	1
Reverse Primer-B2 (100 $\mu$ M)	1
Phusion polymerase	0.5

### 2.1.1.2 DNA Construction by Oligo Assembly

Oligo assembly is a procedure that allows the synthesis of an arbitrary DNA sequence. This is achieved by creating a pool of overlapping oligos. These overlapping units are extended with several PCR cycles. Successful full-length products created in the primary PCR are then amplified at the secondary PCR, with the first and last primer as forward and reverse respectively. Figure 9 constitutes the map for the oligo assembly of TA99.

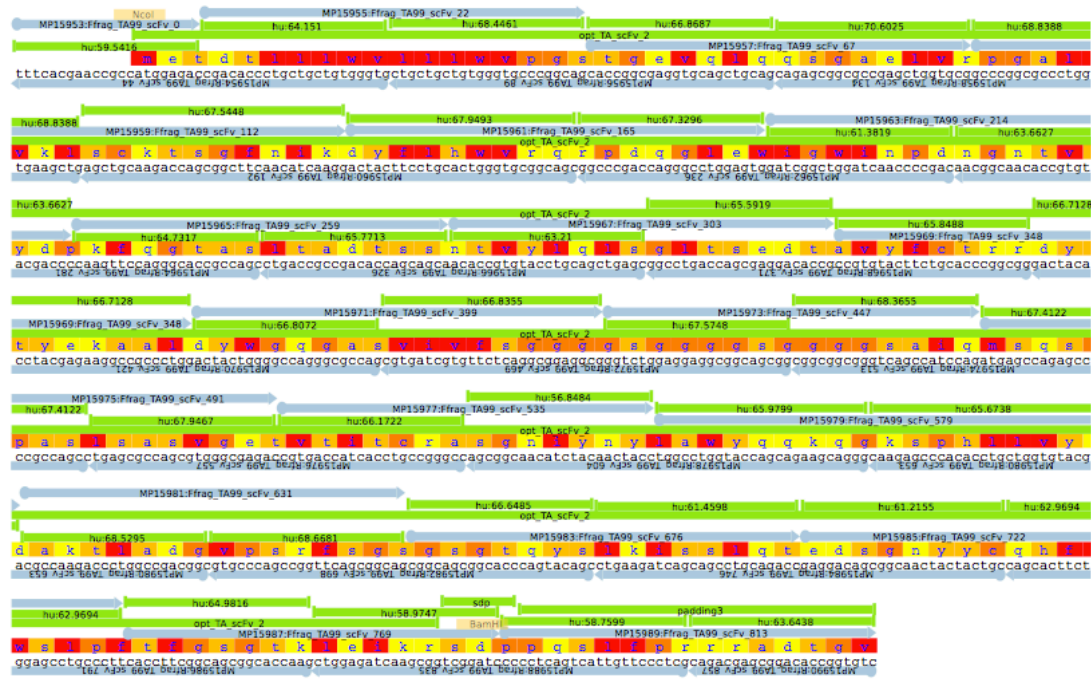


**Figure 9: Oligo assembly of TA99.** An arbitrary DNA sequence can be constructed with a series of overlapping oligos. The complementary oligos form a chain extended in the presence of the polymerase. The fragments that will be successfully extended are subsequently amplified in the secondary PCR.

**Table 6: Primary PCR (Oligo Assembly).**

Reagents:	Volume (µl):
Nuclease Free H <sub>2</sub> O	36.5
10x High Fidelity Buffer	10
dNTPs	1
Template (oligo pool)	2
Phusion polymerase	0.5

Table 7: Secondary PCR (Oligo Assembly).

Reagents:	Volume ( $\mu$ l):
Nuclease Free H <sub>2</sub> O	35.5
10x High Fidelity Buffer	10
dNTPs	1
Template (oligo pool)	2
Forward Primer-A1 (100 $\mu$ M)	1
Reverse Primer-B2 (100 $\mu$ M)	1
Phusion polymerase	0.5

### 2.1.1.3 Alanine Scanning

The alanine scanning was utilised in order to discriminate the contribution of each amino acid residue in the CDR3 of heavy and light TA99 chain. Through the alanine scanning we acquired TA99 alanine substitution mutants bearing a range of affinities. The engineering of the mutants was based on phusion PCR. The phusion PCR introduced the sequence GCC at the junction of the overhang and complementary region.

### 2.1.1.4 Restriction Endonuclease Digestion

The restriction digestions were performed based on the instruction provided by NEB, in order to introduce 'sticky' end on the DNA. The 'sticky' ends facilitates the ligation of two or more DNA fragments. In order to acquire the fragment of the vector backbone 5 $\mu$ g of plasmid stock were digested.

### 2.1.1.5 DNA Ligation and Transformation

The PCR fragments are digested with NEB restriction enzymes, and inserted into an appropriate vector. The ligation is carried out with the Quick ligase kit (NEB, M2200L). The ligation mix is incubated for 5min in room temperature. Then NEB 5-alpha competent *E. coli* (NEB, C2987H) were transformed with 2 $\mu$ l of the ligation mix. The transformation includes three steps. First step is incubation at 4 $^{\circ}$ C for 20min. Then the bacteria are heat shocked at 42 $^{\circ}$ C for 32sec, followed by a recovery step at 37 $^{\circ}$ C

for 30min in SOC medium (New England BioLabs, B90205). After the recovery step the bacteria are spread on an LB agar plate and incubated overnight.

#### **2.1.1.6 Small and Large Scale DNA Preparation**

After the bacterial transformation, a single colony was selected from the LB agar plate and grown overnight in 4ml of Luria-Bertani (LB) Medium (MP Biomedicals LLC, 3002-031). The media was supplemented with 100µg/ml of carbenicillin (VWR International, 69101-3). For small scale DNA preparation (minipreps) we used the QIAprep Spin Miniprep Kit (Qiagen, 27106).

For large scale DNA scale preparation (midiprep) of DNA plasmids, the NucleoBond®Xtra Midi (Mecherey-Nagel, 740410.100) was utilised. The midiprep consisted of: 1) a 50ml Terrific Broth (TB) culture (Merck Chemicals Ltd, 1.01629.0500), 2) 250-500µl of bacterial culture, 3) 100µg/ml of carbenicillin. The midiprep was incubated for 16-18 hours in a bacterial shaking incubator (220 RPM, 37°C).

#### **2.1.1.7 Gel Electrophoresis**

We verified the DNA fragment size, and isolated the fragment by DNA separation using agarose gel electrophoresis. The agarose gels (1%) were prepared in 1x Tris, Boric Acid EDTA (TBE) buffer. The agarose was solubilised by microwave heating of the solution. The 10x TBE buffer consists of 108g Tris, 55g Boric acid, 108g Tris base diluted in 1 litre of de-ionised water (10x).

Once the agarose had been dissolved, the solution was cooled and infused with 0.5-1 µg/ml of ethidium bromide to enable UV visualisation of the DNA. Sample visualisation for loading on the gel was enabled by the loading buffer, which was mixed with the sample at a ratio of 10:1. Agarose gels were electrophoresed at 130V in 1xTBE buffer until appropriate separation was achieved. DNA visualisation was then achieved using an Ngene transilluminator (dark reader blue light box).

#### **2.1.1.8 Gel Extraction**

After the agarose gel electrophoresis and visualisation, the bands were excised from the gel with a clean scalpel. The DNA fragment was extracted from the gel band by

using Qiagen QIAquick (Qiagen, 28106) extraction kits, according to manufacturer's instructions.

## 2.2 PROTEIN WORK

### 2.2.1 Protein Isolation

#### 2.2.1.1 Column A Protein Purification

The TA99 mutant proteins were purified with an 1ml protein A HiTrap column (GE Healthcare Life Sciences, 17-0402-01). The biorad pump was purged with binding buffer, and the pump was calibrated at a rate of 1ml/min. Once the column was attached, 5ml of H<sub>2</sub>O was run through the column, followed by 5ml of binding buffer (Table 8). Once the column was disconnected from the system, the pump was purged with elution buffer. Target eppendorf tubes prefilled with 100µl of pH 9.0 Tris-HCl buffer were prepared for the elution fractions and antibody was eluted with pH 3.5 sodium citrate elution buffer into 1ml fractions.

Table 8: Buffer required for protein purification.

Buffer	Ingredients
Binding Buffer	20mM Sodium Phosphate (Na <sub>3</sub> PO <sub>4</sub> ) 0.15M Sodium Chloride (NaCl) pH 7.2 1L distilled water
Elution Buffer	0.1M Sodium Citrate pH 3-3.5 1L distilled water

#### 2.2.1.2 Calculating Protein Concentration with Nanodrop

The detection threshold of Nanodrop is approximately 0.1mg/ml. The signal peak resides at 280nm, and there should be no material detected at 320nm. The concentration is based on the extinction coefficient (ExPASy programme), shown below:

$$\text{Absorption} = \text{Extinction Coefficient} * \text{Concentration} * L (=1 \text{ in Nanodrop})$$

The fractions that contain protein were pooled together, in order to acquire the total protein sample. Dilute elution fractions were combined and concentrated using Amicon Ultra-15 centrifugal filter units (Merck Millipore, UFC901008), then pooled with peak elution fractions. The pH of the concentrated antibody product was assessed using pH indicator strips and balanced to pH7 with pH9 Tris-HCl.

#### **2.2.1.3 Protein Dialysis**

The concentrated protein was injected into a dialysis cassette and incubated overnight in PBS, at 4°C with gentle agitation mediated by magnetic stirrer to ensure effective buffer transfer. The dialysis cassette was a 10KDa molecular weight cut-off (Thermo Fisher Scientific, 66380).

#### **2.2.1.4 Sodium Dodecyl Sulphate Polyacrylamide Gel Electrophoresis**

Sodium dodecyl sulphate polyacrylamide gel electrophoresis (SDS-PAGE) is used to separate proteins based upon their molecular weight. SDS is an amphipathic detergent that comprises an anionic headgroup and a lipophilic tail. SDS negatively charges proteins to which it binds non-covalently. It thus negates the inherent charge of the native protein, and gives it a uniform negative charge proportional to the length of the peptide chain. The PAGE of proteins labelled with SDS achieves protein separation based on the protein's molecular weight. Following the electrophoresis, the gel can be stained with the Coomassie R-250 to visualise the protein.

The sample preparation included the mixing of the protein with 5µL of sample loading buffer, 2µL of reducing buffer, made up to 20µL final volume. The sample was then boiled at 95°C for 5 minutes.

15µL of each protein sample was loaded on a premade 4-12% SDS-PAGE gel (Lifetechnologies NuPage, NP0301BOX) at 200V, 500mA for 45 minutes on constant voltage mode. As a size reference, 10µL of protein ladder (Thermo Fisher Scientific, Novex LC5801) was run.

#### **2.2.1.5 Coomassie Staining**

Subsequent to the PAGE separation, the gel was covered with 0.25% Coomassie R-250 stain solution and labelled for 60min. The gel was gently agitated on a rotating

plate shaker. The staining solution was then decanted, and the gel was destained with a Coomassie destain solution. Repeated cycles of destaining were performed until the protein bands became clearly visible. Typically, destaining was performed overnight. Finally, the protein gel was covered with cling film and imaged.

### 2.2.2 Surface Plasmon Resonance (SPR)

The affinity of the TA99 mutant scFv was determined by Surface Plasmon Resonance (SPR). In order to determine the sample concentration, the samples were diluted to 1:5 to a final volume of 60 $\mu$ l. A protein sample standard was introduced (cetuximab). The cetuximab was diluted to 20 $\mu$ g/ml. Of the cetuximab sample, 2 $\mu$ l were added into 498 $\mu$ l of PBS-P<sup>+</sup> buffer, and nine serial dilutions (1:2) were performed. Cetuximab at 1.25 $\mu$ g/ml was run as an internal control.

The concentration of the protein samples was normalised to the sample bearing the lowest concentration, and make up to 450 $\mu$ l final volume. The Tyrp1 (Sino Biological, 13224-H08H-50) was reconstituted into 1ml of PBS, and then dialysed for buffer exchange into PBS-P<sup>+</sup>. According to the manufacturer the lyophilised powder contained 32 $\mu$ g of protein, thus the protein concentration after the reconstitution was 32 $\mu$ g/ml. The molecular weight of Tyrp1 is 52.2kDa, so the concentration of Tyrp1 was 615nM [Moles=mass(g)/molecular weight (Da)]. The Tyrp1 solution was diluted to 464nM at a final volume of 700 $\mu$ l.

### 2.2.3 Differential Scanning Fluorimetry (DSF)

Differential Scanning Fluorimetry (DSF) facilitates the calculation of a protein's thermal stability. The protein samples were diluted to 75 $\mu$ g/ml, to a final volume of 22.5 $\mu$ l. The protein samples were added into a 96-well qPCR plate, at triplicates. Then, 2.5 $\mu$ l of Sypro Orange solution (10X) (Thermo Fisher Scientific, S6650) was added. The plate was sealed and centrifuged for 200g, 1min. The samples were run in a Eppendorf qPCR machine, starting at a temperature of 20 $^{\circ}$ C to 99 $^{\circ}$ C gradient, with 0.5 $^{\circ}$ C incremental shifts every 30s.

The data were plotted as Relative Fluorescence Units (RFU) divided by the  $^{\circ}$ C, in order to plot the total fluorescence. The protein peak represents the protein melting point ( $T_m$ ).

## 2.3 TISSUE CULTURE

### 2.3.1 Cell Lines

The cell line of choice for transfection experiments was 293T, which can be efficiently transfected (DuBridge et al., 1987). 293T is an embryonic kidney cell line derived from humans. The 293T cell line was cultured in IMDM (Lonza, 12-726F) supplemented with 1% Glutamax (Gibco, 35050-061), and 10% Fetal Calf Serum (FCS) (Biosera, FB-1001/500).

SupT1 cells are derived from a patient T-cell lymphoblastic leukemia (Levy et al., 1971). SupT1 cells are grown in suspension, and are cultured in RPMI-1640 (Lonza, BE12-167F/12), supplemented with 1% Glutamax (Gibco, 35050-061), and 10% Foetal Calf Serum (FCS).

The human melanoma cell lines that we investigated were T618A, Mel260, Mel275, Mel280, and Mel290 (Ludwig Institute for Cancer Research, Lausanne, Switzerland). The culture medium was RPMI-1640 (Lonza, BE12-167F/12), containing 1% Glutamax (Gibco, 35050-061), and 10% FCS.

In order to produce retroviral supernatant for the *in vivo* model, Phoenix Eco cells were transfected (LGC Standards, ATCC® CRL-3214™). Phoenix Eco derive from 293T, and constitute an ecotropic packaging cell line (Rattmann et al., 2007). This cell line was cultured in DMEM (Gibco, 11995-073) complete medium supplemented with 1% Glutamax (Gibco, 35050-061), and 10% FCS.

For the *in vivo* model, metastatic melanoma was induced with intravenous injection of the B16-F10 melanoma cell line (Fidler, 1973). B16-F10 is a murine melanoma cell line, with C57BL/6 background.

### 2.3.2 Basic Cell Culture Techniques

#### 2.3.2.1 Cryopreservation and recovery of Cell Lines

Cryopreservation facilitates the long-term storage of cell lines. The cells were centrifuged, and resuspended at  $5 \times 10^6$  cells/ml in chilled cryopreservation medium and aliquoted into 1ml aliquots into cryovials (Corning). The cryovials were

transferred into a Mr. Frosty freezing container, which was then placed into a -80 °C freezer. The isopropanol bath of the Mr.Frosty container guarantees a controlled cooling rate of 1°C/min. Twenty-four hours later, the frozen cells were transferred to a liquid nitrogen storage tank for long term storage.

### 2.3.2.2 Cellular Recovery from Cryopreservation

The cryoprotectant Dimethyl sulfoxide (DMSO), which is present in the cryopreservation medium, is toxic to metabolising cells. Hence, it is crucial to minimise DMSO exposure during cellular recovery. The cryopreserved cells were thawed in a 37°C water bath. Once thawed, the cells were washed in 25ml of the pre-warmed complete media, and then resuspended and cultured into appropriate media at 37°C.

### 2.3.2.3 Transient Transfection of 293T Cells for Protein Production

In order to produce and test the TA99 antibody, we transfected 293T cells with the SFG.TA99scFv-rlgG1-Fc.I2.eBFP2 plasmid and GeneJuice (Merck Millipore, 70967). The antibody was produced by the cells, and secreted into the supernatant. The supernatant was then collected at 48 hours, and used in subsequent experiments.

Table 9: Transfecting 293T for antibody secretion

Reagents:	Volume (µl):
RPMI	470
Genejuice	30
Plasmid Construct	12.5 (µg)

## 2.3.3 Primary Cell Culture

### 2.3.3.1 Isolation of PBMCs

Primary T-cells isolated from healthy donors were utilised as effectors in *in vitro* CAR efficacy experiments. For the isolation of Peripheral Blood Monocuclear Cells (PBMCs) we separated blood from healthy donors on Ficoll-Paque Premium (GE Healthcare Life Sciences, 17-5442-02). The blood was mixed 1:1 (50ml total) with plain RPMI, and then layered on 10ml Ficoll. Centrifugation (750g, 40min) creates a gradient of red

blood cell and plasma, with the lymphocytes residing in the interface between the two forming a buffy coat (Böyum, 1968). The cells were washed twice with complete RPMI, and counted. At a concentration of  $10^6$  cells/ml, we plated 2ml per well, in a 24-well plate supplemented with 5 $\mu$ M/ml PHA (Sigma, L9017). Twenty-four later, cells are stimulated with 100U human Interleucine 2 (IL2) (Genscript, Z00368-1).

### **2.3.3.2 Murine Splenocyte Isolation**

The effector T-cells used in the B16 melanoma model were splenocytes isolated from the spleens of C57BL/6 mice. The spleens were transferred in 10cm plates through 40 $\mu$ m strainers. The organs were macerated in 1ml of red-blood cell lysis buffer, ACK (Lonza, 10-548E). After a 3min incubation, the cell suspension was transferred in 50ml falcon tubes, and centrifuged at 400g for 5min. The cells were then resuspended in  $1 \times 10^6$  cells/ml, and activated with 2 $\mu$ g/ml ConA (Sigma, C522275) and 1ng/ml IL-7 (R&D, 207IL025). The cell suspension was plated in T75 flasks at a maximum volume 20ml.

### **2.3.4 Retroviral Supernatant Production**

#### **2.3.4.1 Retroviral Supernatant Production for Transduction of PBMCs**

Generation of retroviral supernatant was achieved by transfecting 293T with three plasmids. The essential plasmids for the generation of particles are the RD114 plasmid (retroviral pseudotyping with RD114 envelope) (Cosset et al., 1995), Gagpol plasmid (pEQ-Pam3-Epeqpam-env Moloney Murine Leukemia Virus gagpol expression plasmid), and the SFG retroviral plasmid. The SFG retroviral plasmid, which includes the LTR and the packaging signal, also carries the transgene. The GeneJuice is mixed with the medium and incubated in room temperature for 5min. Then the plasmids are introduced in the mixture followed by 15min incubation before added on 293T.

**Table 10: Triple transfection of 293T for retroviral production.**

Reagents:	Volume ( $\mu$ l):
RPMI	470
Genejuice	30
Gagpol	4.7 ( $\mu$ g)
Envelope RD114	3.1 ( $\mu$ g)
SFG plasmid	4.7 ( $\mu$ g)

#### 2.3.4.2 Retroviral Supernatant Production for Transduction of Splenocytes

For the transduction of murine splenocytes, ecotropic-pseudotype retrovirus was used with transfection of Phoenix Ecotropic packaging cell line. The cells were plated on 10cm plates, at a concentration of  $1.5 \times 10^6$  cells per plate. The following day, the cells were transfected with the mixture of FuGene with the pCL.Eco and the SFG plasmid. pCL.Eco contains the Eco envelope and gagpol (Naviaux et al., 1996).

**Table 11: Transfecting Phoenix Eco cells for production of ecotropic retrovirus.**

Reagents:	Volume ( $\mu$ l):
Optimem (Gibco, 31985-070)	150
FuGene (E2691)	10
pCL.Eco	1.5 ( $\mu$ g)
SFG plasmid	2.6 ( $\mu$ g)

#### 2.3.4.3 Coating of Tissue Culture Plates with Retronectin

Non-tissue culture treated 24-well plates were coated with 500 $\mu$ l of PBS supplemented with 8 $\mu$ l of retronectin/ml 24 hours before the suspension cell transduction. The plates were wrapped in parafilm and stored at 4°C. Retronectin-supplemented PBS was re-used twice by direct transfer to fresh plates and stored as above until required.

#### **2.3.4.4 Retroviral Transduction of PBMCs**

PBMCs are transduced 48-hours after isolation. The retroviral supernatant is pseudotyped with RD114. For enhanced transduction efficiency, the wells of non-tissue culture treated plate are coated with 4µg retronectin (Clontech, T100B) the day before. Retronectin binds to the viral particles and the cells bringing them in proximity to one another, and thus increasing transduction efficiency.

On the day of the transduction the retronectin is aspirated from the wells, replaced with 250µl of viral supernatant and incubated for 30min at room temperature (RT). In the meantime, the cells are harvested and resuspended at  $0.5 \times 10^6$ /ml. The 250µl of viral supernatant are aspirated. We add 0.5ml of cells, 1.5ml fresh supernatant and 100U/ml of IL2 for each well. The next step includes the centrifugation of the plate for 40min, at 1000g, RT.

#### **2.3.4.5 Retroviral Transduction of Splenocytes**

In order to enhance the transduction efficiency, 24 hours before the transduction the non-tissue culture treated 24-well plates were coated with 18µg Retronectin (Clontech, T100B) per well. On the day of the transduction the wells were blocked with 2% Bovine serum albumin (BSA)-Phosphate-buffered saline (PBS) for 30min. The wells were then washed with PBS (Gibco, 70011-044) twice. In the meantime, the splenocytes were counted and aliquoted at  $2 \times 10^6$  cells for each well of transduction. The splenocytes were resuspended in 1ml neat supernatant, and transferred to the plate. The final step is a centrifugation at 750g for 90 min. Twenty-four hours later, 100U/ml IL-2 (Roche, 11 147 528 001) was administered.

#### **2.3.5 Primary Melanoma Samples**

The primary melanoma samples were obtained from patients with metastatic melanoma at the Royal Marsden hospital. The tumours were homogenized into single cell suspension with the Human Tumour Dissociation kit (Miltenyi, 130-095-929). We followed the kit protocol, where the tumour was cut into 2-4mm pieces and was mixed with the enzymes provided with the kit. The sample was transferred to gentleMACS tubes and homogenized at gentleMACS Program h\_tumor\_01 prior to a 30min incubation at 37°C. After the incubation, we once more ran the sample at

gentleMACS Program h\_tumor\_01. We centrifuged the sample (400g, 5min), and resuspended the cell pellet in PBS. The sample was allocated into FACs tubes for staining, either intracellular or extracellular for detection of Tyrp1 according to flow cytometry protocols at 2.4.1. The samples stained for extracellular Tyrp1 were signal enhanced twice with the FASER Kit PE (Miltenyi, 130-091-764).

**Table 12: Antibodies used for primary melanoma cell labelling: Panel no1.**

Antigen	Fluorophore	Company	Catalogue No
CD45	APC	BioLegend	304012
MCSP	VioBlue	Miltenyi	130-098-791
Tyrp1	PE	GeneTex	GTX11780
IgG2a Isotype Ctrl	Unconjugated	BioLegend	400202
Mouse IgG2a	PE	Invitrogen	M32204
Viability Dye	eFluor780	eBioscience	65-0865-14

**Table 13: Antibodies used for primary melanoma cell labelling: Panel no2.**

Antigen	Fluorophore	Company	Catalogue No
CD45	Pacific Blue	BioLegend	304029
CD31	FITC	Miltenyi	130-092-654
MCAM (CD146)	APC	R&D Systems	FAB932A
Tyrp1	PE	GeneTex	GTX11780
IgG2a Isotype Ctrl	Unconjugated	BioLegend	400202
Mouse IgG2a	PE	Invitrogen	M32204
Viability Dye	eFluor780	eBioscience	65-0865-14

## **2.4 FLOW CYTOMETRY**

### **2.4.1 General Labelling Protocol**

On average,  $2 \times 10^5$  cells were washed with PBS, and labelled with 100 $\mu$ l of the antibody mix. The cells were then washed, and resuspended in PBS. For labelling protocols that required multiple steps, the samples were washed with PBS between individual staining steps. All staining steps were performed at RT, in the dark with 20min incubation per step.

### **2.4.2 Labelling for Extracellular Antigens**

The extracellular labelling is used for detection of antigens on the plasma membrane of the interrogated cells. The cells are washed with 4ml PBS, centrifuged at 800g for 2min, and resuspended in the 100 $\mu$ l of antibody mix. We incubated with the antibodies for 20min at RT. After repeating the wash and labelling for additional staining steps, the cells were resuspended in 500 $\mu$ l 0.4% Paraformaldehyde (PFA)-PBS.

### **2.4.3 Labelling for Intracellular Antigens**

For the detection of intracellular proteins, we used the kit BD Cytofix/Cytoperm (BD, 554714). According to the manual, labelling of extracellular antigens was followed by fixation/permeabilisation. Once the cells were permeabilised, the intracellular labelling was carried out at 4 $^{\circ}$ C for 20min, and resuspended in 500 $\mu$ l 0.4% PFA-PBS.

### **2.4.4 Preparation of Counting Beads**

In order to calculate absolute number of cells via flow cytometry, a pre-determined quantity of counting beads was introduced into the samples. The amount of Flow-Check fluorospheres (Beckman Coulter, 41116148) introduced was  $1 \times 10^6$  beads/ml in an aqueous solution containing preservative surfactant. In order to remove the preservative, the beads were washed once with PBS prior to addition to samples. The washing step entailed centrifugation at 400g for 5min. The beads were then resuspended in PBS, at a volume equivalent to the starting volume. Hence, the

concentration was preserved at  $1 \times 10^6$  beads/ml. In each sample we introduced  $10 \mu\text{l}$  of the solution that contained  $10^4$  beads in total.

#### **2.4.5 Signal Enhancement with Miltenyi FASER Kit PE**

The enhancement of the Tyrp1 staining was achieved by incorporating the FASER Kit PE (Miltenyi, 130-091-764) into the labelling procedure. The procedure was carried out in accordance to the manufacturer's instructions. The enhancement cycle was repeated twice.

#### **2.4.6 Antigen Quantification with QIFIKIT Beads**

QIFIKIT kit (DAKO, K0078) consists of the set-up beads and the calibration beads. The set-up beads have two populations of negative and high-density positive populations. The calibration beads contain five populations of defined antigen molecules per population. The beads were stained with the same secondary antibody used for the melanoma, anti-mouse IgG2a PE. Sequentially, the beads underwent the two PE signal enhancement steps, and finally resuspended in  $350 \mu\text{l}$  PBS. The PE-MFI for each sample was used to plot a standard curve.

#### **2.4.7 Antigen Quantification with QuantiBrite-PE**

An alternative way of antigen quantification was based on the QuantiBrite PE beads (BD Biosciences, 340495). The kit contains a lyophilised pellet that was reconstituted in  $0.5 \text{ml}$  of PBS according to the manufacturer's instructions.

### **2.5 IN VITRO ASSAYS**

#### **2.5.1 CD56 Magnetic Bead Negative Selection**

In order to decrease background in *in vitro* assays, Natural Killer (NK) cells were eliminated from the PBMCs culture. This was achieved by CD56 depletion performed with CD56 beads (Miltenyi, 130-050-401). The protocol was based on the manufacturer's instructions, and the columns we used were LD (Miltenyi, 130-042-901).

### 2.5.2 <sup>51</sup>Cr Release Assay

Measurement of the CAR-T cell cytotoxicity was performed with Chromium (Cr) release assay. We used the radioisotope <sup>51</sup>Cr. One million target cells were loaded with 20µl of <sup>51</sup>Cr and incubated for 1 hour. In the meantime, the PBMCs were harvested from the 24-well plate, counted, and resuspended at a final concentration of 1.6x10<sup>6</sup> cells/ml. After the 1-hour incubation, the target cells were washed 5 times with centrifugation at 400g for 3min, and resuspended at 0.05x10<sup>6</sup> cells/ml. The ratios of effector: target were 32:1, 16:1, 8:1, 4:1. Each condition was carried out in triplicates. In each well of a v-bottom 96-well plate, 100µl of each effectors and targets were added. In order to calculate percentage of killing, we measured background release of targets with no effectors, and maximum release of targets incubated with 1% Triton-X. Once the plate was set up, the plate was centrifuged at 400g for 5min, and incubated at 37°C for 4 hours. The plate was centrifuged again at 400g for 3min, and the 100µl of supernatant was collected and scrutinized for radioactivity with a gamma counter.

Once the measurement was acquired, the percentage was calculated by extrapolation from the following equation:

$$\text{Cr release} = \frac{(\text{Experimental release} - \text{Background release}) \times 100}{\text{Maximum release} - \text{Background release}}$$

The percentage was calculated in Microsoft Office Excel, and the results were plotted in Prism.

### 2.5.3 Co-Culture Assays

#### 2.5.3.1 Preparation of Co-Culture

The effector cells were counted and normalised at 30% of transduction level with the addition of NT T-cells. Target and effector cells were harvested, re-suspended at a concentration 1x10<sup>6</sup> cells/ml and 100µl of each was plated in wells of a 96-well TC-treated plate (1:1 effector: target ratio). Twenty-four hours later, 100µl of supernatant was collected from the wells, and frozen at -80°C for later assessment. The co-culture was terminated at day 1, 3, or 7, and the cells were analysed by flow-cytometry.

### 2.5.3.2 Flow-Cytometry Based Killing Assay (FBK)

Target and effector cells were co-cultured at a 1:1 in 96-well plates, with a total initial cell concentration of  $10^6$ /ml in 100 $\mu$ l. The premise of Flow-Cytometry Based Killing Assay (FBK) is based on counting the absolute number of alive target cells at the end-point of the co-culture. The cells were labelled with viability and appropriate cell surface markers, in order to identify alive target and effector cells. Following the labelling of the cells, they were resuspended for analysis in a fixed number of counting beads ( $10^4$ ). The percentage (%) of target cell killing was calculated based on the absolute number of target cells in the NT T-cell condition. That absolute number of the NT T-cells is set as 100%, and the number of targets in the following T-cell conditions is expressed as a percentage of survival.

Table 14: Panel for Flow-cytometry based killing assay.

Antigen	Fluorophore	Laser	Company	Catalogue No
eGFP (Targets)		Blue		
ahFc	Alexa405	Violet	Jackson ImmoResearch	109-006-088
CD3	APC	Red	BioLegend	300312
Viability	eFluor780	Red	eBioscience	65-0865-18
Counting Beads	-	-	Beckman Coulter	41116148

### 2.5.3.3 T-Cell Differentiation Panel

The differentiation of T-cells was categorised into four cohorts of naïve (Tnaive), stem-cell memory (Tscm), central memory (Tcm), or effector memory (Tem) T-cells. The panel for the differentiation labelling is shown in Table 15. The differentiation panel includes the markers: Cluster of Differentiation (CD)95, CD45RA, and C-C chemokine receptor 7 (CCR7). The differentiation stages and justification are discussed in detail in 5.1.2.

Table 15: Panel for T-cell differentiation profile.

Antigen	Fluorophore	Laser	Company	Catalogue No
	eGFP (Targets)	Blue	-	-
CD45RA	PE	Yellow-Green	eBioscience	12-0458-42
CD8	PeCy7	Yellow-Green	TONBO	60-0088-T100
CD95	Pacific Blue	Violet	BioLegend	305619
CD4	BV650	Violet	BioLegend	317436
CD197	BV685	Violet	BioLegend	353230
ah-Fc	APC	Red	Jackson ImmunoResearch	109-606-088
Viability	eFluor780	Red	eBioscience	65-0865-18
Counting Beads	-	-	Beckman Coulter	41116148

#### 2.5.3.4 T-Cell Exhaustion Panel

Exhaustion reflects the state of T-cells, where antigen stimulation fails to elicit cytotoxic or cytokine secretion response. The exhaustion markers used were PD-1 and T-cell Immunoglobulin Mucin 3 (Tim3). The double negative cells constitute the non-exhausted T-cell cohort. The single positive cells exhibit an exhausted phenotype, whereas the double positive cohort suffers a more severe phenotype. The exhaustion panel is shown in Table 16.

Table 16: Panel for T-cell exhaustion profile.

Antigen	Fluorophore	Laser	Company	Catalogue No
	eGFP (Targets)	Blue	-	-
CD8	PE-Cy7	Yellow-Green	TONBO	60-0088-T100
CD25	v450	Violet	eBioscience	48-0259-42
Tim3	BV510	Violet	BioLegend	345030
PD-1	BV605	Violet	BioLegend	329924
CD4	BV650	Violet	BioLegend	317436
ahFc	AF649	Red	Jackson ImmunoResearch	109-606-088
Viability	AF780	Red	eBioscience	65-0865-18
Counting Beads	-	-	Beckman Coulter	41116148

#### 2.5.3.5 ELISA for IFN- $\gamma$ and IL2

The IL2 and IFN- $\gamma$  ELISA were performed according to the protocol provided by the manufacturer. Specifically, the kit utilised for calculating the IFN- $\gamma$  secretion was the

Human IFN- $\gamma$  ELISA MAX™ Deluxe (BioLegend, 430105). The kit used for the IL2 measurements was the IL2 ELISA MAX™ Deluxe (BioLegend, 431804).

Briefly, a 96-well plate was coated with a protein capture antibody overnight at 4°C. The following day, the plate was washed, and loaded with the protein samples diluted appropriately. The protein samples were incubated on the plate for 2 hours at RT. The plate was washed, and the cytokine detection antibody (biotinylated) was added for 1-hour. Subsequently, the plate was washed, and avidin-horseradish peroxidase (HRP) was added. After 30mins and another wash, the detection substrate was added for 15min, and then the stop solution was added. We detected colorimetric changes by measuring the absorption at 450nm using a plate-reader. Concentration of IFN- $\gamma$  or IL2 was determined according to a standard curve produced by simultaneously assaying serial dilutions of an IFN- $\gamma$  or IL2 standard solutions.

#### **2.5.4 Microscopy**

##### **2.5.4.1 Confocal Imaging of Acetone Fixated Tissue**

Tissue for the confocal microscopy was provided by Dr Jake Henry. Specifically, melanoma was induced in C57BL/6 mice with injection of B16-F10 melanoma cell line. Lungs bearing metastatic melanoma tumours were labelled for confocal analysis. The lungs were extracted from the mice and embedded in Optical Cutting Temperature Compound (VWR, 361603E), and cut into 6 $\mu$ m slices with a cryostat. The slides were kept frozen at -80°C.

On the day of the procedure the slides were air dried at RT for 10min and then fixed in 4°C acetone for 10min. The slides were air dried and hydrated in 100 $\mu$ l of Super Block (SB). Super block contains 500 $\mu$ l mouse serum (Sigma, M6905-10ML), 500 $\mu$ l rat serum (Sigma, R9759-10ML), 200 $\mu$ l FCS, 200 $\mu$ l anti-Fc receptor antibody (2.4G2, produced in the lab), 100 $\mu$ l sodium-azide 10%, 8.5ml PBS. After the hydration step, we added the primary antibody (TA99 secreted from transfected 293T), and it was incubated overnight.

The following day, the slides were washed in PBS, and incubated for 15min with the secondary antibody (1:100 dilution). Finally, the cells were labelled with 300nM DAPI (Sigma, D9542-10MG) for 5min and washed twice. After drying the slide, we added

60µl fluoromount (Southern Biotech, 0100-01), covered with coverslip and sealed with nail polish.

The slides were imaged in a confocal microscope Leica SPE2. The data were analysed with Fiji and Photoshop software.

#### **2.5.4.2 Live-Cell Imaging**

The live-cell imaging was carried out on T618A cells transduced with Proximal Tyrp1, in order to imitate the inherent trafficking pathway of Tyrp1. The cells were propagated the day prior to the imaging, and plated at  $10^5$  cells in 35mm glass-bottom dish (Ibidi, 81158). The media used was phenol red free RPMI (Lonza, 12-918F). For all the subsequent steps in the live-cell imaging, the media utilised was phenol red free.

Immediately before the imaging, the cells were washed with media, and resuspended in staining solution supplemented with 1X CellMask Deep Red (Thermo Fischer Scientific, C10046). After an incubation of 5min, the dish containing the cells was washed three times with media. Fresh media was added to the cells. The data were acquired with an IX71 Olympus inverted microscope, and were consequently analysed in the Imaris analysis software.

## **2.6 IN VIVO PROCEDURES**

### **2.6.1 Experimental Overview**

For the animal model we used 6-8 weeks old C57BL/6 mice. On day 0, the mice were injected with  $10^5$  B16.F2 cells subcutaneously. On day 7, the mice received a 5Gy irradiation, and then were injected with  $5 \times 10^6$  CD8 transduced cells. On day 14, the mice were bled to test for engraftment, and culled on day 23. Tumour measurements were obtained every 2 days.

### **2.6.2 Intravenous Injection of Mice**

The animals were heated in a warming box to 39°C in order to provoke peripheral vasodilatation. Tail vein cannulation was performed using a 27G needle, where 200µl of tumour cells were injected into the animal. Tumour samples or T-cells were

resuspended at appropriate concentration (specified in 4.3.4.1 and 4.3.5.1) in plain RPMI supplemented with 0.1% HEPES buffer.

### 2.6.3 Organ Harvest and Preparation

#### 2.6.3.1 Blood Harvest and Preparation

The blood samples were collected in 1.5ml tubes containing 10 $\mu$ l heparin (Leo Laboratories Ltd, PL0043/0149). Next, 4.5ml of H<sub>2</sub>O was added into the blood sample for 1min, in order to achieve red-blood cell lysis. We immediately added HANKS buffer (Sigma, H1641) to avoid lymphocyte cell damage. The samples were then centrifuged at 800g for 2min, blocked with 200 $\mu$ l 2.4G2, and labelled for extracellular and intracellular antigens.

Table 17: Antibodies for in vivo T cell engraftment screening.

Antigen	Fluorophore	Laser	Company	Catalogue No
CD4	FITC	Blue	BioLegend	100510
CD19	PE	Yellow-Green	eBioscience	12-0193-82
CD8	eFluor405	Violet	eBioscience	48-0081-82
CD3	APC	Red	BD	553066
Viability Dye 785	eFluor780	Red	eBioscience	65-0865-14

#### 2.6.3.2 Tumour Sample Preparation

The tumours were weighted before being macerated in 1ml of liberase/DNAse buffer. Liberase (Roche, 5401020001) was reconstituted in 1ml plain RPMI, and DNAse (Roche, 10104159001) in 5ml of H<sub>2</sub>O, and aliquoted. For the enzymatic master mix, we combined 330 $\mu$ l of liberase with 50 $\mu$ l DNAse, plus 4620 $\mu$ l plain PRMI. The samples were incubated with the enzymatic master mix for 30min at 37°C. Subsequently, the samples were then put through a 70 $\mu$ m strainer and washed. The cell pellet was resuspended in 3ml of complete RPMI, applied on Histopaque (Sigma, 1191-6X100ML), and centrifuged at 700g for 10min at RT, with no brake. The interphase containing the lymphocytes was collected and stained with the panel indicated on Table 17.

### **2.6.3.3 Spleen Harvest and Preparation**

The spleens were excised, and transferred to containers with chilled PBS. The spleens were then macerated with gentle pressure. The cell suspension was red-cell lysed with 1ml of ACK lysis buffer for 5mins. Completion of the red-blood cell lysis was accomplished by adding 5ml of PBS. The cell suspension was then filtered through a 70 $\mu$ m cell strainer. Cells were subsequently centrifuged, and resuspended in PBS for subsequent labelling protocols.

### **2.6.3.4 Bone Marrow Harvest and Preparation**

We harvested femurs and tibias from the animals, transferred to chilled PBS. The bone edges were removed with scissors, and the bone marrow was flushed with PBS into a 50ml falcon tube by using a 25G needle. The cells were pelleted by centrifugation, and resuspended into 1ml of ACK lysis buffer. The cell suspension was incubated with ACK for 5min. PBS (5ml) was added into the solution to terminate the lysis and the cells were filtered through a 70 $\mu$ m cell strainer. The cell suspension was pelleted, and resuspended in PBS for subsequent labelling protocols.

**CHAPTER 3: Results**

**Validating Tyrp1 as a Target on  
Melanoma Cells**

## CHAPTER 3: RESULTS: VALIDATING TYRP1 AS A TARGET ON MELANOMA CELLS

### 3.1 INTRODUCTION

#### 3.1.1 Tyrosinase-Related Protein 1

Tyrp1 is a transmembrane melanosomal enzyme that resides on the surface of the melanosomes (Vijayasaradhi et al., 1995). However, approximately 2% of Tyrp1 is present on the cell surface (Yiqing Xu et al., 1997). An anti-Tyrp1 antibody successfully eradicated metastatic-lung tumours in an *in vivo* model (Hara et al., 1995). Therefore, Tyrp1 constitutes an intriguing target for melanoma. The main advantage is the lineage specific expression of Tyrp1, which would limit possible side effects of the CAR T-cell treatment. We postulated that the low antigen-density Tyrp1 will suffice for CAR recognition.

The first goal was to validate Tyrp1 as a potential CAR target on melanoma. In order to achieve that, we investigated the presence of Tyrp1 on the surface of melanoma cell lines and primary melanomas. In order to interrogate the CAR sensitivity, we developed a cell line with variant densities of Tyrp1.

#### 3.1.2 TA99

As discussed earlier (1.5), TA99 is an antibody against Tyrp1, which caused tumour rejection of B16F10 in C57BL/6 mice (Hara et al., 1995). Upon the fusion of the melanosome to the cell surface, the Tyrp1 is incorporated into the plasma membrane. The luminal domain of Tyrp1 becomes extracellular, and the cytoplasmic domain becomes intracellular (Yiqing Xu et al., 1997). Since the TA99 recognises the Tyrp1 exposed on the cell surface, the binding epitope resides on the luminal domain of Tyrp1, although the exact epitope is unknown. We utilised the TA99 clone for flow-cytometry labelling, as well as the scFv of the anti-Tyrp1 CAR. Hence, in this chapter we discuss the specificity of TA99.

#### 3.1.3 Live-Cell Imaging: Eos

Although a fraction of Tyrp1 is present on the plasma membrane, it is unknown whether it facilitates a role on the cell surface or if it is a stochastic event. The

trafficking pathway of Tyrp1 to the cell surface is also unknown. Hence, we are interested in characterising the Tyrp1 trafficking patterns. In order to achieve that, Tyrp1 was fused to the Eos fluorescent protein.

Eos is a fluorescent tetrameric protein isolated from *Lobophyllia hemprichii*, which emits fluorescence at 516nm. Violet radiation illumination photoconverts Eos to light emittance at 581nm. The tripeptide HYG conveys the fluorescence properties upon Eos. Illumination of violet radiation (405nm) leads to an irrevocable cleavage in the side chain of histidine 62 (Figure 10). Consequently, the Eos protein is photoconverted from green to red fluorescence (Wiedenmann et al., 2004). The tetrameric protein was then engineered in a monomeric format, which is the one used for the purpose of this project (Zhang et al., 2012). We refer to the fluorescent protein as mEos due to its monomeric structure.

mEos has been mainly used in super-resolution microscopy, however we endeavoured to utilise it for conventional confocal microscopy (Jones et al., 2011, Fernández-Suárez and Ting, 2008). The strategy was to fuse Tyrp1 to mEos, and follow the Tyrp1 trafficking pathway. Specifically, we aimed to focus on a Tyrp1-mEos positive cell, zoom in and photoconvert a tenth of the cell. Then, we zoomed out and followed the trafficking of the photoconverted red-fluorescent Tyrp1-mEos molecules.

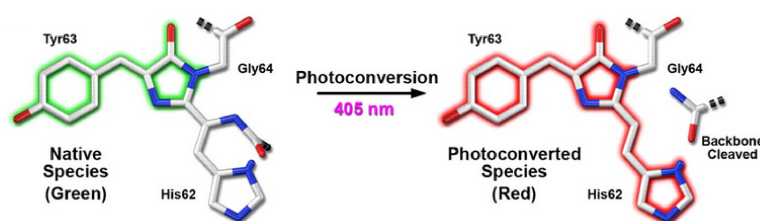


**Figure 10: Green-to-red photoconversion of mEos.** The mEos protein contains the amino acid sequence HYG, which constitutes the chromophore. Violet radiation causes a break in the histidine 62 chain. This cleavage leads to the green-to-red photoconversion (Shaner et al, 2007).

### 3.1.4 Antigen Density Quantification

Tyrp1 is the most abundant protein in melanocytes (Tai et al., 1983)(Virador et al., 2001). However, the prevalence of Tyrp1 expression in melanoma malignancies is controversial. All melanosomal components, including Tyrp1, were shown to have a heterogeneous expression pattern in melanoma (Virador et al., 2001). Although it

was shown that Tyrp1 is expressed in 60% of melanomas, the correlation between Tyrp1 expression and disease progression is disputable (Bolander et al., 2008). Bolander and colleagues observed a reverse correlation between Tyrp1 and progression, in contrast to an older study that proclaimed a positive correlation (Holzmann et al., 1987).

Another unknown parameter regarding the aptness of Tyrp1 as a CAR antigen target is its density on the cell surface. The lower limit for CAR sensitivity is approximately 240 epitopes/cell surface (Watanabe et al., 2015), the exact figure will depend on the method of transduction and the T-cell phenotype as well as CAR density, affinity and accessory molecules that engage in the synapse. It is currently unknown whether the Tyrp1 density is above or below the lower detection limit of CAR T-cells.

In order to address the above concerns and determine whether Tyrp1 is a promising target for melanoma, it was crucial to characterise its surface expression. The characterisation should address three issues: the heterogeneity of expression within a tumour; the prevalence of expression among melanoma cell lines and primary tumours; and finally density quantification in order to determine if it is within the CAR detection range. In order to answer these questions, melanoma cell lines and primary melanoma samples were interrogated with flow cytometry for the expression of Tyrp1.

For the antigen quantification, we used two commercially available kits, the QIFIKIT and the QuantiBrite-PE kit. The QIFIKIT kit employs a secondary antibody to stain the beads coated with a range of antigen densities. The main advantage of the QIFIKIT kit is that the beads are originally unlabelled. Hence, during the experiment the beads are labelled with the same secondary as the cells, excluding confounding discrepancies due the fluorophore brightness. Additionally, the beads can undergo signal enhancement cycles concomitantly with the samples interrogated. This is essential, because the antigen density is low, and signal enhancement was crucial for the antigen detection with flow cytometry. The QIFIKIT was successfully used in order to determine the antigen density in a study comparing the sensitivity of Bispecific T-Cell Engagers (BiTEs) against CARs, as well as other studies (Stone et al., 2012) (Watanabe et al., 2015).

The QuantiBrite-PE beads are pre-labelled with PE. As a result, disparity in the fluorophore brightness between the beads and the samples constitutes a confounding factor. According to the manufacturer these beads cannot be centrifuged, and thus cannot be signal enhanced in parallel to the cells. However, the main advantage of the QuantiBrite-PE beads is their lower limit of detection, which is approximately 500 epitopes/cell. In contrast, the range of QIFIKIT beads commences above 2000 epitopes/cell. The QuantiBrite-PE beads have been used in several studies for antigen quantification (Sennikov et al., 2015, Wang et al., 2010).

### **3.2 AIMS**

- Validation of TA99 specificity and sensitivity.
- Engineering of Tyrp1 constructs for density gradient.
- Demonstration of Tyrp1 presence on engineered cell lines and melanoma cell lines.
- Determination of Tyrp1 antigen-density on cell lines and primary melanomas.

### **3.3 RESULTS**

#### **3.3.1 Cloning of constructs**

##### **3.3.1.1 Generation of TA99 scFV**

For the purpose of this project, we constructed and validated the scFv of TA99. The sequence was extrapolated from the patent “anti-Tyrp1 antibodies”, US Patent: 7951370B2 (Balderes and Kang, 2011). Figure 11 illustrates the TA99 Heavy and Light chain sequence, annotated at the UCL abYsis bioinformatics site ([http://www.bioinf.org.uk/abysis/sequence\\_input/blast/blast\\_form.html](http://www.bioinf.org.uk/abysis/sequence_input/blast/blast_form.html)). This sequence was reconstructed by oligo assembly gene synthesis, and cloned into an SFG retroviral vector (Rivière et al., 1995).

### TA99 Heavy Chain

Query protein sequence	E	V	Q	L	Q	Q	S	G	A	E	L	V	R	P	G	A	L	V	K	L		
Chothia numbering	H1	H2	H3	H4	H5	H6	H7	H8	H9	H10	H11	H12	H13	H14	H15	H16	H17	H18	H19	H20		
CHOTHIA REGIONS												HFR1										
												↑										
S	C	K	T	S	G	F	N	I	K	D	Y	F	L	H	W	V	R	Q	R	P	D	Q
H21	H22	H23	H24	H25	H26	H27	H28	H29	H30	H31	H32	H33	H34	H35	H36	H37	H38	H39	H40	H41	H42	H43
												HFR2										
												↑										
G	L	E	W	I	G	W	I	N	P	D	N	G	N	T	V	Y	D	P	K	F	Q	G
H44	H45	H46	H47	H48	H49	H50	H51	H52	H52A	H53	H54	H55	H56	H57	H58	H59	H60	H61	H62	H63	H64	H65
												HFR3										
												↑										
T	A	S	L	T	A	D	T	S	S	N	T	V	Y	L	Q	L	S	G	L	T	S	E
H66	H67	H68	H69	H70	H71	H72	H73	H74	H75	H76	H77	H78	H79	H80	H81	H82	H82A	H82B	H82C	H83	H84	H85
												HFR4										
												↑										
D	T	A	V	Y	F	C	T	R	R	D	Y	T	Y	E	K	A	A	L	D	Y	W	G
H86	H87	H88	H89	H90	H91	H92	H93	H94	H95	H96	H97	H98	H99	H100	H100A	H100B	H100C	H100D	H101	H102	H103	H104
												HFR4										
												↑										
Q	G	A	S	V	I	V	F															
H105	H106	H107	H108	H109	H110	H111	H112															
												HFR4										
												↑										

### TA99 Light Chain (Kappa)

Query protein sequence	A	I	Q	M	S	Q	S	P	A	S	L	S	A	S	V	G	E	T	V	T		
Chothia numbering	L1	L2	L3	L4	L5	L6	L7	L8	L9	L10	L11	L12	L13	L14	L15	L16	L17	L18	L19	L20		
CHOTHIA REGIONS											LFR1											
											↑											
I	T	C	R	A	S	G	N	I	Y	N	Y	L	A	W	Y	Q	Q	K	Q	G	K	S
L21	L22	L23	L24	L25	L26	L27	L28	L29	L30	L31	L32	L33	L34	L35	L36	L37	L38	L39	L40	L41	L42	L43
											LFR2											
											↑											
P	H	L	L	V	Y	D	A	K	T	L	A	D	G	V	P	S	R	F	S	G	S	G
L44	L45	L46	L47	L48	L49	L50	L51	L52	L53	L54	L55	L56	L57	L58	L59	L60	L61	L62	L63	L64	L65	L66
											LFR3											
											↑											
S	G	T	Q	Y	S	L	K	I	S	S	L	Q	T	E	D	S	G	N	Y	Y	C	Q
L67	L68	L69	L70	L71	L72	L73	L74	L75	L76	L77	L78	L79	L80	L81	L82	L83	L84	L85	L86	L87	L88	L89
											LFR3											
											↑											
H	F	W	S	L	P	F	T	F	G	S	G	T	K	L	E	I	K	R				
L90	L91	L92	L93	L94	L95	L96	L97	L98	L99	L100	L101	L102	L103	L104	L105	L106	L107	L108				
											LFR4											
											↑											

↑ Unusual residue (<1% of sequences)

**Figure 11: Sequence of TA99 heavy and light chains.** TA99 is an anti-Tyrp1 antibody isolated from mice immunised with the melanoma cell line SK-MEL-23. This figure shows the sequence of the clone as published in the patent US 7951370B2. The heavy and light chains are indicated at the top and bottom of the figure, and both were annotated for CDRs and FRs (Framework Regions) at: [http://www.bioinf.org.uk/abysis/sequence\\_input/blast/blast\\_form.html](http://www.bioinf.org.uk/abysis/sequence_input/blast/blast_form.html)

#### 3.3.1.2 Generation of TA99 Constructs

In order to test the specificity of the TA99 scFv, we cloned it and validated its efficacy and specificity with flow-cytometry and confocal microscopy. The TA99 scFv was fused to a secreted version of rabbit IgG Fc domain. The IgG domain is secreted due to the deletion of the transmembrane domain. Cells were transfected with the soluble TA99-Rabbit IgG DNA construct, and the protein was harvested from the cell supernatant. The TA99-Rabbit IgG protein supernatant was used to label cells for Tyrp1, in order to test the efficiency of the scFv we produced. As shown in Figure 12, this construct includes the scFv of TA99 and truncated rabbit IgG.

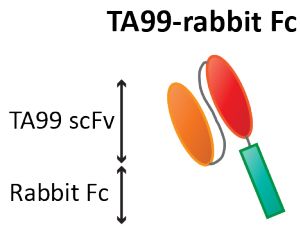


**Figure 12: Secreted TA99-rabbit Fc.** For testing the specificity of TA99, we cloned the TA99 scFv fused to a secreted Rabbit IgG truncation variant. Consequently, cells transfected with the construct will secrete the antibody into the culture supernatant.

### 3.3.1.3 Generation of Tyrp1 Constructs

In order to investigate the specificity of the TA99 scFv, as well as the trafficking of Tyrp1, we cloned the wild type Tyrp1, along with several alterations of the protein. Tyrp1 is a 537aa transmembrane protein with a luminal domain (1-477aa), a transmembrane domain (478-501), and a cytoplasmic domain (502-537) (Vijayasradhi et al., 1995). A di-leucine signal (NQPLLTD) residing on the cytoplasmic domain causes internalization of the protein. Mutations of the signal led to expression of Tyrp1 on the cell surface (Vijayasradhi et al., 1995).

Our aim was to answer whether Tyrp1 is present on the cell surface, and use Tyrp1-expressing cells as targets for cytotoxicity experiments. Hence, it was necessary to produce a positive control for flow cytometry and cytotoxicity assays. Additionally, we aimed to use fluorescent Tyrp1 positive cells to investigate its trafficking. In order to achieve that, Tyrp1 was fused to enhanced Green Fluorescent Protein (eGFP) for live-cell imaging of melanoma cell lines transduced with the Tyrp1-eGFP chimera.

We made four distinct Tyrp1 constructs (Figure 13). Initially we obtained the wild type Tyrp1 from the EST clone 6258285, which we subsequently cloned into an SFG vector with the CD34 marker gene. As illustrated in Figure 13.A, Tyrp1 is comprised of the signal peptide, a luminal, a transmembrane, and a cytoplasmic domain. However, for the purpose of trafficking experiments, we fused Tyrp1 to the fluorescent protein eGFP.

Our goal was to obtain an eGFP chimera, which would not interfere with the inherent trafficking mechanisms of Tyrp1. We also aimed at obtaining a Tyrp1 construct constitutively present on the cell surface to facilitate as a positive control. The design of the positive control was based on the premise that ablation of the di-leucine signal

impairs the physiological trafficking of Tyrp1 to the melanosome. Instead, truncated Tyrp1 is retained on the cell surface (Figure 13.D). For this reason, we constructed a truncated version of Tyrp1, referred to as Trunc. Trunc construct is comprised of the signal peptide, luminal and transmembrane domain. Nevertheless, the cytoplasmic domain was truncated, and was replaced with a 5aa-long serine-glycine (SG) linker followed by eGFP.

Designing a Tyrp1-eGFP chimeric protein that would not be interfering with the trafficking of Tyrp1 was challenging. It is not known whether the signal function is dependent on its proximity to the C-terminus, or whether its distance from the membrane is more critical. For this reason we designed two different variants of Tyrp1-eGFP with the cytoplasmic domain proximal (Figure 13.B) or distal to the cell surface (Figure 13.C). The Proximal is shown in Figure 13.B, with the wild type Tyrp1 protein fused to a SG linker and eGFP. On the other hand, for the Distal construct (Figure 13.C) the SG linker- eGFP has been inserted in-between the transmembrane and cytoplasmic domains. All constructs contain CD34 as a marker gene, separated from Tyrp1 with an IRES sequence.

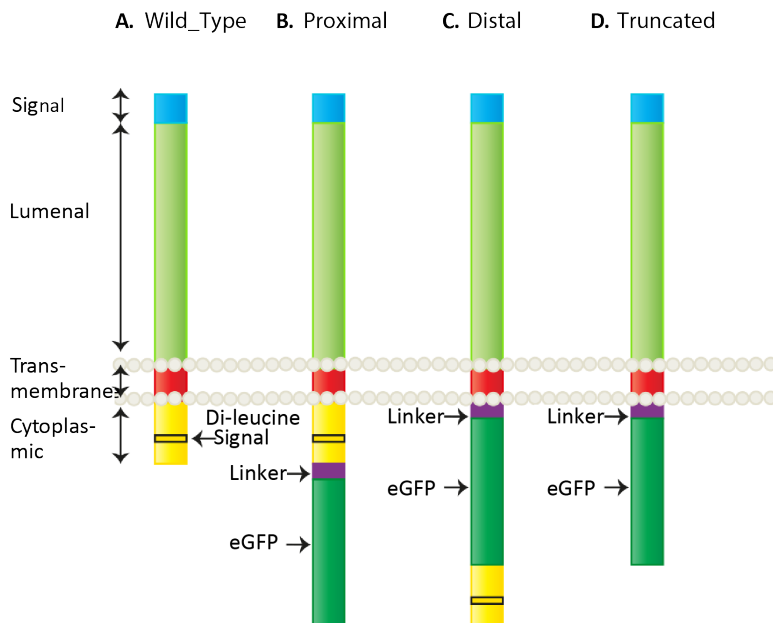


**Figure 13: Tyrp1 Constructs.** Tyrp1 is a 537aa long, type I transmembrane protein. The di-leucine motif, which retains the protein in the intracellular compartment, is indicated as a black rectangle on the cytoplasmic domain. (A) Tyrp1 WT: Wild type Tyrp1 consists of a peptide signal, a luminal, a transmembrane, and a cytoplasmic domain. The cytoplasmic domain contains the di-leucine retention signal. (B) Proximal: This construct contains the wild type Tyrp1 simply fused to the SG linker-eGFP. (C) Distal: This construct constitutes the cytoplasmic-distal Tyrp1, since SG linker-eGFP interposes between the transmembrane and cytoplasmic domains. (D) Trunc: This

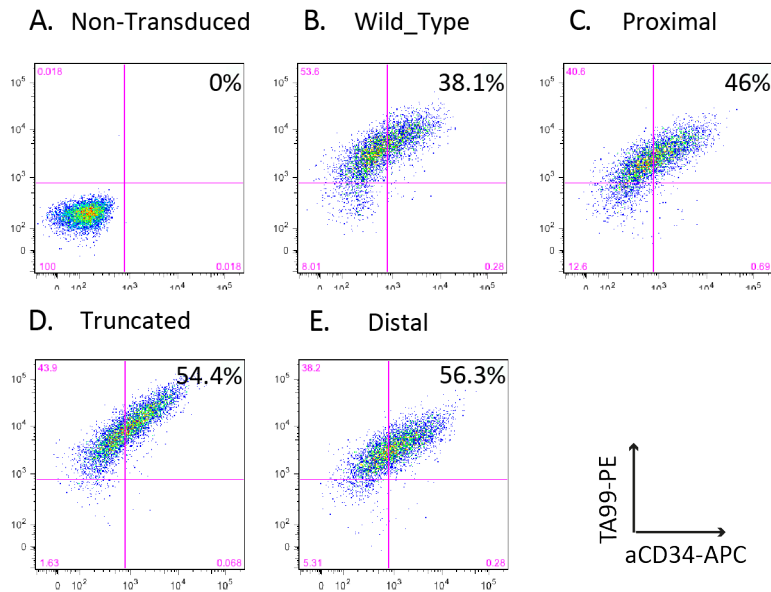
construct was designed as the positive control for surface expression, since the cytoplasmic domain containing the retention signal has been excluded.

### **3.3.2 TA99 Recognises Tyrp1 on the Cell Surface**

#### **3.3.2.1 Identification of Surface Tyrp1 with Flow Cytometry**

Once we obtained the required constructs, we tested the specificity of TA99 scFv with flow cytometry. We transfected 293T cells (DuBridge et al., 1987) to produce the secreted TA99-Rabbit IgG protein. This protein was used to stain the SupT1 cell line that we transduced with different Tyrp1 constructs. SupT1 cells were derived from a patient with T-cell lymphoblastic leukaemia, and do not inherently express Tyrp1 (Levy et al., 1971). These cells are commonly used in our group as targets in functional experiments, because they can be transduced very efficiently, and are an easy-to-maintain suspension cell line. The SupT1 cells used in this experiment had been transduced with a retroviral vector bearing the transgene for either of the four Tyrp1 constructs.

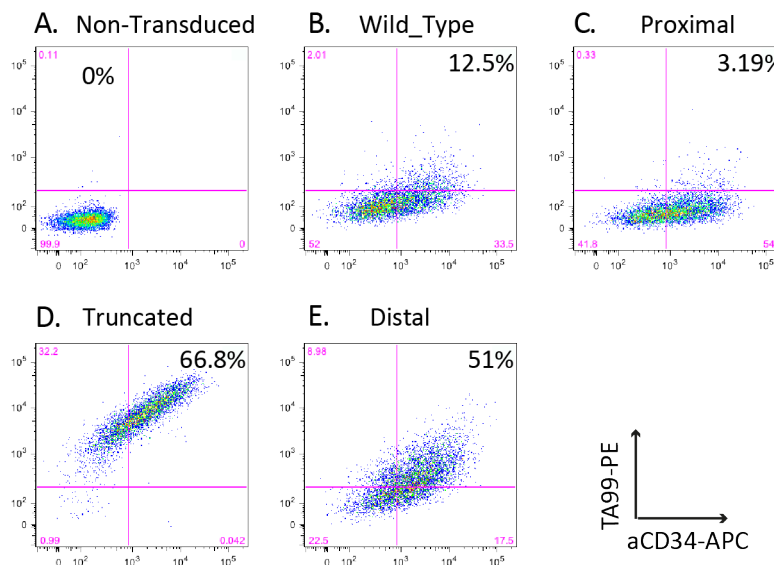
TA99-Rabbit IgG protein supernatant was harvested from the transfected 293T cells. The SupT1 target cells were then labelled with TA99-Rabbit IgG, and subsequently with an anti-Rabbit IgG PE. We also labelled with anti-CD34 APC as a control of the transduction efficiency. Cells were labelled for intracellular, as well as extracellular Tyrp1. Transduced cells were expected to express CD34 and intracellular Tyrp1. We labelled the cells for intracellular Tyrp1 in order to determine the specificity of TA99. The presence of extracellular Tyrp1 was unknown. The results for the intracellular Tyrp1 labelling are shown in Figure 14. SupT1 Non-Transduced (NT) cells constitute the negative control, and indeed no background could be detected for either CD34 or intracellular Tyrp1 (Figure 14.A). In each of the 4 Tyrp1-transduced cell lines, there was a double positive population for Tyrp1 and CD34 (Figure 14.B-E). Therefore, we can conclude that TA99 is a specific antibody against Tyrp1.



**Figure 14: Testing TA99 binding on transduced SupT1 cells with intracellular labelling.** SupT1 targets cells were transduced with four different Tyrp1 constructs. For the labelling, we included SupT1 NT cells as a negative control. The samples were labelled with TA99-Rabbit IgG, secondary anti-Rabbit Fc PE, and anti-CD34 APC. TA99 labelling is displayed on the Y-axis and CD34 on the X-axis. **(A)** SupT1 NT cells are negative for both antigens, and showed no background signal. **(B)** Tyrp1-WT transduced SupT1 cells were double positive for both TA99 and CD34. This confirmed that TA99 was indeed specific for Tyrp1. **(C)** The Proximal transduced cells were also double positive. The fact that the Tyrp1 chimera was expressed and labelled indicates that the fusion of Tyrp1 to eGFP did not interfere with the folding or stability of the Tyrp1 protein. **(D)** The SupT1 bearing the truncated form of Tyrp1 (Trunc) fused with eGFP were also positive for eGFP and CD34. **(E)** Similarly to the previous Tyrp1 constructs, the one consisting of luminal and transmembrane domain linked to eGFP followed by the cytoplasmic domain (Distal) of Tyrp1 was double positive.

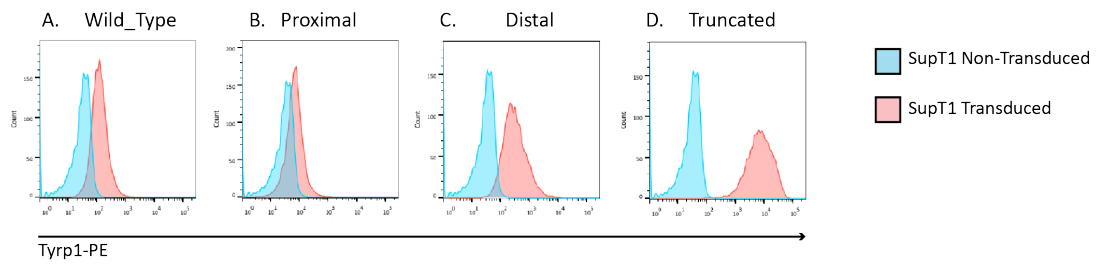
Next, we interrogated the transduced SupT1 cells for the surface expression pattern of Tyrp1 for the four different constructs. Figure 15 depicts the Tyrp1 extracellular labelling of the transduced SupT1 cells. CD34 levels were comparable between the different transduced cells, indicating that discrepancies observed are due to the Tyrp1 structure differences, and not disparity in the transduction levels. There was no detectable background in the negative control (Figure 15.A). On the contrary, Trunc was validated as a positive control, with its presence on the plasma membrane leading to a double positive population of eGFP and Tyrp1 (Figure 15.D). The WT Tyrp1 escapes on the cell surface as shown in Figure 15.B. Although the majority of transduced cells (CD34<sup>+</sup>) are surface-Tyrp1 negative, there is a subpopulation of double positive cells (12.5%). Proximal expressing cells appear to stringently sequester Tyrp1 intracellularly, with only 3.2% cells being double positive (Figure 15.C). Finally, 51% of double cells positive for surface Tyrp1 were detected on the Distal cells (Figure 15.E). Proximal and Distal were engineered to bear eGFP, and also

exhibit a trafficking pattern similar to the WT protein. Neither behaved exactly like the Tyrp1-WT, with Proximal being more stringent than the WT, and Distal having a 5-fold increase in the surface-Tyrp1 positive cells. In subsequent live-cell imaging experiments, Proximal was used as a more accurate trafficking representation to the WT. However, Distal was used in cytotoxicity assays as an intermediate Tyrp1 density variant. Interestingly, we acquired a surface Tyrp1 density range with Tyrp1-WT, Distal, and Trunc constituting low, medium, and high antigen density cell lines.



**Figure 15: Extracellular labelling of SupT1 cells with the TA99 scFv.** The TA99 Rabbit IgG PE is shown in the Y-axis, and X-axis represents the anti-CD34-APC stain. (A) SupT1 NT cells were negative for either antigen. (B) Approximately, 12.5% cells expressing Tyrp1-WT had a detectable cell surface signal. (C) SupT1 cells expressing Proximal exhibited a more stringent pattern of cells, with only 3.19% of cells being positive for surface Tyrp1. (D) The cells transduced with the Trunc had a double positive population, validating that the truncated protein constitutes the positive control. (E) Cells expressing Distal showed a high percentage of surface Tyrp1 positive cells (51%). However, the mean fluorescent intensity was lower than the Trunc double positive cells indicating lower Tyrp1 density per cell in the Distal versus the Trunc cells.

Distal showed a 5-fold increase in the expression of surface Tyrp1 compared to the Tyrp1-WT cells. However, its Mean Fluorescent Intensity (MFI) was lower than the MFI of Trunc cells. This is better shown in Figure 16, where the Tyrp1 labelling of the four transduced populations has been overlaid with the NT cells. The MFI disparity indicates difference in the density of Distal and Trunc expressing cells. The density range acquired with Tyrp1-WT, Distal, and Trunc as low, medium, and high density is also clear in Figure 16. The MFI increased from 1-order of magnitude in NT cells to 2 (A), 3 (C), and 4-orders of magnitude (D) for Tyrp1-WT, Distal, and Trunc respectively.



**Figure 16: Comparison of extracellular abundance of Tyrp1 variants in SupT1 cells.** Each histogram presents the extracellular labelling of each Tyrp1-transduced cell line against non-transduced cells. The overlay allows easier visualization of the difference in surface protein expression on the target cells. **(A)** There is a slight shift between NT and cells expressing the wild type Tyrp1. **(B)** Cells transduced with Proximal cells exhibited a slight shift in comparison to the NT cells, however this shift was not significant when compared with the wild type Tyrp1. **(C)** The Distal construct showed a different phenotype than the wild type one, with a 10-fold increase in protein expression on the surface. **(D)** The truncated form of Tyrp1 showed an increase of the expression by 3-orders of magnitude, acting according to our expectation as a positive control.

### 3.3.2.2 Detection of Tyrp1 in Mouse metastatic Melanoma

By labelling Tyrp1-expressing SupT1 cells, we showed that the TA99 binding to Tyrp1 is specific. To confirm the specificity of the TA99 scFv, we labelled tissue from a metastatic lung melanoma mouse model, and analysed it with confocal microscopy. The metastatic melanoma was induced with an intravenous injection of the B16-F10 melanoma cell line (Fidler, 1973). The 6 $\mu$ m section was labelled with TA99-Rabbit IgG, secondary anti-Rabbit Alexa Fluorophore 555, and DAPI. As a negative control, another slide was labelled with only the secondary antibody and DAPI, which is demonstrated in the first row of Figure 17. The negative control labelling is shown in the first row. The dark area constitutes the melanoma lesion, and appears dark due to melanoma pigmentation. The secondary anti-rabbit antibody did not produce background signal. The bottom row of Figure 17 shows the labelling including TA99. In this slide there is also highly pigmented area, which is dim for DAPI. However, in contrast with the negative control, the DAPI-dim area was bright for Tyrp1. Hence, the melanoma cells present in the lung expressed high levels of Tyrp1. The specificity of TA99 was also confirmed.

## B16 Lung Melanoma

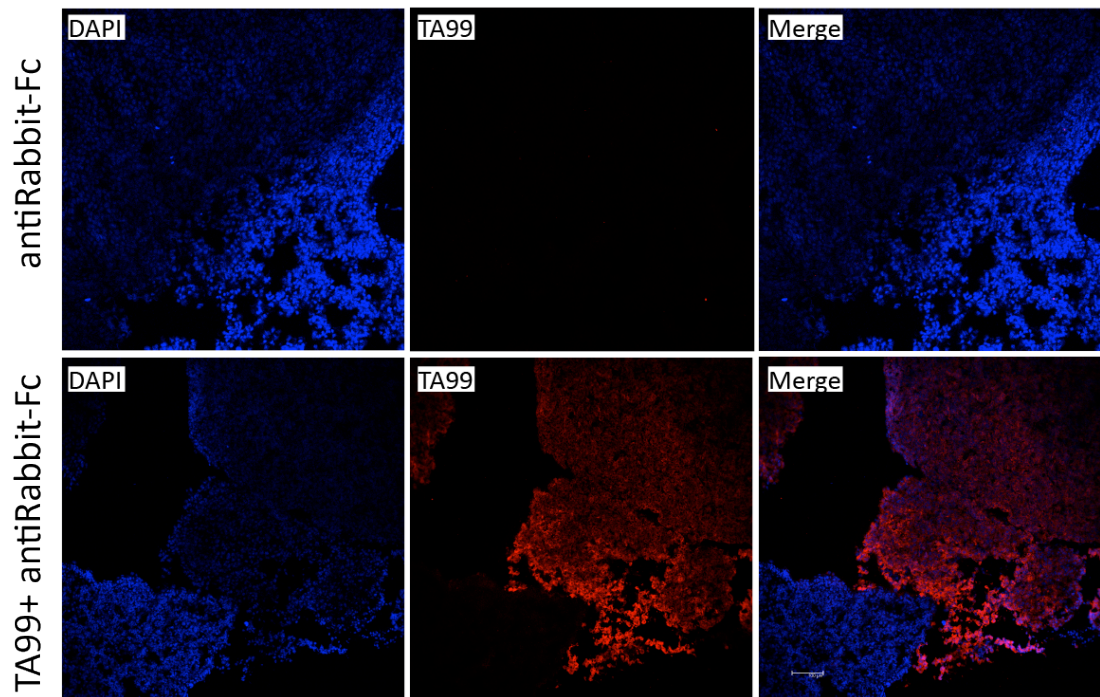


**Figure 17: Confocal imaging of Tyrp1 in mouse metastatic melanoma cryosections.** The channels shown are DAPI, Tyrp1-Aelxa Fluorophore 555, and the two channels have been merged. The top row shows the slide labelled with only DAPI and the secondary antibody. For the purpose of clarifying whether TA99 is specific or not both images included the border of metastatic melanoma tissue and lung tissue. The negative control was negative for Tyrp1, confirming that the secondary antibody does not lead to unspecific labelling. The bottom row shows the slide that was labelled with TA99. The metastatic tissue, which appears dark due to high pigmentation, was bright for Tyrp1 expression. The TA99 antibody is specific and labelled only the melanoma tissue, without causing any background noise. The confocal microscopy was carried out in a Leica SPE2.

### 3.3.2.3 Live-Cell Imaging of Tyrp1-mMEos

As shown in 3.3.1.3, the eGFP-fused Tyrp1 construct showed a more stringent surface expression profile than the WT protein, with a decrease in expression from 12.5% to 3.19%. The alternative eGFP-Tyrp1 fusion protein was Distal, which showed a 5-fold increase in surface Tyrp1 expression compared to Tyrp1-WT. Hence, Proximal was the chosen construct to be used in live-cell imaging experiments. However, preliminary results showed eGFP oligomerisation in the secretory pathway. Others have also reported eGFP oligomerisation (Jain et al., 2001). Oligomerisation led to eGFP saturated areas within the cells, masking individual eGFP positive vesicles. Accurate determination of individual vesicles is crucial for the Imaris software to determine a trafficking pathway.

In order to circumvent this hurdle, we substituted eGFP with the photoconvertible fluorescent protein mEos. mEos is a fluorescent protein, which photoconverts from

green-to-red fluorescence after violet irradiation. The photoconversion properties constitute the main mEos advantage, where violet irradiation is applied to a fraction of the cell. Consequently, only a small proportion of Tyrp1-bearing vesicle will photoconvert to red. The small number of red vesicles renders their identification and trafficking mapping clearer. Both eGFP and mEos have a  $\beta$ -barrel structure, with the tripeptide sequence that constitutes the fluorophore buried in the core of the  $\beta$ -barrel (Ormö et al., 1996)(Yang et al., 1996)(Zhang et al., 2012). We hypothesised that eGFP substitution with mEos would not alter the characteristics of the Proximal chimeric protein. We thus carried out the live-cell imaging of Tyrp1 fused to the fluorescent protein, mEos. The data were acquired with an IX71 Olympus inverted microscope, and were consequently analysed in the Imaris analysis software. In order to visualise vesicles containing fluorescent Tyrp1, we used the Spot feature of Imaris. We transduced the human melanoma cell line T618A with the mEos Proximal protein. The cells analysed were labelled with CellMask Deep-Red that is a commonly-used, cell-surface dye for live-cell imaging. A green-fluorescent cell was identified. In order to convert only a limited number of mEos molecules from green to red, a square of the cell was illuminated with the violet laser (405nm). This square is shown as red in Figure 18. Each vesicle is illustrated as a sphere (Figure 18), and the tracks for each identified sphere were calculated.

The sphere analysis was carried out in both the green and red channel. The vesicles identified as mEos-green are shown in Figure 18.A-D, and mEos-red in Figure 18.E-H, shown between different time-points. The panels in Figure 18.A,E show the area that was photoconverted with a square, as well the total amount of spheres identified. The panels B-D and F-H are zoomed in the photoconverted area and follow the spheres over time. The threshold of accuracy for the Imaris software is a distance no longer than half the sphere's diameter between consequent time-points. A distance longer than that, or the lack of data for intermediate time-points introduces error in the trafficking mapping. The majority of vesicles are lacking data for several time-points, probably due the vesicle moving across z-planes. The error is increased in the green channel due to the high amount of neighbouring spheres identified. Instead,

we chose to analyse the vesicles of the red-fluorescent Tyrp1-mEos. They were sparse, and thus it was easier to follow each individual vesicle path.

Our aim was to investigate whether the Tyrp1-bearing vesicles traffic via the plasma membrane. In order to address this question, we calculated the mean intensity of the red-fluorescence in correlation to the fluorescence of the cell surface dye. In total, we acquired images for 17 time-points. We arbitrarily set the vesicle analysis criterion for each vesicle to be visible in at least 12 time-points. There were four vesicle tracks that met the criterion, and the values of the mean intensity are shown in Table 18. The vesicles with fluorescence overlapping the cell surface bear the value of 0, but the further the vesicle is from the membrane the value increases. The tracks of the vesicles travelling towards or away from the plasma membrane are illustrated in Figure 19. Only the TrackID\_4 vesicle appeared to come in proximity to the cell surface. No trend was detected by analysing the tracks of the Tyrp1 vesicles, and the pattern of trafficking is inconclusive due to the limited number of vesicles analysed.

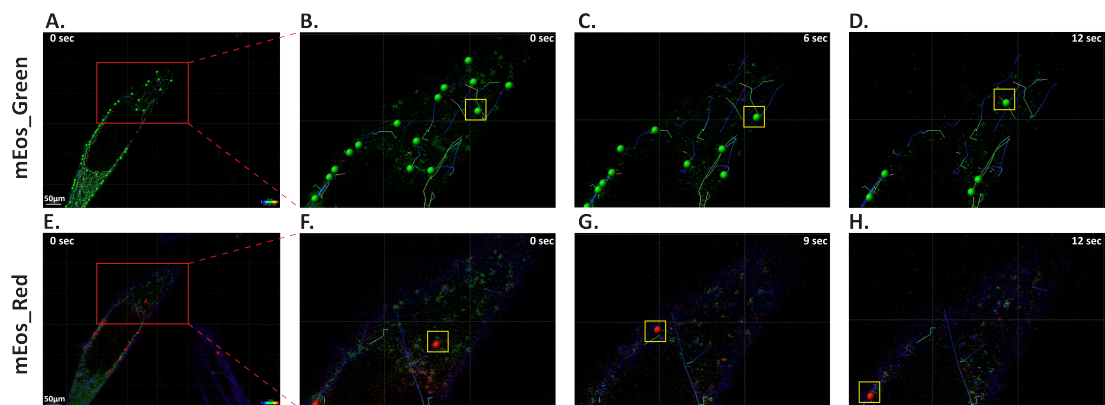


**Figure 18: Live-cell imaging of T618A cells transduced with Proximal fused to mEos.** T618A cells were transduced with Proximal, fused with the red-to-green photoconvertible protein, mEos. The cell membrane was labelled with the fluorescent dye, CellMask Deep Red. An area of the cells was irradiated with the violet laser, in order to photoconvert a fraction of mEos as shown in (A) and (E) with a red rectangle. The top and bottom row show the mEos-green and mEos-red fusion protein respectively. In the panels (B-D) the mEos-green detected vesicles are captured in different time-points. As a reference, one vesicle is highlighted with a yellow rectangle drawn around it. Similarly, a red-Eos vesicle is captured and highlighted over time in panels (F-H). The data were analysed in the Imaris software, where individual vesicle were identified and tracked over the 17 time-points.

**Table 18: Mean intensity values of vesicles in correlation to membrane proximity over time.**

Time Point	TrackID_1	TrackID_2	TrackID_3	TrackID_4
1	1535.31	1141.03		
2	1329.94	1705.65	2114.25	1306.23
3	1377.18	1452.88	1239.09	
4	1592.24	1330.76	1756.85	1487.31
5	1592.59	1015.54	2631.46	239.98
6	1895.51	1531.53	2588.97	940.18
7	1764.70	1405.40	1973.41	
8	1891	1750.97	2312.15	1509.23
9	2258.84	1493.58		1492.94
10		1446.07	1225.28	1762.78
11	2220.41		1518.14	553.04
12	2147.5	3083.82		2087.53
13	2209.99	2180.37	1215.76	
14		2917.7	749.13	1861.530029
15	1856.76	3453.24	1891.09	1692.670044
16		2454.26	1914.56	1821.619995
17	1795.95	2881.51	1191.08	

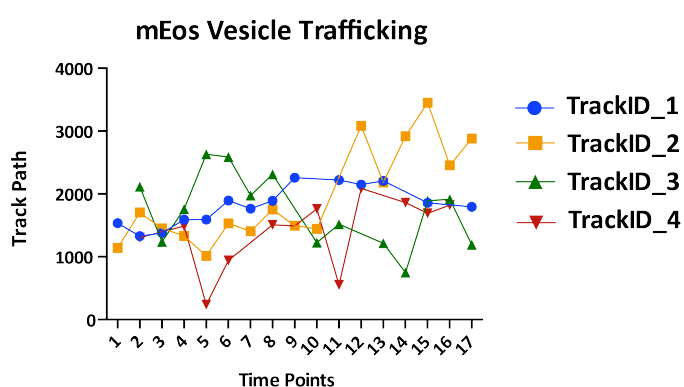


**Figure 19: Illustration of Tyrp1 vesicle trafficking in accordance to membrane proximity.** The four vesicles shown bore data for at least 12 time-points each. Their distance from the membrane was calculated according to the fluorescence of the cell surface dye. The proximity to the membrane is indicated with the value of zero. In contrast the higher the value the higher the distance from the membrane. Only vesicle with ID\_4 shows trafficking towards and away from the membrane.

### 3.3.2.4 Determination of Tyrp1 Expression Profile on Melanoma Cell Lines

Once the TA99 antibody was validated, our aim was to investigate whether Tyrp1 can be detected on the surface of melanoma cells. We labelled a series of human

melanoma cell lines for intracellular expression of Tyrp1, and concomitantly interrogated them for surface Tyrp1. We included the SupT1 NT and Tyrp1-WT cells as negative and positive control, respectively. The human melanoma cell lines we screened were: T618A, Mel260, Mel275, Mel280, and Mel290 (Ludwig Institute for Cancer Research, Lausanne, Switzerland).

In Figure 20, the rows i-ii display the intracellular labelling, and the rows iii-iv the extracellular labelling. In either intracellular or extracellular labelling, there is an isotype Rabbit IgG negative control (i, iii) and the labelling with TA99-Rabbit IgG (ii, iv). The columns A-G represent the different cell lines, starting with SupT1 NT, followed by SupT1 Tyrp1-WT, T618A, Mel260, Mel275, Mel280, and Mel290. The Y-axis represents the TA99 labelling and the X-axis represents CD34. When labelled for intracellular Tyrp1, Tyrp1-WT SupT1 cells had a double positive population for Tyrp1 and the marker gene, CD34 (Figure 20.b-ii). Of the five melanoma cell lines that were labelled, Mel260 and Mel275 were negative for intracellular Tyrp1 (Figure 20.D, E-ii). T618A, Mel280, and Mel290 had high levels of intracellular Tyrp1, with percentages of 97% (Figure 20.C-ii), 45% (Figure 20.F-ii), and 76% (Figure 20.G-ii) respectively.

Once we established which cell lines expressed Tyrp1, the critical question was whether they also had Tyrp1 present on the cell surface. The SupT1 Tyrp1-WT cells were CD34 positive, but only 0.21% was double positive, in contrast to the isotype control that was 0% (Figure 20.B-iii, iv). T618A was positive for surface Tyrp1 with a percentage of 2.33% (Figure 20.C-iv), in contrast to the isotype control that was 0.053% (Figure 20.C-iii). The percentage of surface Tyrp1 for the other two populations was similar with Mel280 exhibiting 0.97% (Figure 20.F-iv), and Mel290 0.16% (Figure 20.G-iv).

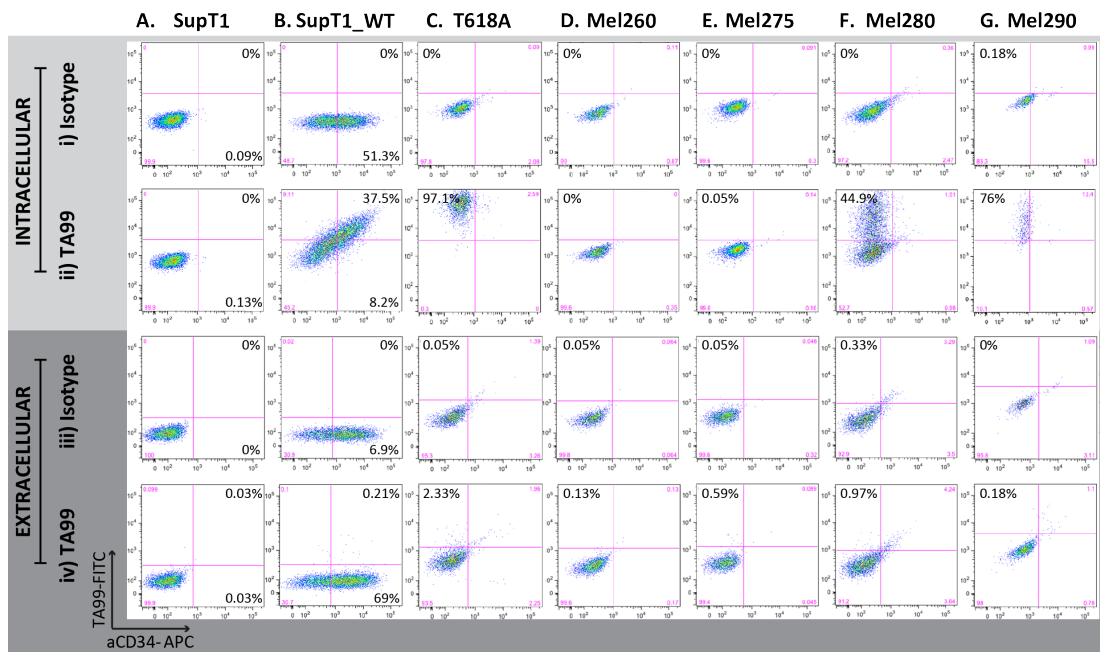


**Figure 20: Labelling human melanoma cell lines for surface Tyrp1.** These cell lines were labelled intracellularly, in order to determine whether they express Tyrp1. The intracellular labelling is shown in rows (i-ii). Row (i) represents the negative control, since these cells were labelled with an isotype control for rabbit IgG. Row (ii) shows the labelling with TA99-rabbit IgG. Rows (iii-iv) demonstrate the extracellular labelling of the cell lines labelled either with the isotype control (iii) or TA99 (iv). The TA99-FITC labelling is shown on the Y-axis, and CD34 labelling is shown on the X-axis. Each column represents a separate cell line. Column A shows SupT1 NT cells that were negative for both intracellular (A-ii) and extracellular (A-iv) Tyrp1, as expected. SupT1 Tyrp1-WT cells were highly positive for intracellular Tyrp1 (B-ii), with a double positive of 37%. When labelled for surface Tyrp1 there was a small population 0.21% that was double positive for Tyrp1 and the marker gene (B-iv). Column C illustrates the cell line T618A, which expressed Tyrp1 in high percentage of cells (97%) (C-ii), and was positive for surface Tyrp1 (2.33%) (C-iv). Mel260 and Mel275 (D, E-ii) were both negative for Tyrp1. Mel280 was 45% positive for intracellular Tyrp1 (F-ii), and the presence of Tyrp1 on the surface was 0.96% (F-iv) from 0.33% for the negative control (F-iii). Finally, column (G) displays the results for the cell line Mel290, which showed a high percentage of intracellular Tyrp1 (76%) (G-ii), however Tyrp1 did not appear to be present on the surface (G-iv).

To visualise the increase in fluorescence due to the surface Tyrp1, we also present the results as overlaying histograms (Figure 21). Each histogram represents a cell line, which contains the isotype-control and the TA99-labelled population. As expected there was no fluorescence increase for the cell lines SupT1 NT (Figure 21.A), Mel260 (Figure 21.C), and Mel275 (Figure 21.D), which were negative for Tyrp1 expression. The cell lines that were positive for intracellular Tyrp1, all show a modest increase in fluorescence for Tyrp1 (Figure 21.B,E-G).

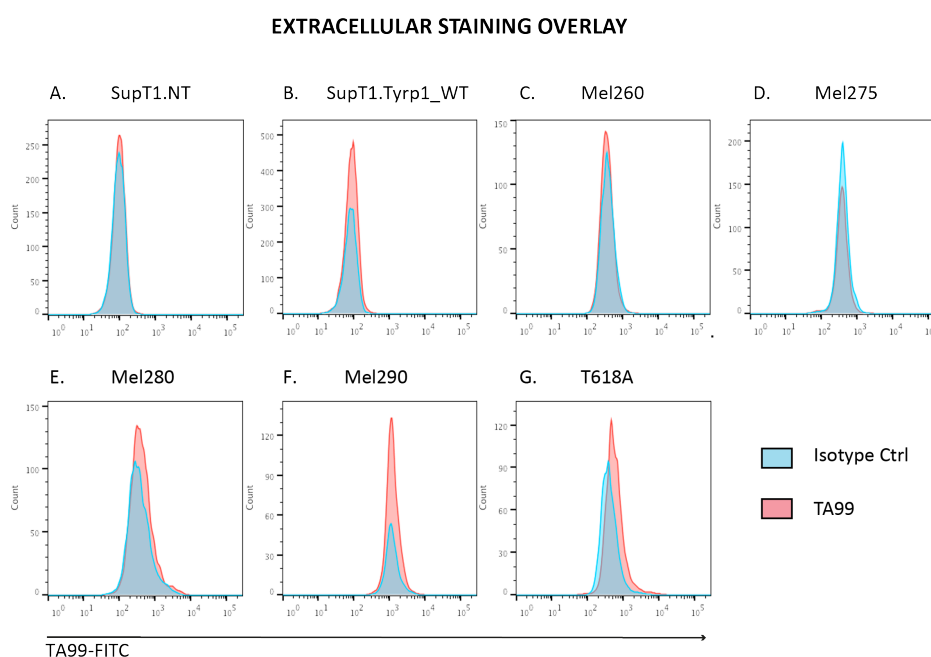


**Figure 21: Overlay for the extracellular labelling of melanoma cell lines.** The histogram overlay represents a direct visual comparison of each sample versus the isotype control. The isotype control is shown in blue and the TA99 labelling in red. The cell lines SupT1 NT (A), Mel260 (C), and Mel275 (D) did not exhibit a shift in the fluorescence, which is expected since they were negative for Tyrp1. The cell lines SupT1 Tyrp1-WT (B), Mel280 (E) and Mel290 (F) had a negligible increase in TA99-FITC fluorescence. However, T618A (G) cells showed a subtle increase in Tyrp1 expression.

### 3.3.2.5 Conclusion

The Tyrp1 constructs were expressed on SupT1 cells after retroviral transduction. After labelling the cells with soluble TA99 scFv, we demonstrated that all Tyrp1 constructs (WT, Proximal, Distal, and Truncated) produced Tyrp1 protein, as shown with intracellular labelling. However, the pattern of Tyrp1 presence on the cell surface of SupT1 varied between the Tyrp1 constructs. Instead, we showed that the plasma membrane expression formed a range of low, low, medium, and high level for WT, Proximal, Distal, and Trunc, respectively.

The specificity of the TA99 scFv was validated through flow cytometry and confocal microscopy. The tissue labelled with TA99 was B16-F10 metastatic melanoma. The scFv delineated the dark areas of the tissue that constituted the metastatic lesion. The neighbouring healthy tissue bore no background labelling from TA99.

We chose Proximal as the protein with the closest trafficking pattern to the WT. We substituted eGFP to the photo-convertible fluorescent protein mEos, and carried out live cell imaging. The vesicles carrying Tyrp1 were recognised as spheres by the Imaris software. The tracks of the vesicles were monitored over time. However, there were

time points where data were missing for individual spheres (vesicles). The lack of time point data renders our result inconclusive.

Finally, we interrogated human melanoma cell lines for the expression of Tyrp1 intracellularly and on the plasma membrane. The cell lines we tested were Mel260, Mel275, Mel280, Mel290, and T618A. Of those, only Mel280, Mel290, and T618A expressed Tyrp1. Despite the low percentage of detectable surface Tyrp1 on intracellular-positive cell lines, the detectable signal insinuates that the protein is present at very-low antigen density. This can either be due to normal trafficking through the membrane, or melanosomes fusing with the plasma membrane, or alternatively, by saturation of the trafficking machinery which leads to misdirected delivery of the vesicle to the cell surface. The low Tyrp1 density might reflect a physiologically low percentage of Tyrp1 being present on the surface. It can also reflect limitation in the sensitivity of the flow cytometry. For this reason, the labelling protocol was optimised to reduce the lower detection threshold as discussed in 3.3.3.1.

### **3.3.3 Labelling Optimisation for Flow Cytometry**

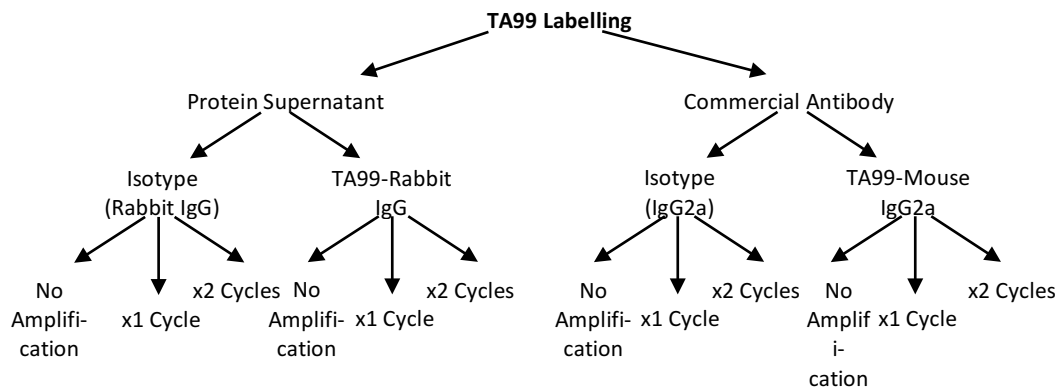
#### **3.3.3.1 Tyrp1 Signal Enhancement**

The results obtained so far suggest that Tyrp1 is present on the surface of melanoma cells, which is consistent with the published literature. Nevertheless, the fluorescent signal is low, and thus the results are inconclusive. It has been previously reported that 2% of Tyrp1 is present on the plasma membrane (Yiqing Xu et al., 1997). It is possible that the level of Tyrp1 present on the surface of melanoma cell lines is below the flow cytometry detection limit. In order to address whether the density of Tyrp1 is negligible, or simply undetectable by flow cytometry, we sought to optimise our staining protocol by enhancing the Tyrp1 signal.

The kit used was the Miltenyi FASER kit PE, which is designed to enhance PE signal. The anti-PE antibody constitutes the activation step, and Streptavidin PE constitutes the enhancement step. Every enhancement cycle consists of two steps, the activation and the enhancement.

The antibody we had been using was protein supernatant harvested from transfected 293T. The supernatant was not titred leading to variability between batches. In order to introduce consistency among experiments, we obtained a commercially available unlabelled TA99- IgG2a by GeneTex, and compared the two antibodies. Hence, an additional condition constituted the labelling with a commercial TA99 antibody. TA99 was isolated from immunized mice, and the isotype is mouse IgG2a.

For the purpose of this labelling we used SupT1 NT, or SupT1 expressing Proximal and Trunc. The SupT1 NT constituted the negative control, and the Trunc cells were the positive. We also labelled the SupT1 cells expressing the WT or Proximal Tyrp1. The labelling protocols were: 1) isotype control, 2) isotype control plus 1x cycle of enhancement, 3) isotype control plus 2x cycles of enhancement, 4) TA99, 5) TA99 plus 1x cycle of enhancement, 6) TA99 plus 2x cycles of enhancement. The cells were labelled with either TA99-Rabbit IgG or an anti-Rabbit isotype. However, the cells were also labelled with the commercial TA99-Mouse IgG2a. Hence, each cell line was labelled for surface Tyrp1 with twelve different methods in total, as shown in the diagram below.



The results on this labelling optimization experiment are demonstrated in Figure 22. Each column represents a cell line. The first row (A-D) represents the labelling with the TA99-Rabbit IgG, whereas the samples in the second row (E-H) were labelled with the commercial TA99-Mouse. One amplification cycle of TA99-Rabbit IgG did not increase the background of SupT1 NT, but the two rounds of amplification did (Figure 22.A). In contrast to that, signal amplification of TA99-Mouse IgG2a labelling did not increase the background (Figure 22.E). SupT1 Tyrp1-WT cells had detectable levels of

surface Tyrp1 only after two cycles of amplification (Figure 22.B,F). Proximal expressing cells showed a similar pattern. In this case the TA99-Rabbit IgG appeared to be superior to TA99-Mouse IgG2a (Figure 22.C,G). The effect of the signal amplification was more prominent in the labelling of SupT1 Trunc. These cells exhibit cell surface signal of Tyrp1 without amplification. However, signal enhancement incrementally increases the fluorescence intensity of Tyrp1 signal by approximately 10-fold (Figure 22.D,H).

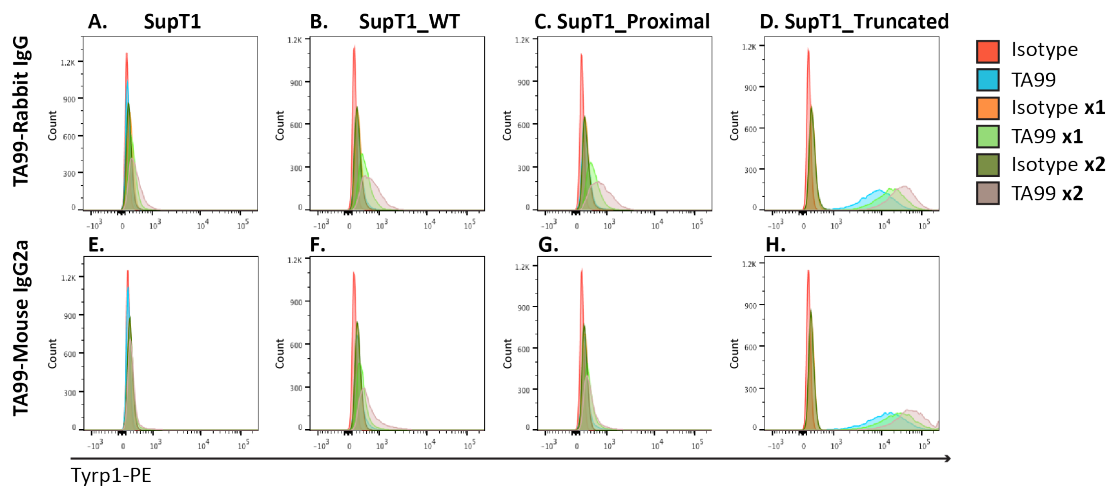


**Figure 22: Histogram overlay of cells labelled with TA99-Rabbit and TA99-Mouse IgG2a amplified for Tyrp1 signal.** Columns demonstrate individual cell lines. The two rows represent the different labelling strategies with either TA99-Rabbit IgG or TA99-Mouse IgG2a. SupT1 NT cells (A, E) were the negative control, and exhibited no positive signal, apart from a slight background increase of TA99-Rabbit IgG, when amplified twice. The SupT1 Tyrp1-WT (B) and Proximal (C) did not appear positive for surface Tyrp1 without amplification. The lack of Tyrp1 signal with one round of enhancement is probably due to the low antigen density rather than inadequate enhancement. The Trunc positive-control cells (D-H) appeared positive without the amplification step. However, the amplification forms a gradient with one round of amplification superior to none, and two rounds of amplification superior to all other approaches.

Figure 23 shows the MFI of Tyrp1-PE fluorescence. The isotype controls using either TA99-Rabbit IgG (Blue) or TA99-Mouse IgG2a (Grey) had low values that were marginally increased by signal enhancement. There is an increase of signal for Tyrp1-WT with both the commercial and our scFv. However, the increase was more significant when the cells were labelled with the commercial one (Figure 23.B). The MFI value for the SupT1 Proximal labelled with the commercial antibody was not increased after enhancement (Figure 23.C). The lack of signal increase after one or two cycles of amplification indicates that the Tyrp1 density on Proximal is negligible, rather than below the detection threshold of flow cytometry. Consistent with previous results, the SupT1 Trunc cells had high MFI values (Figure 23.D). The signal was slightly increased with each cycle of enhancement, with the two rounds of

amplification being marginally superior. Additionally, the commercial antibody produced marginally higher MFI. As the consequent labelling strategy, we chose to carry on with the commercial TA99 antibody to eliminate batch variation of supernatant protein and ascertain consistent results. In the trade-off between signal enhancement and time efficiency, one cycle of signal amplification was applied for labelling the melanoma cell lines. However, for the detection of Tyrp1 on the surface of primary melanoma samples, we amplified the Tyrp1 signal twice.

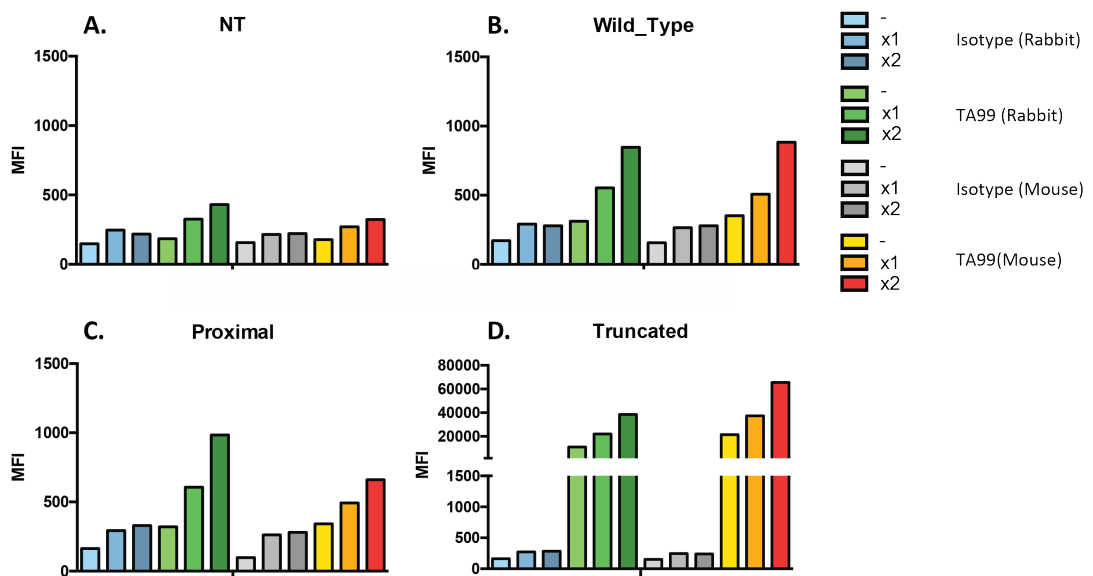


**Figure 23: Enhancement of Tyrp1 signal with the FASER-PE kit.** Our signal for surface Tyrp1 was very weak due to the low density of surface Tyrp1. Therefore, we used a signal amplification kit from Miltenyi, FASER kit PE, in order to enhance the low-density signal. We tested one or two cycles of enhancement. We also compared the TA99 antibody secreted from transfected 293T to a commercial TA99. The SupT1 Tyrp1-WT (B) was positive, but the presence of surface Tyrp1 became more pronounced after the signal enhancement. Also the commercial antibody labelling appeared superior, since it resulted in higher MFI values. For Proximal SupT1 there was no difference observed between commercial and “home-made” antibody (C). Enhancement increased the MFI of the Trunc cells, with a minor difference between each enhancement step (D). This experiment was only carried out once.

### 3.3.3.2 Protocol for Tyrp1 Density Quantification

Tyrp1 is a challenging target for CAR-T cells due to the low density present on the target cell surface. The density of Tyrp1 on melanoma cells is currently undetermined. We have developed a strategy for the detection of low Tyrp1 signal, but it is also crucial to develop a strategy for quantifying the antigen density.

For this purpose, we used two distinct kits, the DAKO QIFIKIT kit, as well as the QuantiBrite-PE kit. As discussed in 3.1.4, the QIFIKIT beads can be signal amplified concomitantly with the melanoma cells. Hence, we aim to validate the signal

amplification compatibility of the QIFIKIT beads. The QIFIKIT kit consists of set-up beads, which include two distinct populations of beads, one negative and one that is coated with a high density of antigen (Figure 24.A). The calibration beads consist of five populations of beads with pre-determined antigen molecules per population, which are used for the standard curve calculation (Figure 24.C).

The QIFIKIT beads were labelled with the same secondary antibody we used to stain the cell lines, and were enhanced twice concomitantly with the target cell lines. Figure 24 demonstrates the set-up and calibration beads before and after signal enhancement. The populations of the calibration beads increased in PE MFI after the signal amplification, but the pattern did not change (Figure 24.D). We gated the separate populations in the histogram with the amplified calibration beads, and extracted the MFI for each of them. The kit includes the lot specific Antibody Binding Capacity (ABC) units. The MFI and ABC of the five populations were converted to logarithmic scale, and these were used for a scatter plot. From the scatter plot (Figure 25) we extrapolated the linear regression  $y=0.9485*x+0.588$ .

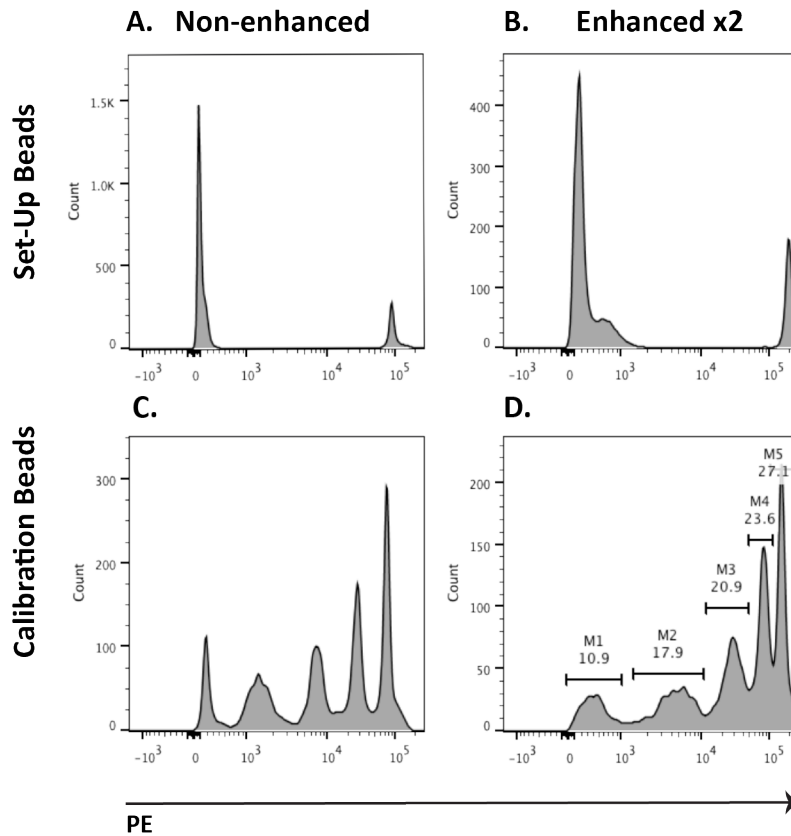


**Figure 24: Bead populations before and after signal amplification.** Top row shows the set-up DAKO QIFIKIT beads before signal amplification (A), and after two cycles of FRASER kit amplification (B). Bottom row shows five populations of DAKO KIFIKIT calibration beads before signal amplification (C), and after two cycles of FRASER kit amplification (D). The calibration beads after signal amplification display increased MFI, while their pattern remains preserved. Gates shown in panel (D) were used to construct the standard curve based on their log values.

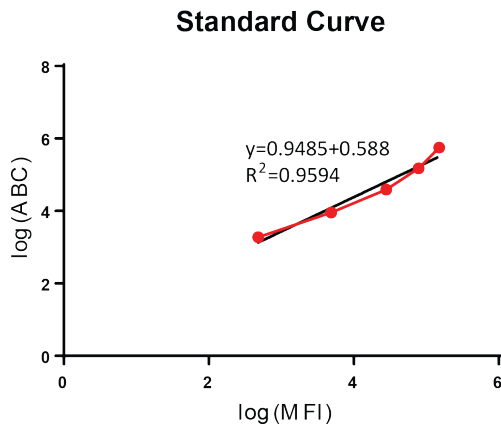


**Figure 25: Standard curve of DAKO QIFIKIT beads following two rounds of FRASER kit signal enhancement.** We calculated the MFI of the five populations contained in the calibration beads vial. The ABC (Antibody Binding Capacity) of the beads was provided with the kit. Using these two we constructed a scatter plot and calculated the linear regression. The R-squared was 0.959.

### 3.3.3.3 Conclusion

Although, SupT1 cells expressing the Tyrp1-WT were positive for the presence of Tyrp1 on the cell surface, no surface Tyrp1 was detected on human melanoma cell

lines. In order to address whether the lack of surface Tyrp1 was due to its absence from the plasma membrane or its level is below the detection limit, we enhanced the signal of Tyrp1 with the signal amplification kit FASER kit PE.

We compared one, two or three cycles of signal amplification. We also compared the TA99 scFv produced in our lab to a commercial TA99 antibody. Although there was no great difference observed between the commercial antibody and our scFv, we chose to use the commercial one for higher reproducibility in subsequent experiments. The three-cycle amplification was marginally superior to the two cycles, and similarly the two were superior to the one cycle. For high signal amplification, as well as cost-effectiveness and time efficiency, the two amplification cycles were used in following experiments.

Our aim was to quantify the density of Tyrp1 on the surface of melanoma cell lines and primary melanoma tissue. In order to perform the quantification, we validated the density quantification kit QIFIKIT. The advantage of this kit is the ability to label and signal enhance the fluorescence on the beads. This enabled us to signal amplify the melanoma cells concomitantly with the quantification beads.

### **3.3.4 Density of Surface Tyrp1**

#### **3.3.4.1 Tyrp1 Density on Melanoma Cell Lines**

After optimising the signal-enhancement and antigen-quantification strategies, we proceeded with determining the surface density of Tyrp1 on transduced SupT1 and human melanoma cell lines. The cell lines interrogated were SupT1 NT, Distal, and Trunc; together with the melanoma cell lines T618A, Mel280, and Mel290. We proceeded with these three melanoma cell lines, because we determined that they express Tyrp1. We have also detected low levels of surface Tyrp1, as shown in 3.3.2.4. The SupT1 Tyrp1-Promixal cells were not included in this experiment due to their similarity to the WT. The linear regression was used to calculate the ABC of the cell lines labelled. Figure 26 shows the cell lines labelled with either an IgG2a isotype control (i) or TA99-Mouse IgG2a (ii), and enhanced with the FASER kit. Tyrp1-PE is shown on the Y-axis, and the X-axis shows a blank channel. All cell lines apart from Mel280 showed no background for the isotype control. However, SupT1 Tyrp1-WT,

Distal, SupT1-Trunc, T618A, and Mel290 exhibited a remarkable increase in Tyrp1-PE fluorescence, when labelled with TA99. The background for both Tyrp1-WT and Distal cells was 0.16%, which increased to 23.5% and 59.8% respectively (Figure 26.B,C). Similarly, the percentage of positive amplified T618A was 92.0% (Figure 26.E-ii), and Mel290 91.2% (Figure 26.G-ii). The detection of Tyrp1 on the membrane of melanoma cells after signal enhancement confirms its presence on the surface. Hence, the lack of surface Tyrp1 detection on those cell lines previously tested in 3.3.2.4 was a result of flow cytometry detection limit.

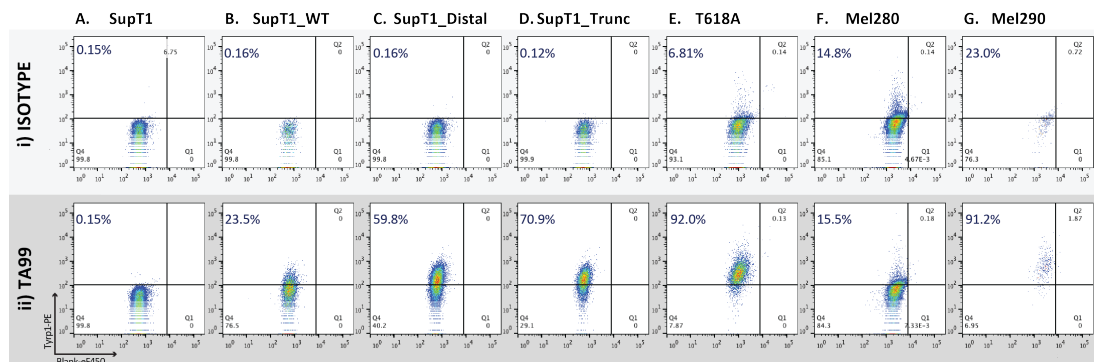


**Figure 26: SupT1 and melanoma cell lines enhanced twice with FASER-PE kit.** The cell lines included in this experiment were SupT1 NT (A), Tyrp1-WT (B), Distal (C), and Trunc (D), along with the melanoma cell lines T618A (E), Mel280 (F), and Mel290 (G). The Y-axis illustrates the Tyrp1-PE signal, and the X-axis is a blank channel. Top row (i) includes the labelling with the isotype, and row (ii) the TA99 stain. Tyrp1-WT and Distal cells showed a positive population of 23.5% (B-ii) and 59.8% (C-ii) for surface Tyrp1. The percentage of Trunc for surface Tyrp1 expression was 70.9% (D-ii). T618A displayed a population of 92.0% surface Tyrp1 positive cells (E-ii). Finally, Mel290 was also positive, with 91.2% (G-ii).

The Tyrp1 density on the melanoma cell lines was quantified with QuantiBrite-PE beads, QIFIKIT beads, or QIFIKIT beads enhanced once with the FASER-PE. Each sample was analysed in duplicates. The Tyrp1 signal amplification was concomitant for the melanoma cells and the QIFIKIT beads. Based on the linear regression of each condition, we calculated the number of surface antigens per cell.

$$\text{Log}(ABC) = a \times \text{log}(MFI) + b$$

The Log (MFI) was imported into the equation, which was solved for Log(ABC). Subsequently, we back transformed the log, and finally subtracted the isotype control ABC from the sample ABC. The final number showed the antigen density on each cell line. The number of Tyrp1 epitopes/cell are demonstrated in Table 19, and the graphical representation of the numbers is displayed in Figure 27. The calculated values are similar between the three protocols. The difference in density was

marginal between the different beads. The only statistically significant difference was observed for Mel290 cells, with QIFIKIT beads enhanced once being superior to non-amplified QIFIKIT, and QuantiBrite being superior to both. The relative consistency in the density prediction of the two kits indicates the robustness of the method. It is worth mentioning that the lowest point in the QIFIKIT standard curve is approximately 2000 epitopes/cell, whereas the lower threshold of the QuantiBrite beads was approximately 470 epitopes/cell. Hence, the majority of the data points in the QIFIKIT calculation and fewer points in the QuantiBrite calculation have been extrapolated, since they reside outside the standard curve.

**Table 19: Density of Surface Tyrp1 density on melanoma cell lines.**

Cell Line	Antigen Density(QIFIKIT)	Antigen Density (QIFIKITx1)	Antigen Density (QuantiBrite)
SupT1	-23.10	4.42	-15.02
SupT1_WT	211.21	303.80	150.86
SupT1_Distal	240.54	338.23	175.65
SupT1_Truncated	401.22	527.07	308.16
T618A	1172.53	1193.74	1131.89
Mel280	19.48	-8.17	18.13
Mel290	4017.95	4657.38	4984.30

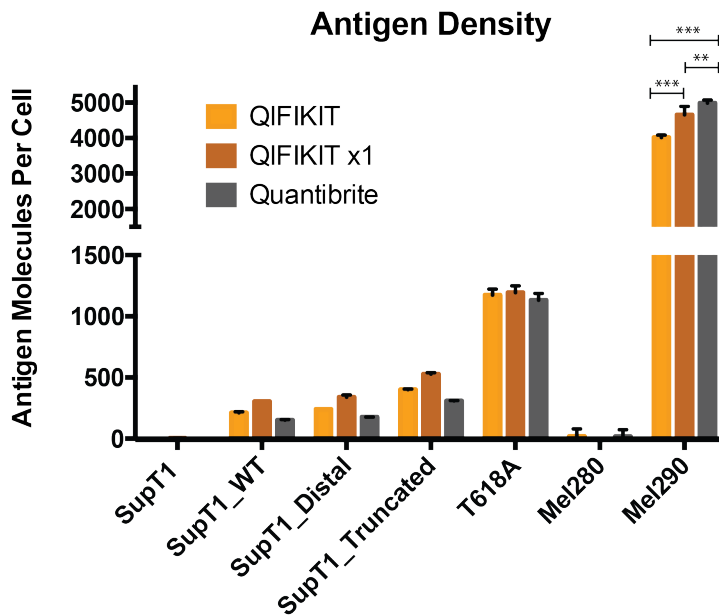


**Figure 27: Tyrp1 density on the cell surface of target cell lines.** This graph demonstrates the antigen density of transduced SupT1, as well as melanoma cell lines. It also shows the direct comparison between the QIFIKIT beads and QuantiBrite beads. An additional condition is the signal enhancement of the cells along with the QIFIKIT beads. The values as indicated in Table 19 are comparable. The difference is statistically significant for the quantification of Mel290. Although the reason for this discrepancy is unknown. The QuantiBrite lower detection threshold is approximately 500 epitopes/cell, in contrast to the 2000 epitopes/cell lower threshold of the QIFIKIT kit. However, the Mel290 density is within the standard curve limits for both the QIFIKIT and QuantiBrite kit.

### 3.3.4.2 Tyrp1 Density on Primary Melanoma

T-cell sensitivity is limited to a lower detection level of 240-770 epitope/cell (Stone et al., 2012)(Watanabe et al., 2015). Our aim is to exploit the presence of Tyrp1 on the surface, and design a chimeric antigen receptor based on the TA99 scFv. However, the density of Tyrp1 on the surface of melanoma malignancies is unknown. Our aim is to investigate whether the surface Tyrp1 expression on primary melanoma cells is heterogeneous and prevalent, as well as quantify the density of Tyrp1.

In order to examine the expression profile of Tyrp1 on melanoma cells we acquired primary melanoma samples, which we labelled and interrogated with flow cytometry. The labelling procedure described in 3.3.3.2, included the incorporation of the signal amplification kit, and the QIFIKIT beads for antigen density measurement. The primary melanoma cells were labelled for surface Tyrp1, and enhanced twice in parallel with the QIFIKIT beads. Based on the beads, we calculated the standard curve, and extrapolated the antigen density of the melanoma cell lines.

Since we are interested in interrogating only the melanoma cells, it is pivotal to discriminate them from the different cell types of the tumour microenvironment. We designed a panel that included aCD45-eFluor450, aMCAM (or CD146)-APC, TA99-IgG2a, anti-Mouse IgG2a PE and viability dye-eFluor780. CD45 is a leukocyte marker (Trowbridge et al., 1991), and was used to identify and exclude the CD45 positive leukocyte population. Melanoma Cell Adhesion Molecule (MCAM) is a glycoprotein expressed on the cell surface of melanoma cells with a prevalence of 70% in primary melanoma and 90% in metastatic melanoma (Pearl et al., 2008). The MCAM marker was used in combination with the CD45 to identify the melanoma cells in the tumour sample. The phenotype of the melanoma population was CD45<sup>-</sup>MCAM<sup>+</sup>.

The samples screened were derived from four melanoma patients. Samples Metastatic Melanoma (MM)18, MM24, and MM25 were derived from metastatic Lymph Node (LN) lesions. Patient MM25 underwent excision of right (R) and left (L) axillary LN lesions, both of which lesions were analysed. Finally, sample MM20 was derived from a subcutaneous melanoma lesion. Figure 28 demonstrates the intracellular and extracellular Tyrp1 labelling of the primary melanoma samples. The extracellularly labelled samples also underwent two cycles of Tyrp1 signal amplification. We also included T618A as a positive control for Tyrp1 expression. The intracellular labelling constituted a crucial control, since the presence or absence of Tyrp1 on the melanoma cell surface is meaningful only in the context of the intracellular presence of Tyrp1 in the melanoma cells. The cells analysed were gated for singlets, and alive cells that were CD45<sup>-</sup>MCAM<sup>+</sup>. The Y-axis constitutes a blank control, and the X-axis consists of the Tyrp1-PE signal. The columns A-F in Figure 28 represent the distinct cell lines. The first two rows (Figure 28.i-ii) demonstrate the intracellular labelling, and the last two (Figure 28.iii-iv) demonstrate the extracellular Tyrp1 labelling. Each line is shown in a column (Figure 28).

We used T618A cell line as the positive control for the primary melanoma stains (Figure 28.A). As shown in Figure 20 and Figure 26, T618A is positive for Tyrp1, and after signal amplification the percentage of surface Tyrp1 was 92%. Additionally, T618A is MCAM positive. Hence, T618A cells were labelled concomitantly with each primary melanoma, but only a single representation has been included in Figure 28.

The surface Tyrp1 density on T618A cells was calculated at 368 epitopes/cell (Table 20).

The samples MM18 and MM24 (Figure 28.B,D-ii) were positive for intracellular Tyrp1 (41.7% and 28.3% respectively), however there was no Tyrp1 present on the surface of the cells (Figure 28.B,D-iv). For the patient sample MM20 there were limited amount of cells. The intracellular isotype labelling for MM20 was 23.8%, which constitutes a high background (Figure 28.C-i). Nevertheless, the levels of MM20 intracellular Tyrp1 were 3-fold higher than the background (Figure 28.C-ii). Unfortunately after the 7-step labelling for the extracellular labelling and amplification, there were no remaining cells for MM20 sample (Figure 28.C-iii,iv). Finally, the MM25 samples were both positive for intracellular Tyrp1, albeit at low levels with MM25\_R 21.4% (Figure 28.E-ii), and MM25\_L 15.4% (Figure 28.F-ii). However, there was a difference between the extracellular profile for the different lymph nodes. The MM25\_L was not positive for surface Tyrp1 (Figure 28.F-iv). On the contrary, the MM25\_R had a distinct population of surface-Tyrp1 positive cells (3.33%) (Figure 28.E-iv), which we calculated at 162 surface Tyrp1 epitopes/cell (Table 20). For sample MM25\_R, we calculated the whole as well as the distinct Tyrp1-positive population. Table 20 contains the antigen-density values calculated based on the QIFIKIT beads, which is also shown in Figure 29.

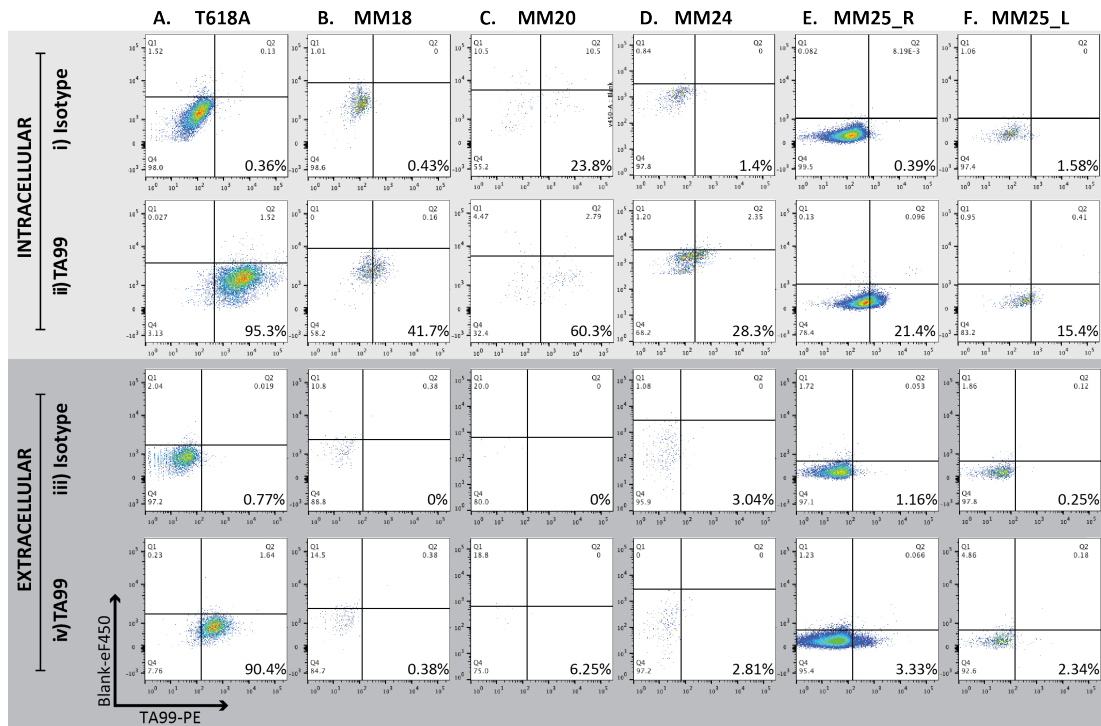


**Figure 28: Primary melanoma samples interrogated for intracellular and surface expression of Tyrp1.** The cells shown were alive, single, CD45 negative and MCAM positive. Tyrp1-PE signal is shown on the X-axis, and blank-eF450 is shown on the Y-axis. The columns (A-F) illustrate the different cell lines. The rows (i-ii) represent the intracellular labelling, and the rows iii-iv represent the extracellular labelling. For both intracellular and extracellular interrogation, the samples were labelled with either an isotype control (i, iii) or the TA99 antibody (ii, iv). We used the melanoma cell line T618A (A) as a positive control, since it is MCAM positive, as well as positive for both intracellular and extracellular Tyrp1. The samples MM18 and MM24 had low levels of intracellular Tyrp1 (B, D-ii) with no evidence of surface Tyrp1 (B, D-iv). The MM20 samples was sparse, especially in the extracellular labelling after the 7-step labelling, thus no conclusion could be drawn regarding the presence of surface Tyrp1 on MM20 melanoma cells (C-iv). The patient with MM25 had two lesions excised from either axillary LN. The right node was 21.4% positive for intracellular Tyrp1 (E-ii), and a distinct population of 3.3% surface Tyrp1 positive cells (E-iv). Finally, the left LN was only 15.4% positive for intracellular Tyrp1 (F-ii), and there was no Tyrp1 present on the surface (F-iv).

**Table 20: Tyrp1 density of primary melanoma samples.**

Melanoma Sample	MCAM (%)	Antigen Density
T618A	99.1	367.89
MM18	6.68	2.61
MM20	0.24	33.08
MM24	2.54	0
MM25_L	6.82	-1.22
MM25_R	48.9	-26.56
MM25_R (Positive Population)	48.9	162.36

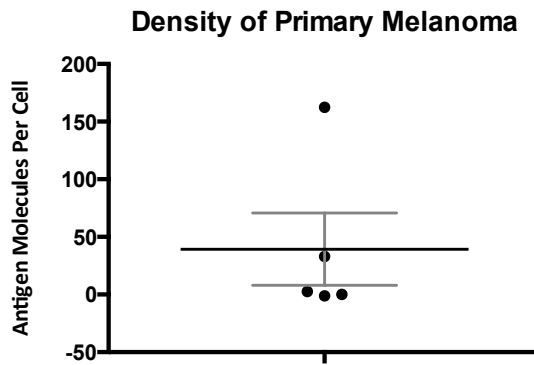


**Figure 29: Graph illustration of primary melanoma Tyrp1 antigen density on the cell surface.** The antigen density of the primary melanoma cell lines was calculated according to the QIFIKIT beads. The samples MM18, MM24, and MM25L had not surface Tyrp1. The density for MM20 was estimated to be 33moleculas/cell surface, but due to low cell numbers this finding is inconclusive. The density for the whole MM\_R population was calculated to be -27 epitopes/cell, but the distinct positive population had a density of 162 epitopes/cell.

### 3.3.4.3 Conclusion

In order to determine whether the cell surface expression of Tyrp1 on melanoma is within CAR T-cell detection range, we quantified the Tyrp1 antigen density. The density was quantified on melanoma cell lines and primary melanoma samples. The calculation was based on the density quantification kit QIFIKIT or the QuantiBrite, and the signal amplification kit FASER kit PE. The three melanoma cell lines, which express Tyrp1, were interrogated for the presence of Tyrp1 on their cell surface. The density quantification between the QIFIKIT and QuantiBrite kits was comparable. However, the low threshold of the QuantiBrite kit is lower, providing potentially more accurate results for the low density cells.

Based on to the QuantiBrite quantification, the Tyrp1 antigen density on the melanoma cell lines T618A, Mel280, and Mel290 was 1132, 18, and 4984 epitopes/cell, respectively. All three cell lines expressed Tyrp1, but the cell surface density was diverse. Nevertheless, two of the three cell lines bear an antigen density above the proposed CAR T-cell detection limit that is 240-770 epitopes/cell (Stone et al., 2012)(Watanabe et al., 2015).

Furthermore, we calculated the density of surface Tyrp1 on four primary melanoma samples. One patient had two axillary LN lesions, which were analysed separately. The presence of Tyrp1 on the surface of primary melanomas is heterogeneous. Of the five lesions analysed in total only one had a subpopulation positive for surface Tyrp1. Of the two lesions isolated from the same patient, one was negative for

surface Tyrp1. The second lesion bore only a subpopulation of cells expressing surface Tyrp1.

### 3.4 DISCUSSION

Tyrp1 is an intracellular protein, which resides on the surface of melanosomes (Vijayasaradhi et al., 1995). Tyrp1 is also present on the cell surface, but at low density (Yiqing Xu et al., 1997). Despite low density of surface Tyrp1, an anti-Tyrp1 antibody caused the eradication of metastatic melanoma tumours in mice (Hara et al., 1995). The clone of this antibody was TA99. The successful eradication of the melanoma tumour after anti-Tyrp1 antibody, along the lineage specificity of the antigen render it a promising melanoma target. The main aims in this chapter were three: 1) the validation of the specificity and sensitivity of the TA99 scFv, 2) construction of Tyrp1 protein chimeras to eGFP and mEos, 3) validation and quantification of surface Tyrp1 density on melanoma cell lines and primary melanomas.

First, the construction and validation of the TA99 scFv was described. In order to corroborate the specificity of TA99, we performed labelling of a murine lung bearing B16 melanoma metastasis. The metastatic regions were delineated by the presence of melanin. These areas appeared dark in the confocal, and they were all Tyrp1 positive when labelled with TA99. The non-metastatic areas were Tyrp1-negative, thus TA99 was only specifically localised to the melanoma cells. This is in accordance with reports confirming not only that TA99 is specific, but also it is the most sensitive antibody for immunohistochemical analysis of melanocytes in paraffin-embedded and frozen tissue (Bhawan, 1997)(Dean et al., 2002).

We aimed to create positive and WT controls of Tyrp1 expression. We transduced the SupT1 cell line with the Tyrp1 constructs. SupT1 cells do not inherently express Tyrp1. Apart from acquiring Tyrp1-WT, we engineered three additional Tyrp1 constructs fused to eGFP for live-cell imaging experiments. In order to retain Tyrp1 on the plasma membrane and use it as a positive control, we truncated the cytoplasmic domain and substituted it with eGFP. We also produced two Tyrp1 fusion

proteins to eGFP. In Proximal and Distal constructs the cytoplasmic domain was either proximal or distal to the membrane, either followed or preceded by eGFP.

Cells expressing the aforementioned Tyrp1 variants were interrogated for the presence of intracellular and surface Tyrp1 by flow cytometry. All constructs were positive for intracellular Tyrp1, thus all four Tyrp1 proteins were expressed. However, the profile of surface Tyrp1 expression varied between protein constructs. A limited proportion of wild type protein was present on the surface (12.5%) of transduced cells. The Distal protein was also present on the cell surface, but at a higher percentage of 51%. A higher percentage of cells were positive for surface Tyrp1 in the Trunc cells (66.8%). The percentage reflects the proportion of positive cells. However, the Trunc protein also led to higher MFI. We speculate that the higher MFI is directly related to a higher Tyrp1 density on the cell surface. The Proximal construct was designed to imitate the Tyrp1-WT trafficking pattern, but with eGFP incorporated for imaging. Interestingly, this construct exhibited a surface-Tyrp1 phenotype more stringent than the WT protein. Proximal expressing cells showed decreased MFI when labelled for intracellular Tyrp1, compared to Tyrp1-WT. This decrease was approximately half an order of magnitude, which might reflect reduced stability of the Proximal protein. In this case, the lower percentage of surface Tyrp1 in Proximal versus WT could be due to reduced stability, rather than more stringent sequestration of the protein. To conclude, the constructs Tyrp1-WT, Proximal, Distal, and Trunc constitute a low, low, medium and high density gradient of surface Tyrp1. Consequently, we sought to characterise Tyrp1 as an antigen. Although several carrier proteins have been identified to be responsible for the trafficking of Tyrp1, the trafficking pathway has not been elucidated (Wasmeier et al., 2006) (Setty et al., 2007). Our first aim was to investigate the trafficking pathway of Tyrp1 to the cell surface. In order to achieve that, we carried out, live-cell imaging of melanoma cells expressing fluorescent Tyrp1. Initially, Tyrp1 was fused to eGFP. However, the eGFP oligomerisation hindered the identification of individual vesicles that was essential for the trafficking study. Hence, eGFP was substituted to mEos. mEos is a green-to-red photoconvertable protein (Wiedenmann et al., 2004). The structure of mEos is similar to the eGFP forming a  $\beta$ -barrel structure barrel (Ormö et al., 1996)(Yang et al.,

1996)(Zhang et al., 2012). We thus postulated that the eGFP substitution to mEos would not modify the expression profile of surface Tyrp1, which was validated with the eGFP fusion protein.

In order to reliably identify and track Tyrp1-bearing vesicles, one of two requirements needed to be met. The vesicle should not cross a distance longer than half its diameter in order for the Imaris software to follow the movement. Alternatively, the vesicles should be sparse and in distance between them, so the software could discriminate individual vesicles and reliably track their movement. Due to high transduction levels, eGFP or mEos-green cells showed big areas of fluorescence. In these areas, the software could not recognise individual vesicles. Both proteins have been shown to form dimers or oligomers (Jain et al., 2001)(Zhang et al., 2012). However, photoconversion of a cell fraction led to a limited amount of mEos-red vesicles. This allowed the software to more reliably recognise the vesicles, as well as track them over time.

The sparsity of mEos-red vesicles led to a reliable identification of individual spheres. However, the absence of these vesicles from several time-points introduces an error in the vesicle tracking calculation. The live-cell imaging is carried out in a single plane instead of a z-stack. This is acceptable since the T618A cell line is adherent and relatively flat, so not many z-planes are required. However, the lack of data for the vesicles at different time-points suggests that the vesicles move in different planes out of focus. An alternative explanation would be that the time intervals between scannings were longer than required. Nevertheless, we analysed four vesicles that were present for 12 time-points or more. Of the four vesicles analysed, only TrackID\_4 vesicle appeared to be approaching the membrane twice, but did not fuse with it. There was no pattern observed for the trafficking of Tyrp1-bearing vesicles.

The presence of Tyrp1 on the cell surface was demonstrated with flow cytometry. Five cell lines were interrogated for the presence of intracellular Tyrp1. The three cell lines that were positive for intracellular Tyrp1 were T618A, Mel280, and Mel290. T618A and Mel290 were positive for the presence of Tyrp1 on the plasma membrane. The antigen density of the surface-Tyrp1 positive cells was quantified to 1132-1173 and 4018-4984 molecules/cell surface for T618A and Mel290 respectively. This

antigen density is above the detection limit of CARs (Stone et al., 2012)(Watanabe et al., 2015).

In order to validate the potential of Tyrp1 as a viable melanoma target, we sought to identify the density of Tyrp1 on the surface of primary melanoma tumours. The tumours were either subcutaneous or lymph-node metastases. Of the five lesions analysed, all expressed intracellular Tyrp1 at a percentage range of 15.4-41.7%. The correlation of Tyrp1 expression and melanoma progression is unclear, with published studies reporting both a positive and a negative correlation (Holzmann et al., 1987)(Bolander et al., 2008). Bolander and colleagues reported that 60% of melanoma tumours are positive for Tyrp1. Based on the limited amount of samples we acquired, the prevalence of Tyrp1 expression in metastatic melanoma was 100%. Despite the high prevalence of Tyrp1 expression, the expression pattern within the tumour was heterogeneous, which is in accordance to the literature (Virador et al., 2001).

Finally, the primary melanoma cells were also labelled for surface Tyrp1. Of those five samples, only MM25\_R was positive for surface Tyrp1, with a distinct population of 3.3%. The antigen density for this distinct population was 162 epitopes/cell. This density is close to the CAR T-cell cytotoxic limit of 240 epitopes/cell (Watanabe et al., 2015). Hence, anti-Tyrp1 CAR might have been efficacious against this sample. However, the prevalence of surface Tyrp1 is low, with only one in five lesions having Tyrp1 present on the cell surface. Additionally, based on sample MM25\_R, the surface Tyrp1 expression is heterogeneous within the sample, and between different lesions in the same patient. Although the preliminary data on primary melanoma tumours were discouraging, they were also inconclusive due to the limited amount of samples tested.

## **CHAPTER 4: Results**

### **Testing and Optimising the TA99-CAR**

## CHAPTER 4: RESULTS: TESTING AND OPTIMISING THE TA99-CAR

### 4.1 INTRODUCTION

The Tyrosinase-Related Protein 1 antigen is a promising melanoma target due to its unique and prevalent expression in melanoma (Bolander et al., 2008). Tyrp1 is an intracellular protein localised in melanocytes, however small amount can be detected on the cell surface. The presence of Tyrp1 on the cell surface was discussed in detail in Chapter 3. The antigen density of Tyrp1 was shown to be 1131 and 4984 epitopes/cell on the melanoma cell lines T618A and Mel290, which is above the CAR detection threshold (Stone et al., 2012)(Watanabe et al., 2015). The primary melanoma cells showed no or low presence of surface-Tyrp1. However, the observed lack of surface-Tyrp1 might be an artefact of fast cycling through the membrane. If that is the case, T-cells bearing with anti-Tyrp1 CAR could potentially recognise and eliminate the low-density Tyrp1 targets.

In order to evaluate the efficacy of an anti-Tyrp1 CAR, the anti-Tyrp1 antibody TA99 scFv was engineered into a second generation CAR format. A CAR is an artificial receptor that renders the T-cells specific for a target cell surface antigen. It consists of an extracellular, transmembrane and intracellular domain. The intracellular domain contains the intracellular module of the CD3 $\zeta$  chain, and co-stimulation domains. The TA99-CAR bears the co-stimulation endodomain of CD28, which promotes IL2 production and prevents T-cells anergy (Alvarez-Vallina and Hawkins, 1996)(Maher et al., 2002). The transmembrane domain anchors the protein to the cell surface. Finally, the extracellular domain is comprised of the scFv and a spacer. The scFv bestows the antigen specificity, whereas the spacer conveys flexibility to the extracellular domain (Moritz and Groner, 1995).

#### 4.1.1 The Importance of CAR Spacers

Currently three generations of CAR structures have been developed, however there is no conventional optimal CAR design to date. The optimal structure for an individual CAR against a specific antigen is empirical, not universal. One of the parameters affecting the CAR efficacy is the spacer, for which optimisation is required. This is most likely due to the highly specific architecture of the immune synapse, where the

size and structure of antigen-CAR complex plays a significant role. The spacer bestows flexibility to the CAR construct that is essential to overcome steric hindrance during antigen recognition and binding (Wilkie et al., 2008).

Furthermore, there is an inverse correlation between optimal spacer length and the distance of the antigen epitope from the target cell membrane (Guest et al., 2005). A longer spacer is required for an epitope proximal to the membrane, compared to shorter spacer required for epitope distal to the membrane. This relationship is probably due to the optimal distance between the T-cells and the target cell for formation of the immune synapse (Hudecek et al., 2013)(Hombach et al., 2007). It was finally shown that even after spacer-length optimisation, the CARs targeting the proximal-to-membrane epitope were superior in cytotoxicity and cytokine production (Haso et al., 2013).

The epitope recognised by TA99 is undetermined, thus we are unable to predict the optimal length of the spacer required for maximum efficacy. For this reason, we conducted a spacer optimisation by comparing four distinct spacers with different lengths (see 4.3.2).

## 4.2 AIMS

- *In vitro* validation of TA99-CAR specificity, efficacy and sensitivity.
- Identification of optimal spacer for TA99-CAR.
- *In vitro* validation of the TA99-CAR in a murine scaffold.
- *In vivo* investigation of murine TA99-CAR efficacy in a melanoma mouse tumour model

## 4.3 RESULTS

### 4.3.1 Validation of TA99-CAR *In Vitro*

#### 4.3.1.1 Engineering of the Human and Murine TA99-CAR

Our aim was to construct an anti-Tyrp1 CAR based on the TA99 scFv, and investigate whether we can successfully target the Tyrp1 present at low levels on the cell surface. In order to achieve that, we tested the efficacy of the TA99-CAR *in vitro* and *in vivo*. The specificity of TA99 scFv was demonstrated in Chapter 3 (3.3.2). For the *in vitro* experiment the CAR was introduced into Peripheral Blood Mononuclear Cells (PBMCs) isolated from blood of healthy donors. For the *in vivo* experiments the CAR was introduced into splenocytes of C57BL/6 mice. Since the CAR would be introduced into the cells originating from both human and mouse, we cloned the TA99 scFv into the structure of both human and murine CAR.

First, we engineered a second generation CAR, with all domains derived from human proteins. The ectodomain comprised the TA99 scFv, and the IgG1 CH2-CH3 spacer domain separated with a hinge. The CH2-CH3 spacer is derived from the immunoglobulin IgG1, and is illustrated in Figure 30. The transmembrane domain facilitates the anchoring of the CAR to the plasma membrane. The intracellular part of the TA99 CAR consists of the CD28 endodomain, and CD3 $\zeta$  (Figure 31.A).

The TA99 scFv was also incorporated into a second generation murine CAR format (Figure 31.B). Analogous to the human CAR, the extracellular part of the murine CAR (muCAR) consisted of the TA99 scFv, with the murine CD8 stalk facilitating as a spacer. It also included a transmembrane domain, and the intracellular modules that mediated the signalling. The intracellular modules were the murine CD28 and CD3 $\zeta$ . All the constructs were cloned into an SFG retroviral vector backbone.

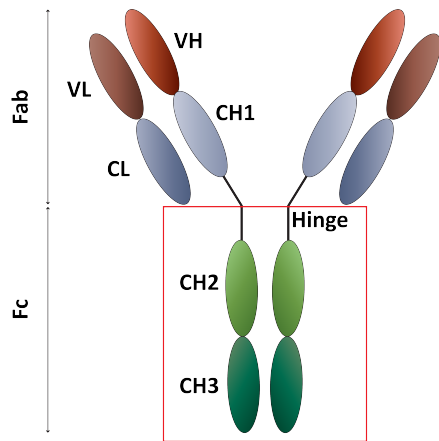


**Figure 30: The Fc spacer domain is derived from the antibody constant heavy region CH2-CH3.** An antibody consists of four chains, two light and two heavy chains. The heavy chain contains the variable region, three constant regions, and the hinge. The hinge regions of two heavy chains form disulphide bonds, leading to dimerization.

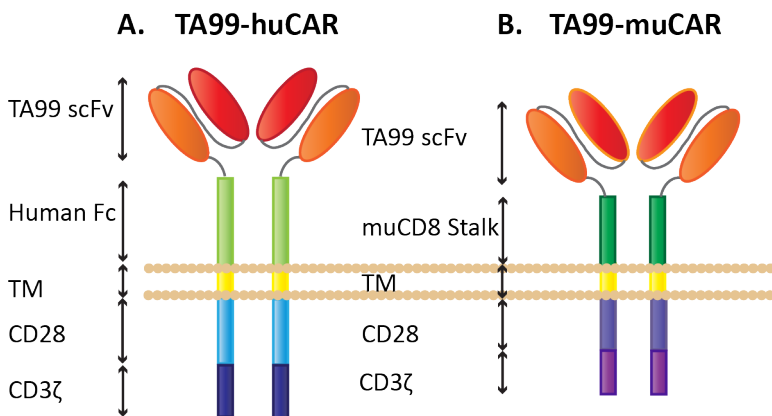


**Figure 31: The structure of the human and mouse TA99 CAR.** Both CARs consist of an extracellular, a transmembrane, and an intracellular domain. TA99 heavy and light chains are tethered with a SG linker. The extracellular domain includes the TA99 scFv that provides the target specificity of the molecule, a hinge, and a spacer that provides flexibility. **(A)** The spacer for the human CAR is the CH2-CH3 domain from human IgG1, and the transmembrane sequence is derived from human CD28. Two modules comprise the intracellular domain of the CAR, and these are the human CD28 intracellular domain, and CD3ζ. The activation signal transmitted by CD3ζ without co-stimulation leads to energy, and thus the co-stimulatory signalling CD28 was incorporated. **(B)** The murine CAR is similarly structured to the human one, apart from the spacer that is the murine CD8 ectodomain. All the domains were derived from mouse sequence. The muCAR is also a second generation with the intracellular compartment being CD28-CD3ζ.

#### 4.3.1.2 Labelling Optimisation for CAR Detection

Prior to each functional experiment, it is essential to investigate whether the T-cells are expressing the transduced CAR construct, and what percentage of the cells bear the CAR protein. It is important to calculate the transduction efficiency, because it is required also for normalisation between different CARs prior the functional assay set-up. The transduction efficiency is determined based on a marker gene co-expressed in the CAR transgene cassette, or the direct labelling of the CAR protein. The muCAR was co-expressed with murine CD19 that functions as a marker gene. We

incorporated the marker gene in splenocytes in order to enable easy and accurate identification of the transduced splenocytes in murine tissues.

The human T-cells used for the in vitro experiments were not introduced into a complex environment. Therefore, no marker gene was required to enable the T-cell identification. Consequently, the transduction efficiency of the primary human T-cells was established by directly labelling the cells for the presence of the CAR. The flow cytometric detection of the CAR was optimised by testing four labelling methods. We pursued labelling with an anti-Human (Fragment Crystallisable) Fc antibody that recognised the CH2-CH3 domain of the CAR spacer. An anti-Mouse Fragment Antigen Binding (Fab) recognised the variable fragment of TA99. We also produced soluble Tyrp1 fused with the His tag, and labelled the T-cells with the Tyrp1-His protein supernatant. Finally, we tested the labelling capacity of Protein-L. Protein-L is a bacterial protein that binds to antibody variable light chains, and has been previously used for labelling CAR molecules (Zheng et al., 2012).

The results of the CAR labelling optimisation protocol are shown in Figure 32. The columns represent the labelling methods, whereas the rows represent the different cells used in the experiment. Specifically, the first and second row illustrate non-transduced PBMCs or PBMCs transduced with the TA99-CAR transgene, respectively. The Y-axis shows a blank channel for all the plots, and the X-axis depicts the positive signal for each labelling method.

No background noise was observed with any protocol, as shown for PBMC NT (Figure 32.A-D). The transduction efficiency ranged from 2.39 to 95.3%. Labelling the cells with the anti-Human Fc antibody was superior, with 95.3% of the cells being CAR positive (Figure 32.E). The labelling with aMouse Fab antibody led to an estimated transduction efficiency of 60.7% (Figure 32.F). Compared to the anti-Human Fc antibody, the estimated transduction level decreased 3-fold when the cells were labelled with Tyrp1-His protein supernatant. The reason for that might be the reduced stability of the soluble Tyrp1, or low protein concentration in the supernatant. Finally, the bacterial Protein-L failed to label the TA99-CAR positive cells. Labelling the cells with aHuman Fc antibody was specific, and the most

efficacious, therefore this protocol was used in subsequent experiments for the labelling of the TA99-CAR.

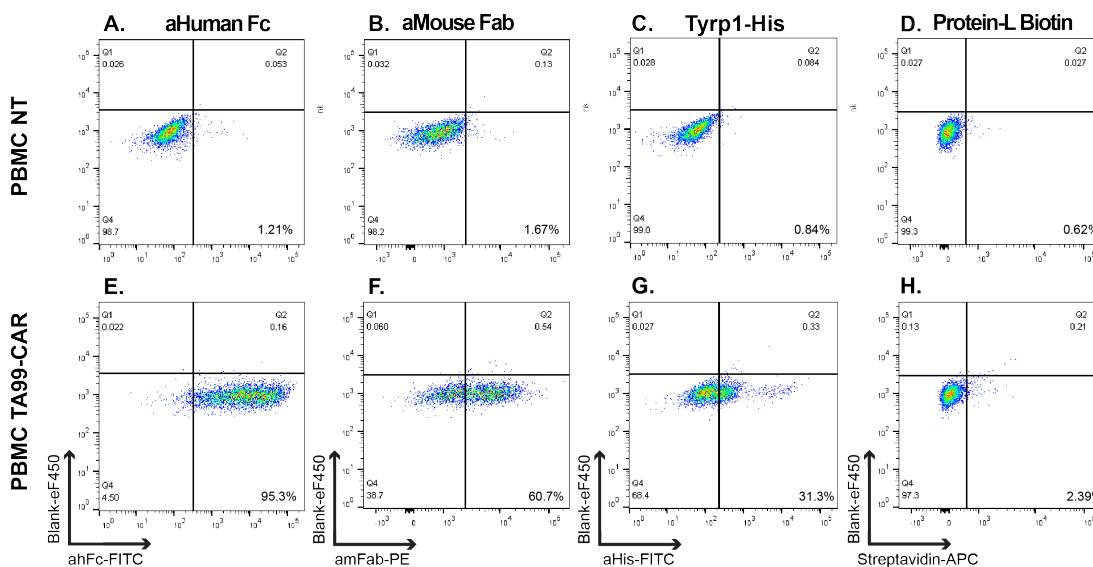


**Figure 32: Optimisation protocol for labelling the TA99-CAR positive cells.** Non-transduced (A-D) and TA99-CAR positive cells (E-F) were labelled for the presence of the CAR with four distinct methods. Each method is represented in a separate column, with the axes labels underneath. The Y-axis represents a blank control, and the X-axis shows the signal detection channel. (A-D) No background labelling was detected on the PBMC NT, confirming the specificity of the proteins used. (E) The cells labelled with the anti-Human Fc antibody were 95.3% positive for TA99 expression. (B) The transduction efficiency was underestimated when labelled with the anti-Mouse Fab (60.7%). (C) The Tyrrp1-His protein supernatant was even less efficacious in identifying the CAR positive cells. (D) Protein-L failed altogether in recognising the light chain of the TA99 scFv, and showed no positive signal.

#### 4.3.1.3 Transduction Efficiency of TA99-CAR PBMCs

As mentioned earlier, determining the PBMC transduction efficiency prior to the functional set-up is crucial for obtaining a clear and reproducible result. First, we need to confirm the presence of the CAR in the PBMCs. Additionally, normalisation of the transduction levels between different CARs is essential for reliable results. Discrepancies in transduction levels above 10% constitute a confounding factor, and the levels need to be normalised to the lowest transduction percentage. The normalisation is achieved with the addition of NT PBMC in the CAR-bearing cell populations with the higher transduction level.

The estimation of the transduction efficiency is repeated for each separate experiment. Although there is donor variation in the transduction level, this variation is usually within 10-15% range. The transduction threshold accepted for carrying out a functional experiment is above 20%. In Figure 33, a representative labelling for the CAR transduction efficiency is shown. The cells were labelled for CD4 and CD8 and

illustrated in A-C and D-F respectively. The signal for CD4 or CD8 is shown on the Y-axis. A control CAR was used in the functional experiment as a negative control of cytotoxicity and cytokine production. The transduction levels of CD4 cells for the control aCD33-CAR, and TA99-CAR were 15.6% and 18.1% (Figure 33.B-C). The percentage of CD8 CAR positive cells was higher, with 21.5% and 24.3% of transduction efficiency for aCD33-CAR and TA99-CAR respectively (Figure 33.E-F). The total transduction level was 37.1% for the aCD33-CAR, and 42.4% for the TA99-CAR. The total level of CAR expression was above 20%, which is sufficient for carrying out a functional assay. The CAR level discrepancy was less than 10%, thus no normalisation was required.

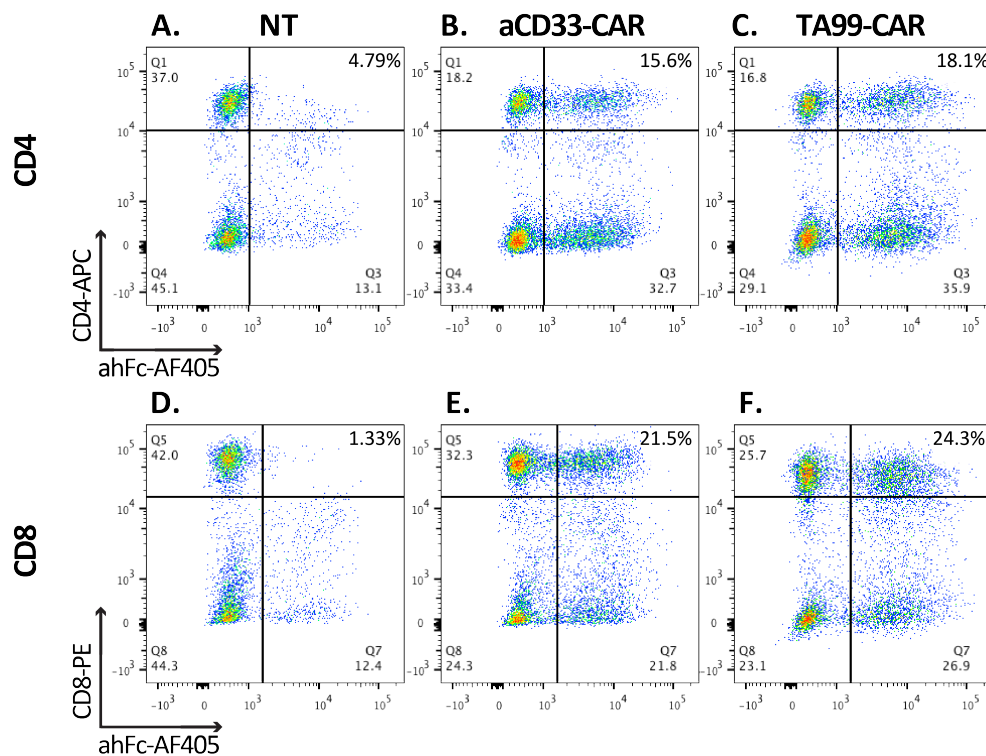


**Figure 33: Level of CAR expression in cells transduced with a CAR transgene.** The PBMC cells were labelled for both CD4 (A-C) and CD8 (D-F), as well as the presence of the aCD33 or TA99-CAR. The Y-axis represents either the CD4 or CD8 signal, and the X-axis represents the CAR expression signal. There was some background signal observed in the NT PBMCs (A,D), probably due to cross-reactivity between the CD4/CD8 antibodies and the aHuman Fc (ahFc) antibody. The CD4 and CAR positive cells were 15.6% for the aCD33-CAR (B), and 18.1% for the TA99-CAR (C). The CD8 and CAR positive cells were 21.5% and 23.4% for the aCD33-CAR (E) and TA99-CAR (F), respectively.

#### 4.3.1.4 Cytotoxicity Assay for *In Vitro* TA99-CAR Validation

We have so far established that the TA99 scFv is specific for Tyrp1, and that Tyrp1 is present on the cell surface at low-density. Our aim was to determine whether a CAR with the scFv of TA99 is functional. An additional question to be addressed was

whether the surface antigen density of Tyrp1 is sufficient for recognition and elimination by TA99-CAR T-cells.

To address those questions, we isolated PBMCs from the blood of healthy donors. The PBMCs were transduced with the TA99-CAR transgene, as well as the transgene for a control CAR, against CD33 or CD19. The CAR not specific for Tyrp1 is used as a negative control. Prior to the assay the PBMCs were CD56 depleted to eliminate natural killers from the experiment. On day 10 after the PBMC isolation, we setup a <sup>51</sup>Chromium cytotoxicity assay. The assay requires the targets cells to be loaded with the radioactive isotope Chromium 51 (<sup>51</sup>Cr). The <sup>51</sup>Cr is internalised and retained in the cytoplasm of the target cells, which is subsequently released in the supernatant when the cells are lysed. The effectors (PBMCs transduced with either TA99-CAR or aCD33-CAR) were incubated for 4 hours with the <sup>51</sup>Cr loaded target cells. After incubation, we harvested the supernatant from the wells and measured radioactivity with a gamma counter. By measuring the radioactivity of the supernatant it was possible to estimate the proportion of lysed target cells.

As discussed in 3.3.4.1, the surface Tyrp1 density of the SupT1 engineered cells was 151, 176, and 308 epitopes/cell for Tyrp1-WT, Distal, and Trunc respectively. The antigen density of Proximal is negligible and has not been calculated. The density of Tyrp1 on the human melanoma cell line T618A is 1132 epitopes/cell. B16 is a mouse melanoma cell line derived from C57BL/6 mice with a surface Tyrp1 density of 1844 epitopes/cells (data not shown). Our aim was to use B16 as a melanoma mouse model for *in vivo* validation of the TA99-CAR. Hence, before the animal model, we sought to determine whether B16 cells are susceptible to TA99-CAR T-cells *in vitro*.

Each graph in Figure 34 summarises the cytotoxic capacity of the three effectors against a specific target. When the T-cells were incubated with non-transduced SupT1, there was no cytotoxic activity observed apart from background signal (Figure 34.A). Although against the Tyrp1-WT and Proximal cells there was an increase of the TA99-CAR cytotoxicity, the lysis percentage was only marginally higher than the background (Figure 34.B-C). On the contrary, 33.5% of the Trunc cells were lysed (Figure 34.D).

Of the two melanoma cell lines, B16 (Figure 34.E) and T618A (Figure 34.G), only the T618A cells were lysed by the TA99-CAR T-cells (18.7%). We postulated that the T-cells were not able to lyse B16 due to low antigen density on the surface of target cells. In order to investigate this hypothesis, we also included B16 cells transduced with Trunc (Figure 34.F). Only 18.9% of the B16 cells expressing Trunc were lysed, which is comparable to T618A lysis, but lower than SupT1 transduced with the same transgene. This result indicates that the wild-type B16 cells are not susceptible to *in vitro* lysis by CAR T-cells. We have previously shown that both melanoma cell lines express the surface Tyrp1, however the antigen density is close to the CAR T-cell lower detection level. Therefore, the 4-hour incubation might be suboptimal, leading to impeded T-cell cytotoxicity.

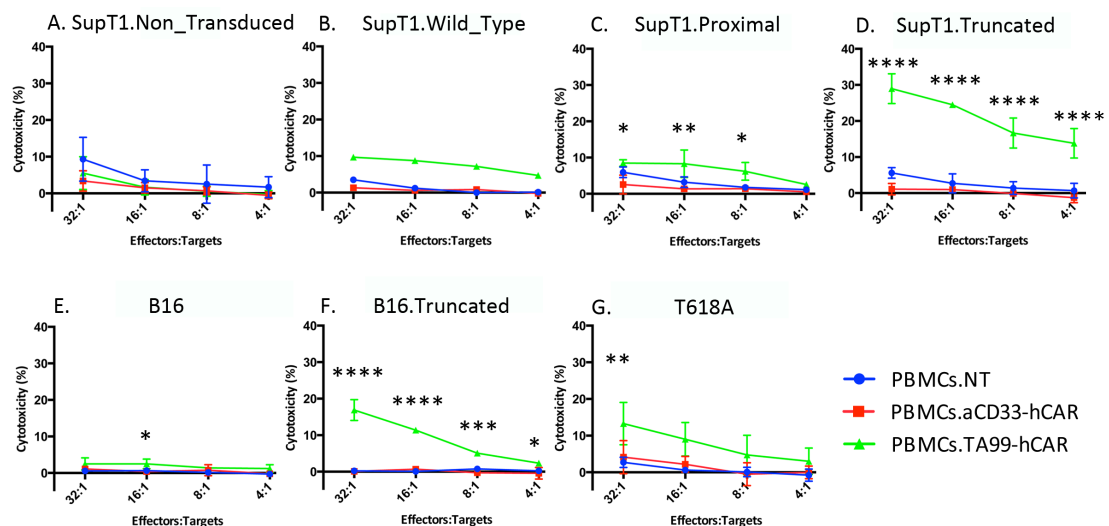


**Figure 34:** <sup>51</sup>Cr release assay with TA99-humanCAR T-cells. The targets cells were co-cultured with the effectors for 4-hours at ratios 32:1, 16:1, 8:1, 4:1 (effectors: targets). The effectors are displayed in different colours PBMCs NT (blue), PBMCs non-specific CAR (red), PBMCs TA99-CAR (green). Each graph shows the percentage of lysed cells of a distinct target cell line. The background killing of the three different effectors was low (<5%) (A). However, it was unclear whether the 7.9% cytotoxicity observed for of TA99-CAR T-cells against Tyrp1-WT and Proximal cells is significant (B-C). The superior cytotoxicity of the TA99-CAR versus the control CAR against SupT1 Proximal was statistically significant at the ratios 32:1, 16:1, and 8:1 (p=0.0113, p=0.0040, p=0.385, respectively). The TA99-CAR was cytotoxic against the positive control of Trunc cells (33.5%), confirming that TA99-CAR is functional (p=<0.0001) (D). There was no lysis of the melanoma cell line B16 (p=0.356) (E). On the contrary, 18.9% of the B16 cells transduced with Trunc were lysed by TA99-CAR T-cells (p=<0.0001) (F). Finally, TA99-CAR T-cells were cytotoxic against the human melanoma cell line T618A (G) with a percentage of killing 18.7% (p=0.0090). Three repeats were carried out, and the statistical significance was tested with a two-way Anova. The difference between the TA99-CAR to the control CAR is significant were indicated.

#### 4.3.1.5 Interferon- $\gamma$ Production by TA99-CAR T- cells

Although the TA99-CAR is functional, there was no cytotoxic activity against the melanoma cell line B16, and the observed cytotoxicity against T618A cells was modest. In order to closely examine the capacity of T-cells to lyse low antigen targets,

we increased the incubation time rendering the experiment parameters less stringent. The readout for the co-culture was IFN- $\gamma$  cytokine produced by T-cells, analysed with an Enzyme-Linked Immunosorbent Assay (ELISA). For the ELISA, supernatant from each condition was collected at a 24-hour time-point.

Figure 35 demonstrates the ELISA results. There was no detectable background from the non-transduced PBMCs (Figure 35.Blue) or the PBMCs transduced with a non-specific CAR (Figure 35.Red). The TA99-CAR cytokine levels are shown as green bars in Figure 35. There was no detectable background cytokine production when TA99-CAR T-cells encountered SupT1 NT targets or were incubated without target cells. However, TA99-CAR T-cells produced IFN- $\gamma$  in the presence of Tyrp1-WT and Trunc cells. The concentration of IFN- $\gamma$  produced by TA99-CAR T-cells incubated with Trunc SupT1 cells was 6452pg/ml. This value is the average of three independent experiments on different donors. The Trunc constituted the positive control. Despite the low antigen density on the cell surface of the Tyrp1-WT and Proximal SupT1 targets, T-cells were sensitive enough to produce 1325.7pg/ml and 776.3pg/ml of IFN- $\gamma$ , respectively.

Although TA99-CAR T-cells failed to lyse B16 cells, they produced IFN- $\gamma$  during the co-culture (743.5pg/ml). We also included the B16 cells transduced with Trunc. Consistent with the  $^{51}\text{Cr}$  cytotoxicity assay, T-cells were reactive against Trunc B16 and T618A cells, with 2906.4pg/ml and 3068.7pg/ml IFN- $\gamma$  produced respectively.

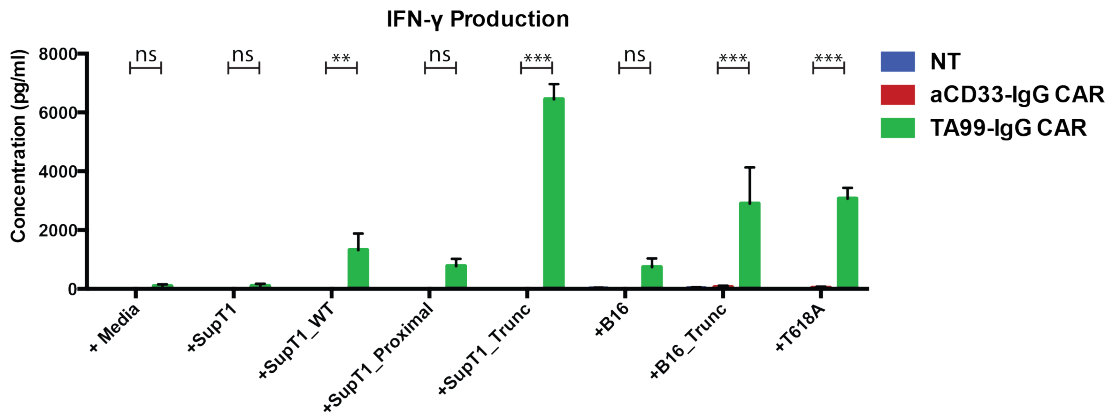


**Figure 35: IFN- $\gamma$  cytokine production after 24-hour co-culture.** The effectors were non-transduced T-cells (NT), T-cells transduced with the non-specific aCD33-CAR as a negative control, and TA99-CAR transduced T-cells. The effectors were incubated with SupT1 NT, or SupT1 expressing WT, Proximal, or Trunc Tyrp1. T-cells were also incubated with B16, and B16 expressing Trunc. Finally, T-cells were co-cultured with T618A. Neither the negative control, NT (**blue**) nor the aCD33-CAR T-cells (**red**) produced any IFN- $\gamma$ . The TA99-CAR T-cells (**green**) produced IFN- $\gamma$  when co-cultured with all Tyrp1-expressing targets. TA99-CAR T-cells produced 6452pg/ml of IFN- $\gamma$  against Trunc. IFN- $\gamma$  production was modest against the other two targets with 1325.7pg/ml for Tyrp1-WT, and 776.3pg/ml for the Proximal. The same pattern was also observed for the B16 cells. The IFN- $\gamma$  secretion for B16 NT and Trunc was 743.5pg/ml, and 2906.4pg/ml respectively. Finally, the T-cell secretion of IFN- $\gamma$  when exposed to the melanoma cell line T618A was 3068.7pg/ml. The statistical significance was calculated with two-way Anova (\*\*  $p=0.0079$ , \*\*\*  $p<0.0001$ ).

#### 4.3.1.6 Conclusion

In conclusion, the TA99-CAR is specific and functional against cells with Tyrp1 present on their cell surface. We observed limited cytotoxicity against the low density Tyrp1-WT and Proximal cell lines. The IFN- $\gamma$  production was a more sensitive read-out than cytotoxicity in measuring the CAR sensitivity against low-antigen targets. We detected IFN- $\gamma$  production against B16 cells, although the T-cells failed to lyse those cells.

#### 4.3.2 TA99-CAR Spacer Optimisation

##### 4.3.2.1 Engineering the TA99-CAR with Four Distinct Spacers

The epitope recognised by TA99 resides in the luminal domain of Tyrp1 (Groux-Degroote et al., 2008). However, the epitope itself and where it resides within the luminal domain is unknown. Hence, we cannot comprehensively predict the optimal spacer length required for maximum efficacy. For this reason, we examined four distinct spacers. We employed a commonly used spacer of the immunoglobulin family, IgG CH2-CH3 domain including the hinge region (Thomas et al., 2016). Alternatively, hinge can be used alone as a CAR spacer (Hudecek et al., 2013). The hinge region causes the dimerization of the CAR due to intra-chain disulphide bond

formation (Liu and May, 2012). Another spacer from the immunoglobulin family is IgM (Forman et al., 2015). IgM consists of four constant heavy domains CH1-CH2-CH3-CH4 (Schroeder and Cavacini, 2010). The domains incorporated in the CAR format are CH2-CH3-CH4, thus the IgM spacer has an additional domain compared to IgG making it longer. The last spacer we utilised was the CD8a ectodomain, which comprises a single immunoglobulin-like domain and a 30-50aa stalk of highly glycosylated residues (Classon et al., 1992). CD8a also forms dimers, similarly to the immunoglobulin-based CAR spacers, and has been incorporated in CARs used in clinical trials (Leahy et al., 1992) (Patel et al., 1999)(Porter et al., 2011). Our aim is to compare the four spacers in the context of the TA99 CAR, and identify which one is optimal.

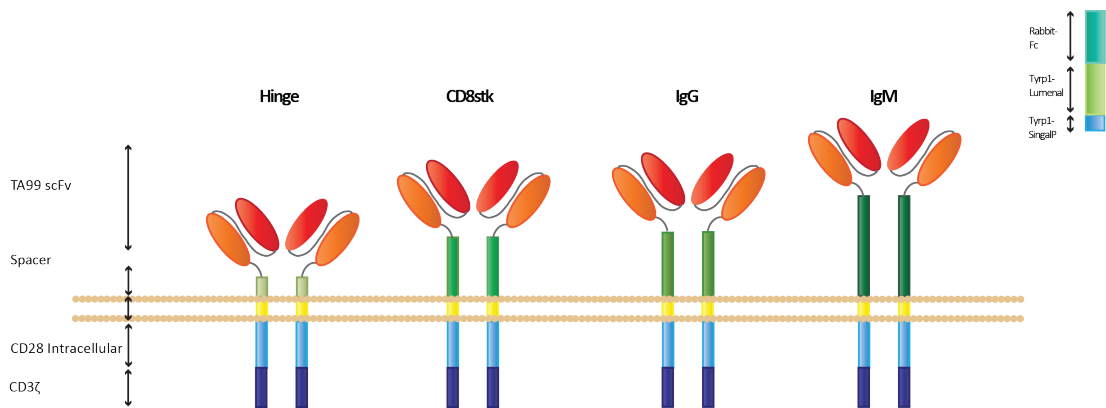


**Figure 36: Four spacers were analysed for identification of optimal TA99-CAR structure.** We sought to determine the optimal spacer for the TA99-CAR. Therefore, we tested four spacers of varying lengths. Three were based on immunoglobulin domains, and the fourth was derived from T-cell co-receptor CD8. The first spacer employed was the hinge sequence of the immunoglobulin IgG1, which causes dimerization of the CAR molecule. The CH2-CH3 domains of IgG1, as well as the hinge were combined to form the IgG spacer. The IgM spacer is longer, because it contains an extra domain CH2-CH3-CH4. Finally, the ectodomain of CD8 (CD8stk) was utilised, which also causes dimerization. Hence, all spacers used in this thesis caused dimerization of the CAR. The constructs are displayed with order of incrementally increasing length.

#### 4.3.2.2 Transduction Efficiency of TA99-CAR Spacer Variants

As stated in previous chapters, the estimation of the T-cell transduction levels is crucial. Since the CAR constructs bear different spacers, labelling the cells with an anti-Human Fc antibody is not feasible. Hence, the cells were labelled with supernatant of soluble Tyrp1-Rabbit.

The transduction levels for the PBMCs transduced with the different constructs are shown in Figure 37. The signal for CD4 or CD8 is represented in the Y-axis, and the labelling for the TA99-CAR on the X-axis. The different PBMC populations are shown

in separate columns. The transduction levels between CARs with the IgG, hinge, or CD8 spacer were comparable for both CD4 (Figure 37.C-E), and CD8 (Figure 37.I-K) T-cells. The range of transduction for those constructs was 28.6-31.7% for CD4 and 23.6-14.9% for CD8. In opposition to that, the transduction levels for the IgM spacer CAR were consistently lower with 18% and 9.5% transduced CD4 and CD8 cells respectively (Figure 37.F,L). The transduction level for all the TA99-CAR spacer variants was higher than 20%, but the disparity between the IgM variant to the rest required normalisation.

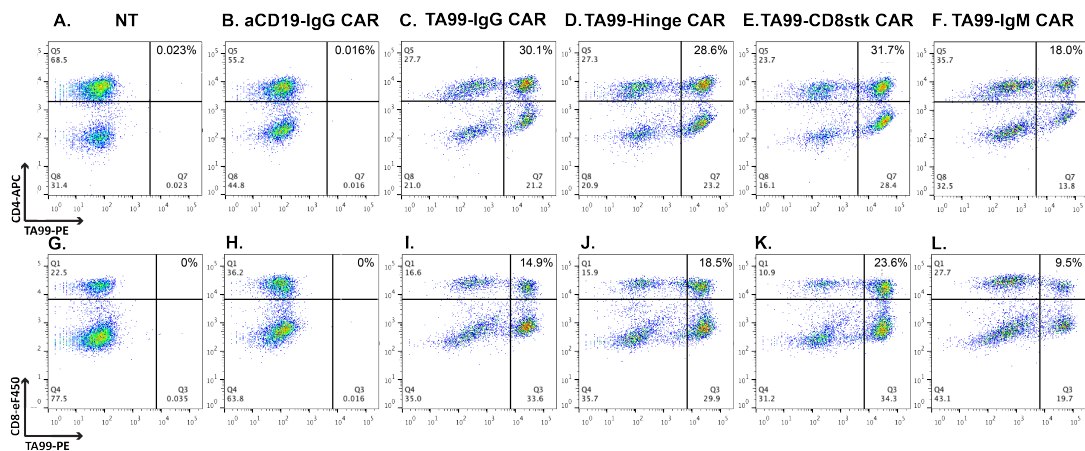


**Figure 37: Transduction levels of TA99-CAR cells bearing different spacers.** The Y- and X-axis show the signal for CD4/CD8 and signal for the transgene expression. The columns represent different PBMCs populations. (A, G) PBMCs NT cells constitute the negative control for labelling and cytotoxic assays. (B,H) The control CAR is also an additional negative control. The CD4<sup>+</sup> CAR expression levels for the spacer constructs IgG, hinge and CD8 were 30.1% (C), 28.6% (D), 31.7% (E) respectively. The transduction level of CD4 T-cells for the IgM spacer variant was lower at 18.0% (F). The same pattern was observed for CD8 T-cells, with the IgM spacer variant also having the lowest levels, at 9.5% (L). The transduction level for the IgG, hinge, and CD8 spacer CD8 T-cells was 14.9%, 18.5%, and 23.6% respectively.

#### 4.3.2.3 Cytotoxic Capacity Comparison of TA99-CAR Spacers

The TA99 spacer variants were interrogated for their cytotoxic capacity. In order to compare the cytotoxic efficacy of the TA99-CAR bearing different spacers, we carried out <sup>51</sup>Cr release cytotoxic assay. The PBMCs were cultured for 4-hours with six distinct cell lines of various Tyrp1 densities. These lines were the engineered SupT1 expressing Tyrp1-WT, Proximal, Distal, and Trunc. The CAR T-cells were also cultured against the melanoma cell lines T618A, B16, and B16 transduced with Trunc.

The cytotoxicity of the TA99 CAR T-cells is shown in Figure 38. The negative control conditions constituted of PBMCs NT (grey), and a control CAR that is non-specific for Tyrp1 (blue). In a previous chapter we demonstrated that the TA99-CAR with the IgG

spacer is functional (see 4.3.1.4). Our aim is to explore whether the hinge, IgM or CD8 spacer are superior. In contrast to the rest of the TA99-CARs, IgM spacer variant showed non-specific cytotoxicity against SupT1 NT (11.0%) (Figure 38.A). The IgG and IgM variant showed similar cytotoxicity against SupT1 Tyrp1-WT and Proximal. The cytotoxicity levels for the 16:1 ratio were 23.6% and 24.9% for the IgG and IgM variant against Tyrp1-WT cells. Similarly, the cytotoxicity levels for the IgG and IgM variant against SupT1 Proximal were 18.4% and 18.1%, respectively. It is promising that cytotoxicity was observed against the low antigen-density targets (Figure 38.B-C). No lysis was observed against the Tyrp1-WT targets by the hinge or CD8 spacer variant (5.4%, 8.7%). The cytotoxicity of IgG and IgM was also similar against the SupT1 Distal (40.3%, 40.2%) and Trunc targets (36.1%, 39.7%), with no statistically significant difference between them (Figure 38.D-E). The CD8 spacer variant was less efficacious (19.6%), and the hinge variant showed the least cytotoxicity (15.0%) against the positive control cell line SupT1\_Trunc (Figure 38.E).

The IgG and IgM variant also recognised and lysed the human melanoma cell line T618A at 40.9% and 39.3% respectively (Figure 38.H). The cytotoxic capacity of the hinge and CD8 spacer variants was mitigated at 5.25% and 13.6%. Finally, the hinge and CD8 spacer variants failed to lyse the B16 NT and Trunc targets (Figure 38.F-G). The cytotoxicity of TA99-CAR IgG variant was calculated at 11.3%, and of the IgM variant at 7.35% against B16. Interestingly, the cytotoxicity of the IgG and IgM variants did not increase against B16 expressing Trunc (9.1% and 6.0%, respectively). This observation suggests that the inability of the CAR T-cells to lyse B16 cells is not due to the low density of surface Tyrp1.

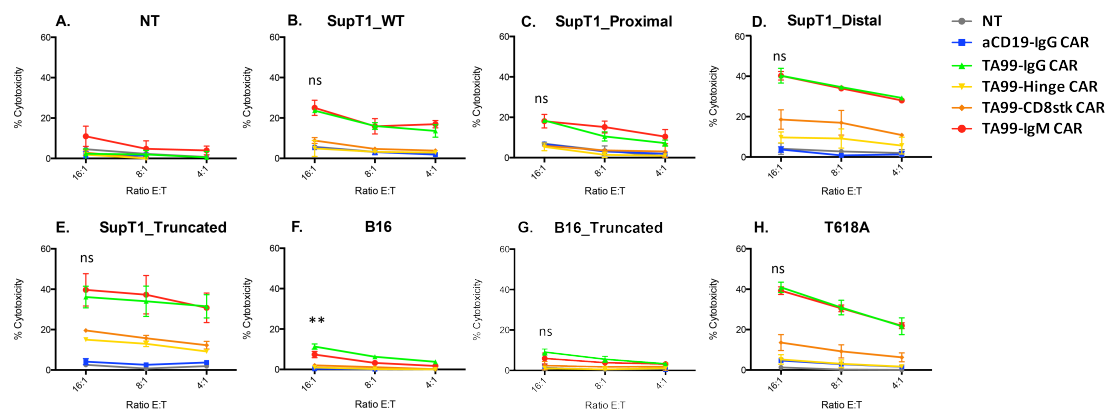


**Figure 38: Comparison of cytotoxic capacity between TA99-CARs with different spacer variants.** PBMC NT and control CAR function as negative controls for T-cell background toxicity. The other four effectors in this experiment constitute the four spacer variants of the TA99-CAR. Each graph shows the cytotoxicity of all the effectors against a different target cell line. (A) SupT1 NT cell line does not express the antigen, and thus facilitates as a negative control. The IgM variant non-specifically lysed 11% of the SupT1 NT cells. (B) The IgG and IgM spacer CAR variants lysed 23.6% and 24.9% of the SupT1 Tyrp1-WT targets, in contrast to the hinge and CD8 spacer variants that lysed only 5.4% and 8.7%. Both IgG and IgM were superior to hinge ( $p < 0.0001$ ) and CD8 ( $p < 0.0004$ ). (C) The density of SupT1 cells expressing Proximal is lower than Tyrp1-WT. In consistency with that, the cytotoxicity of IgG and IgM variants was 18.4% and 18.1% against SupT1 Proximal. (D) The IgG and IgM CAR T-cells lysed 40.3% and 40.2% of the SupT1 Distal targets, and 36.1% and 39.7% of the SupT1 Trunc targets. Both IgG and IgM were superior to hinge ( $p < 0.0001$ ) and CD8 ( $p = 0.0005$ ) (E). The lysis achieved by the hinge and CD8 CARs was only 19.6% and 15% against the SupT1 Trunc targets. Both IgG and IgM were superior to hinge ( $p = 0.0303$  and  $0.0091$ ), but only IgM variant was marginally significant against CD8 ( $p = 0.0418$ ) (F-G) The hinge and CD8 spacer variants failed to lyse B16 NT or B16 Trunc cells. The lysis achieved by IgG and IgM against B16 cells was 11.3% and 7.35% of the target population. This difference between IgG and IgM CAR was statistically significant ( $p = 0.0089$ ). The cytotoxicity of IgG and IgM variants was reduced against B16 Trunc (9.1%, 6.0%). (H) Finally, the lytic capacity of the IgG and IgM variants against T618A was 40.9% and 39.3% respectively, in contrast the hinge and CD8 spacer variants that shown a lytic capacity of 5.25% and 13.6%. Both IgG and IgM were superior to hinge and CD8 variants ( $p < 0.0001$ ) against T618A. Two repeat were conducted for this experiment, the statistical analysis was a two-way Anova test.

#### 4.3.2.4 Interferon- $\gamma$ Production Comparison of TA99-CAR Spacers

We observed in chapter 4.3.1.5 that the threshold of TA99-CAR T-cells was lower for cytokine production than cytotoxicity. Our aim was to compare the TA99-CAR spacer variants in regard to the cytotoxic capacity and sensitivity. In order to investigate their sensitivity, we carried out a co-culture for testing the IFN- $\gamma$  production of the T-cells against cell lines with a range of antigen densities.

The concentration of IFN- $\gamma$  produced for each condition is shown in Figure 39. The cells transduced with TA99-CARs bearing the hinge or CD8 spacer failed to produce IFN- $\gamma$  in any condition (Figure 39). TA99-CAR IgM variant exhibited production of IFN- $\gamma$  in the absence of target cells, or targets negative for Tyrp1 (980.8pg/ml and 906.7pg/ml). The background production of IFN- $\gamma$  by the IgG variant was 214pg/ml. The IFN- $\gamma$  concentration for the IgG and IgM variants against SupT1 Tyrp1-WT was 192p/ml, and 975pg/ml respectively, which is not above their background threshold.

The cytokine production capacity of the IgG and IgM CAR T-cells increased approximately 2-fold against SupT1 Distal (550.3pg/ml, 1780.3pg/ml). Similar pattern was observed for the SupT1 Trunc target cells cultured with IgG and IgM TA99-CAR (346.1pg/ml, 1970pg/ml).

The cytokine production of the IgG TA99-CAR was 290.5pg/ml against B16, which is similar to the background level of the CAR. The IgM variant also failed to produce IFN- $\gamma$  above its background threshold (812.6pg/ml). Finally, we observed an increase in the background IFN- $\gamma$  production by the control aCD19-CAR (1324.9pg/ml). However, the IFN- $\gamma$  concentration released by the IgG and IgM TA99-CAR variants was significantly higher (5752.4pg/ml, 5600.0pg/ml).

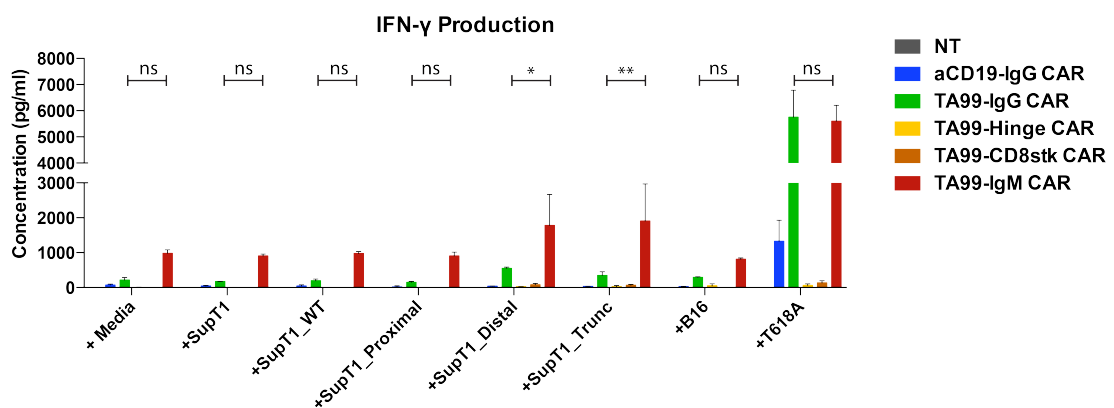


**Figure 39: Comparison of IFN- $\gamma$  production induced by TA99-CAR spacer variants.** The effectors employed in this experiment were the negative controls PBMC NT and aCD19-CAR, as well as the TA99-CAR spacer variants. The T-cells were cultured in the presence of different targets, and the IFN- $\gamma$  production was measured with an ELISA assay. The hinge and CD8 spacer variants produced no IFN- $\gamma$ , regardless the condition they were cultured in. The background cytokine production of the IgG and IgM variants was 980.8pg/ml and 214pg/ml in the absence of target cells. The cytokine production was increased approximately 2-fold for both the IgG and IgM variant in the presence of Distal SupT1 cells (550.3pg/ml, 1780.3pg/ml). The disparity in IFN- $\gamma$  production between the IgG and IgM variant was statistically significant ( $p=0.0368$ ). In the presence of the melanoma target T618A, the IgG spacer variant showed a 27-fold increase in IFN- $\gamma$  production (5752.4pg/ml), and the IgM variant showed a 6-fold increase (5600.0pg/ml). The results were statistically analysed in GraphPad Prism with two-way Anova test. These set of data represent the result from three independent donors.

#### 4.3.2.5 Conclusion

We compared several spacer variants of the TA99-CAR in order to identify the optimal spacer for subsequent experiments. We had already shown that the TA99-CAR bearing the IgG spacer was efficacious, and we sought to determine whether altering the spacer would increase the CAR capacity. The hinge and CD8 spacer variants were inferior for both cytotoxicity and IFN- $\gamma$  production. The two optimal candidates were IgG and IgM spacers. Both spacer variants were efficacious in lysing low and medium density targets. The cytotoxicity discrepancies between the two variants were mostly

not significant. The IgG spacer was shown to have superior lytic capacity only against B16. Regarding the IgM spacer variant, we observed non-specific lysis of SupT1 NT cells, and high IFN- $\gamma$  concentration in the absence of the Tyrp1 antigen. In the physiological condition of T618A, IgG and IgM spacer variants produced 27-fold and 6-fold increase of IFN- $\gamma$  concentration. In conclusion, the IgG variant was superior to the IgM variant regarding IFN- $\gamma$  production. The IgG TA99-CAR was also more specific with lower background cytotoxicity and cytokine production. Therefore, the optimal candidate chosen for downstream use was the IgG variant.

### **4.3.3 *In vitro* Validation of the Murine TA99-CAR Efficacy**

Our aim was to test the efficacy of the TA99-CAR in a melanoma mouse model. We used splenocytes from C57BL/6 mice as effector T-cells. Since the T-cells were not derived from human cells, we engineered a murine TA99-CAR. Apart from the TA99 scFv that is humanised, the TA99-muCAR consisted of murine domains. We engineered the TA99-muCAR, in order to ascertain that the CAR would be functional in the context of the murine T-cells. Prior to carrying out the *in vivo* model, we sought to validate the cytotoxic capacity of the TA99-muCAR *in vitro*.

#### **4.3.3.1 Splenocyte Transduction Efficiency**

The C57BL/6 splenocytes were transduced with a control CAR (aEGFRvIII) and the TA99-muCAR. It is crucial to validate the T-cell product before setting-up a functional assay, in order to ascertain that the transgene is expressed in the effector T-cells. Therefore, the splenocytes were labelled and interrogated with flow cytometry for the expression of the CAR transgene.

Identifying the introduced T-cells in the mouse system at the end of an *in vivo* model is challenging, due to cell diversity. Labelling the muCAR with an anti-Fab antibody bears the risk of cross-reactivity with other antibodies of the multi-colour panel, and thus increase of the background noise. It is possible to label the muCAR with soluble Tyrp1-His supernatant. However, labelling the CAR with Tyrp1-His led to an underestimation of the transduction efficiency by 3-fold. For this reason, we incorporated the murine CD19 marker gene into the cassette, separated from the CAR with a 2A self-cleaving peptide. The marker gene was added to allow the reliable

identification of the CAR bearing cells in the mouse model. The CD19 single positive cells were B-cells, which are inherently positive for CD19. The cells that were double positive for CD19 and CD4, or CD19 and CD8 constituted the transduced T-cell population.

The transduction efficiency of the C57BL/6 splenocytes for CAR expression is shown in Figure 40. The transduction level of CD4 T-cells for the aEGFRvIII-muCAR and TA99-muCAR was 6.36% and 10.0%, respectively. The CAR levels of CD8 T-cells were 4.83% for the aEGFRvIII-muCAR, and 13.5% for the TA99-muCAR. The total transduction level for the control and the TA99-muCAR was 11.2% and 23.5%. Efficiently transducing splenocytes is more challenging than transducing PBMCs. We accommodate for this by accepting transduction efficiencies below 20%.

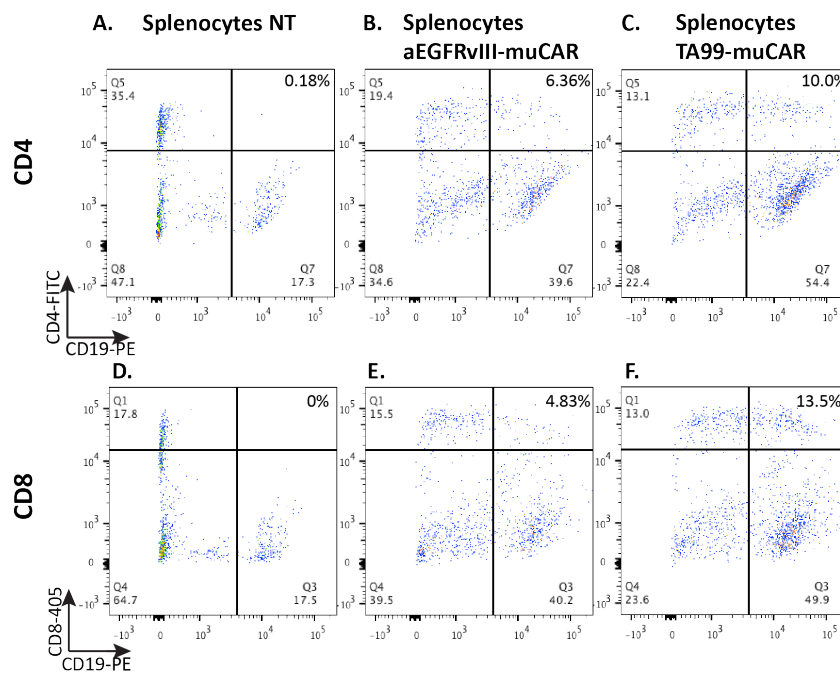


**Figure 40: Splenocyte muCAR expression levels.** The splenocytes transduced with aEGFRvIII-muCAR and TA99-muCAR were labelled along NT splenocytes for CAR expression. The Y-axis represents the CD4 or CD8 labelling, whereas the X-axis represents the labelling for the marker gene, CD19. The plots (A-C) show the labelling for CD4, and the plots (D-E) show the labelling for CD8. There was no background labelling in the NT cells (A,D). The CAR-expression level of CD4 positive cells was 6.36% for aEGFRvIII-muCAR, and 10.0% for TA99-muCAR (B-C). The expression level of the CD8 T-cell population was 4.83% and 13.5% for the aEGFRvIII-muCAR and TA99-muCAR, respectively.

#### 4.3.3.2 Cytotoxic Capacity of Murine TA99-CAR

Analogous to the  $^{51}\text{Cr}$  cytotoxicity assay we carried out for the validation of the human TA99-CAR, we carried a cytotoxicity experiment to validate the efficacy of the TA99-muCAR. However, the effector cells utilised in this experiment were transduced

murine splenocytes, instead of PBMCs. The splenocytes were transduced 24-hours after the isolation from the spleen of C57BL/6, and the  $^{51}\text{Cr}$  release was carried out on Day 5 after isolation. The targets used were SupT1 NT, or SupT1 expressing Tyrp1 Proximal and Trunc.

The cytotoxic capacity of the TA99-muCAR is illustrated in Figure 41. The background of both CAR T-cell cohorts was 9.1% (Figure 41.A). The cytotoxicity level of TA99-CAR T-cells against Proximal cells did not rise above the background, with a lysis of 11.9% target population (Figure 41.B). However, these T-cells exhibited cytotoxic capacity of 37.0% against the Trunc cells (Figure 41.C).

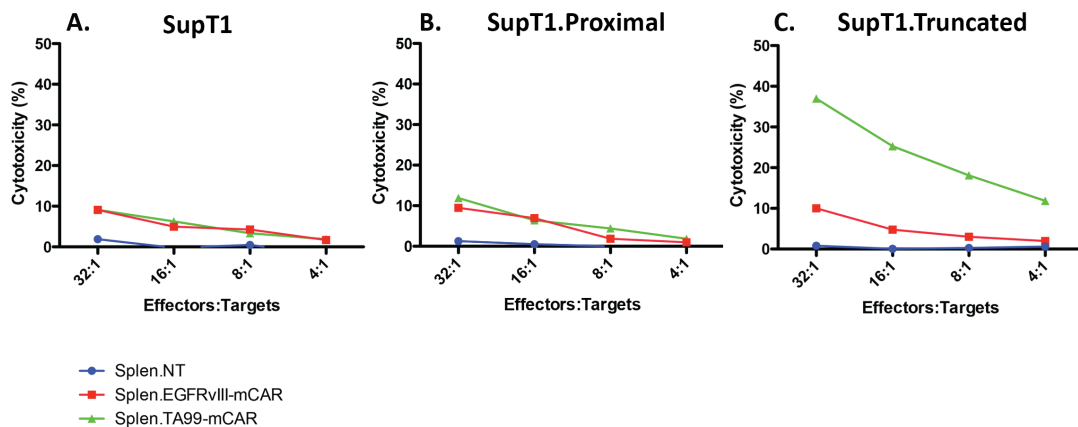


**Figure 41: Cytotoxic capacity of TA99-muCAR T-cells.** The targets used were SupT1 NT, SupT1 Proximal and Trunc cells. (A) The background cytotoxicity of both EGFRvIII-muCAR and TA99-muCAR was 9.1%. Graph (B) illustrates the cytotoxicity of splenocytes against SupT1 cells expressing Proximal. The cytotoxicity of TA99-muCAR T-cells against Proximal cells was not significantly increased over the background. (C) Finally, the lytic capacity of the TA99-muCAR T-cells against Trunc expressing cells was 37.0% of the target population.

#### 4.3.3.3 Conclusion

In conclusion, the TA99-muCAR was cytotoxic against the positive control target cells that express the Tyrp1 on the surface (37% lysis). The cytotoxic capacity of the TA99-muCAR met the efficacy criterion for its implementation in downstream *in vivo* melanoma models.

#### 4.3.4 B16 Melanoma Tumour Model

We have quantified the density of the surface Tyrp1 on B16 cells at 1844 epitopes/cell. However, the cytotoxic capacity of TA99-CAR T-cells against the B16 cell line has been modest (shown in 4.3.1.4). Patel and colleagues have reported that B16 cultured *in vitro* are negative for surface Tyrp1. However, B16 cells freshly

isolated from murine tissue showed an increase in surface Tyrp1 levels by 3-orders of magnitude. They compared the capacity of the TA99 to induce antibody-dependent cell-mediated cytotoxicity against cultured or freshly-isolated B16 cells. The cytotoxicity increased from 10% to 90% for cultured or freshly isolated B16 cells, respectively (Patel et al., 2008). Although, Patel and colleagues did not detect surface Tyrp1 on the cultured B16 cells, that could have been an artefact of lower detection level of flow cytometry. Nevertheless, there was a significant increase of the Tyrp1 density on B16 cells freshly isolated from the mouse microenvironment. Hence, we deemed worthwhile to carry out a mouse model, in order to determine whether the density augmentation would be sufficient to elicit a TA99-muCAR mediated tumour eradication.

#### **4.3.4.1 Experimental Set up for *In Vivo* Model**

The experiment outline is shown in Figure 42. The melanoma cell line used was B16-F2 on syngeneic C57BL/6. There were five mice in each group. On day 0, the mice were injected with  $10^5$  cells B16-F2 cells intradermally. On day 2, we culled five control mice, in order to isolate splenocytes. The splenocytes were activated with  $2\mu\text{g/ml}$  ConA and  $1\text{ng/ml}$  IL-7, and 24-hours later the splenocytes were transduced in the absence of IL2. The T-cells were transduced with the TA99-muCAR or a non-specific muCAR (aEGFRvIII). The day after the transduction we administered  $100\text{U/ml}$  IL2 to the cells, and harvested them after 48 hours.

Seven days after the B16 cell administration, the mice received 5Gy whole body irradiation. Approximately 4-hours post-irradiation, the mice were intravenously inoculated with the CAR T-cells. The amount of T-cells administrated was calculated to a dose of  $5 \times 10^6$  CD8 transduced cells. CAR T-cell engraftment was tested in mouse blood samples 7-days post T-cell injection. The tumour sizes were measured three times per week, and when the tumour volumes exceeded the allowed size the mice were culled. On day 23, the experiment was terminated.

### Animal Model Set Up

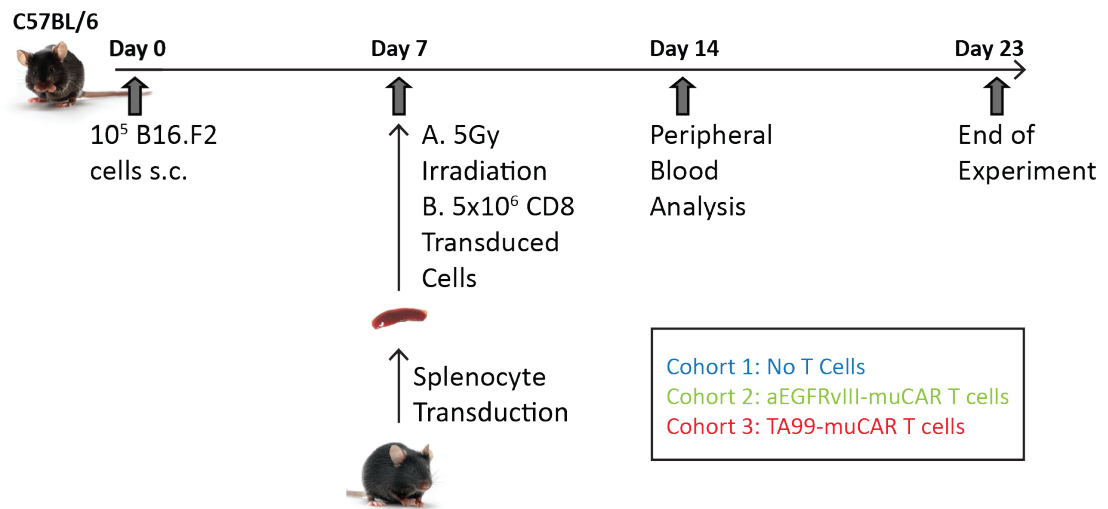


**Figure 42: B16 *in vivo* melanoma model outline.** Induced B16 melanoma tumours in C57BL/6 mice. On day 0, we injected  $10^5$  B16 cells intradermally to 8-week old C57BL/6 mice. On day 7, we administered  $5 \times 10^6$  CD8 transduced T-cells. On day 14, the mice were bled, in order to test for T-cell engraftment in the blood sample. On day 23, the experiment was ended. The tumours were measured every 2-3 days, and tumour volumes were monitored in order to prevent the tumour size exceeding the allowed threshold.

#### 4.3.4.2 Transduction Efficiency of CAR-Bearing Splenocytes

Before the CAR T-cell administration, we determined the T-cell transduction efficiency. The cells were labelled for CD4, CD8, and CD19, which is the CAR transgene marker gene. The CAR expression levels of the transduced splenocytes are illustrated in Figure 43. The splenocytes are not a pure T-cell population. B-cells are also present in the isolated population, the CD19 single positive cells represented the B-cell population. The double positive cells for CD4/CD8 and CD19 marker gene were the transduced T-cell population. The CAR expression levels of CD4 T-cells were 7.65% for the aEGFRvIII-muCAR, and 10.1% for the TA99-muCAR (Figure 43.B-C). Similarly, the aEGFRvIII-muCAR and TA99-muCAR were expressed at 23.3% and 20.1% in the CD8 T-cell population (Figure 43.E-F).

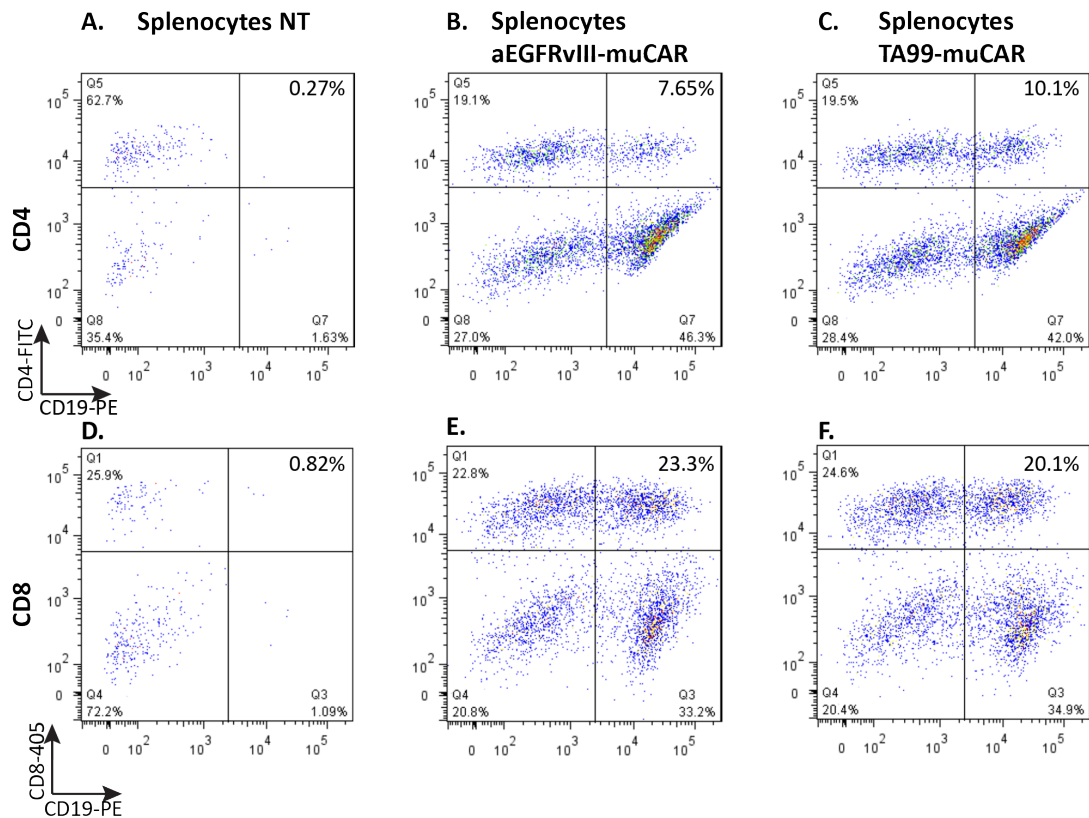


**Figure 43: CAR expression level in transduced splenocytes.** The CD4 signal is shown on the Y-axis of the panels (A-C), and the CD8 signal is shown in panels (D-F). The signal for the marker gene CD19 is shown in the X-axis. The double positive population constitutes the cohort of transduced T-cells. The transduction efficiency was 7.65% for CD4 aEGFRvIII-muCAR cells (B), and 10.1% for CD4 TA99-muCAR T-cells (C). The transduction of aEGFRvIII-muCAR CD8 T-cells was 23.3% (E), and TA99-muCAR 20.1% (F).

#### 4.3.4.3 CAR T-cell Engraftment

Seven days after CAR T-cell administration, a blood sample was acquired in order to test for T-cell engraftment. We calculated the concentration of transduced CD8<sup>+</sup>/CD4<sup>+</sup> per  $\mu$ l of blood. The CAR T-cell blood concentration is shown in Figure 44. The average concentration of the aEGFRvIII-muCAR cells was 14.2 cells/  $\mu$ l of blood, in comparison to the concentration of TA99-muCAR T-cells that engrafted at a concentration of 49.2 cells/  $\mu$ l of blood. The concentration disparity between control CAR and TA99-muCAR T-cells was statistically significant.



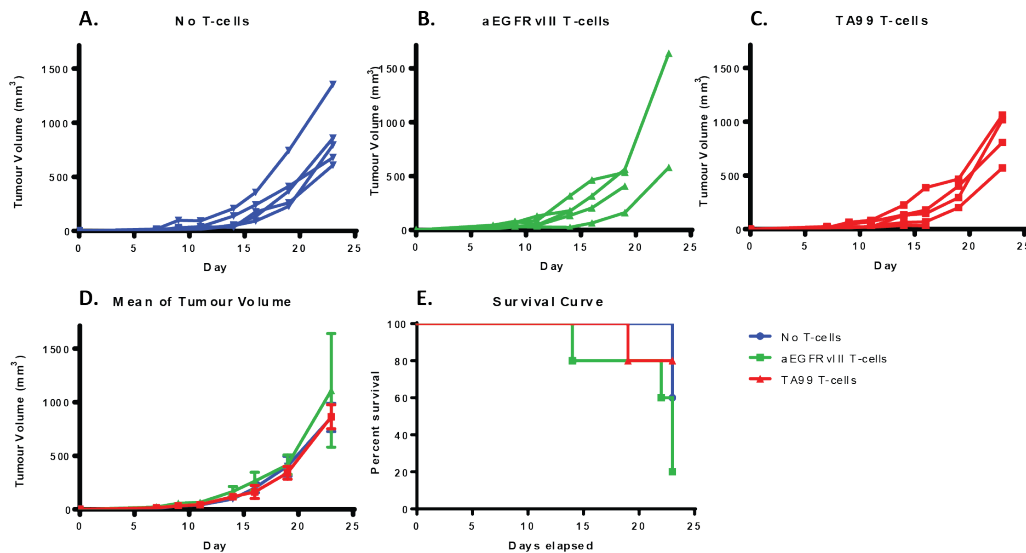


**Figure 45: Tumour volume and survival of B16 melanoma tumour mice treated with CAR-transduced splenocytes.** The three cohorts consisted of No T-cells, aEGFRvIII-muCAR, and TA99-muCAR. The tumour volumes were measured in three dimensions (length, width, height), and expressed in mm<sup>3</sup>. The three cohorts are demonstrated in different colours; No T-cells (Blue), aEGFRvIII-muCAR T-cells (green), TA99-muCAR T-cells (red). The tumour volume of each cohort is shown in graphs (A-C). The average tumour volume of each cohort is summarised in graph (D), which was 857.9mm<sup>3</sup>, 1110.5mm<sup>3</sup>, and 864.0mm<sup>3</sup> for the cohorts No T-cells, aEGFRvIII-muCAR, TA99-muCAR, respectively. The tumours progressed regardless of the therapeutic regimen administered. Finally, the survival curve for the mice in the three cohorts is shown in (E).

The experiment was ended on day 23, and no efficacy was observed for the TA99-muCAR in the mouse B16 melanoma treatment. Three mice from the control cohort, four from the aEGFRvIII-CAR cohort, and one mouse for the TA99-CAR cohort had been already culled due to large tumour volume. The remaining mice were culled on day 23, and LN and tumours were processed. Cells isolated from the tissue were interrogated for the presence of CD4, CD8, and CD19.

Transduced cells did not engraft in the lymph nodes, regardless of CD4 or CD8 status (data not shown). There were no transduced CD4 cells in the tumour compartment either. However, CD8<sup>+</sup>CD19<sup>+</sup> T-cells were detected in the tumours of mice inoculated with TA99-muCAR (Figure 46). CD8 is displayed on the Y-axis and CD19 on the X-axis. Cells that are CD19<sup>+</sup> single were B-cells, whereas the cells of interest were the double positive for CD8<sup>+</sup>CD19<sup>+</sup>. The cohort of mice that received no T-cells constituted the negative control (Figure 46.A-B). The two cohorts that were inoculated with T-cells bore a double positive population. The cohort of mice inoculated with aEGFRvIII-muCAR T-cells showed an engraftment of 0.11% (Figure 46.C). The cohort of TA99-muCAR T-cells was comprised of four mice (Figure 46.D-G), with engraftment within

the range of 0.07-0.25%. The tumour engraftment is limited in both CAR T-cell cohorts.

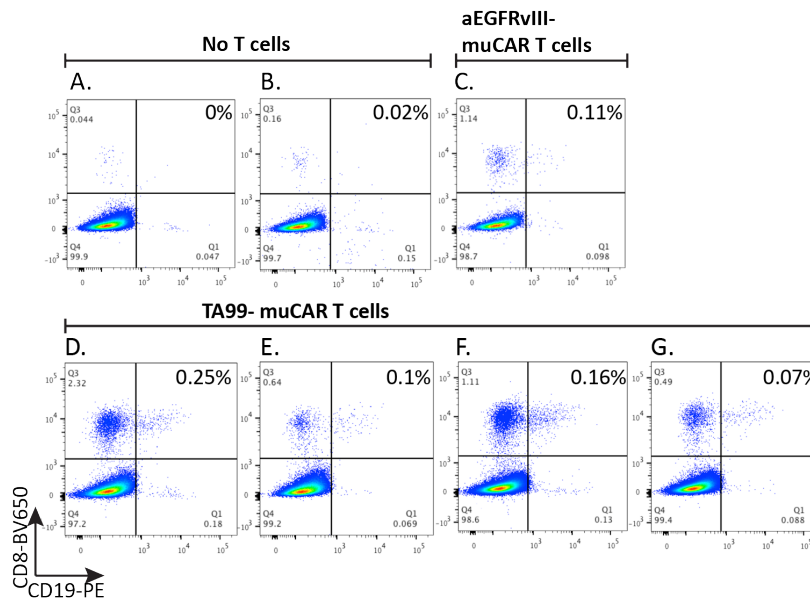


**Figure 46: CD8<sup>+</sup> CAR T-cell tumour infiltrating lymphocytes.** Seven mice remained at the end of the experiment. Control cohort: 2 mice (A-B); aEGFRvIII-muCAR cohort: 1 mouse (C); TA99-muCAR cohort: 4 mice (D-G). The plots above contain data from the tumour site, and the cells displayed were alive and single cells. CD8 is on the Y-axis and CD19 on the X-axis. CD19 was the marker gene on the muCAR construct. The CD19<sup>+</sup> single positive cells were B-cells, and the double positive cells are the transduced T-cells bearing the CAR and the marker gene. The CD8<sup>+</sup>CD19<sup>+</sup> aEGFRvIII-muCAR account for 0.11% (C). The range of the TA99-muCAR infiltration percentage is 0.07-0.25% (D-F).

To gain an insight regarding the inability of TA99-muCAR T-cells to eradicate the B16-melanoma tumours, we interrogated the transduced CD8<sup>+</sup> cells for granzyme B expression. Granzyme B is a protease residing in the lytic granules of cytotoxic T-cells, which induces DNA fragmentation and apoptosis in the target cells (Heusel et al., 1994). Therefore, we used granzyme B labelling as an indicator of T-cell cytotoxic capacity (Curtsinger et al., 2005).

The profile of CAR T-cell expression for granzyme B is shown in Figure 47. The cells interrogated for the presence of granzyme B are all CD8<sup>+</sup>. The marker gene signal of CD19 is shown on the Y-axis, and the X-axis is occupied by the granzyme B signal. For the mouse that were inoculated with aEGFRvIII-muCAR T-cells, 8.59% of the CD8<sup>+</sup> population were transduced T-cells negative for granzyme B. Only 3.58% CAR T-cells were positive for granzyme B expression (Figure 47.C). Of the CD8 positive cells residing within the tumour of the TA99-muCAR cohort, 13.9-17.4% are granzyme B CAR T-cells. There are 9 to 17-fold less granzyme B positive TA99-muCAR T-cells than

the granzyme B negative cells (Figure 47.D-G). The reason why the majority of CAR T-cells are granzyme B negative is unknown. Nevertheless, the lack of granzyme B might constitute the cause for the lack of tumour eradication by TA99-muCAR T-cells.

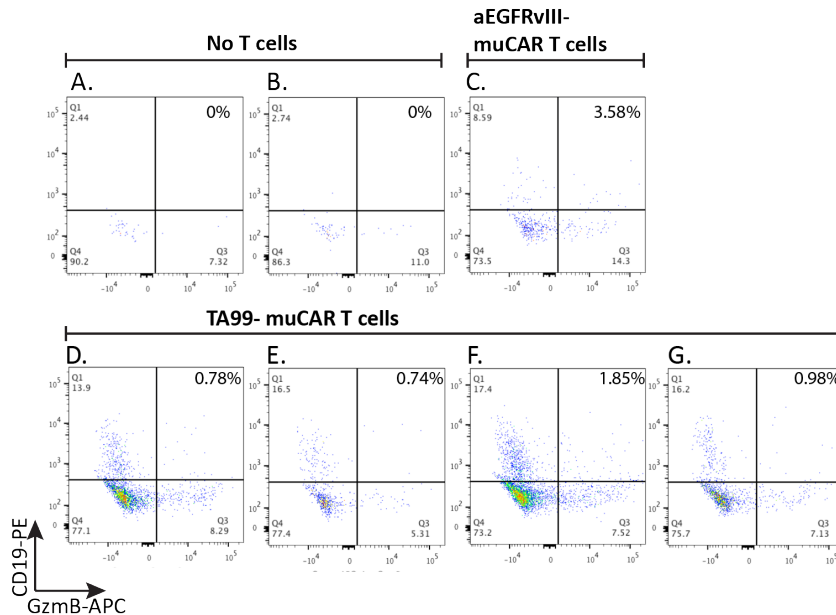


**Figure 47: Granzyme B expression in CD8<sup>+</sup> CAR T-cells.** The cells in all graphs were gated for CD8 expression. CD19 is shown on the Y-axis and granzyme B on the X-axis. (C) In the aEGFRvIII-muCAR T-cell population, 8.59% were CAR T-cells negative for granzyme B, and 3.58% positive. In the TA99-muCAR T-cell cohort, the range of CAR T-cells negative and positive for granzyme B was 13.9-17.4%, and 0.74-1.85%, respectively (D-G).

#### 4.3.4.5 Conclusion

The murine TA99-CAR was shown to be functional *in vitro* against the SupT1 cell line expressing Trunc Tyrp1. Although the TA99-muCAR was not tested against B16 *in vitro*, the human TA99-CAR showed limited cytotoxicity against the B16 cell lines in the <sup>51</sup>Cr release assay. We indicated that this was due to low antigen density (Figure 34). Published data showed that the presence of Tyrp1 on the plasma surface is 1000-fold higher in freshly isolated murine cells than in cultured cells (Patel et al., 2008). We thus used the B16 melanoma model despite the limited B16 cell lysis *in vitro*. Nevertheless, the TA99-muCAR failed to eradicate, or stop the tumour progression of B16 melanoma *in vivo*. The average engraftment of CAR T-cells in the tumour site was 0.15% of the cells present in the tumour site. The majority of the infiltrating CAR T-cells was negative for granzyme B. This may be the reason why the TA99-CAR T-cells failed to eradicate the tumour.

### 4.3.5 B16 Transduced with Tyrp1 for Tumour Model

The TA99-muCAR T-cells failed to eradicate the melanoma tumours. In order to address whether the lack of response was due to the low antigen density, we developed an animal model with B16 expressing Trunc Tyrp1. The B16\_Trunc cell tumour cells facilitated as a positive control to increase the Tyrp1 density on the cell surface.

#### 4.3.5.1 Experimental Set up for *In Vivo* Model

The experiment set-up of the *in vivo* model was similar to the one described in 4.3.4.1. The outline for the B16 Trunc mouse model is illustrated in Figure 48. In this model the melanoma tumours were induced by either B16 or B16 Trunc cell inoculation. There were four cohorts, each consisting of four mice. There were two cohorts inoculated with B16 cells. One of the B16 melanoma tumour cohorts was injected with TA99-muCAR T-cells. Likewise, two cohorts of mice were inoculated B16\_Trunc cells. One received no T-cells, and the other received TA99-muCAR T-cells. The experiment was ended at day 24.

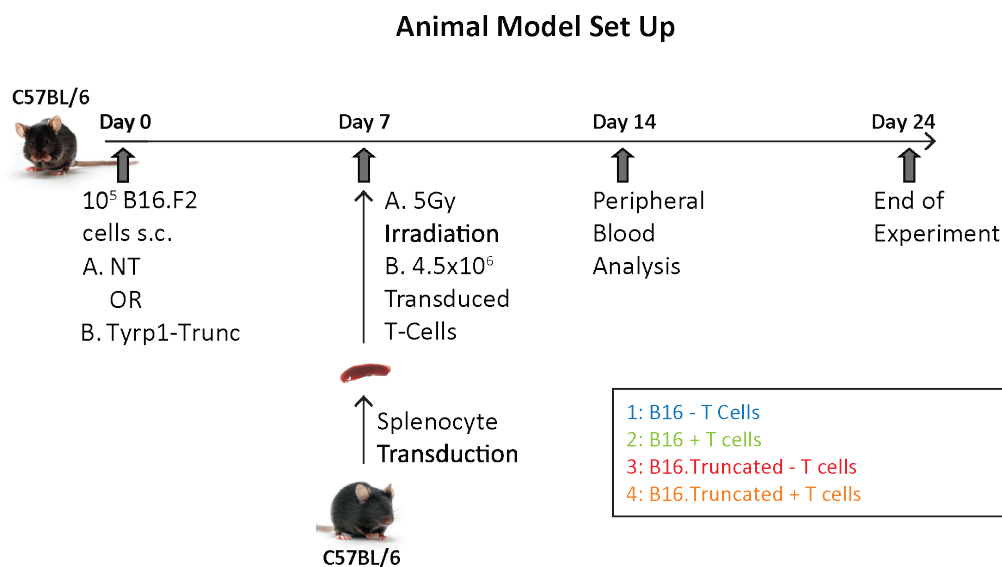


**Figure 48: Outline for B16 Trunc *in vivo* melanoma model.** On day 0, the mice were intradermally inoculated with  $10^5$  of either B16 or B16 Trunc cells. On day 2 we culled five control mice, in order to isolate splenocytes. The T-cells were transduced with the TA99-muCAR, and administered to mice at day 7 at a dose of  $4.5 \times 10^6$  transduced T-cells per mouse. The four cohorts of mice were: 1) B16 tumours with no T-cell dose, 2) B16 melanoma tumour mice inoculated with TA99-muCAR T-cells, 3) B16 Trunc melanoma tumours with no T-cell dose, 4) administration of TA99-muCAR T-cells to mice bearing B16 Trunc melanoma tumours. The experiment was terminated at day 24.

### 4.3.5.2 Transduction Efficiency of CAR-Bearing Splenocytes

The T-cell dose was calculated based on the transduction level of the T-cell population. In order to perform this calculation, the T-cells were labelled for the expression of the CAR transgene. The labelling panel comprised CD4, CD8, and the CD19 marker gene. The transduction efficiency is shown in Figure 49. The double positive  $CD4^+CD19^+$  or  $CD8^+CD19^+$  cells constitute the transduced population. The percentage of CD4 T-cells expressing the CAR transgene is 4.51% (Figure 49.B). Similarly, 7.09% of the cell population is double positive for  $CD8^+CD19^+$  (Figure 49.D). Although the total CAR T-cell expression level is just 11.6%, we proceeded with the T-cell administration since the dose is based solely on the transduced population.

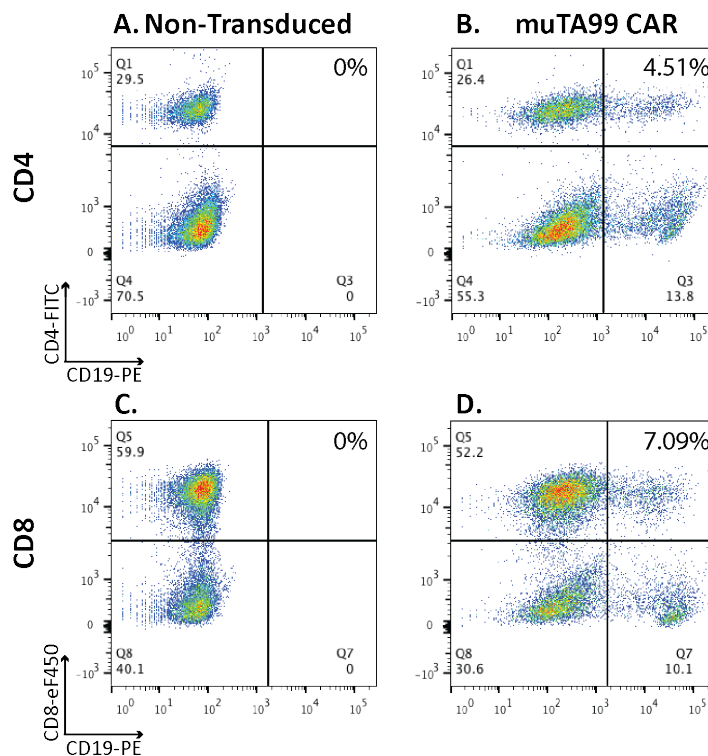


**Figure 49: TA99-muCAR expression level in transduced splenocytes.** The CD4 signal is shown on the Y-axis of the panels (A-B), and the CD8 signal is shown in panels (C-D). The signal for the transduction marker gene CD19 is shown in the X-axis. The transduced T-cells are double positive for CD19 and CD4/CD8. The transduction efficiency was 4.51 for CD4 TA99-muCAR cells (B), and 7.09% for CD8 TA99-muCAR T-cells (D). The total percentage of CAR-bearing T-cells is 11.6%.

### 4.3.5.3 CAR-T-cell Engraftment

In total  $4.5 \times 10^6$  CAR T-cells were administered to the mice bearing B16 NT or Trunc tumours. A week after the T-cell administration, we investigated the presence of CAR T-cells in the circulating blood of treated mice. The concentration of CAR T-cells per  $\mu\text{l}$  of blood is not feasible due to experimental error. Nevertheless, the percentage of

CAR bearing T-cells is shown in Figure 50. The percentage of CD4 T-cell engraftment is 0.47% and 0.64% in mice bearing B16 or B16 Trunc tumours, respectively (Figure 50.A). The engraftment of CD8 CAR T-cells was superior in B16 Trunc mice with a percentage of 0.44% versus 0.19% of B16-tumour bearing mice (Figure 50.B).

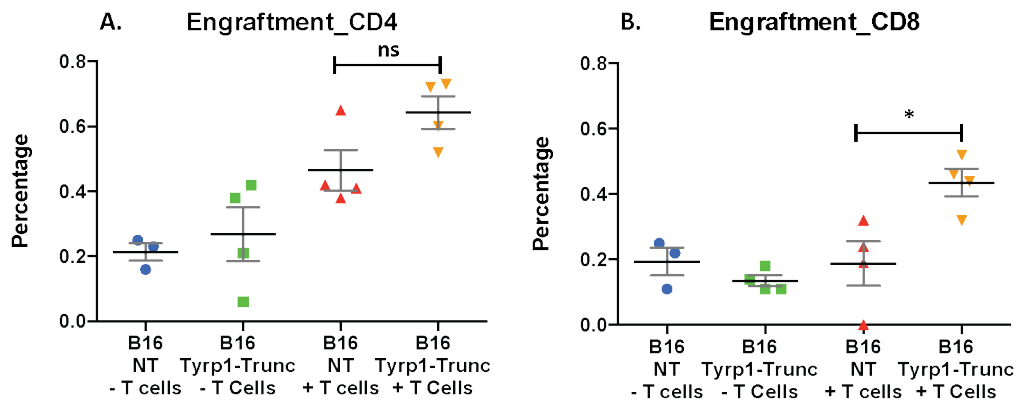


**Figure 50: CD4 and CD8 CAR-bearing T-cells in the circulating blood of B16 melanoma mouse model animals.** The blood sample was acquired seven days after the administration of the T-cells. **(A)** The engraftment of CD4 CAR T-cells was 0.47% and 0.64% in mice bearing B16 and B16 Trunc tumours, respectively. **(B)** The percentage of CD8 CAR T-cells was 0.19% for mice bearing B16 tumours, and 0.44% for mice bearing B16 Trunc tumours. The discrepancy in the engraftment of CD8 CAR T-cells between the B16 NT and Trunc cohorts was statistically significant ( $p=0.0122$ ). The statistical significance was calculated with a one-way Anova in GraphPad Prism.

#### 4.3.5.4 *In Vivo* Mouse Model Tumour Volumes

The tumour volumes for each cohort were measured and calculated every two days. The tumour size measurements, as well as the survival curve of the mice are shown in Figure 51. The graphs A-D demonstrate the volume of each individual tumour per cohort. The average tumour size of each cohort has also been calculated. The average volume for the B16 melanoma mice was  $317.5\text{mm}^3$  and  $360.5\text{mm}^3$  for the cohorts of no T-cells or TA99-muCAR T-cells respectively (Figure 51.E). In mice bearing the B16 Trunc melanomas, the volume for the no T-cells was  $353.8\text{mm}^3$ , and for the CAR T-cell cohort  $650.0\text{mm}^3$ . The latter cohort appears to have a higher average tumour volume, which is an artefact due to the survival of all four mice at the end point (Figure 51.F). In the remaining three cohorts, mice bearing the largest tumours had been culled at earlier time-points. Nevertheless, the TA99-muCAR had no measurable effect against B16 NT or Trunc tumours.

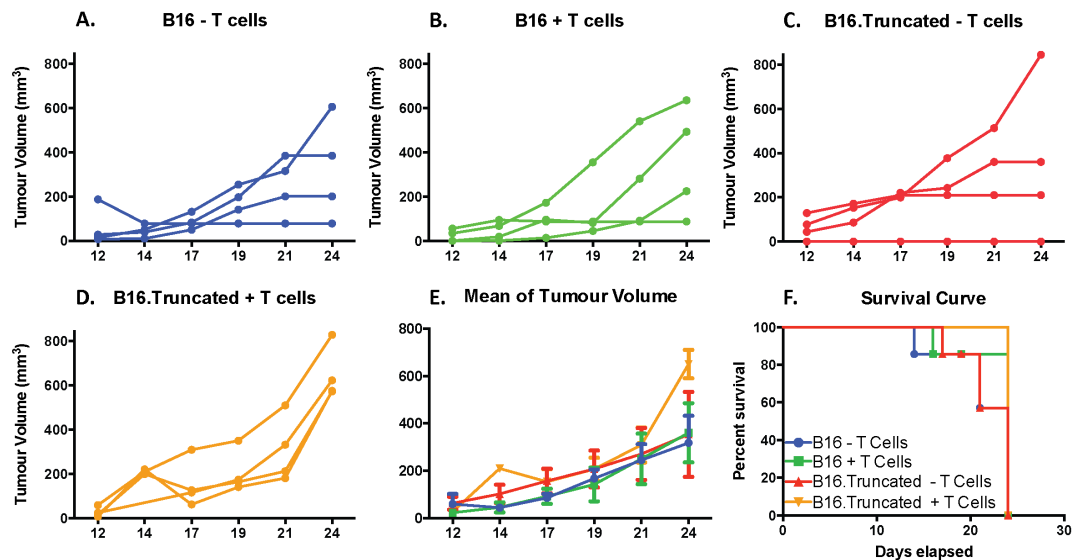


**Figure 51: Tumour volume and survival curve for the B16 Trunc *in vivo* mouse model.** The four cohorts consisted of mice inoculated with B16 NT or Trunc tumour cells, and subsequently injected with TA99-muCAR T-cells or no T-cells. The tumour volume of individual mice within each cohort is shown in graphs (A-D). The average tumour volume of each cohort is summarised in graph (E), which was 317.5mm<sup>3</sup>, 360.5mm<sup>3</sup>, 353.8 mm<sup>3</sup>, and 650.0 mm<sup>3</sup> for the respective cohorts. The tumour progression was uninterrupted despite the administration of TA99-muCAR T-cells to mice bearing B16 NT or Trunc tumours. The survival curve for the mice in the three cohorts is shown in (F).

The experiment was terminated at day 24. In order to determine the engraftment of the CAR T-cells, the cell composition of the LN and tumour compartments were analysed. CAR T-cells failed to engraft in the LN compartment (data not shown). Figure 52 demonstrates the engraftment results for CD8 T-cells in the tumour microenvironment. The CD8 signal is shown in the Y-axis, and the CD19 of the X-axis. The plots A-B represent the two surviving mice of the cohort inoculated with B16 tumour cells and not treated with CAR T-cells. Similarly, the plot F represents the data from the surviving mouse of the B16 Trunc tumour cohort, which did not receive CAR T-cells either. In the cohort of B16 tumour model mice injected with CAR T-cells three mice survived to day 24. There were no CAR T-cells engrafted at the tumour site (Figure 52.C-E). Interestingly, no host CD8 T-cells were present either, leading us to the conclusion that there was no T-cell infiltration. Among the four mice of the B16 Trunc model injected with CAR T-cells cohort, only one mouse had 2.06% CAR T-cells present at the tumour site (Figure 52.H). However, the cell number acquired for this condition is limited, thus the obtained result might be skewed. There was no T-cell infiltration observed in the other three mice (Figure 52.G,I,J). Similarly, CD4 CAR T-cells failed to infiltrate and engraft at the tumour site (data not shown). The lack of

T-cell infiltration to the tumour is the most likely reason why tumour eradication did not occur.

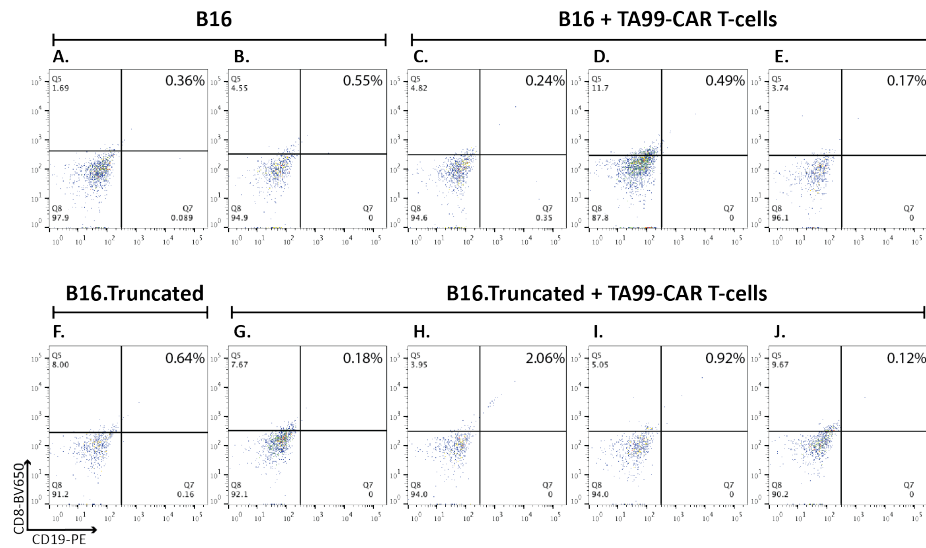


**Figure 52: CD8 CAR T-cell tumour infiltrating lymphocytes in tumour microenvironment.** The plots demonstrate data from individual mice for each cohort: 1) one cohort was inoculated with B16 tumour cells, but received no T-cell treatment; 2) the second cohort received B16 tumour cells and TA99- CAR T-cell treatment; 3) the third cohort of mice was inoculated with B16 cells transduced with Trunc, but received no T-cells; 4) the fourth cohort of mice was also inoculated with Tyr-1-Trunc expressing B16 cells, and was subsequently injected with TA99-CAR T-cells. CD8 signal is shown on the Y-axis, and CD19 on the X-axis. The two surviving mice in cohort 1 are shown in (A) and (B), and only one mouse was remaining cohort 3 (F). Mice of cohorts 2 and 4 received TA99-muCAR T-cells. There are no double positive cells observed in cohort 2 (C-E). Only one mouse of cohort 4 showed infiltration of transduced T-cells (2.06%) (H). The remaining three mice of cohort 4 showed no evidence of CAR T-cell infiltration (G,I,J).

#### 4.3.5.5 Conclusion

The B16 Trunc cells were used in order to induce a melanoma tumour with higher antigen density than B16 tumours. However, the TA99-muCAR T-cell still failed to eradicate the B16 Trunc tumour. Additionally, the T-cells did not engraft to the tumour microenvironment. Hence, the lack of tumour eradication by the CAR T-cells was not due to low antigen density.

#### 4.4 DISCUSSION

The majority of clinical trials using CARs as a therapeutic regimen have been against haematological malignancies (Brentjens et al., 2013)(Davila et al., 2014)(Grupp et al., 2015)(Brentjens et al., 2010)(Porter et al., 2011). The field has recently started expanding towards treatment of melanoma tumours. The antigens that are being targeted with CARs in melanoma include melanoma markers, such as the Melanoma-Associated Chondroitin Sulphate Proteoglycan (MCSP) (Beard et al., 2014)(Krug et al., 2015)(Uslu et al., 2016). MCSP is expressed on the surface of approximately 85% of malignant melanomas (de Bruyn et al., 2010). A CAR targeting GD2 has also been engineered for melanoma treatment (Gargett et al., 2016). The anti-GD2 CAR is to this date the only CAR employed for melanoma treatment undergoing a clinical trial (NCT02107963).

TA99-CAR is the first CAR described to target an intracellular antigen. Melanosomal proteins, such as Tyrp1 and Pmel-17 TCRs have been used as targets in treatment of B16-melanoma bearing mice (Abad et al., 2008)(Xie et al., 2010). However, TA99-CAR combined the advantages of the CARs, for example the lack of HLA-restriction. At the same time, TA99-CAR may overcome the main hurdle of the CAR field, which is the limitation to surface antigens.

First, we demonstrated that the TA99-CAR is cytotoxic against the Trunc expressing SupT1 cell line, which constitutes the positive control for Tyrp1 surface expression. Cytotoxicity was also observed against the melanoma cell line T618A (18.7%). The cytokine production was a more sensitive read-out. TA99-CAR produced IFN- $\gamma$  against the SupT1 Trunc (6452pg/ml) and T618A (2906.4pg /ml), as well as SupT1-WT and B16 cells (1325.7pg/ml, 361.5pg/ml).

The modular design of CAR structure allows for case-specific adjustments to achieve best functionality. The optimal spacer choice depends on the antigen targeted by the CAR. The relationship between the length of the CAR spacer and the antigen distance from the membrane is inverse and aims to maintain the dimensions of the TCR immune synapse (Guest et al., 2005). The exact location of the Tyrp1 epitope recognised by TA99 is unknown, therefore we investigated which is the optimal

spacer for the TA99-CAR. There were four different sized spacers tested in total. The hinge and CD8 spacer led to decreased capacity for cytotoxicity and IFN- $\gamma$  production. The IgG and IgM spacers led to cytotoxicity against SupT1 Tyrp1-WT and T618A. However, the IgM CAR indiscriminately eliminated 11% of the SupT1 NT cells. It also led to high background IFN- $\gamma$  production (906.7pg/ml). In the presence of the physiological target T618A, the IgG spacer variant produced 27-fold higher IFN- $\gamma$  (5752.4pg/ml) concentration than the baseline. On the contrary, the IgM variant showed a 6-fold increase (5600.0pg/ml). The IgG1 spacer appears to be the optimal spacer for the TA99-CAR.

During the TA99-CAR validation, we observed that the antigen threshold was higher for cytotoxicity than it was for IFN- $\gamma$  production. However, the opposite pattern was observed during spacer optimisation. The discrepancy between the two sets of experiments is the ratio of CD8/CD4 T-cells. The CD8/CD4 ratio during the spacer optimisation experiments was approximately 0.5. However, the ratio of CD8/CD4 T-cells was inconsistent between donors for the CAR validation experiments. Watanabe and colleagues demonstrated that the antigen threshold for CD8 T-cells CAR cytotoxicity was 240 epitopes/cell, and for cytokine production it was 5320 epitopes/cell (Watanabe et al., 2015). Our results, are contradictory to this study, as we observed lower threshold for cytokine production when the ratio was skewed towards CD8 cells.

Another difference between those two sets of experiments was the transduction efficiency. The average transduction efficiency for the CAR validation study was <50%, whereas the percentage of transduction for the spacer optimisation study was 30-40%. This led to disparity in the absolute number of transduced T-cells added in those experiments.

The TA99-muCAR was validated *in vitro*. Nevertheless, TA99-muCAR T-cells also failed to elicit a response in the high antigen density model. The CAR T-cells either failed to engraft or engrafted but did not express granzyme B. The B16 melanoma model has not been used for CAR validation, hence the optimal cell dose and conditions are undetermined.

Anti-Tyrp1 or anti-Pmel-17 TCR T-cells successfully eradicate subcutaneous B16 melanoma tumours (Abad et al., 2008)(Xie et al., 2010). However, the cell dose is substantially different. Abad and colleagues administered  $10^7$  CD8 T-cells, whereas Xie and colleagues administered  $5 \times 10^5$  CD4 T-cells. The major difference is the administration of IL2, which is widely used in adoptive T-cell therapy mouse models (Abad et al., 2008)(Quatromoni et al., 2011)(Quatromoni et al., 2012). B16 originated as a spontaneous mouse melanoma, and hence is poorly immunogenic (Celik et al., 1983). Additionally, B16 cells express high levels of PD-L1 and PD-1 (Pilon-Thomas et al., 2010)(Kleffel et al., 2015), which restrict the T-cell function. The lack of T-cell response against B16 in our model could be caused by a combination of unfavourable conditions, such as PD-L1 T-cell inhibition and lack of IL-2 administration.

According to Hara and colleagues, the TA99 antibody successfully eradicated B16 melanoma tumours (Hara et al., 1995), in contrast to TA99 CAR T-cells. This is probably due to fundamental differences in the animal models, as well as limited transduction and expansion of our TA99 CAR T-cells. The TA99 antibody successfully eradicated B16 tumour metastases when injected concomitantly or two days after the B16 tumour inoculation. A four-sever day delay in TA99 antibody administration increased the number of lung metastases by approximately 4-5 fold, suggesting that the TA99 antibody has a prophylactic role, but its efficacy is significantly reduced when challenged with established tumours.

## **CHAPTER 5: Results**

### **Manipulating the Affinity of the TA99- CAR to Increase Sensitivity**

## CHAPTER 5: RESULTS: MANIPULATING THE AFFINITY OF THE TA99-CAR TO INCREASE SENSITIVITY

### 5.1 INTRODUCTION

#### 5.1.1 Relation of CAR Affinity to Density Sensitivity

The TA99 CAR was shown to be efficacious against high and medium antigen density targets (4.3.1). However, the density of Tyrp1 on the cell surface of melanoma cells is heterogeneous and low. In order to increase the CAR sensitivity, we manipulated the binding affinity of TA99 for Tyrp1.

In TCR studies it was shown that the increase of the affinity above the 1-100 $\mu$ M physiological range hindered its sensitivity against low density targets (Matsui et al., 1994)(González et al., 2005)(Thomas et al., 2011). According to the serial triggering model, one antigen can trigger up to 200 TCRs, due to the fast dissociation rate of TCRs from the antigen (Valitutti et al., 1995). However, increase in affinity can impede serial triggering. Consequently, the loss of serial triggering is speculated to cause the decrease in the sensitivity of high affinity TCRs (Thomas et al., 2011).

However, the kinetic properties of CARs are different to the TCR, having higher affinity and slower dissociate rate, as discussed in chapter 1.8 (Poulsen et al., 2011)(Matsui et al., 1994). The effect of affinity on the CAR sensitivity has been a controversial subject. Despite the reverse correlation between TCR sensitivity and affinity, the majority of the CAR studies support that high affinity results in superior CAR sensitivity (Chames et al., 2002)(Chmielewski et al., 2004)(Hudecek et al., 2013)(Caruso et al., 2015)(Liu et al., 2015)(Lynn et al., 2016). Only Turatti and colleagues reported that low affinity CARs were superior against low density targets (Turatti et al., 2007).

The investigation of CAR affinity-efficacy correlation has not been exhaustive. The lack of data on the CAR scFv stability constitutes a caveat in the research to date, since the stability could be a confounding factor. There are also inconsistencies between the studies, which render the interpretation of the results difficult. Such inconsistencies are the diversity in functional read-outs and time-points, and the affinity-range disparities between studies. Hence, a thorough study on the

correlation between CAR efficacy and affinity is necessary. We aimed to obtain TA99-CAR variants with a wide range of affinity towards Tyrp1, and test their efficacy and sensitivity.

### 5.1.2 Differentiation and Exhaustion Markers in T-Cells

Apart from characterising the CAR cytotoxic and cytokine-secretion capacity, the TA99-CAR constructs were also tested for differences in their differentiation or exhaustion status. The differentiation panel includes the markers: Cluster of Differentiation (CD)95, CD45RA, and C-C chemokine receptor 7 (CCR7). The four differentiation stages of T-cells are naïve (Tnaive), stem-cell memory (Tscm), central memory (Tcm), and effector memory (Tem).

The discrimination between Tnaive and Tscm is facilitated by the expression of CD95. CD95 is a member of the TNFR family, which mediates cell apoptosis upon ligand engagement (Krammer, 2000). Tscm express high levels of CD95, in contrast to Tnaive that are CD95<sup>-</sup> (Gattinoni et al., 2011).

The CD45 marker (discussed in 1.7.3) is a phosphatase that inhibits T-cells signalling, and exists in CD45RA or CD45RO isoforms (Beverley, 1992). CD45RA is expressed on the naïve subset of T-cells, whereas CD45RO is expressed on the subset of memory T-cells that exhibit effector functions (Michie et al., 1992).

The chemokine receptor CCR7 mediates the homing of T-cells to the peripheral lymphoid organs, such as the lymph nodes. The Tcm, which are CCR7<sup>+</sup>, do not bear immediate effector function, but can differentiate to CCR7<sup>-</sup> cells upon secondary antigen stimulation. On the contrary, the CCR7<sup>-</sup> Tem cells migrate to infected tissues and bear immediate effector function (Sallusto et al., 1999). The summary of the marker pattern to evaluate the differentiation profile is shown in Table 21.

**Table 21: Expression pattern of differentiation markers.**

Marker	Tnaive	Tscm	Tcm	Tem
CD95	-	+	+	+
CD45RA	+	+	-	-
CCR7	+	+	+	-

Exhaustion describes dysfunctional T-cells, which have lost the capacity for cytotoxicity and cytokine secretion after antigen stimulation. It was first detected in mice with chronic lymphocytic choriomeningitis virus infection (Zajac et al., 1998). Exhaustion has been reported in a wide variety of situations, such as chronic infections and cancer (Virgin et al., 2009)(Fourcade et al., 2010). PD-1, which is an inhibitory T-cell receptor, is expressed on T-cells exhausted in HIV infection or cancer (Day et al., 2006)(Gehring et al., 2009)(Ahmadzadeh et al., 2009)(Mumprecht et al., 2009).

Another exhaustion marker identified in HIV and cancer patients is the T-cell Immunoglobulin Mucin 3 (Tim3), which causes T-cell apoptosis upon ligand interaction (Jones et al., 2008). PD-1 and Tim3 can be co-expressed on exhausted T-cells, and the double positive phenotype reflects a more severe exhaustion and dysfunction (Fourcade et al., 2010). Both PD-1 and Tim3 pathways must be reversed in order to restore T-cell function (Sakuishi et al., 2010).

### **5.1.3 Alanine Scanning for Engineering TA99 Mutants**

In order to acquire the range of TA99 affinity mutants, the CDR3 of both the heavy and light TA99 chains were mutated utilising a technique called alanine scanning. Site-directed mutagenesis with alanine scanning results in each amino acid being individually replaced to an alanine. This substitution enables the identification of the essential-for-binding amino acids (Hollis et al., 1995). The side-chain interactions of the substituted amino acid are hindered, while the perturbation in protein conformation is minimal due to alanine's small side-chain (Burks et al., 1997). The alanine scanning mutagenesis has been extensively used to map the antigen-binding site of antibodies (Kelley and O'Connell, 1993)(Vajdos et al., 2002).

### **5.1.4 Surface Plasmon Resonance (SPR) for Kinetic Analysis**

Surface Plasmon Resonance (SPR) is an optical method that can be used used to measure the kinetics of an antibody binding to an antigen. The phenomenon of SPR occurs in thin conducting films at an interface between media of different refractive index, as shown in Figure 53. Here, the media are the glass of the sensor chip and the aqueous macromolecule containing sample solution, while the conducting film is a

thin layer of gold on the sensor chip surface. The antibody is captured on the modified gold surface, and the ligand is injected into the flow. The binding and dissociation of the ligand from the antibody changes the refractive index of the light. The change in angle is proportional to the mass of bound material, which is subsequently translated into Response Units (RU). The increase in RU following the injection of the ligand into the flow represents the association rate. In the same principle, the decrease in RU represents the dissociation rate of the ligand from the binder. The SPR method has been reviewed in several publications (Patching, 2014)(Puiu and Bala, 2016)(Wang and Fan, 2016). This is the standard technique employed for determining the kinetics of TCRs or CARs to their target (Zhong et al., 2013)(Zhao et al., 2015)(Liu et al., 2015). We utilised the SPR technology, in order to measure the binding kinetics of the TA99 WT and mutant scFvs to Tyrp1.

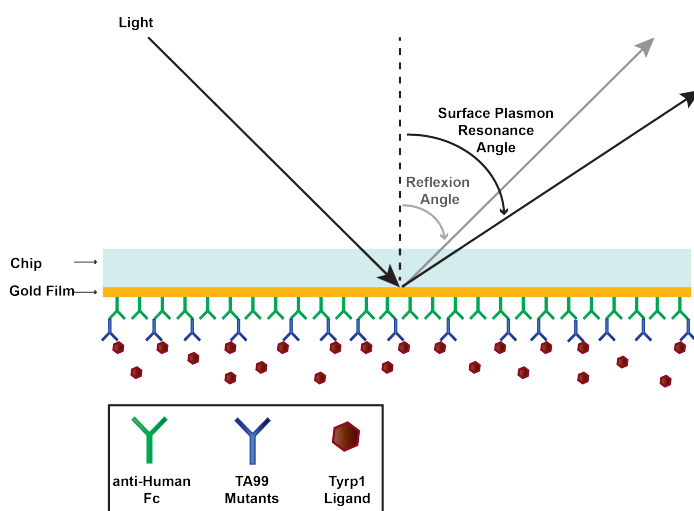


**Figure 53: The principle of Surface Plasmon Resonance.** A glass slide coated with a gold film creates the sensor surface. The anti-human Fc antibody, and subsequently the TA99 scFv are captured on the sensor surface. The Tyrp1 antigen is injected into the flow cell, and the refractive index changes according to the mass of protein bound on the sensor. The machine detects the change in the angle and translates it into binding kinetics.

### 5.1.5 Differential Scanning Fluorimetry (DSF) for Protein Stability Analysis

Differential Scanning Fluorimetry (DSF) is a method that determines the thermal stability of a protein. The principle of this technique is based on a fluorescent dye (Sypro Orange), which is quenched in solution, but fluoresces in hydrophobic environments. The solution containing the dye and the protein undergo an incremental increase of the temperature (0.5°C). The dye is not fluorescent in aqueous environment, but as the protein starts unfolding the dye binds the exposed hydrophobic regions of the protein, and fluoresces. The peak of fluorescent intensity

constitutes the protein melting temperature  $T_m$ . A decrease in fluorescence is observed after the peak due to protein aggregation and precipitation (Niesen et al., 2007)(Senisterra and Patrick J. Finerty, 2009)(Simeonov, 2013). DSF was implemented in order to measure the stability of TA99, and ascertain that the stability of the mutants was comparable to the WT. Our aim was to exclude the possibility of the scFv stability leading to different CAR efficacy, and constituting a confounding factor in our study.

## 5.2 AIMS

- Engineering the TA99 CDR3 heavy and light mutants via alanine scanning.
- Measuring the binding kinetics for the TA99 WT and mutants.
- Characterising the mutants for thermal stability.
- Validating the influence of affinity on the TA99-CAR efficacy in low, medium, high density targets.
- Interrogating mutant TA99-CARs for increase in sensitivity.

## 5.3 RESULTS

### 5.3.1 Production of CDR3 Heavy and Light TA99 Mutants

#### 5.3.1.1 Alanine Scanning

Our aim was to study the impact of affinity on the efficacy of the TA99-CAR, and determine a pattern or optimal range for maximum capacity. In order to achieve that, we obtained a range of affinities for the TA99 scFv via alanine scanning, and introduced this affinity range into a CAR format. Specifically, the CDR3 of the heavy and light chain were alanine scanned. For each mutated construct, one amino acid has been substituted into an alanine. In total, we engineered ten heavy chain and nine light chain mutants, shown in Figure 54. The caveat of alanine scanning is the lack of information acquired from the residues that were originally an alanine.

#### CDR3: Heavy Chain:

R	D	Y	T	Y	E	K	A	A	L	D	Y
CGG	GAC	TAC	ACC	TAC	GAG	AAG	GCC	GCC	CTG	GAC	TAC
H1	H2	H3	H4	H5	H6	H7	-	-	H8	H9	H10

#### CDR3: Light Chain:

Q	H	F	W	S	L	P	F	T
CAG	CAC	TTC	TGG	AGC	CTG	CCC	TTC	ACC
L1	L2	L3	L4	L5	L6	L7	L8	L9

**Figure 54: The sequence of the heavy and light CDR3 mutants of TA99 scFv.** The CDR3 heavy and light chains were alanine scanned, and nineteen mutants were obtained in total. Of these mutants ten bore mutations in the heavy chain (top), and nine in the light chain (bottom).

#### 5.3.1.2 Crystallographic Structure of TA99 mutants

After the design and cloning of the nineteen mutants, we transfected 293T cells with the TA99 WT and mutant scFv. The protein supernatant was collected 48h after the transfection. The mutants were fused to human Fc, which enabled the detection of the scFv with flow cytometry and on capture on a modified sensor chip surface in SPR.

Of the nineteen mutants that were engineered, protein could not be detected for eight mutants. These eight mutants (H5, H7, H8, L1, L2, L3, L4, L7) probably produced unstable protein, and thus we were unable to isolate it. Of the remaining eleven mutants, for reasons discussed below, eight were chosen to be tested in a CAR format. For the eight mutants that were validated *in vitro*, we show location and

structure of each amino acid that was substituted to an alanine. The structure of the TA99 variable regions was predicted based on homology modelling using the structural biology software BioLuminate (Schrödinger, LLC). The heavy chain is shown in green, the light chain in cyan, and each residue substituted to alanine is shown in deep blue. The protein structure is rotated in clockwise direction.

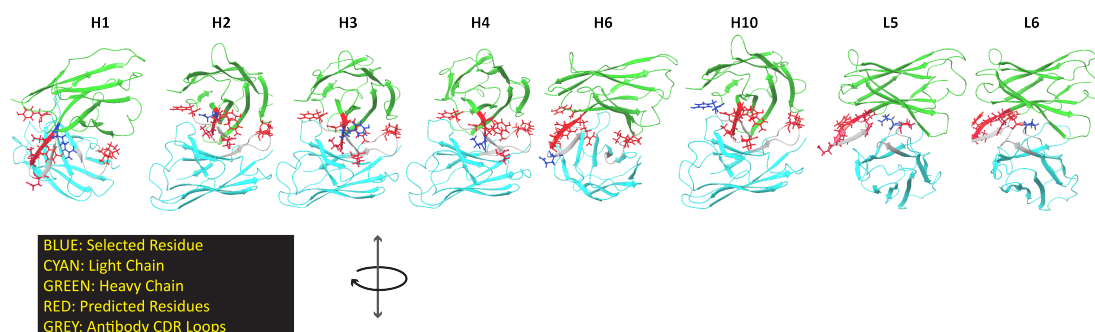


**Figure 55: Structural homology model of the TA99 mutants.** The structure of TA99 scFv was predicted in the BioLuminate software. In each separate structure we indicate the amino acid residue that has been substituted to an alanine (deep blue). The heavy and light chains are illustrated in green and cyan.

### 5.3.2 Binding Kinetics and Protein Characterisation of TA99 Mutants

#### 5.3.2.1 Kinetic Profiling of TA99 Mutants

The next step in acquiring the affinity range of TA99-CARs was the characterisation of the TA99 binding kinetics to the Tyrp1 ligand. The binding kinetics of the WT and mutant TA99 scFvs were measured via Surface Plasmon Resonance (SPR) on the Biacore® instrument, performed by Dr Shimobi Onuoha. The protein concentration for all the constructs was normalised.

Figure 56 illustrates the sensograms acquired from SPR. In a sensogram, the X-axis constitutes the time (s), and the Y-axis displays the response units (RU). The change in RU is proportional to the mass of material bound on the sensor. When Tyrp1 is introduced into the flow cell at time 0 ( $t_0$ ), the increase in response indicates the association or on-rate of Tyrp1 to the TA99 variant. At time 1 ( $t_1$ ) the flow of Tyrp1 ligand in the cell stopped, and the decrease in intensity indicates the dissociation or off-rate.

The increase in intensity for TA99 WT was rapid, indicating that the association rate was also rapid. At  $t_1$  there was no decrease in response for the TA99-WT, reflecting the slow dissociation rate of TA99 from Tyrp1. The increase in response was similarly

step for the mutants H4, L5, L6, L8, and L9. The off-rate for these mutants was slow, based on the stable level of the curve after the end of Tyrp1 injection. Hence, these mutants shared similar kinetics to the WT as discussed below. On the other hand, the intensity curve for the mutants H1, H2, H3, H6 and H10 was different to the TA99 WT (Figure 56). The increase in response was less steep than the WT, which was a result of decreased on-rate. The curve profile after the end of Tyrp1 injection was also altered. The decrease in response was more distinct, especially for H3 and H1. Finally, protein was detected for the mutant H9, but no binding to Tyrp1 occurred. Therefore, we concluded that the H9 mutant lost its specificity to Tyrp1.

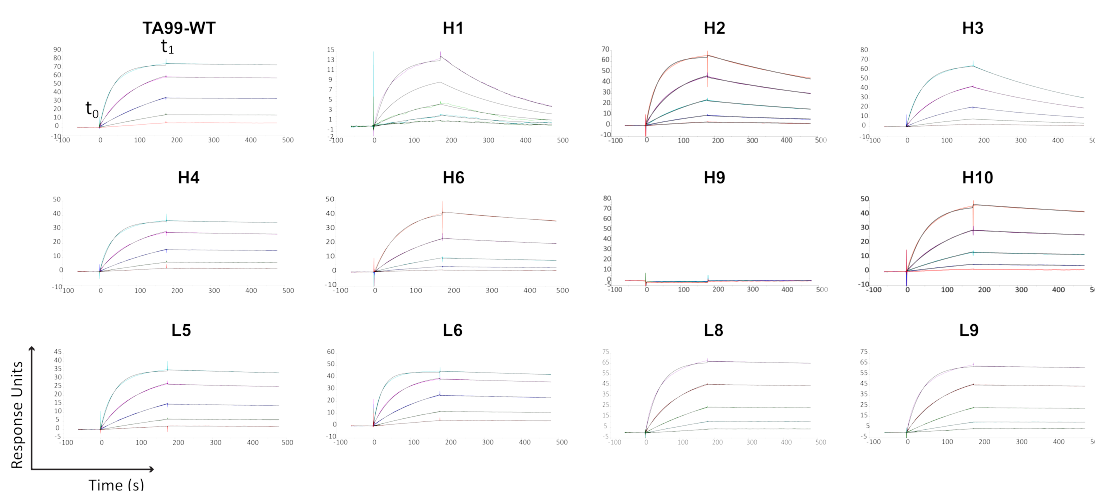


**Figure 56: Sensograms illustrating the binding kinetics of the TA99 WT and mutant scFvs.** The X-axis shows the time (s), and the Y-axis shows the response units (or intensity). The intensity increases proportionally to the mass bound to the sensor surface. At time  $t_0$ , Tyrp1 started being injected in the flow cell. As Tyrp1 was incrementally bound to TA99, the intensity increased, showing the association rate. At time  $t_1$  the Tyrp1 stopped being injected, thus the decrease in intensity signified the dissociation of Tyrp1 from TA99. The association rate of TA99 WT was rapid, and the dissociation slow. The same pattern was observed from the mutants H4, L5, L6, L8, and L9. On the contrary, the slope for the association intensity was less rapid for H1, H2, H3, H6, and H10 mutants. The dissociation rate for H6 and H10 was not significantly faster than WT. However, the decrease in intensity was distinct for the mutants H1-3. Finally, the mutant H9 did not interact with Tyrp1.

The affinity or dissociation constant ( $K_D$ ) is calculated as a fraction of the association and dissociation rate. Specifically, the dissociation rate ( $K_d$ ) constitutes the numerator, and the association rate ( $K_a$ ) constitutes the denominator. High  $K_a$  entails rapid association, and low  $K_d$  entails slow dissociation. An antibody with high association rate, and low dissociation rate has high affinity and low  $K_D$ .

The values for the TA99 WT and mutants are shown in Table 22. The TA99 WT and mutants did not fluctuate for the on-rate, with a narrow range of  $7.71\text{-}11.84 \times 10^4 \text{ M}^{-1} \text{ s}^{-1}$  (Table 22). However, the disparity in the dissociation rate was more prominent,

with a range between  $0.62\text{-}42.9 \times 10^{-4} \text{ s}^{-1}$ . The half-life, which is calculated based on the off-rate, was 186.3min for the TA99 WT. Overall, the half-life range was distributed between 2.7min and 186.3min.

A clear way to underline the kinetic differences between the WT and mutants is shown in Figure 57. This graph includes three parameters. The X-axis depicts the dissociation rate ( $K_d$ ), while the Y-axis depicts the association rate ( $K_a$ ). The third parameter is shown in the diagonal lines, and it constitutes the affinity ( $K_D$ ) that is calculated based on the on- and off-rate. The association rate does not fluctuate significantly, and thus all the TA99 variants appear close to the  $10^5 \text{ M}^{-1}\text{s}^{-1}$ . On the contrary, there is a disparity in the dissociation values between the TA99 variants. This resulted in changes of the scFv affinity for Tyrp1. TA99 WT, L8, and L9 exhibit the highest affinities with 0.63nM, 0.75nM, and 0.68nM respectively (Table 22). The half-life for these variants is also high (149-186.3min).

On the contrary, the mutants H1, H2, and H3 bear the lowest affinity values with 54.6nM, 13.7nM, and 44.6nM respectively. Their half-life is substantially reduced compared to the 186.3min half-life of the WT, with 2.7, 8.4, and 4.7 respectively.

The kinetic profile of the mutants L8 and L9 is almost identical to the WT. Hence, the function of the L8 and L9 mutants was postulated to be similar to the WT TA99. In order to render the in vitro experiment informative as well as efficient, we excluded L8 and L9 from subsequent characterisation.

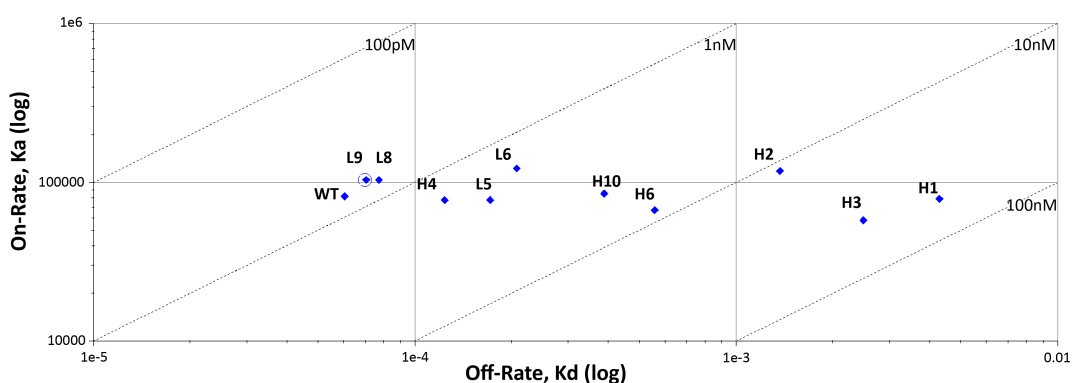


**Figure 57: Kinetic characterisation of the binding of WT and mutant TA99 scFvs.** This isotherm plot contains three parameters. The off- ( $K_d$ ) and on-rate ( $K_a$ ) are displayed on the X- and Y-axis, respectively. The diagonal lines delineate the affinity isotherms. The fluctuation of the association rate is minimal, and thus the data points all fall within the  $10^5 \text{ M}^{-1}\text{s}^{-1} K_a$  line. On the contrary, the data points are widely spread for the dissociation rate ( $K_d$ ). The disparity in  $K_d$  leads to differences in the affinity ( $K_D$ ). The mutants WT, L9, and L8 have an affinity lower than 1nM, as delineated by the isothermic line. The mutants H4, L5, L6, H10, and H6 fall within the range of 1nM-10nM of  $K_D$ . Finally, the mutants H1-3 fall within the range of 10nM-100nM.

Table 22: Kinetic Profiling of TA99 Mutants and WT.

	Ka (1/Ms) ( $\times 10^4$ )	Kd ( $s^{-1}$ ) ( $\times 10^{-4}$ )	Half-Life (min)	KD (nM)
TA99-WT	8.11	0.62	186.3	0.87 $\pm$ 0.13
TA99-H1	7.9	42.9	2.7	54.6 $\pm$ 0.25
TA99-H2	11.84	13.72	8.4	13.7 $\pm$ 1.8
TA99-H3	5.37	24.8	4.7	44.6 $\pm$ 1.3
TA99-H4	7.73	1.24	93.1	1.61
TA99-H6	6.72	5.58	20.7	8.3
TA99-H9	-	-	-	-
TA99-H10	8.54	3.79	30.5	4.53
TA99-L5	7.71	1.72	67.2	2.22
TA99-L6	12.3	2.07	55.8	1.41 $\pm$ 0.28
TA99-L8	10.42	0.775	149.0	0.75
TA99-L9	10.34	0.703	164.3	0.68

### 5.3.2.2 Stability of TA99 Mutants

As discussed above, our goal was to examine the effect of the affinity on the CAR efficacy. In order to achieve that, it was crucial to exclude potential confounding factors. Disparity in stability between the TA99 variants constitutes such a confounding factor.

In order to ascertain that the stability between TA99 variants was comparable, we carried out Differential Scanning Fluorimetry (DSF) described in 5.1.5. Each protein was measured in triplicates. Figure 58 displays the apparent melting temperature ( $T_m$ 50) for the TA99 WT and mutant scFvs. The  $T_m$ 50 for the WT protein was 56.25°C. The range of  $T_m$  for the mutants was 55.92-56.83°C. The range is limited to 0.91°C, which would not constitute a confounding factor in the CAR efficacy study.

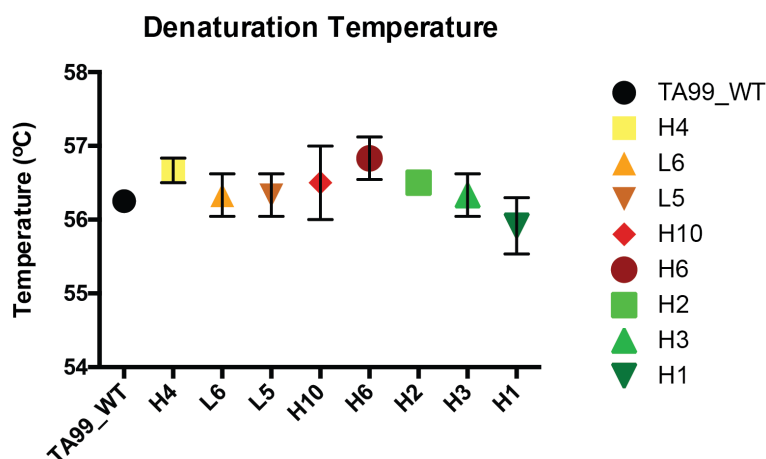


**Figure 58: Denaturation temperature of TA99 variants.** The thermal stability of the TA99 WT and mutants was measured with DFS. The temperature was incrementally increased (0.5°C), and the  $T_m$  of each protein was calculated. The WT TA99 unfolded at 56.25°C. The lowest denaturation temperature was 55.92°C for H1. The fluctuation in denaturation temperatures is negligible.

### 5.3.2.3 Conclusion

Our aim was to obtain a range of TA99 scFv variants with different affinities towards Tyrp1, in order to introduce them into CAR format and investigate the influence of affinity in CARs. We engineered nineteen TA99 mutants, of which eleven resulted in stable protein. These eleven TA99 mutants, as well as the WT TA99, were analysed with SPR for measuring their binding kinetics to Tyrp1. The affinity of the WT TA99 was 0.87nM and the half-life was 186.3min. Although the association rate of the TA99 mutants did not change dramatically, the dissociation rate was significantly reduced. Hence, the affinity values ranged from 0.68nM to 54.6nM, and the half-life was decreased from 186.3min to 2.7min.

The difference in the apparent melting temperature between TA99 WT and mutants was negligible. Hence, the scFv stability was excluded as a confounding factor in our investigation of potential correlation between affinity and CAR cytotoxicity.

In total we obtained eleven mutants that produced a functional protein, and ten that bound Tyrp1. Of these ten mutants, L8 and L9 were kinetically similar to TA99 WT, thus they were excluded from subsequent functional assays. The affinity gradient we carried forward for *in vitro* validation consisted of the mutants: H1, H2, H3, H4, H6, H10, L5, and L6.

### 5.3.3 Functional Characterisation of TA99-CAR Affinity Gradient

After the TA99 affinity gradient was obtained, the CARs bearing the affinity range of the TA99 mutants were interrogated for functional capacity. Our aim was to investigate whether the affinity affects the efficacy or sensitivity of the CARs, and whether there is an optimal CAR affinity range. In order to compare the different affinity CARs, we carried out assays for the cytotoxic efficacy, cytokine production, as well as differentiation and exhaustion status.

The functional experiments were carried out with T-cells normalised for transduction efficiency at 30%. The ratio of effector-to-target cells was 1:1. Since only 30% of the T-cells were transduced, the ratio of transduced T-cells to targets was approximately 1:3.

#### 5.3.3.1 Transduction Efficiency of TA99-CAR Affinity Gradient

In order to ascertain that all T-cell cohorts are expressing the respective CAR transgene they were transduced with, the T-cells were labelled with CD8 and anti-human Fc for detection of the CAR. The transduction efficiency was validated with flow cytometry. Establishing the transduction efficiency also enabled the normalisation of the transduction levels to 30% prior to the experimental set-up.

The flow cytometry dot plots are shown in Figure 59. Although T-cells from three donors were utilised in this cohort of experiments, only one representative donor is shown in Figure 59. The X-axis represents the TA99-CAR labelling, and the Y-axis represents the labelling for CD8. The NT T-cells showed no background signal for TA99 (Figure 59.A). The aCD19-CAR was used as a reference CAR for cytotoxicity and cytokine production. The transduction of CD8<sup>+</sup> T-cells ranged between 35.5-53%, while the CD8<sup>-</sup> T-cells fluctuated from 28.2-35.8%. The transduction disparity was negligible. Nonetheless, the T-cells were all normalised to 30% transduction efficiency by adding NT T-cells, in order to obtain the 1:3 transduced effector-to-target ratio.

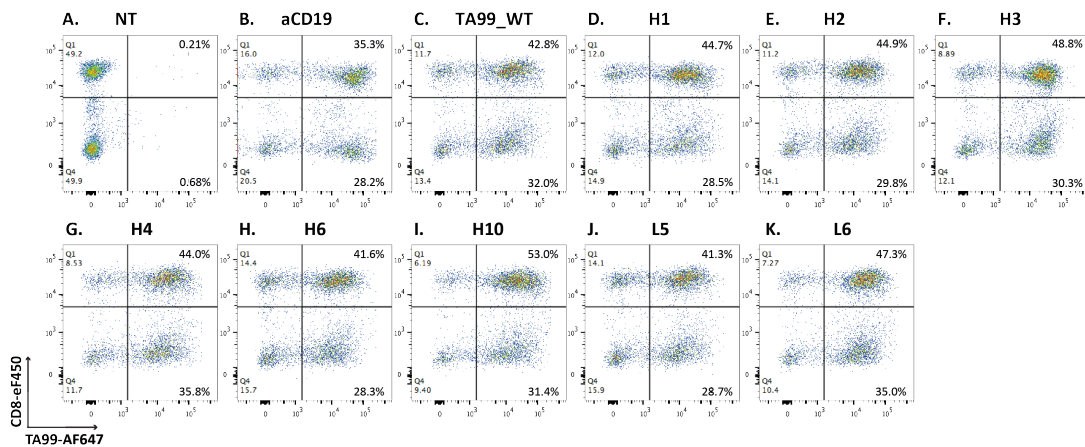


**Figure 59: Transduction efficiency of T-cells bearing the TA99 affinity variants.** The transduction efficiency of the TA99-CAR transduced T-cells was validated with flow cytometry. The X- and Y-axis display the labelling for the CAR or CD8, respectively. No background signal was detected for the negative control NT T-cells (A). The transduction of the aCD19-CAR was 35.3% and 28.2% for CD8<sup>+</sup> and CD8<sup>-</sup> T-cells respectively. The T-cells transduced with the WT TA99 were 42.8% and 32.0% for CD8<sup>+</sup> and CD8<sup>-</sup> cells respectively. The labelling of the heavy chain mutants is shown in (D-I), and the light chain mutants in (J-K). The transduction fluctuation was negligible with TA99-CAR expression levels between 41.3-53.0% for CD8<sup>+</sup>, and 28.3-35.8% for CD8<sup>-</sup> T-cells.

### 5.3.3.2 Cytotoxic Capacity of TA99-CAR Affinity Gradient

The cytotoxic capacity of the TA99-CARs was measured with Flow-cytometry Based Killing (FBK) assay. The absolute number of target cells remaining in the co-culture were measured. The survival of the target cells in the NT T-cell condition was set as 100%. The target survival in the remaining conditions was normalised according to the NT (100%), and was also expressed as a percentage. The survival percentage decreased with the increase of the target lysis exerted by the CAR T-cells. The survival of the targets was measured in three time-points: 1, 3, and 7 days after the co-culture initiation. Only the graphs from time points Day (D)1 (Figure 60) and D7 (Figure 61) are shown.

The cell-lines utilised for the functional characterisation of the TA99 affinity gradient CARs were the SupT1 expressing WT, Distal or Trunc Tyrp1, and the human melanoma cell line T618A. We also introduced the SupT1 NT as negative control, and SupT1 expressing CD19 as a target for the control aCD19-CAR.

Figure 60 demonstrates the survival percentage of the target cell-lines at the time point D1. The NT and aCD19 control T-cells are displayed in grey. The TA99 affinity gradient CARs are shown in decreasing order of affinity. The highest affinity CAR, which is the WT, is shown on the left. The H1 TA99-CAR variant bears the lowest

affinity, and is located at the far right. The variants with  $K_D$  less than 10nM are shown in red. The mutants H1, H2, H3 that bear  $K_D$  values higher than 10nM are represented in green. There was minimal lysis of the SupT1 NT cells observed (Figure 60.A). The survival in all the conditions ranged between 85.87-131.97%. The mutant H6 displayed the highest background with 85.87% survival, which is within the acceptable range of background lysis.

The TA99\_WT CAR did not cause any lysis of the SupT1 cells expressing WT Tyrp1 (Figure 60.B), but only moderately lysed the SupT1\_Distal (53.59% survival) (Figure 60.C). The TA99\_WT efficacy was similar against SupT1\_Trunc and T618A (44.79% and 54.31% cell survival, respectively). However, there was a pattern observed for the TA99 mutants. The pattern observed in the Tyrp1-WT condition included two nodules (Figure 60.B). The target cell survival was low for the H4 CAR (41.43%) and it incrementally increased to 103.35% for the H10 mutant CAR. However, the continuity of the pattern was disturbed at that point of affinity (4.53nM). The next nodule bore the same pattern, with H6 being very efficacious (28.62%), and the efficacy consistently decreased till H1, where no cytotoxicity occurred (142.90%).

The same two-nodule pattern was observed against the SupT1\_Distal and SupT1\_Trunc target cells. The survival of the SupT1 expressing Distal was 29.4% for the H4 CAR, which increased to 73.56% for the H10 CAR (Figure 60.C). The SupT1\_Distal cell survival was decreased for the H6 CAR (33.26%), which again increased to 76.7% for the H1 CAR. The two-nodule pattern was similar for the SupT1\_Trunc cell condition (Figure 60.D). However, the fluctuations were narrower. Within the H4-H10 nodule the range of survival was 25.17-51.89%, and the range for the H6-H1 nodule was 22.89-40.67%.

The human melanoma cell line constituted a more physiological target than SupT1, since it inherently expresses Tyrp1 at an average density of 1131 epitopes/cell (see chapter 3.3.4.1). The efficacy of the WT CAR was 54.31% as mentioned above. However, in Figure 60.E the two-nodule pattern was not as distinct, and the mutant CAR efficacy was similar between CAR mutants, with a range of 30.48-53.91%. All TA99 mutant CARs were marginally superior to the WT.

Finally, we included SupT1 cells expressing CD19 (Figure 60.F). Our reference CAR was aCD19. The aim was to use this previously validated CAR as a positive control for the assays. The efficacy of the aCD19-CAR was limited, with 67.28% target survival. Another noteworthy observation was the high background cytotoxicity of the H6 mutant CAR (52.97%). Nevertheless, there was only one repeat of the SupT1\_CD19 condition. Hence, the low efficacy of the aCD19-CAR or the high background of the H6 mutant CAR could be donor specific, rendering the observations inconclusive.

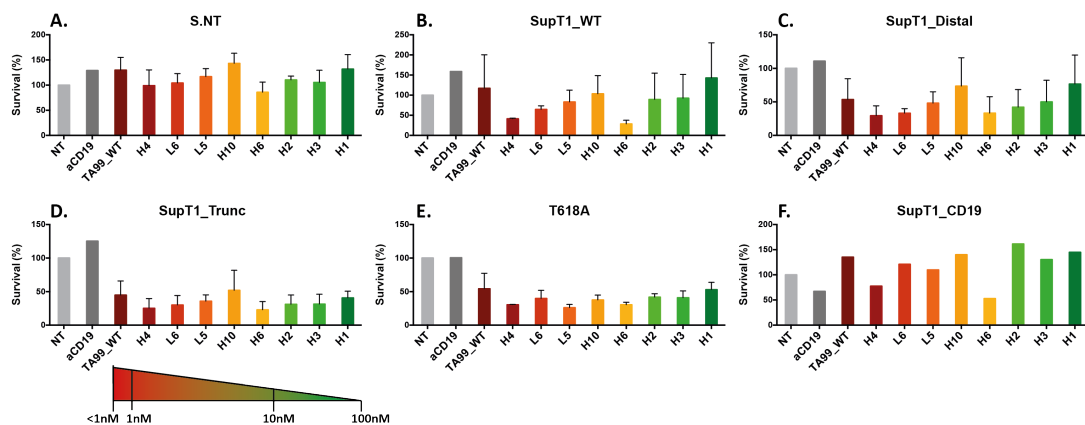


**Figure 60: Cytotoxic capacity of the TA99-CAR affinity gradient at D1.** The Y-axis represents the percentage of survival of the target cells. The X-axis consists of the range of CARs employed. The control T-cells (NT and aCD19-CAR) are illustrated in grey colours. The TA99\_WT and mutants with  $K_D$  less than 10nM are shown in red colours, whereas the mutants H1, H2, and H3 with  $K_D$  above 10nM are shown in green. (A) The SupT1 NT target cells constitutes a negative control, in order to measure potential background cytotoxicity of the CARs. The TA99 mutants formed a two-nodule pattern in their efficacy against SupT1\_WT (B) and SupT1\_Distal (C). The one nodule constituted of the effectors H4 to H10 (41.43-103.35%), and the second nodule of the effector H6 to H1 (28.62-142.9%) (B). The target survival increased with  $K_D$  up to the affinity value of 4.53nM (H10), at which point the survival declined again. The same pattern was observed where increase in  $K_D$  led to an increase of target survival. The same pattern was observed in SupT1\_Distal (C) and SupT1\_Trunc (D), although the trend was not so prominent in the latter. (E) The cytotoxicity divergence was subtle in the T618A target cell condition, where the target cell survival ranged between 30.48-53.91%. (F) The SupT1\_CD19 target cell line was introduced as a positive control for the aCD19-CAR efficacy (67.28%). No statistically significant differences were observed compared to the WT TA99-CAR, as calculated with One-way Anova. The results illustrated in this figure constitute the repeat of two donors.

The cytotoxicity assay was also carried out at the time point D7, which constitutes a challenging time point for T-cells. The target cells proliferate at a faster rate than T-cells, so by D7 the targets have outgrown the T-cells. Hence, if the CAR is not efficacious in lysing the target cells, by D7 the targets represent the majority of cells within the well.

As shown in Figure 61.B, the SupT1\_WT cells proliferated in all the CAR conditions compared to the NT T-cells. The proliferation of the SupT1\_Distal and Trunc targets cells was less prominent. However, only L6, H2, and H3 CARs sustained the

SupT1\_Distal cells at low survival levels (Figure 61.C). The survival of the Distal expressing SupT1 cells was 22.47% in the L6 CAR condition, whereas the survival was reduced to 4.35% and 4.12% in the H2 and H3 CAR conditions, respectively. Although the L6 CAR was not efficacious against SupT1\_Trunc cells (Figure 61.D), the H2 and H3 CARs sustained the target cells at 7.26% and 9.7% survival levels, respectively.

There was no disparity between the different TA99 CARs against the T618A cell line (Figure 61.E). The range of TA99-CAR efficacy was 8.94-32.67%. The efficacy of the TA99 WT CAR was 20.93%. The efficacy of the H2 and H3 CARs was 11.14% and 19.36% respectively. The highest efficacy was observed for the H4 CAR at 8.94% remaining T618A target cells.

Finally, the survival of CD19 expressing SupT1 cells was variable in the aCD19-CAR condition. One donor failed to sustain the target cells levels below 108.39%. Whereas, the second donor sustained the SupT1\_CD19 cells at 0.31% at D7.

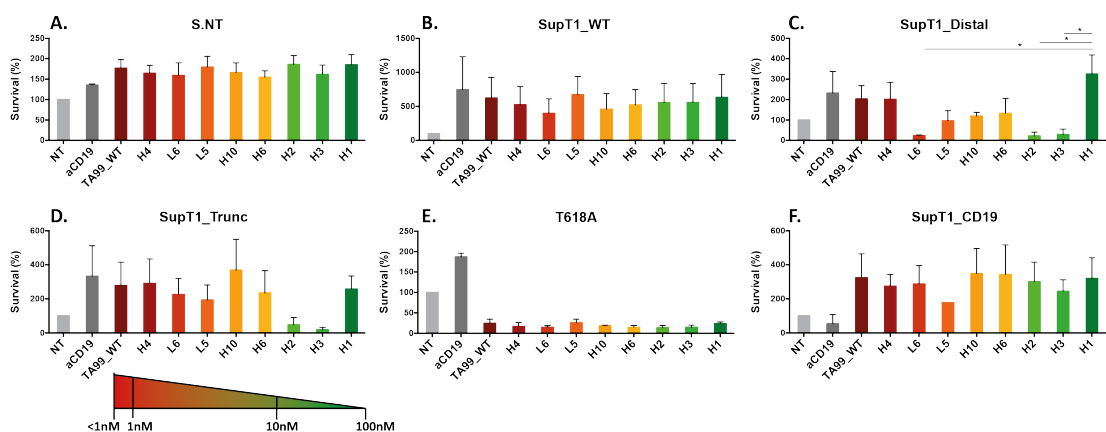


**Figure 61: Cytotoxic capacity of the TA99-CAR affinity gradient at D7.** As before, the Y-axis represents the percentage of survival of the target cells, and the X-axis represents the CARs employed. The control T-cells (NT and aCD19-CAR) are illustrated in grey colours. The TA99\_WT and mutants with  $K_D$  less than 10nM are shown in red colours, where the mutants H1, H2, and H3 with  $K_D$  less above 10nM are shown in green. This FBK was carried out at D7 after the co-culture set-up. This time-point is challenging the T-cells capacity to sustain the target cells at low level, while the target cells are proliferating and expanding. The SupT1 NT cells had expanded above 100% (A). Similarly, the SupT1\_WT had also expanded, especially compared to the NT T-cell condition (B). With the increase in antigen density, the cytotoxic capacity of the H2 and H3 CARs was also increased. For example, the H2,H3, as well L6 CARs sustained the SupT1\_Distal cells at 4.35%, 4.12%, and 22.47%, respectively (C). (D) The survival percentage of SupT1\_Trunc when exposed to the H2 and H3 CARs was 7.26% and 9.7%. (E) The TA99-CARs were efficacious in eliminating the T618A cells and sustaining them at 8.94-32.67%. Specifically, the H2 and H3 CARs was 11.14% and 19.36%. (F) Finally, the survival levels of the CD19 expressing cells varied between donors, rendering this condition inconclusive. There was no statistical significance of the mutant CARs compared to the WT, as calculated with One-way Anova. The difference in efficacy between L6, or H2, or H3 to H1 CAR was significant ( $p=0.0325$ ,  $p=0.0313$ , and  $p=0.378$  respectively) for the SupT1\_Distal target cells (C). Three independent repeats were carried out for this read-out experiment.

### 5.3.3.3 Cytokine Production of TA99-CAR Affinity Variants

We also interrogated the affinity gradient CARs for cytokine production. Interleukin-2 (IL2) is essential for T-cell proliferation and survival (Miyazaki et al., 1995). Additionally, activated cytotoxic T-cells produce Interferon- $\gamma$  (IFN- $\gamma$ ), thus we used it as a marker of activation upon antigen recognition (Lu et al., 1998).

T-cells transduced with the CAR gradient were cultured in the presence of SupT1 or the human melanoma cell line T618A. The IFN- $\gamma$  T-cell secretion is shown in Figure 62. In the presence of NT SupT1 cells, the concentration of IFN- $\gamma$  produced by all T-cells was less than 150pg/ml (Figure 62.A). The IFN- $\gamma$  concentration was also low when the SupT1\_WT cells were used as targets, with only the WT TA99-CAR producing marginally higher concentration at 178.51pg/ml (Figure 62.B).

The NT T-cells produced 146.2pg/ml concentration of IFN- $\gamma$  in the presence of SupT1\_Distal targets (Figure 62.C). However, the majority of the TA99-CARs produced IFN- $\gamma$  levels marginally higher than the NT T-cells background. The WT, H4, and L6 CAR T-cells produced 209.13pg/ml, 162.07pg/ml, and 180.33pg/ml, respectively. The cytokine production of the H6 and H2 CARs was also above background level, with concentrations of 179.53pg/ml and 205.84pg/ml. Finally, the CAR that produced the highest concentration of IFN- $\gamma$  against the SupT1\_Distal cells was the H3 (299.95pg/ml) (Figure 62.C). The same expression pattern was observed in the SupT1\_Trunc condition (Figure 62.D). The IFN- $\gamma$  secretion level was 249.72pg/ml for the WT TA99-CAR, whereas the cytokine production was higher for the T-cells expressing the H2 and H3 mutant CARs (369.92pg/ml and 383.08pg/ml, respectively).

In total, the CAR expressing T-cells released higher amounts of IFN- $\gamma$  cytokine when challenged with the T618A cell line (Figure 62.E). Although the background level of NT T-cells remained low (163.1pg/ml), the concentration produced by the WT TA99-CAR was 694.53pg/ml. The range of cytokine production for the CARs H4, L5, H10, H6, and H1 was 306.76-489.42pg/ml. The production was higher for the mutant CARs L6, H2, and H3 with a concentration at 591.69pg/ml, 839.48pg/ml, and 614pg/ml, respectively.

Finally, in the presence of SupT1\_CD19, the NT and TA99-CARs released a range of low IFN- $\gamma$  concentration, which was 74.32-104.95pg/ml (Figure 62.F). On the contrary the aCD19-CAR T-cells released a high concentration of IFN- $\gamma$  at 2438.4pg/ml.

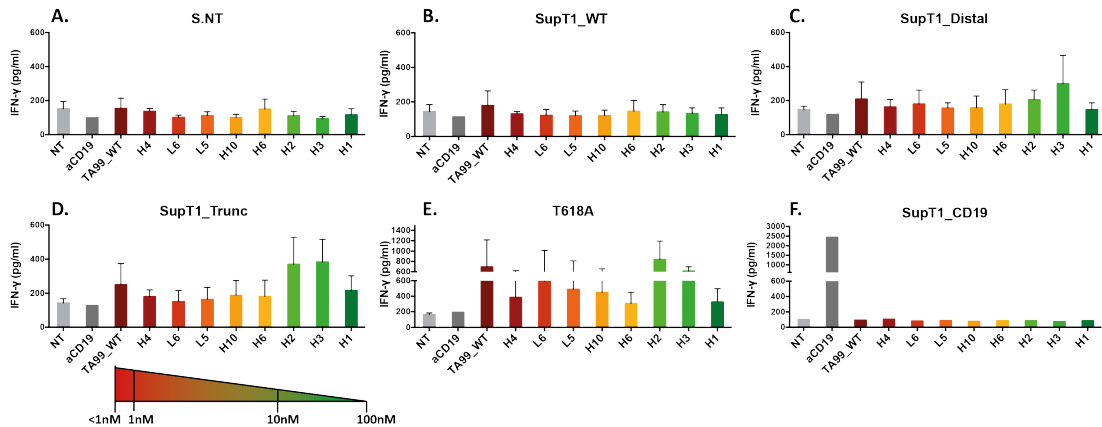


**Figure 62: IFN- $\gamma$  production of the TA99-CAR affinity gradient.** In this graph the distinct CAR constructs are displayed in the X-axis, whereas the Y-axis constitutes the concentration for the IFN- $\gamma$  cytokine (pg/ml). (A) There was low background detected for the T-cells against the NT SupT1 cells, with the IFN- $\gamma$  concentration not exceeding the 150pg/ml. (B) Low cytokine production was also observed in the SupT1\_WT condition, where only the TA99\_WT produced subtly higher levels of IL2 (178.51pg/ml) than the NT T-cells. (C) When the T-cells expressing the WT, H4 and L6 CARs were cultured with the SupT1\_Distal cells they produced 209.13pg/ml, 162.07pg/ml, and 180.33pg/ml, respectively. Additionally, The H6 and H2 CARs produced above the level IFN- $\gamma$  at a concentration of 179.53pg/ml and 205.84pg/ml. The H3 mutant CAR produced the highest level of IFN- $\gamma$  in the presence of SupT1\_Distal (299.95pg/ml). (D) In the presence of SupT1\_Trunc, the TA99\_WT produced 249.72pg/ml of IFN- $\gamma$ , and the highest concentration was produced by H2 (369.92pg/ml) and H3 (383.08pg/ml). (E) In the TA99-WT against T618A condition 694.53pg/ml of IFN- $\gamma$  was released, which was 4-fold higher than the background. The cytokine level produced by H4, L5, H10, H6, and H1 was lower with a range of 306.76-489.42pg/ml. The mutant CARs L5 and H3 produced levels comparable to WT with 591.69pg/ml and 614pg/ml of IFN- $\gamma$ , respectively. Finally, the H3 mutant produced the highest IFN- $\gamma$  concentration at 839.48pg/ml. (F) The aCD19-CAR release 2438.4pg/ml of IFN- $\gamma$ . The IFN- $\gamma$  release was measured from two independent experimental repeats.

The secretion of the IL2 cytokine was also measured (Figure 63). The production of IL2 in the NT SupT1 condition was low (29.07-54.4pg/ml). The exception consisted of the aCD19 and WT TA99-CAR, which produced 136.64pg/ml and 124.54pg/ml of IL2, respectively (Figure 63.A). The T-cells produced no IL2 against the Tyrp1-WT SupT1 cells (Figure 63.B). The baseline IL2 production for the SupT1\_Distal cells was 57.75pg/ml (Figure 63.C). The CARs rising above the baseline level were L6 (124.35pg/ml) and H10 (110.98pg/ml).

The pattern differed for the SupT1\_Trunc targets cells (Figure 63.D). The CARs that released the highest IL2 concentration against SupT1\_Trunc were L6 (100.1pg/ml) and H3 (124.98pg/ml). However, the production of IL2 was similar for the NT T-cells at 99.98pg/ml.

Against T618A, the WT TA99-CAR T-cells produced 148.03pg/ml of IL2, which was 3-fold higher than the baseline (Figure 63.E). The IL2 concentrations were similar for the CARs H4 (152.4pg/ml), L5 (156.48pg/ml), and H6 (170.72pg/ml). The expression was higher for the mutant CARs L6 (819.16pg/ml), H10 (401.73pg/ml), H2 (501.2pg/ml), and H3 (651.23pg/ml).

The last target cell line was the CD19 expressing SupT1 cells (Figure 63.F). The IL2 concentration was below 55pg/ml for all the TA99-CARs and the NT T-cells. However, the aCD19-CAR T-cells released a high concentration of 1910.12pg/ml of IL2.

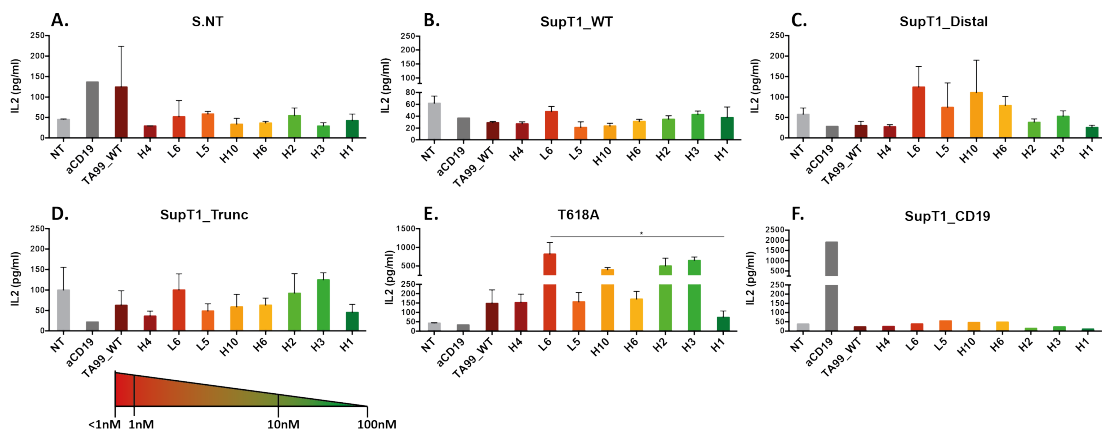


**Figure 63: IL2 production of the TA99-CAR affinity gradient.** The different CAR constructs are represented in the X-axis, and are shown in declining order of affinity. The Y-axis displays the concentration of IL2 measured in pg/ml. (A) As expected, the T-cells produced low concentration of IL2 in the control target condition (29.07-54.4pg/ml), with the exception of the aCD19 and WT CARs that produced 136.64pg/ml and 124.54pg/ml of IL2, respectively. (B) In the presence of SupT1\_WT, none of the CAR variants led to cytokine production above the background level. (C) The cytokine level produced by L6 and H10 mutant CARs was 124.35pg/ml and 110.98pg/ml, respectively, which was approximately 2-fold higher than the baseline (57.75pg/ml). (D) For the SupT1-Trunc the background cytokine levels were higher (99.98pg/ml). Only the H3 CAR released marginally higher concentration at 124.98pg/ml. (E) The WT TA99-CAR T-cells produced 3-fold higher cytokine than the background, with a concentration of 148.03pg/ml. Similar levels of IL2 were produced by the mutant CARs H4 (152.4pg/ml), L5 (156.48pg/ml), and H6 (170.72pg/ml). However, the IL2 concentration was higher for the mutant CARs L6 (819.16pg/ml), H10 (401.73pg/ml), H2 (501.2pg/ml), and H3 (651.23pg/ml). (F) The last target cell line was SupT1\_CD19. The aCD19 CAR produced 1910.12pg/ml of IL2 against the CD19 expressing cells, which concentration was 34-fold higher than the background noise. Two independent repeats were carried out for this the measurement of the IL2 T-cell production.

### 5.3.3.4 Conclusion

The affinity gradient of TA99-CARs was interrogated for cytotoxic and cytokine secretion capacity. The cytotoxicity was screened at three distinct time-points, however results from only the two time-points are shown in this chapter (D1, D7). For the D1 FBK time-point, we observed a two-nodule pattern, where there was a consistent increase in target survival for the CARs H4, L6, L5, H10. Then, the same pattern was observed for CARs H6, H2, H3, and H1. This two-nodule pattern was

observed against all Tyrp1 expressing SupT1 cells. However, in the presence of the T618A cells, the mutant TA99-CARs were all marginally superior to the WT TA99-CAR, with a target survival range of 30.48-53.91%.

The D7 time-point was more challenging for the T-cells, since the target cells are expanding at a faster rate than that of the T-cells. Hence, by day 7 the target cells have expanded several fold. The only CARs that maintained the SupT1\_Distal target survival at low levels were the mutant CARs L6, H2, and H3. In the presence of SupT1\_Trunc, only the H2 and H3 CARs eliminated their targets. The overall cytotoxic capacity of the TA99-CARs was enhanced in the presence of the T618A melanoma cell line, where the survival of target cells was limited to 8.94-32.67%. The target survival for the H2 and H3 CARs was 11.14% and 19.36% against T618A.

The cytokine production also showed that H2 and H3 CARs have potential. These two CARs secreted the highest concentration of IFN- $\gamma$  in the presence of SupT1\_Trunc and T618A cells. The L6 CAR also produced a high amount of IFN- $\gamma$  against T618A. Specifically, the WT TA99-CAR produced 694.53pg/ml of IFN- $\gamma$ , whereas the H3 produced 839.48pg/ml.

The mutant CARs L6, H2, and H3 show a similar pattern regarding IL2 cytokine secretion capacity. The concentration of IL2 they produced against the SupT1\_Trunc and T618A targets was higher to the other TA99-CARs. In the T618A condition, the IL2 concentration for the CARs L6, H2, and H3 was 819.16pg/ml, 501.2pg/ml, and 651.23pg/ml, respectively.

We expected to identify a trend of either increasing or decreasing efficacy in regard to affinity. According to the data however, there was no apparent pattern in how the affinity affects the CAR capacity. The data indicate that the three CARs mutants L6, H2, and H3 might bear improved T-cell capacity compared to the control TA99 CAR. Nevertheless, the L6 is kinetically distinct to the H2 and H3 mutants. The L6 bears the affinity of 1.41nM, and a half-life of 55.8min. The kinetics of H2 are an affinity of 13.7nM, and a half-life of 8.4min, whereas the affinity of H3 is 44.6nM and has a 4.7min half-life. It is intriguing that the three CARs with potentially increased efficacy bear a wide range of affinities between them, instead of residing in the same binding kinetic region.

### 5.3.4 Determining the Differentiation and Exhaustion Status of the Mutant TA99-CAR T-Cells.

#### 5.3.4.1 Differentiation Profile of Mutant TA99-CAR Expressing T-Cells

Our aim was to validate the function of the mutant TA99 CARs, and discern differences in their behaviour. These differences would facilitate extrapolating a trend in the relationship between affinity and efficacy. There was a two-nodule trend observed in the D1 cytotoxicity assay. However, this pattern was not consistent in the D7 cytotoxicity assay or the cytokine production. In an attempt to detect differences caused by the mutant CARs, we sought to examine whether the mutant CARs altered the differentiation and exhaustion T-cell profile compared to the WT TA99-CAR.

The stages of T-cell differentiation were determined based on the markers CCR7, CD95, and CD45RA, in order to categorise them into Tnaive, Tscm, Tcm, or Tem (Figure 64). The subpopulations were expressed as a ratio of the absolute number of cells in each subset, divided by the absolute number of T-cells in that condition. The reason the results are shown as ratios instead of absolute numbers is to normalise for differences in cell number between the CAR conditions. The four differentiation categories represent all T-cells, hence each bar of the Figure 64 reaches 1 on the Y-axis. The differentiation stages from Tnaive to Tem are shown in progressively darker shades of red. Despite the lack of target cells in the Media only condition, the majority of the TA99-CAR T-cells are Tem with a ratio range of 0.66-0.74 (Figure 64.A). Only a minority of cells are Tnaive and Tcm.

Similarly, the Tem constitute the majority of T-cells when co-cultured with the NT SupT1 cells (Figure 64.B). The ratio of Tem ranges between 0.52-0.71. The proportion of Tcm is similar between the different TA99-CARs. However, the mutant CARs L6, H2, H3, and H1 bear a subtly increased proportion of Tnaive T-cells. This difference against the WT TA99-CAR is not statistically significant.

The pattern of subset proportion is similar between the SupT1 target cells expressing WT, Distal, and Trunc Tyrp1 (Figure 64.C-E). As before the majority of cells are terminally differentiated to Tem. However, the mutant CARs L6, H10, H2, H3, and H1 exhibit marginally elevated levels of Tnaive cells. The proportion of Tcm cells

between the conditions is comparable. There were no disparities in the differentiation profile of the TA99-CAR T-cells challenged with T618A (Figure 64.F). The ratio range for Tnaive T-cells was 0.15-0.24, in contrast to the Tem that was 0.46-0.6.

The T-cells bearing the aCD19 CAR, when exposed to the non-specific target cells, exhibited a pattern of approximately 1:1 ratio for Tnaive: Tem. In the media condition, the ratio of Tnaive, Tcm, and Tem was 0.32, 0.09, and 0.44, respectively (Figure 64.A). However, this pattern drastically changed when the aCD19-CAR T-cells encountered CD19 expressing target cells (Figure 64.G). The Tnaive compartment is diminished to 0.057, while the Tcm and Tem increased to 0.21 and 0.59, respectively.

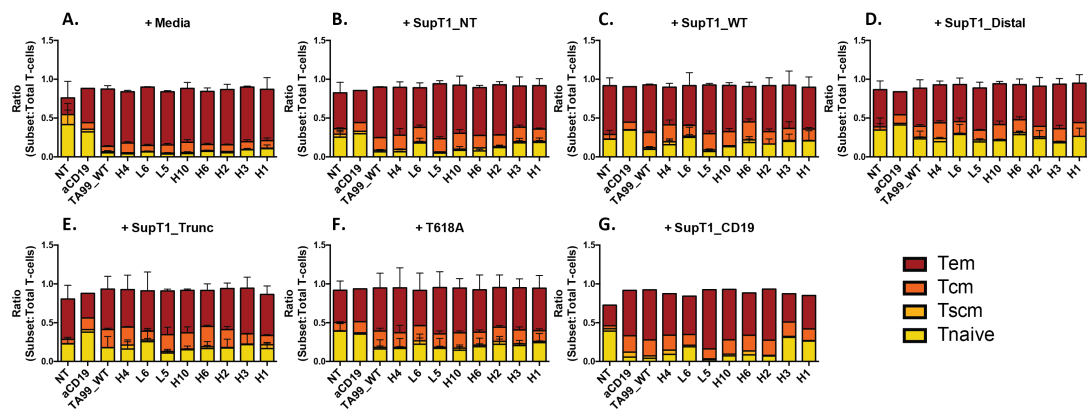


**Figure 64: Differentiation profile of mutant TA99-CAR expressing T-cells.** The T-cells were categorised as Tnaive, Tscm, Tcm or Tem based on flow cytometry and the differentiation markers CD95, CCR7, and CD45RA. The absolute number of each subset was divided with the number of T-cells in the specific condition, in order to derive the T-cell ratio subset. The different CAR T-cells were cultured in the presence of no target cells (A), or target cell lines expressing different density of Tyrp1 (B-F). We also included CD19 positive targets, as a positive control for our reference CAR, aCD19 (G). The differentiation profile between the TA99 WT and mutant CARs is similar, with the majority of T-cells being terminally differentiated to Tem. The proportion of Tcm for the TA99-CARs, although small, is also consistent between different CARs and different cell lines. There are some fluctuations for the Tnaive subset in the presence of Tyrp1 expressing SupT1 cells, with L6, H2, H3, and H1 having a marginally higher Tnaive representation (B-E). (F) The subset proportion for Tnaive, Tcm, and Tem remained constant between different TA99-CAR T-cells in the presence of T618A. Although the aCD19 T-cells exhibited a profile of 1:1 composition between Tnaive and Tem in the CD19 negative cell lines, this proportion was skewed in favour of Tem in the presence of SupT1\_CD19 (G). The results shown in this figure were based on two repeats.

### 5.3.4.2 Exhaustion Profile of Mutant TA99-CAR Expressing T-Cells

As discussed earlier, we aimed to pinpoint the differences between the various WT and mutant TA99-CARs. Part of the characterisation was the profiling of their exhaustion phenotype. Exhaustion constitutes the lack of cytotoxic or cytokine-secretion response to an antigenic stimulus. The two commonly used exhaustion markers are PD-1 and Tim3. Exhausted T-cells can express either one or both PD-1

and Tim3, with double positive T-cells exhibiting a more severe phenotype (Fourcade et al., 2010)(Sakuishi et al., 2010).

Figure 65 displays the characterisation of the CAR T-cells in regard to their exhaustion profile (D7). The absolute cell count of each subset was divided by the T-cell number, normalising thus for number disparities. The results are expressed as a ratio of each category being divided by the total number of T-cells. The three categories presented are double negative (PD1<sup>-</sup>Tim3<sup>-</sup>), single positive (PD1<sup>-</sup>Tim3<sup>+</sup>), and double positive (PD1<sup>+</sup>Tim3<sup>+</sup>). There were no PD1<sup>+</sup>Tim3<sup>-</sup> single positive cells in the raw data, and thus this category has not been included. The double negative category includes cells that are not exhausted, whereas the single and double positive populations consisted of T-cells with different severities of exhaustion.

In the absence of target cells, the majority of T-cells exhibited a single positive phenotype (Figure 65.A). The range for negative, single, or double positive populations was 0.1-0.22, 0.33-0.6, and 0.14-0.32, respectively. Hence, the T-cells were in a state of exhaustion. This pattern does not significantly alter in the presence of SupT1\_NT or SupT1\_WT target cells (Figure 65.B-C), except for the CARs L6, H2, H3, and H1. Although the double positive population of those CARs is comparable to the rest of the constructs, the proportion of negative to single positive is skewed in favour of the negative cells. The negative population for L6 (0.33), H2 (0.3), H3 (0.32), and H1 (0.29) is approximately 1.5-fold higher than the WT TA99-CAR (0.18) (Figure 65.C).

In the condition of SupT1-Distal, the exhausted single positive subset has been reduced, and in return the non-exhausted negative population has been enlarged compared to other target cells (Figure 65.D). The increase in the negative population is prominent for all the TA99-CARs apart from WT, H4, and L5, which is at least 1.5-fold less than that of the other TA99-CARs.

The exhaustion phenotype of T-cells co-cultured with SupT1\_Trunc target cells is consistent to the one observed in the presence of NT of WT expressing SupT1 cells. The cells are mainly in a single marker exhaustion stage, with the exception of L6, H2, H3, and H1 mutant CARs (Figure 65.E). The ratio of the negative population of L6, H2,

H3, and H1 CARs was 0.32, 0.33, 0.36, and 0.31 respectively, compared to the WT that was 0.23.

The T-cells were also exposed to the human melanoma cell line T618A (Figure 65.F). In this case, the proportion of the non-exhausted PD1<sup>-</sup>Tim3<sup>-</sup> cells was similar between the different CARs. However, we observed a decrease in the severely exhausted double positive population for the CARs L6, H3, and H1, which was approximately half of that of the WT TA99-CAR (0.22).

Finally, the profile of the aCD19-CAR was overall variable between conditions. However, the PD1<sup>-</sup>Tim3<sup>-</sup> was slightly increased, and the single positive population decreased in the presence of SupT1\_CD19 (Figure 65.G).

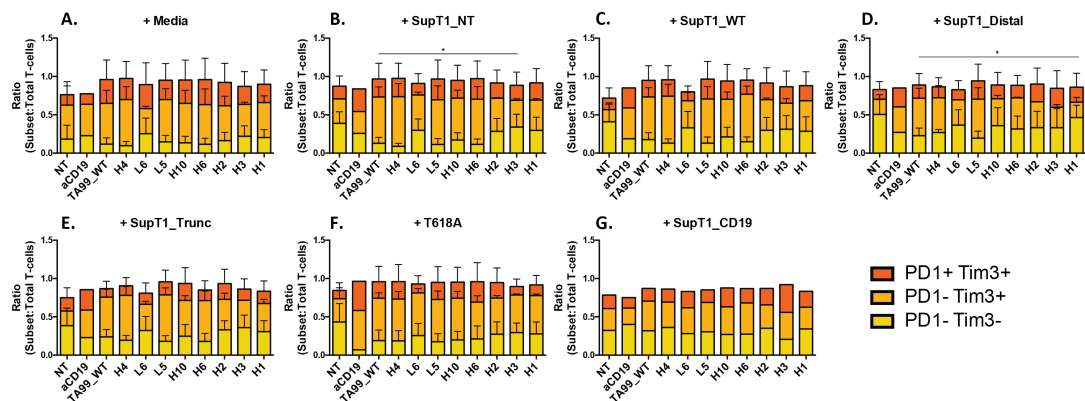


**Figure 65: Exhaustion profile of mutant TA99-CAR expressing T-cells.** The exhaustion status of the CAR T-cells was discriminated based on the exhaustion markers PD-1 and Tim3. The T-cells were placed into three categories: **1)** negative population PD1<sup>-</sup>Tim3<sup>-</sup> that constitutes the non-exhausted T-cells, **2)** the single positive population PD1<sup>-</sup>Tim3<sup>+</sup> that represents mildly exhausted T-cells, **3)** the double positive population PD1<sup>+</sup>Tim3<sup>+</sup> that represents the severely exhausted T-cells. **(A)** In the media condition, the cells were mainly single positive, with the ratio being approximately 3-fold higher than the negative or double population ratio. **(B-C)** This also applies for the condition of SupT1\_NT or SupT1\_WT as target cells. However, in these conditions the mutant CARs L6, H2, H3, and H1 exhibited 1.5-fold increase of the PD1<sup>+</sup>Tim3<sup>+</sup> population. The decrease in the single positive population between TA99\_WT and H3 is statistically significant, in the presence of SupT1\_NT, as calculated with a One-way Anova ( $p=0.418$ ). **(E)** Similarly, the CARs with the least exhausted phenotype in the presence of SupT1\_Trunc were also the L6, H2, H3, and H1, exhibiting at least 1.4-fold higher naive population compared to the WT CAR. **(D)** For the T-cells challenged with SupT1\_Distal, the population of single positive cells was reduced, and the negative population was increased in comparison to other target cell lines. The negative PD1<sup>-</sup>Tim3<sup>-</sup> population was increased for all the TA99-CARs by 1.5-fold approximately, with the exception of the WT, H4, and L5 CARs that exhibited a more modest increase. The single positive population was significantly decreased in the H1 CAR T-cells compared to the TA99\_WT ( $p=0.281$ ). **(F)** The non-exhausted population was similar in proportion between the TA99-CARs in the presence of T618A. However, the double positive population varied, with the mutant CARs L6, H3, and H1 bearing half of the severely exhausted T-cells compared to the other TA99-CARs. **(G)** Although the aCD19-CAR was variable in the different non-specific categories, overall the exhaustion negative population marginally increased in the condition of SupT1\_CD19. The exhaustion profiling was evaluated based on two repeats from two independent donors.

### 5.3.4.3 Conclusion

In an attempt to discern the behavioural differences between T-cells expressing the TA99-CAR mutants, we delineated their differentiation and exhaustion profile. However, the differentiation status between the CARs did not vary significantly. The majority of TA99-CAR T-cells were terminally differentiated (Tem) regardless which target they were exposed to. The only noteworthy observation is the marginal decrease in the differentiation of the T-cells bearing the L6, H2, H3, and H1 CAR.

A similar observation derived from the exhaustion study on the TA99-CAR T-cells. The majority of T-cells within each TA99-CAR condition was single positive for the exhaustion marker Tim3. However, in the presence of SupT1 target cells, the L6, H2, H3, and H1 CARs exhibited a decreased exhaustion phenotype compared to the other CARs. In the presence of the human melanoma cell line T618A, the proportion of double positive exhausted T-cells was lower for the four aforementioned CAR mutants. This is interesting, since the L6, H2 and H3 CARs were the ones with the superior cytotoxic capacity.

### 5.3.5 Correlation Between Affinity and Mutant TA99-CAR Efficacy

#### 5.3.5.1 Analysis of Correlation Between Affinity and CAR Efficacy

Despite the robust characterisation of the WT and mutant TA99-CARs, no pattern was discerned regarding the effect of the affinity on the CAR efficacy. Differences were observed between the mutants and the WT TA99-CAR. Nevertheless, there was no clear or consistent trend. We sought to ascertain that a potential affinity-efficacy interrelationship had not been overlooked. For this purpose, we calculated the correlation between the affinity, and the functional read-outs, FBK (D1, D3, D7) and cytokine secretion.

The correlation statistics are expressed based on the value  $r$  (Spearman). The value  $r$  ranges between 1 to -1. The value 1 signifies a perfect positive correlation between the parameters interrogated. The inverse correlation is expressed as -1, and 0 indicates the lack of correlation between the parameters. Consequently, a flat trend-line indicates no correlation. Whereas, a positive or a negative slope signifies a positive or inverse correlation, respectively.

Figure 66 illustrates the correlation between affinity (in log scale), and the cytotoxicity or cytokine secretion capacity. The slopes in the graph demonstrating the cytotoxicity at day 1 are flat, or slightly positive. For example, the slopes for SupT1\_Distal and T618A are subtly positive, with r-values 0.4 and 0.38 respectively (Figure 66.A). There is a weak positive correlation for the T618A target condition at the cytotoxicity assay (day 3) (Figure 66.B). The r-value is 0.42 for T618A. However, the SupT1\_Trunc condition appears to cause a significant inverse correlation between affinity and cytotoxicity with r-value -0.73. No correlation was observed in the conditions SupT1\_WT and SupT1\_Distal at day 3. At day 7, there is also no distinct correlation pattern, with SupT1\_Trunc causing negative value (-0.38), and SupT1\_WT causing a subtle positive correlation (0.25) (Figure 66.C). Nevertheless, the r-values were not significant unless otherwise underlined.

The correlation between affinity and cytokine secretion was equally inconsistent between each target condition. Regarding the IFN- $\gamma$  production, the T-cell capacity positively correlated (0.53) with the increase of  $K_D$  against the SupT1\_Trunc targets (Figure 66.D). On the contrary, the T618A caused an inverse correlation between IFN- $\gamma$  and affinity, with an r-value of -0.75 that was statistically significant. Finally, the IL2 production was not affected by the affinity, apart from the SupT1\_WT condition where there was a subtle positive correlation (0.32) (Figure 66.E).

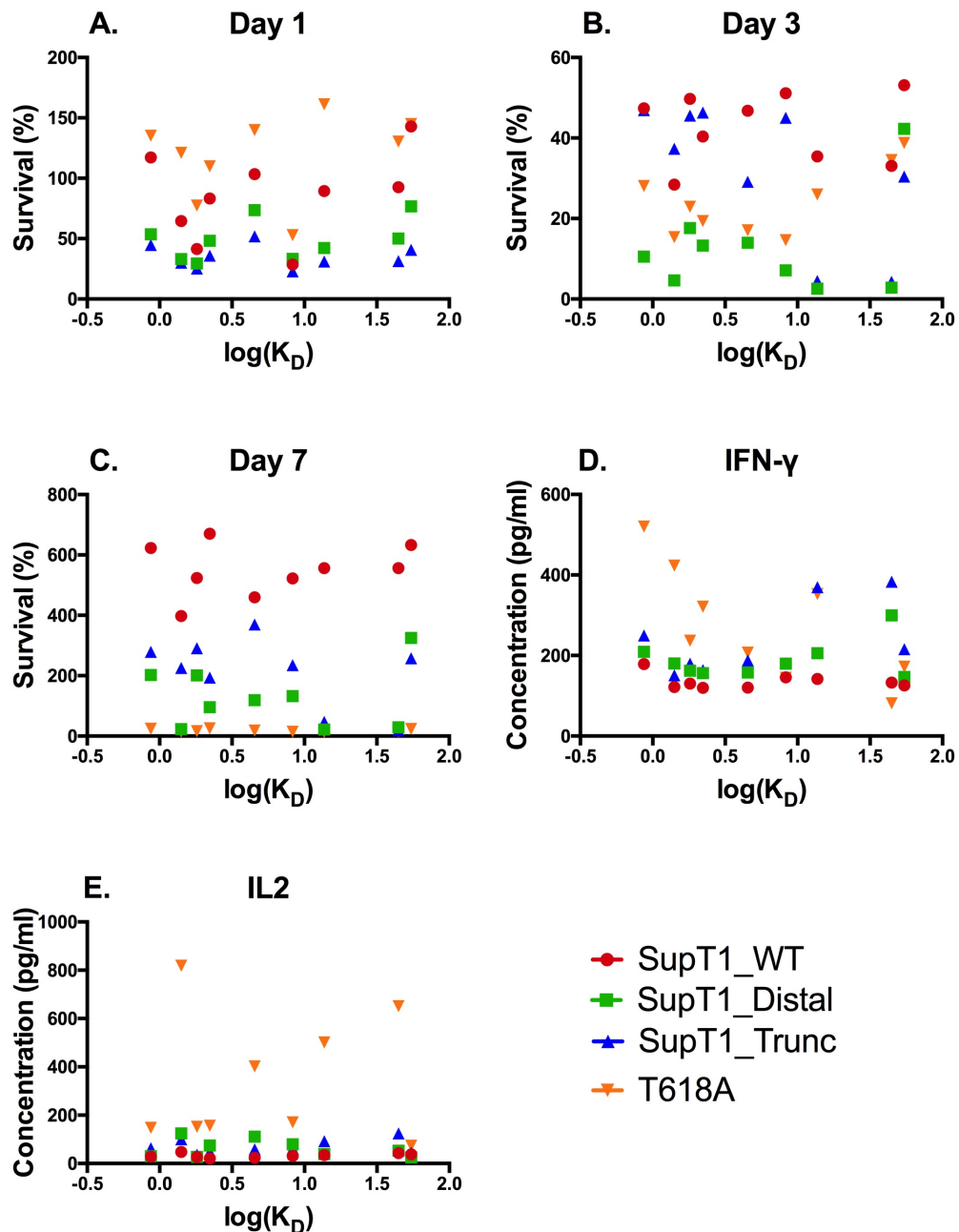


**Figure 66: Correlation between affinity and efficacy of the TA99-CAR mutants.** The statistical value for calculating the correlation is the r-value. A value >0-1 indicates a positive correlation, with 1 being the perfect correlation. Respectively, -1 indicates perfect inverse correlation. Zero r-value signifies lack of correlation. In the conditions SupT1\_Distal and SupT1\_WT, no correlation was observed between affinity and functionality. On the contrary, in the presence of SupT1\_Trunc there was negative correlation between K<sub>D</sub> and target survival. This correlation was statistically significant at day 3 ( $p=0.0311$ ), where the r-value was -0.73 (B). This was in accordance with the positive correlation we observed between IFN- $\gamma$  secretion and K<sub>D</sub> with SupT1\_Trunc cells as targets (D). The pattern was reversed for the target cell line T618A, where we observed a positive correlation between K<sub>D</sub> and cytotoxicity at day 1 and 3 (A-B), and a significant inverse correlation with IFN- $\gamma$  secretion ( $p=0.255$ ) (D).

### 5.3.5.2 Conclusion

Overall, there was no consistent pattern of affinity-efficacy correlation among the different target cell lines. However, there was some consistency in correlation

pattern for individual target cell lines. Specifically, there was no strong indication of correlation in the SupT1\_Distal or SupT1\_WT conditions throughout different functional read outs.

Regarding the CAR cytotoxicity, the T618A caused a mild positive correlation to  $K_D$ , which means that increasing the  $K_D$  results in increased target survival, and impeded target lysis. The negative effect of increased  $K_D$  in the CAR efficacy was also reflected in the inverse correlation observed between IFN- $\gamma$  secretion and affinity. The conclusion would be that decrease in affinity ( $\uparrow K_D$ ) hinders the T-cell function.

However, the opposite conclusion could be made based on the correlation observed in the presence of SupT1\_Trunc. In detail, the target survival was inversely correlated to the  $K_D$ , suggesting that decrease in affinity ( $\uparrow K_D$ ) enhances the T-cell cytotoxicity, and thus leads to lower target survival. This coincided with the positive correlation between  $K_D$  and production of IFN- $\gamma$ , which mean that a decrease in affinity also enhanced the cytokine secretion.

The two patterns observed for SupT1\_Trunc and T618A are conflicting. Additionally, the majority of the r-values were not supported by statistical significance. Hence, the correlation between CAR efficacy and affinity remains inconclusive.

## 5.4 DISCUSSION

The TA99-CAR was designed to target a predominantly intracellular antigen that resides on the cell surface of the target cells at low density. The CAR T-cells are not sensitive to low antigen density, and their cytotoxic threshold is 240-770 epitopes/cell (Stone et al., 2012)(Watanabe et al., 2015). However, cytokine secretion required 5320 epitopes/cell (Watanabe et al., 2015). There were no intermediate densities studies between 240-5320 in this study. However, no cytokine secretion was observed by Stone and colleagues at a density of 770 epitopes/cell. Hence, the threshold for CAR T-cell IFN- $\gamma$  secretion is within a 770-5320 epitopes/cell window. The Tyrp1 density varied between different human melanoma cell lines, and also varied between the fresh melanoma samples we processed (3.3.4.1 and 3.3.4.2). The density of the two melanoma cell lines that bore Tyrp1 on the surface was 1131.9 epitopes/cell and 4984.3 epitopes/cell. Primary melanomas either bore no Tyrp1 on their cell surface, or the density was below the 200 epitopes/cell threshold. Therefore, it was crucial to increase the sensitivity of the TA99-CAR.

Our approach was based on reports regarding TCRs that lose their sensitivity when the affinity is increased (Matsui et al., 1994) (González et al., 2005)(Thomas et al., 2011). The loss of serial triggering when the affinity is high is speculated to be the reason for the decrease in TCR sensitivity. The correlation between affinity and CAR efficacy is more controversial. Most studies regarding CAR affinity support that increase in affinity benefits the sensitivity as well (Chames et al., 2002)(Chmielewski et al., 2004)(Hudecek et al., 2013)(Caruso et al., 2015)(Liu et al., 2015)(Lynn et al., 2016). Only one study reported the opposite finding (Turatti et al., 2007).

The aforementioned studies on the CAR-to-affinity correlation harbour several caveats. For example, the stability of the scFv in the CAR binding moiety has not been taken into account as a possible confounding factor. Additionally, the majority of these studies examines only two or three CARs with different affinities. The pattern they observe could be a false positive, due to the limited amount of the data points observed. We sought to exclude as many confounding factors as possible. We engineered the affinity of a single scFv, in contrast to other publications where two distinct scFv were utilised. We also ascertained that the stability of the TA99 scFv

mutants were comparable to each other, and to the WT. In our study, the affinity correlation was examined on an affinity gradient of nine CARs in total. The lack of a wider affinity range in our data points constituted a drawback of this study.

The aim was to create an affinity range of TA99-CARs, and test the sensitivity of the different affinity mutants. Additionally, it was of interest to discern any trend in the effect of affinity towards the CAR efficacy. In order to investigate those two scientific questions, we mutated the CDR3 of TA99 heavy and light chain to obtain the affinity variant. The TA99 mutants were then tested with SPR to determine their binding kinetics. The WT TA99 has an affinity of 0.87nM, and a half-life of 186.3min. Of the eleven TA99 mutants tested, ten bound Tyrp1 at varying degrees of affinity, and one mutant lost its specificity to Tyrp1. In total, we acquired a range of ten mutants plus the WT, with an affinity range of 0.87-54.6nM. Regarding the association time for the serial triggering, the kinetic range is translated into a half-life range of 2.7-186.3min of interaction. Eight mutants and the WT TA99 were validated *in vitro*. Two mutants were omitted due to their resemblance to the WT kinetic profile. Their exclusion was based on the assumption that their behaviour would resemble that of the WT.

Although, it would be preferable to acquire mutants with affinity that reached the  $\mu\text{M}$  scale, it still bore an adequate width in the range of affinity and half-life. An advantage in our binding kinetic study was the lack of significant variation in the association rate. This limits the comparison to two parameters, the dissociation rate and the efficacy. Having big fluctuations in the association rate would render the extrapolation of a correlation more challenging.

The functional characterisation of the mutant CARs consisted of comparing their cytotoxicity and cytokine secretion capacity. The cytotoxicity was measured at day 1 and 7. In the day 1 time-point, a two nodule pattern was observed. According to this pattern, the increase of target survival was positively correlated with the increase in affinity, for an affinity window of 1.61-4.53nM (H4-H10 CARs). Then the target survival was drastically decreased, and the same positive  $K_D$ -target survival pattern was repeated for the affinity window of 8.3-54.5nM (H6-H1). This pattern was consistent among the Tyrp1 expressing SupT1 cells. In the presence of the T618A melanoma cells, all mutant CARs were superior to the WT.

However, in the more challenging assay of cytotoxicity measurement at day 7, the CARs that managed to sustain their targets at low levels were the H2 and H3 CARs. The affinity of the H2 and H3 mutants was 13.7nM and 44.6nM, respectively. The mutant CAR L6 was also capable of maintaining the SupT1\_Distal targets at low levels. Interestingly, the affinity of L6 (1.41nM) was approximately 10-fold higher than the affinity of H2, and 32-fold higher than the affinity of H3. Finally, all TA99-CARs were efficacious against T618A at day 7.

The mutant CARs H2 and H3 also produced the highest concentration of IFN- $\gamma$  in the presence of SupT1\_Trunc and T618A cells, compared to the other TA99-CARs. Specifically, in the presence of the T618A target cells, the WT and L6 also produced high amounts of IFN- $\gamma$ , 694.53pg/ml and 591.69pg/ml, respectively. Nevertheless, the H3 was the most efficacious with a secretion of 839.48pg/ml of IFN- $\gamma$ . The mutant CARs L6, H2, and H3 also secreted higher concentration of IL2.

The overall cytokine production was decreased compared to the initial experiments shown in 4.3.1.5. Although the ratio between effectors to targets was 1:1 for both experimental set-ups, the absolute number of cells differed. Initially,  $10^6$  T-cells were cultured with an equivalent number of targets. However, subsequent co-cultures were carried out in 96-well plates, and thus the absolute number was reduced to  $10^5$  effector cells per well. In subsequent work, we have observed that maintaining the ratio of effectors-to-targets, while changing the absolute number, affects the lytic and cytokine secretion capacity, which is positively correlated with increasing absolute number of cells.

Cytotoxicity and cytokine secretion assays indicate that the CARs L6, H2 and H3 are potentially superior compared to the WT TA99 and other mutants, although to reliably draw conclusions additional repeats are required. Based on our data, there was distinct pattern observed between affinity and its effect on CAR efficacy. In order to characterise the TA99-CAR T-cells further, we investigated their differentiation and exhaustion profile. There were not major differences in the differentiation and exhaustion status between the different CARs. The TA99-CAR T-cells existed mainly in a state of Tem. However, the mutant CARs L6, H2, H3, and H1 showed a subtly

elevated level of naive T-cells. Similarly, those four mutant CARs also exhibited a less exhausted phenotype compared to the other TA99-CARs.

Overall, the three mutant CARs L6, H2 and H3 bore improved cytotoxic capacity, and moderately increased cytokine secretion. Additionally, they exhibited marginally less differentiated and exhausted phenotype. Hence, the mutant CARs L6, H2, and H3 appear to have increased sensitivity compared to the WT TA99 CAR, since they were efficacious against the SupT1 cells expressing Distal and Trunc Tyrp1. The density of Tyrp1 on the cell surface of SupT1\_Distal and SupT1\_Trunc is close to the lower detection limit of CAR recognition (175.7 and 308.2 epitopes/cell respectively). Hence, the aim to increase the TA99-CAR sensitivity was achieved.

Our second aim was to identify a correlation pattern between the affinity and the CAR efficacy. Since no such pattern was identified based on the data examination, we also calculated the correlation between the affinity and efficacy using the GraphPad Prism software. In the presence of the low density cell line SupT1\_Trunc, lower affinity positively correlated with the increase in cytotoxicity and IFN- $\gamma$  secretion. The opposite trend was observed for the human melanoma cell line T618A, which bears an antigen density of 1131 epitopes/cell. In this case, we observed that lower affinity mildly correlated with lower CAR cytotoxic capacity, and decrease production of IFN- $\gamma$ . The correlation data were mostly not statistically significant, and the correlation values were low, which rendered the results inconclusive.

We envisioned that decreasing the CAR affinity would enable the serial triggering to occur, and hence increase the CAR sensitivity. Nevertheless, we observed no total positive or inverse correlation. Bearing in mind the limitations of this study, the results showed no trend between the affinity and CAR efficacy. The mutant CARs L6, H2, and H3, which appear to be more efficacious than the original TA99 CAR, are spread apart within the affinity range instead of clustering in close affinity values.

**CHAPTER 6:**  
**FINAL DISCUSSION**

## CHAPTER 6: FINAL DISCUSSION

### 6.1 SUMMARY OF RESULTS ON THE TYRP1 ANTIGEN

Melanoma is the 9<sup>th</sup> most common cancer in Europe, and 19<sup>th</sup> worldwide. According to the statistic reviews, the annual melanoma incidences have been tripled in the last 30 years (Reed et al., 2012). The efforts of the scientific community led to the development of chemotherapy, immunotherapy, small molecule inhibitors, and ACT for melanoma patients. Despite the development of new therapeutic strategies, these strategies extend the life of malignant-melanoma patients for just a few months. Hence, more efficacious and less toxic therapeutic regimens are necessary.

The CAR field is rapidly expanding, and is also very promising as a cancer therapeutic regimen. However, the difficulty of designing a CAR is in identifying an optimal antigen target. This optimal target should be expressed only on the surface of the tumour cells, and not the healthy tissue. Since the tumour is derived from the healthy cells identifying such optimal targets is not feasible. Additionally, the pool of antigenic candidates for CAR targeting is limited to antigens expressed on the cell surface, since CARs are unable to detect intracellular antigens.

Nevertheless, there have been reports claiming that intracellular proteins can reside on the cell surface at low antigen densities. Targeting such antigens with CAR T-cells would expand the group of potential CAR antigen candidates. The melanosomal enzyme Tyrp1 constituted an intriguing candidate for this project. Although it resides on the membrane of the melanosome organelles in melanocytes, it has been shown that approximately 2% of Tyrp1 is present on the cell surface (Yiqing Xu et al., 1997).

Although the trafficking of Tyrp1 to the surface is unclear, it is postulated that Tyrp1 is present on the plasma membrane due to saturation of the secretion pathway, or the fusion of melanosomes to the cell membrane, (Jimbow et al., 1997). Truschel and colleagues showed that internalisation of the surface Tyrp1 results in recycling back to the cell surface instead of its transfer to the melanosomes (Truschel et al., 2009). This indicates that there is a pool of Tyrp1 molecules that are present on the plasma membrane and might play a role, however this role is unknown.

The development of anti-Typr1 auto-antibodies by melanoma patients first insinuated the presence of Typr1 on the cell surface (Mattes et al., 1983, Kemp et al., 1998). The melanoma tumour rejection in mice by an anti-Typr1 antibody (TA99 clone) provided additional evidence (Hara et al., 1995) (Patel et al., 2008) (Ly et al., 2013). Of the total Typr1 protein pool, 2% is present on the cell surface (Yiqing Xu et al., 1997). In addition, freshly isolated melanoma cells exhibit 1000-fold higher MFI than melanoma cells cultured in vitro (Patel et al., 2008). Nevertheless, little information is available regarding the density of Typr1 on the plasma membrane.

Hence, our first milestone was to validate Typr1 as a potential CAR target. Specifically, we aimed to confirm the expression of Typr1 on the surface of melanoma cells, and quantify the molecules of Typr1 that are present on the cell surface. Determining the Typr1 antigen density is crucial for the validation of Typr1 as a potential CAR antigen. First, Stone and colleagues reported that the sensitivity threshold of a CAR is approximately 770 epitopes/cell (Stone et al., 2012). The CAR was cytotoxic against the 770 epitopes/cell antigen density target, but not against targets with 300 epitopes /cell surface density. The sensitivity threshold against was higher for the production of cytokines, and the CAR did not release IFN- $\gamma$  against the 770 epitopes/cell surface antigen density target. A similar pattern was observed by Watanabe and colleagues, however the antigen densities slightly different. CAR cytotoxicity was observed against targets bearing 240 epitopes/cell. However, for cytokine production more than 5320 epitopes/cell were required to elicit a CAR T-cell response (Watanabe et al., 2015). There were no intermediate densities studied so the actual threshold for cytokine production is not known. The antigen density of the CD19 antigen, which has been successfully targeted with CAR T-cells in the clinic bears an antigen density of of  $13 \times 10^3$  molecules per CLL cell (Ginaldi et al., 1998).

In order to investigate whether the antigen density of Typr1 is within the CAR T-cell sensitivity window, we developed a labelling technique for signal enhancement and antigen quantification. Five human melanoma cell lines were interrogated for expression of Typr1. Of those five cell lines, two did not express Typr1 as shown with intracellular labelling, thus the melanoma cell line prevalence of Typr1 expression is 60%. The density of Typr1 on the surface of the three melanoma cell lines, which

expressed the antigen, was determined. Specifically, the antigen density was 1132 epitopes/cell, 18 epitopes/cell, and 4984 epitopes/cell for T618A, Mel280, and Mel290, respectively. Hence, approximately 66% of the human melanoma cell lines studied had Tyrp1 present on their cell surface, at a density above the detection limit. Of course, the sample size is limited, thus the percentage of 66% is preliminary and not conclusive.

Although the measurement of Tyrp1 antigen density on the surface of melanoma cell lines is important, it is crucial to determine the density on primary melanoma samples. In total we screened samples from four melanoma patients. Three patients underwent an excision of melanoma metastatic LN, and the fourth patient underwent an excision of a subcutaneous lesion. The patient MM25 had two lesions excised, from both the right and left axillary LN. The total amount of samples that was thus analysed was five. The samples were first interrogated for the expression of Tyrp1 through intracellular labelling. The percentage of melanoma cells that expressed Tyrp1 varied between donors with a range of 15.4-60.3%. It is worth mentioning that very few cells were acquired from sample MM20, so no reliable conclusions could be drawn.

All five samples showed some expression of Tyrp1, however, the presence of Tyrp1 on the surface was less prevalent. The sample MM20 had no cell events, so it is excluded from the result interpretation. Two additional samples from different patients had a low cell number, but Tyrp1 was absent from their cell surface. Finally, the patient bearing the two lesions in the axillary LN showed heterogeneity. The left axillary LN had no evidence of surface Tyrp1. On the contrary, the right axillary LN had a 3.3% population positive for surface Tyrp1. The density of that population was 162 epitopes/cell, which is marginally lower than the reported CAR cytotoxicity threshold.

In summary, the antigen density of Tyrp1 on melanoma cell lines was 66% prevalent, with an antigen density within the CAR T-cell cytotoxic level. However, the prevalence of surface Tyrp1 on primary melanoma samples was 25% in the four samples analysed. The melanoma subpopulation that had Tyrp1 present on the surface bore 162 epitopes/cell, which is below the CAR detection limit. Additionally, the presence

of surface Tyrp1 was heterogeneous. The primary melanoma samples expressed varying levels of Tyrp1 as shown with intracellular labelling for Tyrp1. Also, the samples derived from the MM25 patient were heterogeneous, with one lesion bearing no surface Tyrp1 and the other lesion bearing a subpopulation of surface Tyrp1 cells. This subpopulation constituted only 3.3% of the whole melanoma population. Hence, the presence of Tyrp1 on the cell surface shows intra- and inter-tumour heterogeneity, as well as heterogeneous expression between different patients. Unfortunately, only a limited number of melanoma samples were analysed, due to difficulty in acquiring the samples. Analysis of additional samples would be required to confirm the prevalence and heterogeneity of surface Tyrp1, however due to the difficulty in acquiring the samples this might not be feasible.

## **6.2 SIGNIFICANCE OF RESULTS ON THE TYRP1 ANTIGEN**

Using Tyrp1 as a melanoma target raises two concerns. First, Tyrp1 is not exclusively expressed on melanoma tissue, but in healthy melanocytes too. Consequently, treatment targeting the Tyrp1 antigen can affect the healthy tissue, causing vitiligo, uveitis or hearing loss. Tyrp1 auto-antibodies have been shown to cause vitiligo (Kemp et al., 1998). TA99 antibody administration caused a small scale vitiligo in mice treated with the high dose of the antibody (Hara et al., 1995). In a phase I clinical study, anti-Melan-A TCR T-cells were used against melanoma, with mild adverse effects noted, and no autoimmunity observed (Mackensen et al., 2006). Unfortunately, Mackensen and colleagues observed a selective decrease of the antigen in the post-infusion metastasis.

This leads to a second concern regarding the level of Tyrp1 in the metastatic tissue. Although, Tyrp1 was shown to be the dominant glycoprotein in normal melanocytes and pigmented melanomas (Tai et al., 1983), the protein levels decrease in the amelanotic stages (Orlow et al., 1998). The published data are contradictory. Bolander and colleagues demonstrated that the majority of melanomas are Tyrp1 positive, however its expression level is inversely correlated with cancer progression (Bolander et al., 2008). On the contrary, another study showed that Tyrp1 is positively correlated with tumour stage and progression (Holzmann et al., 1987). Despite the

fact that Tyrp1 is characterised in all of the studies as an abundant molecule in both healthy and melanoma tissue, it is inconclusive how it correlates to the tumour progression.

Our results support the inverse correlation between Tyrp1 expression and tumour progression, as the percentage of Tyrp1 expression was low and heterogeneous. Based on our current results, Tyrp1 constitutes a suboptimal target on all three levels of validation: prevalence, heterogeneity, and antigen density. Hence, an anti-Tyrp1 CAR, without additional therapeutic regimens, would not be a viable product for the treatment of melanoma patients.

There are a few potential strategies that could bestow an additive effect on the anti-Tyrp1 CAR treatment. First of all, the TA99-CAR could be incorporated into an OR logic gate, where the T-cells would target Tyrp1 and another melanoma antigen. The additional antigen would facilitate the lysis of Tyrp1 negative cells, and thus address the heterogeneity of the antigen. OR gate CAR T-cells have been previously engineered for the treatment of B-cell malignancies, and target CD22 and CD19 positive tumour cells (Pule et al., 2016).

Alternatively, increase in melanogenesis would lead to upregulation of tyrosinase, Tyrp1, and Tyrp2, and consequently ameliorated expression of Tyrp1 on the cell surface. All three proteins are regulated by the Microphthalmia-associated transcription factor (MITF). MITF is the key regulator of melanocyte pigmentation and is activated by environmental factors, such as UV irradiation (Yamaguchi et al., 2007). Several stimuli have been shown to activate MITF, and lead to increased melanogenesis. One of the MITF inducing agents is forskolin, which facilitates as a melanocyte-stimulating hormone agonist (Lekmine and Salti, 2008). Forskolin is a natural compound derived from the plant *Coleus forskohlii* (Kanne et al., 2015). Other natural compounds have been shown to increase the melanogenesis through MITF induction, such as cholecalciferol (vitamin D3), Ginsenosides Rb1 and Rg1 extracted from *Panax ginseng*, and the retinoic acid (Oikawa and Nakayasu, 1974)(Lotan and Lotan, 1980)(Tomita et al., 1986)(Lin et al., 2014).

A small molecule derived from a library comprised of carboxylic acid and amine was also shown to enhance the melanogenesis. This small molecule (A7) increased the

production of melanin by 1.8 fold (McNaughton et al., 2009). Tyrosinase is the crucial enzyme for the melanin production, however its dependence on Tyrp1 for heterodimerisation and stabilisation indicates that Tyrp1 is present in order for melanin production to occur (Kobayashi et al., 1998).

Tyrp1 constitutes a proof of principle for targeting intracellular antigens that are present on the cell surface at low antigen density. It has been previously shown, that tumour cells have proteins on their surface that are conventionally intracellular. Examples of such potential antigens are heat-shock proteins (Ferrarini et al., 1992), cytokeratins (Gires et al., 2006), and nucleolin (Christian et al., 2003). This observation challenges the boundaries of CAR T-cell application, opening a new field of potential targets.

### **6.3 SUMMARY OF RESULTS ON THE AFFINITY CORRELATION TO CAR EFFICACY**

The antigen Tyrp1 does not constitute a promising target for CAR T-cell clinical trials. However, it belongs to the group of intracellular proteins that reside on the cell surface. Hence, an anti-Tyrp1 CAR was designed to interrogate the possibility of targeting a low-density target with a potential high circulation rate through the membrane. To our knowledge, targeting a low-surface density intracellular protein is a novel approach, and has not been described before.

The anti-Tyrp1 CAR was a second generation CAR, bearing the scFv of the TA99 clone. TA99 was utilised to successfully eradicate B16 melanoma tumours in an *in vivo* model (Hara et al., 1995). The specificity of TA99 as a scFv was validated with flow cytometry and confocal microscopy. In order to validate the TA99-CAR and gain an insight into the CAR sensitivity threshold, we engineered four cell lines that expressed either WT or mutations of Tyrp1. The cytoplasmic domain of Tyrp1 dictates the efficient trafficking of the protein to the melanosomes (Vijayasaradhi et al., 1995). The cell lines expressing Proximal, Distal, or Trunc Tyrp1 bore the cytoplasmic domain at a proximal, distal position to the membrane, or the domain was altogether omitted. The antigen density of the cells expressing Proximal Tyrp1 was negligible. However, the density for the cells expressing WT, Distal, and Trunc was 151 epitopes/cell, 176 epitopes/cell, and 308 epitopes/cell, respectively.

The TA99-CAR T-cells failed to lyse the SupT1 cells expressing the WT Tyrp1, which had the lowest antigen density. However, the CAR T-cells lysed the targets expressing the Distal and Trunc Tyrp1. Hence, the cytotoxic threshold of the TA99-CAR was 176 epitopes/well. The difference in density between the WT and Distal targets is marginal with only 20 epitopes/cell disparity. The ability of the CAR to lyse only the latter might be a result of the minimal density difference. Alternatively, the rate of circulation through the membrane might be different for the two Tyrp1 proteins. The Tyrp1 molecules on the cell surface will stochastically bind to the CAR and remain bound for a half-life of 186min. A high circulation rate would lead a faster rate of replenishment of Tyrp1 antigens for the T-cell to bind, and undergo signal triggering.

The CAR sensitivity was higher for the secretion of IFN- $\gamma$ . There was no cytokine secretion against the cells expressing Distal Tyrp1, and the secretion against Trunc was marginally higher than the baseline. The CAR T-cells secreted IFN- $\gamma$  cytokine in the presence of the T618A melanoma cell line, which bore 1132 epitopes/cell. This observation is in accordance with published literature, where the CAR T-cell cytotoxic threshold was lower than the level for IFN- $\gamma$  secretion. According to Watanabe and colleagues, the CAR T-cells were unable to produce cytokines against targets with a 240 epitopes/cell density, but secreted IFN- $\gamma$  against a 5320 epitopes/cell density cell line. There was no intermediate density (Watanabe et al., 2015). Similarly, another report showed that there was no IFN- $\gamma$  CAR T-cell production against a cell line with density of 770 epitopes/cell (Stone et al., 2012). In this study we narrow the window of the cytokine production threshold to lower than 1132 epitopes/cell. Hence, the threshold lies within the 770-1132 epitope/cell, assuming there is no significant variation in the sensitivity between different CARs. The CARs utilised in the two studies, and our project were 2<sup>nd</sup> generation consisting of CD28 and CD3 $\zeta$ .

TCR proteins are capable of recognizing low-density antigens. TCR activation is mediated by kinetic segregation (van der Merwe et al., 2000). Upon synapse formation the two membranes are in close proximity with the MHC-TCR complex being 15nm, compared to the CD45 phosphatase, which is approximately 28-50nm (van der Merwe et al., 1995) (McCall et al., 1992). The membrane proximity leads to

the exclusion of CD45 from the synapse, and consequently increased concentration of kinases (Burroughs et al., 2006).

Since, TCR and CAR molecules are activated in a similar manner we seek to imitate the properties that bestow sensitivity on the TCR. The serial triggering renders the TCR sensitive to low antigen targets. According to the serial triggering model, a single MHC-antigen complex can trigger up to 200 TCRs (Valitutti et al., 1995). The optimal dwell time in order to achieve serial triggering is crucial for both TCR and BiTEs (González et al., 2005) (Bortoletto et al., 2002). Thomas and colleagues demonstrated that TCR-T cells with a dissociation constant  $K_D$  2.5nM, which is higher than the normal affinity range (1 $\mu$ M-100 $\mu$ M), required 2-log higher antigen concentration to cause the same response to the original TCR (KD 1.8  $\mu$ M) (Thomas et al., 2011). They showed that incremental increase of affinity is inversely correlated to the ability to recognise low density antigen. The increased affinity also increased the interaction half-life by 300-fold, impeding thus the serial triggering.

The kinetic properties of the TCR and CAR proteins vary significantly. Although the affinity range of the TCR is 1-100 $\mu$ M, the affinity range of CARs is 1-100nM (Poulsen et al., 2007)(Poulsen et al., 2011). According to the serial triggering model, we postulated that decreasing the affinity of the CAR would result in increased its sensitivity. However, the majority of the published studies report that the affinity is positively correlated with the CAR efficacy (Chames et al., 2002)(Chmielewski et al., 2004)(Hudecek et al., 2013)(Caruso et al., 2015)(Liu et al., 2015)(Lynn et al., 2016). Only one study supports the inverse correlation between affinity and CAR capacity (Turatti et al., 2007).

All the aforementioned studies have several disadvantages and inconsistencies. For example, confounding factors, such as the stability of the scFvs, have not been taken into consideration. Stability discrepancy can lead to different cytotoxic profiles between CARs, which would not be a result of the affinity, but improper folding or aggregation of the scFv. In half the publications, the scFv that bestows the specificity to the CAR are derived from different antibody clones, and could potentially recognise distal epitopes. Epitopes proximal to the target cell surface are superior for CAR lysis, thus epitope distance constitutes an additional confounding factor (Guest

et al., 2005) (Haso et al., 2013). Finally, a major drawback in the published literature, is that four of those studies have based their conclusions on solely two affinity variants, with no data for intermediate values. Hence, no trend or optimal value can be extrapolated, apart from a binary indication of high or low affinity superiority. A more thorough and consistent investigation on the correlation between affinity and CAR efficacy was necessary.

The second milestone of this project was the investigation of the effect affinity has on the efficacy of the TA99-CAR. This milestone was divided in two aims, increasing the sensitivity of the TA99-CAR and discerning a trend between affinity and efficacy. In order to acquire an affinity range, we mutated the CDR3 of the TA99 heavy and light chain. The affinity of the TA99 WT and mutant scFvs was measured with SPR. The affinity of the WT TA99 was 0.87nM, and we obtained two mutants with marginally higher affinities (0.75nM, 0.68nM). These two mutants were excluded from functional studies due to their kinetic similarities to the WT. The affinity range of the TA99 mutants was 1.41-54.6nM. The on-rate was consistent between the WT and mutants. On the contrary, the disparity of the off-range was wide, resulting in a range of half-life between 2.7-186.3min.

The WT and mutant TA99-CARs were tested for cytotoxicity, cytokine production, as well as differentiation and exhaustion profile against a range of antigen density targets. There was a two-nodule pattern observed for the cytotoxicity at day 1. The target lysis correlated with increase in affinity for the affinity range of 1.61-4.53nM, with the 4.53nM CAR being the least efficacious. The next affinity point CAR (8.3nM) successfully lysed the cells, and the lysis is decreased as the  $K_D$  is increased from 8.3nM to 54.5nM. This pattern was observed against the WT, Distal and Trunc expressing cell lines. The cytotoxicity against the T618A target cells was similar between the TA99 mutants, and consistently superior to the WT CAR.

The pattern of cytotoxicity at day 7 did not constitute of two maximums. The L6, H2, and H3 mutant CARs, which had an affinity of 1.41nM, 13.7nM, and 44.6nM, were the only CARs that sustained the Distal target cells at low levels, despite the high target cell proliferation rate. Only the H2 and H3 CARs were efficacious against the Trunc cells. Interestingly, all CARs, including the WT and mutants, lysed the higher

density target T618A, suggesting that there is no optimal CAR affinity for antigen densities above 1000 epitopes/cell.

The mutant CAR H3 produced the highest concentration of IFN- $\gamma$  against the Distal Tyrp1 targets. For the marginally higher density targets, which are the Trunc cells, both H2 and H3 secreted IFN- $\gamma$  in the cell supernatant. Finally, in the presence of the T618A cells, the three mutant CARs, L6, H2, and H3 produced the highest concentration of cytokine. Although this suggests that the lower affinity CAR is more sensitive against low antigen density for cytokine production, there was no such pattern observed between the intermediate affinity CARs. The pattern was reversed for the production of the IL2 cytokine, with L6 being the most sensitive against the low antigen Distal cells. The same three CARs showed subtly elevated levels of the Tnaive cell population, as well as a marginally reduced exhaustion profile.

To recapitulate, our aim was to improve the CAR sensitivity, and also determine a positive or negative correlation between the affinity of a CAR and its efficacy. The data suggest an increase in sensitivity for the CAR mutants L6, H2, and H3. Their efficacy increased with the increment in antigen density. The cytotoxic threshold of the WT CAR at the day 7 time-point was 1132 epitopes/cell, in contrast to the threshold of the three mutants that was decreased to 176 epitopes/cell. The cytokine production threshold varied between the CARs and the cytokines. The threshold of the H3 mutants was 176 epitopes/cell for the production of IFN- $\gamma$ . On the contrary, the threshold of H2 and L6 was 308 epitopes/cell and 1132 epitopes/cell, respectively. Regarding the production of IL2, the L6 mutant was the most sensitive with observed IL2 secretion at 176 epitopes/cell, whereas the threshold of the H2 and H3 mutants was 308 epitopes/cell. For either cytokine, the secretion was the most efficacious for the high density target T618A (1132 epitopes/cell). Nevertheless, due to large error bars and lack of statistical significance in some conditions more repeats are required to render the results conclusive.

Our second aim was to determine whether the affinity is inversely or positively correlated to the CAR efficacy, however, no consistent pattern was observed. To ascertain that no pattern existed, the correlation curves between the affinity and the different efficacy assays were calculated. There was an inverse correlation between

cytotoxicity and affinity at the 308 epitopes/cell density. The opposite observation was seen for the 1132 epitopes/cell target cell line. The correlation values were low and not statistically significant. Hence, there was no evidence of strong correlation between affinity and CAR efficacy.

#### **6.4 SIGNIFICANCE OF RESULTS ON THE AFFINITY CORRELATION TO CAR EFFICACY**

We aimed at eliminating the majority of the confounding factors that were part of the affinity-efficacy literature to date. First of all, the same scFv was used across the affinity range. The mutants were obtained by mutating the CDR3 residues, in contrast to Liu and colleagues that utilised mutants derived from antibody humanisation (Liu et al., 2015). Antibody humanisation implements mutations in the framework of the antibody, rather than the CDR3. Hence, the lower affinity is potentially due to decreased stability of the antibody. We also ascertained that the stability of the mutants was not a confounding factor in our study, by measuring the thermal stability of the TA99 mutants by DSF. The denaturation temperature ranged between 55.92°C to 56.83°C, which is a minimal change in thermal stability.

The affinity depends on the association and dissociation rate. However, each parameter could affect the T-cell signalling in different ways. Our theory is based on the serial triggering model. The serial triggering model is affected by the dissociation rate, which dictates the half-life of interaction between the antigen and the CAR. It is optimal that the affinity gradient we acquired had a narrow range of association rate, and a wide range of dissociation rate. This allowed us to examine the effect of the half-life on the CAR sensitivity, without the association rate constituting a confounding factor.

Another important advantage of our study was the amount of affinity mutants interrogated. The majority of the literature implemented two CARs with different affinities, in order to investigate the relation between the affinity and the capacity of the CAR. The limited amount of data-points, combined with potential discrepancies in the scFv stability constitute significant drawbacks in the current literature. In our study, we implemented nine affinity variants. The higher amount of data-points

provided insight into the intermediate affinities, and constituted a more complex and reliable platform for detection of an affinity-efficacy correlation.

Finally, the antigen density utilised in the literature is generally high, with at least a 100-fold increase in MFI between the targets and the negative control. This density is not challenging to the CAR T-cells, and fails to provide insight into the lower threshold of the CAR sensitivity. We engineered the SupT1 cell line, which is inherently Tyrp1 negative, to express very low, or low Tyrp1 antigen density. The antigen density range we used was 151-1132 epitopes/cell. Consequently, we determined the CAR cytotoxic sensitivity to be 176 epitopes/cell, which is lower than reported (Watanabe et al., 2015). Also we narrowed the threshold for cytokine production within a window of 770-1132 epitopes/cell. The lack of cytokine production at 770 epitopes/cell was published by Stone and colleagues (Stone et al., 2012).

There were also some limitations in this project. The range of affinities we interrogated was 0.87-54.6nM. This resulted in a significant decrease of the interaction half-life from 186.3min to 2.7min. Nevertheless, the affinity range is not within the TCR 1-100 $\mu$ M. It would be interesting to expand the range to the  $\mu$ M scale, in order to discern the entire perspective of CAR T-cell behaviour in regards to the affinity. To this end, it would also be useful to gain an insight into the effect of the association rate on the CAR efficacy. This was not possible in our study, since the range of the association rate was narrow.

Overall, our approach was superior to the published literature. We excluded many of the aforementioned confounding factors, and we also implemented a higher amount of affinity data-point, in order to increase the accuracy of the data. Our data showed that there was no strong correlation between the affinity and the CAR efficacy. The three CARs that were shown to bear an improved capacity were spread within the affinity range (1.41nM, 13.7nM, 44.6nM), showing no pattern in the effect of affinity on the efficacy of the TA99-CAR, however additional repeats are required to render the results conclusive. Additionally, an unknown confounding factor could be the key player in mediating differences between the CAR mutants rather than the affinity. A potential confounding factor might be the CAR density. Although the CAR density was

not quantified, there was no correlation between the CAR efficacy and the MFI of the CAR expression as examined with calculating correlation curve (data not shown).

## 6.5 FUTURE PERSPECTIVES

The data from this study demonstrate the lack of correlation between the affinity of a CAR and its efficacy. Although the CAR efficacy was increased in some mutants, this capacity enhancement did not correlate to the affinity. In order to render this observation reproducible, further work is required.

First of all, a wider range would be optimal. It would be interesting to interrogate a CAR affinity range between  $>1\text{nM}$ - $1\mu\text{M}$ . The decrease of the CAR affinity within the TCR  $\mu\text{M}$  scale would enable the direct comparison between CAR and TCR sensitivity, and the validation of the serial triggering importance in CAR triggering.

The serial triggering model is based on the dissociation rate of the TCR, which dictates the interaction time between the TCR and the antigen. However, it would also be interesting to investigate the role of the association time on the CAR efficacy. It has been shown that TCRs with association rate higher than the diffusion-to-the-membrane rate can rebind the same antigen, effectively increasing the aggregate dwell time (Aleksic et al., 2010). It would be interesting to investigate the rebinding phenomenon in CARs, and examine its role in the sensitivity.

Since the manipulation of the CAR efficacy is speculated to affect the CAR sensitivity, it should be scrutinised in varying antigen densities. Although we implemented four distinct antigen densities in our study, there was no data-points between 308 epitopes/cell and 1132 epitopes/cell. The threshold of cytokine production lies within the range 770-1132 epitopes/cell. Hence, additional information between the 308-1132 epitopes/cell is crucial. Also, the CAR density could be introduced as an additional parameter, since it could be a potential confounding factor.

Finally, there is no guarantee that the behaviour of all CARs in regards to affinity is the same. In order to establish an optimal affinity range for future CAR studies and clinical trials, it is crucial to demonstrate that the same pattern is consistent for all CARs. In order to claim a universal optimal affinity range, additional CARs should be examined bearing a plethora of scFv. This would increase the reliability of the

suggested range. Investigating the optimal affinity value for each CAR is laborious, time- and cost-ineffective. The determination of a universal affinity range that is optimal for CAR T-cells would render the design and production of CARs more high-throughput, reducing the time and cost between development and clinical application.

## REFERENCES

- Abad, J.D., Wrzensinski, C., Overwijk, W., De Witte, M.A., Jorritsma, A., Hsu, G., Gattinoni, L., Cohen, C.J., Paulos, C.M., Palmer, D.C., et al. (2008). T-Cell Receptor Gene Therapy of Established Tumors in a Murine Melanoma Model. *J. Immunother. Hagerstown Md* 1997 *31*, 1–6.
- Ahmadzadeh, M., Johnson, L.A., Heemskerk, B., Wunderlich, J.R., Dudley, M.E., White, D.E., and Rosenberg, S.A. (2009). Tumor antigen-specific CD8 T cells infiltrating the tumor express high levels of PD-1 and are functionally impaired. *Blood* *114*, 1537–1544.
- Ahmed, N., Brawley, V.S., Hegde, M., Robertson, C., Ghazi, A., Gerken, C., Liu, E., Dakhova, O., Ashoori, A., Corder, A., et al. (2015). Human Epidermal Growth Factor Receptor 2 (HER2) –Specific Chimeric Antigen Receptor–Modified T Cells for the Immunotherapy of HER2-Positive Sarcoma. *J. Clin. Oncol.* *33*, 1688–1696.
- Aivazian, D., and Stern, L.J. (2000). Phosphorylation of T cell receptor zeta is regulated by a lipid dependent folding transition. *Nat. Struct. Biol.* *7*, 1023–1026.
- Akiba, H., Oshima, H., Takeda, K., Atsuta, M., Nakano, H., Nakajima, A., Nohara, C., Yagita, H., and Okumura, K. (1999). CD28-independent costimulation of T cells by OX40 ligand and CD70 on activated B cells. *J. Immunol. Baltim. Md 1950* *162*, 7058–7066.
- Alam, S.M., Travers, P.J., Wung, J.L., Nasholds, W., Redpath, S., Jameson, S.C., and Gascoigne, N.R.J. (1996). T-cell-receptor affinity and thymocyte positive selection. *Nature* *381*, 616–620.
- Aleksic, M., Dushek, O., Zhang, H., Shenderov, E., Chen, J.-L., Cerundolo, V., Coombs, D., and van der Merwe, P.A. (2010). Dependence of T Cell Antigen Recognition on T Cell Receptor–Peptide MHC Confinement Time. *Immunity* *32*, 163–174.
- Aleksic, M., Liddy, N., Molloy, P.E., Pumphrey, N., Vuidepot, A., Chang, K.-M., and Jakobsen, B.K. (2012). Different affinity windows for virus and cancer-specific T-cell receptors: implications for therapeutic strategies. *Eur. J. Immunol.* *42*, 3174–3179.
- Ali, S.A., Shi, V., Maric, I., Wang, M., Stroncek, D.F., Rose, J.J., Brudno, J.N., Stetler-Stevenson, M., Feldman, S.A., Hansen, B.G., et al. (2016). T cells expressing an anti-B-cell maturation antigen chimeric antigen receptor cause remissions of multiple myeloma. *Blood* *128*, 1688–1700.
- Alvarez-Vallina, L., and Hawkins, R.E. (1996). Antigen-specific targeting of CD28-mediated T cell co-stimulation using chimeric single-chain antibody variable fragment-CD28 receptors. *Eur. J. Immunol.* *26*, 2304–2309.
- Alvarez-Vallina, L., and Russell, S.J. (1999). Efficient Discrimination between Different Densities of Target Antigen by Tetracycline-Regulatable T Bodies. *Hum. Gene Ther.* *10*, 559–563.

Ambrosini, G., Adida, C., and Altieri, D.C. (1997). A novel anti-apoptosis gene, survivin, expressed in cancer and lymphoma. *Nat. Med.* 3, 917–921.

Ando, H., Kondoh, H., Ichihashi, M., and Hearing, V.J. (2007). Approaches to Identify Inhibitors of Melanin Biosynthesis via the Quality Control of Tyrosinase. *J. Invest. Dermatol.* 127, 751–761.

Aroca, P., Solano, F., Garcia-Borrón, J.C., and Lozano, J.A. (1991). Specificity of dopachrome tautomerase and inhibition by carboxylated indoles. Considerations on the enzyme active site. *Biochem. J.* 277 ( Pt 2), 393–397.

Artyomov, M.N., Lis, M., Devadas, S., Davis, M.M., and Chakraborty, A.K. (2010). CD4 and CD8 binding to MHC molecules primarily acts to enhance Lck delivery. *Proc. Natl. Acad. Sci. U. S. A.* 107, 16916–16921.

Atkins, M.B., Hsu, J., Lee, S., Cohen, G.I., Flaherty, L.E., Sosman, J.A., Sondak, V.K., Kirkwood, J.M., and Eastern Cooperative Oncology Group (2008). Phase III trial comparing concurrent biochemotherapy with cisplatin, vinblastine, dacarbazine, interleukin-2, and interferon alfa-2b with cisplatin, vinblastine, and dacarbazine alone in patients with metastatic malignant melanoma (E3695): a trial coordinated by the Eastern Cooperative Oncology Group. *J. Clin. Oncol. Off. J. Am. Soc. Clin. Oncol.* 26, 5748–5754.

Bäckström, B.T., Milia, E., Peter, A., Jaureguiberry, B., Baldari, C.T., and Palmer, E. (1996). A motif within the T cell receptor alpha chain constant region connecting peptide domain controls antigen responsiveness. *Immunity* 5, 437–447.

Bäckström, B.T., Hausmann, B.T., and Palmer, E. (1997). Signaling efficiency of the T cell receptor controlled by a single amino acid in the beta chain constant region. *J. Exp. Med.* 186, 1933–1938.

Balch, C.M., Gershenwald, J.E., Soong, S., Thompson, J.F., Atkins, M.B., Byrd, D.R., Buzaid, A.C., Cochran, A.J., Coit, D.G., Ding, S., et al. (2009). Final Version of 2009 AJCC Melanoma Staging and Classification. *J. Clin. Oncol.* 27, 6199–6206.

Balderes, P.J., and Kang, X. Anti-Typr1 Antibodies.

Baniyash, M., Garcia-Morales, P., Luong, E., Samelson, L.E., and Klausner, R.D. (1988). The T cell antigen receptor zeta chain is tyrosine phosphorylated upon activation. *J. Biol. Chem.* 263, 18225–18230.

Beard, R.E., Zheng, Z., Lagisetty, K.H., Burns, W.R., Tran, E., Hewitt, S.M., Abate-Daga, D., Rosati, S.F., Fine, H.A., Ferrone, S., et al. (2014). Multiple chimeric antigen receptors successfully target chondroitin sulfate proteoglycan 4 in several different cancer histologies and cancer stem cells. *J. Immunother. Cancer* 2, 25.

Beatty, G.L., Haas, A.R., Maus, M.V., Torigian, D.A., Soulen, M.C., Plesa, G., Chew, A., Zhao, Y., Levine, B.L., Albelda, S.M., et al. (2014). Mesothelin-specific chimeric

antigen receptor mRNA-engineered T cells induce anti-tumor activity in solid malignancies. *Cancer Immunol. Res.* 2, 112–120.

Berkhout, B., Alarcon, B., and Terhorst, C. (1988). Transfection of genes encoding the T cell receptor-associated CD3 complex into COS cells results in assembly of the macromolecular structure. *J. Biol. Chem.* 263, 8528–8536.

Berrocal, A., Cabañas, L., Espinosa, E., Fernández-de-Misa, R., Martín-Algarra, S., Martínez-Cedres, J.C., Ríos-Buceta, L., and Rodríguez-Peralto, J.L. (2014). Melanoma: Diagnosis, Staging, and Treatment. Consensus group recommendations. *Adv. Ther.* 31, 945–960.

Berson, J.F., Harper, D.C., Tenza, D., Raposo, G., and Marks, M.S. (2001). Pmel17 initiates premelanosome morphogenesis within multivesicular bodies. *Mol. Biol. Cell* 12, 3451–3464.

Bertolotto, C. (2013). Melanoma: From Melanocyte to Genetic Alterations and Clinical Options. *Scientifica* 2013.

Beverley, P.C. (1992). Functional analysis of human T cell subsets defined by CD45 isoform expression. *Semin. Immunol.* 4, 35–41.

Bhawan, J. (1997). Mel-5: a novel antibody for differential diagnosis of epidermal pigmented lesions of the skin in paraffin-embedded sections. *Melanoma Res.* 7, 43–48.

Bhuin, T., and Roy, J.K. Rab proteins: The key regulators of intracellular vesicle transport. *Exp. Cell Res.*

Bolander, Å., Agnarsdóttir, M., Strömberg, S., Ponten, F., Hesselius, P., Uhlen, M., and Bergqvist, M. (2008). The Protein Expression of TRP-1 and Galectin-1 in Cutaneous Malignant Melanomas. *Cancer Genomics - Proteomics* 5, 293–300.

Boross, P., Jansen, J.H.M., Pastula, A., van der Poel, C.E., and Leusen, J.H.W. (2012). Both activating and inhibitory Fc gamma receptors mediate rituximab-induced trogocytosis of CD20 in mice. *Immunol. Lett.* 143, 44–52.

Bortoletto, N., Scotet, E., Myamoto, Y., D’Oro, U., and Lanzavecchia, A. (2002). Optimizing anti-CD3 affinity for effective T cell targeting against tumor cells. *Eur. J. Immunol.* 32, 3102–3107.

Böyum, A. (1968). Isolation of mononuclear cells and granulocytes from human blood. Isolation of mononuclear cells by one centrifugation, and of granulocytes by combining centrifugation and sedimentation at 1 g. *Scand. J. Clin. Lab. Investig. Suppl.* 97, 77–89.

Brentjens, R., Yeh, R., Bernal, Y., Riviere, I., and Sadelain, M. (2010). Treatment of Chronic Lymphocytic Leukemia With Genetically Targeted Autologous T Cells: Case

Report of an Unforeseen Adverse Event in a Phase I Clinical Trial. *Mol. Ther.* *18*, 666–668.

Brentjens, R.J., Davila, M.L., Riviere, I., Park, J., Wang, X., Cowell, L.G., Bartido, S., Stefanski, J., Taylor, C., Olszewska, M., et al. (2013). CD19-Targeted T Cells Rapidly Induce Molecular Remissions in Adults with Chemotherapy-Refractory Acute Lymphoblastic Leukemia. *Sci. Transl. Med.* *5*, 177ra38-177ra38.

de Bruyn, M., Rybczynska, A.A., Wei, Y., Schwenkert, M., Fey, G.H., Dierckx, R.A., van Waarde, A., Helfrich, W., and Bremer, E. (2010). Melanoma-associated Chondroitin Sulfate Proteoglycan (MCSP)-targeted delivery of soluble TRAIL potently inhibits melanoma outgrowth in vitro and in vivo. *Mol. Cancer* *9*, 301.

Bultema, J.J., Ambrosio, A.L., Burek, C.L., and Pietro, S.M.D. (2012). BLOC-2, AP-3, and AP-1 Proteins Function in Concert with Rab38 and Rab32 Proteins to Mediate Protein Trafficking to Lysosome-related Organelles. *J. Biol. Chem.* *287*, 19550–19563.

Burns, W.R., Zhao, Y., Frankel, T.L., Hinrichs, C.S., Zheng, Z., Xu, H., Feldman, S.A., Ferrone, S., Rosenberg, S.A., and Morgan, R.A. (2010). A high molecular weight melanoma-associated antigen-specific chimeric antigen receptor redirects lymphocytes to target human melanomas. *Cancer Res.* *70*, 3027–3033.

Burroughs, N.J., Lazic, Z., and van der Merwe, P.A. (2006). Ligand Detection and Discrimination by Spatial Relocalization: A Kinase-Phosphatase Segregation Model of TCR Activation. *Biophys. J.* *91*, 1619–1629.

Carpenito, C., Milone, M.C., Hassan, R., Simonet, J.C., Lakhali, M., Suhoski, M.M., Varela-Rohena, A., Haines, K.M., Heitjan, D.F., Albelda, S.M., et al. (2009). Control of large, established tumor xenografts with genetically retargeted human T cells containing CD28 and CD137 domains. *Proc. Natl. Acad. Sci.* *106*, 3360–3365.

Caruso, H.G., Hurton, L.V., Najjar, A., Rushworth, D., Ang, S., Olivares, S., Mi, T., Switzer, K., Singh, H., Huls, H., et al. (2015). Tuning Sensitivity of CAR to EGFR Density Limits Recognition of Normal Tissue While Maintaining Potent Antitumor Activity. *Cancer Res.* *75*, 3505–3518.

Casas, J., Brzostek, J., Zarnitsyna, V.I., Hong, J., Wei, Q., Hoerter, J.A.H., Fu, G., Ampudia, J., Zamoyska, R., Zhu, C., et al. (2014). Ligand-engaged TCR is triggered by Lck not associated with CD8 coreceptor. *Nat. Commun.* *5*, 5624.

Celik, C., Lewis, D.A., and Goldrosen, M.H. (1983). Demonstration of Immunogenicity with the Poorly Immunogenic B16 Melanoma. *Cancer Res.* *43*, 3507–3510.

Chames, P., Willemsen, R.A., Rojas, G., Dieckmann, D., Rem, L., Schuler, G., Bolhuis, R.L., and Hoogenboom, H.R. (2002). TCR-like human antibodies expressed on human CTLs mediate antibody affinity-dependent cytolytic activity. *J. Immunol. Baltim. Md 1950* *169*, 1110–1118.

Chapman, P.B., Einhorn, L.H., Meyers, M.L., Saxman, S., Destro, A.N., Panageas, K.S., Begg, C.B., Agarwala, S.S., Schuchter, L.M., Ernstoff, M.S., et al. (1999). Phase III multicenter randomized trial of the Dartmouth regimen versus dacarbazine in patients with metastatic melanoma. *J. Clin. Oncol. Off. J. Am. Soc. Clin. Oncol.* *17*, 2745–2751.

Chapman, P.B., Hauschild, A., Robert, C., Haanen, J.B., Ascierto, P., Larkin, J., Dummer, R., Garbe, C., Testori, A., Maio, M., et al. (2011). Improved survival with vemurafenib in melanoma with BRAF V600E mutation. *N. Engl. J. Med.* *364*, 2507–2516.

Chen, Y.T., Stockert, E., Tsang, S., Coplan, K.A., and Old, L.J. (1995). Immunophenotyping of melanomas for tyrosinase: implications for vaccine development. *Proc. Natl. Acad. Sci.* *92*, 8125–8129.

Chițu, V., Fajka-Boja, R., Tóth, G.K., Váradi, G., Hegedüs, Z., Frankó, A., Szücs, K.S., and Monostori, E. (2001). Comparative study on the effect of phosphorylated TCR zeta chain ITAM sequences on early activation events in Jurkat T cells. *Peptides* *22*, 1963–1971.

Chmielewski, M., Hombach, A., Heuser, C., Adams, G.P., and Abken, H. (2004). T Cell Activation by Antibody-Like Immunoreceptors: Increase in Affinity of the Single-Chain Fragment Domain above Threshold Does Not Increase T Cell Activation against Antigen-Positive Target Cells but Decreases Selectivity. *J. Immunol.* *173*, 7647–7653.

Chothia, C., Boswell, D.R., and Lesk, A.M. (1988). The outline structure of the T-cell alpha beta receptor. *EMBO J.* *7*, 3745–3755.

Choudhuri, K., Wiseman, D., Brown, M.H., Gould, K., and van der Merwe, P.A. (2005). T-cell receptor triggering is critically dependent on the dimensions of its peptide-MHC ligand. *Nature* *436*, 578–582.

Choudhuri, K., Parker, M., Milicic, A., Cole, D.K., Shaw, M.K., Sewell, A.K., Stewart-Jones, G., Dong, T., Gould, K.G., and van der Merwe, P.A. (2009). Peptide-major histocompatibility complex dimensions control proximal kinase-phosphatase balance during T cell activation. *J. Biol. Chem.* *284*, 26096–26105.

Christian, S., Pilch, J., Akerman, M.E., Porkka, K., Laakkonen, P., and Ruoslahti, E. (2003). Nucleolin expressed at the cell surface is a marker of endothelial cells in angiogenic blood vessels. *J. Cell Biol.* *163*, 871–878.

Christinck, E.R., Luscher, M.A., Barber, B.H., and Williams, D.B. (1991). Peptide binding to class I MHC on living cells and quantitation of complexes required for CTL lysis. *Nature* *352*, 67–70.

Classon, B.J., Brown, M.H., Garnett, D., Somoza, C., Barclay, A.N., Willis, A.C., and Williams, A.F. (1992). The hinge region of the CD8 alpha chain: structure, antigenicity, and utility in expression of immunoglobulin superfamily domains. *Int. Immunol.* *4*, 215–225.

Claverie, J.-M., Prochnicka-Chalufour, A., and Bougueleret, L. (1989). Implications of a Fab-like structure for the T-cell receptor. *Immunol. Today* *10*, 10–14.

Cohen, C.J., Li, Y.F., El-Gamil, M., Robbins, P.F., Rosenberg, S.A., and Morgan, R.A. (2007). Enhanced antitumor activity of T cells engineered to express T-cell receptors with a second disulfide bond. *Cancer Res.* *67*, 3898–3903.

Cohen-Solal, K.A., Sood, R., Marin, Y., Crespo-Carbone, S.M., Sinsimer, D., Martino, J.J., Robbins, C., Makalowska, I., Trent, J., and Chen, S. (2003). Identification and characterization of mouse Rab32 by mRNA and protein expression analysis. *Biochim. Biophys. Acta BBA - Proteins Proteomics* *1651*, 68–75.

Cooper, M.D., Peterson, R.D.A., and Good, R.A. (1965). A new concept of the cellular basis of immunity. *J. Pediatr.* *67*, 907–908.

Cordoba, S.-P., Choudhuri, K., Zhang, H., Bridge, M., Basat, A.B., Dustin, M.L., and Merwe, P.A. van der (2013). The large ectodomains of CD45 and CD148 regulate their segregation from and inhibition of ligated T-cell receptor. *Blood* *121*, 4295–4302.

Cosset, F.L., Takeuchi, Y., Battini, J.L., Weiss, R.A., and Collins, M.K. (1995). High-titer packaging cells producing recombinant retroviruses resistant to human serum. *J. Virol.* *69*, 7430–7436.

Curtsinger, J.M., Lins, D.C., Johnson, C.M., and Mescher, M.F. (2005). Signal 3 Tolerant CD8 T Cells Degranulate in Response to Antigen but Lack Granzyme B to Mediate Cytolysis. *J. Immunol.* *175*, 4392–4399.

Daniels, M.A., Teixeira, E., Gill, J., Hausmann, B., Roubaty, D., Holmberg, K., Werlen, G., Holländer, G.A., Gascoigne, N.R.J., and Palmer, E. (2006). Thymic selection threshold defined by compartmentalization of Ras/MAPK signalling. *Nature* *444*, 724–729.

Davila, M.L., Riviere, I., Wang, X., Bartido, S., Park, J., Curran, K., Chung, S.S., Stefanski, J., Borquez-Ojeda, O., Olszewska, M., et al. (2014). Efficacy and Toxicity Management of 19-28z CAR T Cell Therapy in B Cell Acute Lymphoblastic Leukemia. *Sci. Transl. Med.* *6*, 224ra25-224ra25.

Davis, M.M., and Bjorkman, P.J. (1988). T-cell antigen receptor genes and T-cell recognition. *Nature* *334*, 395–402.

Day, C.L., Kaufmann, D.E., Kiepiela, P., Brown, J.A., Moodley, E.S., Reddy, S., Mackey, E.W., Miller, J.D., Leslie, A.J., DePierres, C., et al. (2006). PD-1 expression on HIV-specific T cells is associated with T-cell exhaustion and disease progression. *Nature* *443*, 350–354.

Dean, N.R., Brennan, J., Haynes, J., Goddard, C., and Cooter, R.D. (2002). Immunohistochemical labeling of normal melanocytes. *Appl. Immunohistochem. Mol. Morphol. AIMM* *10*, 199–204.

- Deneka, M., Neeft, M., Popa, I., van Oort, M., Sprong, H., Oorschot, V., Klumperman, J., Schu, P., and van der Sluijs, P. (2003). Rabaptin-5 $\alpha$ /rabaptin-4 serves as a linker between rab4 and  $\gamma$ 1-adaptin in membrane recycling from endosomes. *EMBO J.* 22, 2645–2657.
- Du, X., Ho, M., and Pastan, I. (2007). New immunotoxins targeting CD123, a stem cell antigen on acute myeloid leukemia cells. *J. Immunother. Hagerstown Md* 1997 30, 607–613.
- DuBridge, R.B., Tang, P., Hsia, H.C., Leong, P.M., Miller, J.H., and Calos, M.P. (1987). Analysis of mutation in human cells by using an Epstein-Barr virus shuttle system. *Mol. Cell. Biol.* 7, 379–387.
- Eshhar, Z., Waks, T., Gross, G., and Schindler, D.G. (1993). Specific activation and targeting of cytotoxic lymphocytes through chimeric single chains consisting of antibody-binding domains and the gamma or zeta subunits of the immunoglobulin and T-cell receptors. *Proc. Natl. Acad. Sci.* 90, 720–724.
- Falchook, G.S., Lewis, K.D., Infante, J.R., Gordon, M.S., Vogelzang, N.J., DeMarini, D.J., Sun, P., Moy, C., Szabo, S.A., Roadcap, L.T., et al. (2012). Activity of the oral MEK inhibitor trametinib in patients with advanced melanoma: a phase 1 dose-escalation trial. *Lancet Oncol.* 13, 782–789.
- Falcón-Pérez, J.M., Starcevic, M., Gautam, R., and Dell'Angelica, E.C. (2002). BLOC-1, a novel complex containing the pallidin and muted proteins involved in the biogenesis of melanosomes and platelet-dense granules. *J. Biol. Chem.* 277, 28191–28199.
- Falkson, C.I., Ibrahim, J., Kirkwood, J.M., Coates, A.S., Atkins, M.B., and Blum, R.H. (1998). Phase III trial of dacarbazine versus dacarbazine with interferon alpha-2b versus dacarbazine with tamoxifen versus dacarbazine with interferon alpha-2b and tamoxifen in patients with metastatic malignant melanoma: an Eastern Cooperative Oncology Group study. *J. Clin. Oncol. Off. J. Am. Soc. Clin. Oncol.* 16, 1743–1751.
- Fernández-Suárez, M., and Ting, A.Y. (2008). Fluorescent probes for super-resolution imaging in living cells. *Nat. Rev. Mol. Cell Biol.* 9, 929–943.
- Ferrarini, M., Heltai, S., Zocchi, M.R., and Rugarli, C. (1992). Unusual expression and localization of heat-shock proteins in human tumor cells. *Int. J. Cancer J. Int. Cancer* 51, 613–619.
- Fidler, I.J. (1973). The relationship of embolic homogeneity, number, size and viability to the incidence of experimental metastasis. *Eur. J. Cancer* 9, 223–227.
- Foley, K., Bertin, J., Chan, K., Hutchings, A., Inoue, T., Kirshner, J., Korbut, T., Li, L., Mihalek, R., Rao, P., et al. (2007). The oxidative stress inducer STA-4783 enhances the in vivo efficacy of multiple anti-cancer therapies in mouse tumor models. *Mol. Cancer Ther.* 6, A290–A290.

- Forman, S.J., BROWN, C.E., JONNALAGADDA, U., and MARDIROS, A. (2015). Chimeric antigen receptors (cars) having mutations in the fc spacer region and methods for their use.
- Fourcade, J., Sun, Z., Benallaoua, M., Guillaume, P., Luescher, I.F., Sander, C., Kirkwood, J.M., Kuchroo, V., and Zarour, H.M. (2010). Upregulation of Tim-3 and PD-1 expression is associated with tumor antigen-specific CD8+ T cell dysfunction in melanoma patients. *J. Exp. Med.* *207*, 2175–2186.
- Garcia, K.C., Degano, M., Stanfield, R.L., Brunmark, A., Jackson, M.R., Peterson, P.A., Teyton, L., and Wilson, I.A. (1996). An  $\alpha\beta$  T Cell Receptor Structure at 2.5 Å and Its Orientation in the TCR-MHC Complex. *Science* *274*, 209–219.
- Garfall, A.L., Maus, M.V., Hwang, W.-T., Lacey, S.F., Mahnke, Y.D., Melenhorst, J.J., Zheng, Z., Vogl, D.T., Cohen, A.D., Weiss, B.M., et al. (2015). Chimeric Antigen Receptor T Cells against CD19 for Multiple Myeloma. *N. Engl. J. Med.* *373*, 1040–1047.
- Gargett, T., Yu, W., Dotti, G., Yvon, E.S., Christo, S.N., Hayball, J.D., Lewis, I.D., Brenner, M.K., and Brown, M.P. (2016). GD2-specific CAR T Cells Undergo Potent Activation and Deletion Following Antigen Encounter but can be Protected From Activation-induced Cell Death by PD-1 Blockade. *Mol. Ther. J. Am. Soc. Gene Ther.* *24*, 1135–1149.
- Gattinoni, L., Lugli, E., Ji, Y., Pos, Z., Paulos, C.M., Quigley, M.F., Almeida, J.R., Gostick, E., Yu, Z., Carpenito, C., et al. (2011). A human memory T-cell subset with stem cell-like properties. *Nat. Med.* *17*, 1290–1297.
- Gehring, A.J., Ho, Z.Z., Tan, A.T., Aung, M.O., Lee, K.H., Tan, K.C., Lim, S.G., and Bertolotti, A. (2009). Profile of tumor antigen-specific CD8 T cells in patients with hepatitis B virus-related hepatocellular carcinoma. *Gastroenterology* *137*, 682–690.
- Ghetie, M.-A., Marches, R., Kufert, S., and Vitetta, E.S. (2004). An anti-CD19 antibody inhibits the interaction between P-glycoprotein (P-gp) and CD19, causes P-gp to translocate out of lipid rafts, and chemosensitizes a multidrug-resistant (MDR) lymphoma cell line. *Blood* *104*, 178–183.
- Gil, D., Schamel, W.W.A., Montoya, M., Sánchez-Madrid, F., and Alarcón, B. (2002). Recruitment of Nck by CD3 epsilon reveals a ligand-induced conformational change essential for T cell receptor signaling and synapse formation. *Cell* *109*, 901–912.
- Ginaldi, L., De Martinis, M., Matutes, E., Farahat, N., Morilla, R., and Catovsky, D. (1998). Levels of expression of CD19 and CD20 in chronic B cell leukaemias. *J. Clin. Pathol.* *51*, 364–369.
- Gires, O., Mack, B., Rauch, J., and Matthias, C. (2006). CK8 correlates with malignancy in leukoplakia and carcinomas of the head and neck. *Biochem. Biophys. Res. Commun.* *343*, 252–259.

González, P.A., Carreño, L.J., Coombs, D., Mora, J.E., Palmieri, E., Goldstein, B., Nathenson, S.G., and Kalergis, A.M. (2005). T cell receptor binding kinetics required for T cell activation depend on the density of cognate ligand on the antigen-presenting cell. *Proc. Natl. Acad. Sci. U. S. A.* *102*, 4824–4829.

Govern, C.C., Paczosa, M.K., Chakraborty, A.K., and Huseby, E.S. (2010). Fast on-rates allow short dwell time ligands to activate T cells. *Proc. Natl. Acad. Sci. U. S. A.* *107*, 8724–8729.

Groux-Degroote, S., van Dijk, S.M., Wolthoorn, J., Neumann, S., Theos, A.C., De Mazière, A.M., Klumperman, J., van Meer, G., and Sprong, H. (2008). Glycolipid-dependent sorting of melanosomal from lysosomal membrane proteins by luminal determinants. *Traffic Cph. Den.* *9*, 951–963.

Grupp, S.A., Maude, S.L., Shaw, P.A., Aplenc, R., Barrett, D.M., Callahan, C., Lacey, S.F., Levine, B.L., Melenhorst, J.J., Motley, L., et al. (2015). Durable Remissions in Children with Relapsed/Refractory ALL Treated with T Cells Engineered with a CD19-Targeted Chimeric Antigen Receptor (CTL019). *Blood* *126*, 681–681.

Guest, R.D., Hawkins, R.E., Kirillova, N., Cheadle, E.J., Arnold, J., O'Neill, A., Irlam, J., Chester, K.A., Kemshead, J.T., Shaw, D.M., et al. (2005). The Role of Extracellular Spacer Regions in the Optimal Design of Chimeric Immune Receptors: Evaluation of Four Different scFvs and Antigens. [Miscellaneous Article]. *J. Immunother.* May *28*, 203–211.

Hara, I., Takechi, Y., and Houghton, A.N. (1995). Implicating a role for immune recognition of self in tumor rejection: passive immunization against the brown locus protein. *J. Exp. Med.* *182*, 1609–1614.

Harding, F.A., McArthur, J.G., Gross, J.A., Raulet, D.H., and Allison, J.P. (1992). CD28-mediated signalling co-stimulates murine T cells and prevents induction of anergy in T-cell clones. *Nature* *356*, 607–609.

Haso, W., Lee, D.W., Shah, N.N., Stetler-Stevenson, M., Yuan, C.M., Pastan, I.H., Dimitrov, D.S., Morgan, R.A., FitzGerald, D.J., Barrett, D.M., et al. (2013). Anti-CD22–chimeric antigen receptors targeting B-cell precursor acute lymphoblastic leukemia. *Blood* *121*, 1165–1174.

Helip-Wooley, A., Westbroek, W., Dorward, H.M., Koshoffer, A., Huizing, M., Boissy, R.E., and Gahl, W.A. (2007). Improper Trafficking of Melanocyte-Specific Proteins in Hermansky–Pudlak Syndrome Type-5. *J. Invest. Dermatol.* *127*, 1471–1478.

Hermiston, M.L., Zikherman, J., and Zhu, J.W. (2009). CD45, CD148, and Lyp/Pep: critical phosphatases regulating Src family kinase signaling networks in immune cells. *Immunol. Rev.* *228*, 288–311.

Heusel, J.W., Wesselschmidt, R.L., Shresta, S., Russell, J.H., and Ley, T.J. (1994). Cytotoxic lymphocytes require granzyme B for the rapid induction of DNA fragmentation and apoptosis in allogeneic target cells. *Cell* *76*, 977–987.

- Hill, G.J., Krementz, E.T., and Hill, H.Z. (1984). Dimethyl triazeno imidazole carboxamide and combination therapy for melanoma. IV. Late results after complete response to chemotherapy (Central Oncology Group protocols 7130, 7131, and 7131A). *Cancer* 53, 1299–1305.
- Hodi, F.S., O'Day, S.J., McDermott, D.F., Weber, R.W., Sosman, J.A., Haanen, J.B., Gonzalez, R., Robert, C., Schadendorf, D., Hassel, J.C., et al. (2010). Improved Survival with Ipilimumab in Patients with Metastatic Melanoma. *N. Engl. J. Med.* 363, 711–723.
- Hoffee, M.G., Tavares, D., and Lutz, R.J. (2012). Anti-CD33 antibodies and methods for treatment of acute myeloid leukemia using the same.
- Holler, P.D., and Kranz, D.M. (2003). Quantitative Analysis of the Contribution of TCR/pepMHC Affinity and CD8 to T Cell Activation. *Immunity* 18, 255–264.
- Hollis, G.F., Lewis, C.M., and Ludmerer, S.W. (1995). In vitro antibody affinity maturation using alanine scanning mutagenesis.
- Holzmann, B., Bröcker, E.B., Lehmann, J.M., Rüter, D.J., Sorg, C., Riethmüller, G., and Johnson, J.P. (1987). Tumor progression in human malignant melanoma: five stages defined by their antigenic phenotypes. *Int. J. Cancer* 39, 466–471.
- Hombach, A.A., Schildgen, V., Heuser, C., Finnern, R., Gilham, D.E., and Abken, H. (2007). T Cell Activation by Antibody-Like Immunoreceptors: The Position of the Binding Epitope within the Target Molecule Determines the Efficiency of Activation of Redirected T Cells. *J. Immunol.* 178, 4650–4657.
- Hombach, A.A., Heiders, J., Foppe, M., Chmielewski, M., and Abken, H. (2012). OX40 costimulation by a chimeric antigen receptor abrogates CD28 and IL-2 induced IL-10 secretion by redirected CD4(+) T cells. *Oncoimmunology* 1, 458–466.
- Hudecek, M., Lupo-Stanghellini, M.-T., Kosasih, P.L., Sommermeyer, D., Jensen, M.C., Rader, C., and Riddell, S.R. (2013). Receptor Affinity and Extracellular Domain Modifications Affect Tumor Recognition by ROR1-Specific Chimeric Antigen Receptor T Cells. *Clin. Cancer Res.* 19, 3153–3164.
- Iezzi, G., Karjalainen, K., and Lanzavecchia, A. (1998). The Duration of Antigenic Stimulation Determines the Fate of Naive and Effector T Cells. *Immunity* 8, 89–95.
- Irles, C., Symons, A., Michel, F., Bakker, T.R., van der Merwe, P.A., and Acuto, O. (2003). CD45 ectodomain controls interaction with GEMs and Lck activity for optimal TCR signaling. *Nat. Immunol.* 4, 189–197.
- Itoh, Y., Hemmer, B., Martin, R., and Germain, R.N. (1999). Serial TCR Engagement and Down-Modulation by Peptide:MHC Molecule Ligands: Relationship to the Quality of Individual TCR Signaling Events. *J. Immunol.* 162, 2073–2080.

Jackson, I.J. (1988). A cDNA encoding tyrosinase-related protein maps to the brown locus in mouse. *Proc. Natl. Acad. Sci. U. S. A.* *85*, 4392–4396.

Jackson, I.J., Chambers, D.M., Tsukamoto, K., Copeland, N.G., Gilbert, D.J., Jenkins, N.A., and Hearing, V. (1992). A second tyrosinase-related protein, TRP-2, maps to and is mutated at the mouse slaty locus. *EMBO J.* *11*, 527–535.

Jain, R.K., Joyce, P.B., Molinete, M., Halban, P.A., and Gorr, S.U. (2001). Oligomerization of green fluorescent protein in the secretory pathway of endocrine cells. *Biochem. J.* *360*, 645–649.

James, S.E., Greenberg, P.D., Jensen, M.C., Lin, Y., Wang, J., Till, B.G., Raubitschek, A.A., Forman, S.J., and Press, O.W. (2008). Antigen Sensitivity of CD22-Specific Chimeric TCR Is Modulated by Target Epitope Distance from the Cell Membrane. *J. Immunol.* *180*, 7028–7038.

James, S.E., Greenberg, P.D., Jensen, M.C., Lin, Y., Wang, J., Budde, L.E., Till, B.G., Raubitschek, A.A., Forman, S.J., and Press, O.W. (2010). Mathematical Modeling of Chimeric TCR Triggering Predicts the Magnitude of Target Lysis and Its Impairment by TCR Downmodulation. *J. Immunol.* *184*, 4284–4294.

Jimbow, K., Gomez, P.F., Toyofuku, K., Chang, D., Miura, S., Tsujiya, H., and Park, J.S. (1997). Biological Role of Tyrosinase Related Protein and its Biosynthesis and Transport From TGN to Stage I Melanosome, Late Endosome, Through Gene Transfection Study. *Pigment Cell Res.* *10*, 206–213.

Johnson, L.A., Scholler, J., Ohkuri, T., Kosaka, A., Patel, P.R., McGettigan, S.E., Nace, A.K., Dentchev, T., Thekkat, P., Loew, A., et al. (2015). Rational development and characterization of humanized anti-EGFR variant III chimeric antigen receptor T cells for glioblastoma. *Sci. Transl. Med.* *7*, 275ra22.

Jones, R.B., Ndhlovu, L.C., Barbour, J.D., Sheth, P.M., Jha, A.R., Long, B.R., Wong, J.C., Satkunarajah, M., Schweneker, M., Chapman, J.M., et al. (2008). Tim-3 expression defines a novel population of dysfunctional T cells with highly elevated frequencies in progressive HIV-1 infection. *J. Exp. Med.* *205*, 2763–2779.

Jones, S.A., Shim, S.-H., He, J., and Zhuang, X. (2011). Fast, three-dimensional super-resolution imaging of live cells. *Nat. Methods* *8*, 499–505.

Jorgensen, J.L., Esser, U., Groth, B.F. de S., Reay, P.A., and Davis, M.M. (1992). Mapping T-cell receptor–peptide contacts by variant peptide immunization of single-chain transgenics. *Nature* *355*, 224–230.

Journe, F., Boufker, H.I., Van Kempen, L., Galibert, M.-D., Wiedig, M., Salès, F., Theunis, A., Nonclercq, D., Frau, A., Laurent, G., et al. (2011). TYRP1 mRNA expression in melanoma metastases correlates with clinical outcome. *Br. J. Cancer* *105*, 1726–1732.

- Kalergis, A.M., Boucheron, N., Doucey, M.A., Palmieri, E., Goyarts, E.C., Vegh, Z., Luescher, I.F., and Nathenson, S.G. (2001). Efficient T cell activation requires an optimal dwell-time of interaction between the TCR and the pMHC complex. *Nat. Immunol.* *2*, 229–234.
- Kanne, H., Burte, N.P., Prasanna, V., and Gujjula, R. (2015). Extraction and elemental analysis of *Coleus forskohlii* extract. *Pharmacogn. Res.* *7*, 237–241.
- Kelley, R.F., and O’Connell, M.P. (1993). Thermodynamic analysis of an antibody functional epitope. *Biochemistry (Mosc.)* *32*, 6828–6835.
- Kemp, E.H., Waterman, E.A., Gawkrödger, D.J., Watson, P.F., and Weetman, A.P. (1998). Autoantibodies to tyrosinase-related protein-1 detected in the sera of vitiligo patients using a quantitative radiobinding assay. *Br. J. Dermatol.* *139*, 798–805.
- Kershaw, M.H., Westwood, J.A., Parker, L.L., Wang, G., Eshhar, Z., Mavroukakis, S.A., White, D.E., Wunderlich, J.R., Canevari, S., Rogers-Freezer, L., et al. (2006). A Phase I Study on Adoptive Immunotherapy Using Gene-Modified T Cells for Ovarian Cancer. *Clin. Cancer Res. Off. J. Am. Assoc. Cancer Res.* *12*, 6106–6115.
- Kim, P.W., Sun, Z.-Y.J., Blacklow, S.C., Wagner, G., and Eck, M.J. (2003). A zinc clasp structure tethers Lck to T cell coreceptors CD4 and CD8. *Science* *301*, 1725–1728.
- Kim, S., Davis, M., Sinn, E., Patten, P., and Hood, L. (1981). Antibody diversity: somatic hypermutation of rearranged VH genes. *Cell* *27*, 573–581.
- Kleffel, S., Posch, C., Barthel, S.R., Mueller, H., Schlapbach, C., Guenova, E., Elco, C.P., Lee, N., Juneja, V.R., Zhan, Q., et al. (2015). Melanoma Cell-Intrinsic PD-1 Receptor Functions Promote Tumor Growth. *Cell* *162*, 1242–1256.
- Kobayashi, T., and Hearing, V.J. (2007). Direct interaction of tyrosinase with Tyrp1 to form heterodimeric complexes in vivo. *J. Cell Sci.* *120*, 4261–4268.
- Kobayashi, T., Urabe, K., Winder, A., Tsukamoto, K., Brewington, T., Imokawa, G., Potterf, B., and Hearing, V.J. (1994a). DHICA Oxidase Activity of TRP1 and Interactions With Other Melanogenic Enzymes. *Pigment Cell Res.* *7*, 227–234.
- Kobayashi, T., Urabe, K., Winder, A., Jimenez-Cervantes, C., Imokawa, G., Brewington, T., Solano, F., Garcia-Borrón, J.C., and Hearing, V.J. (1994b). Tyrosinase related protein 1 (TRP1) functions as a DHICA oxidase in melanin biosynthesis. *EMBO J.* *13*, 5818–5825.
- Kobayashi, T., Imokawa, G., Bennett, D.C., and Hearing, V.J. (1998). Tyrosinase Stabilization by Tyrp1 (the brown Locus Protein). *J. Biol. Chem.* *273*, 31801–31805.
- Kollias, N., Sayre, R.M., Zeise, L., and Chedekel, M.R. (1991). New trends in photobiology: Photoprotection by melanin. *J. Photochem. Photobiol. B* *9*, 135–160.
- Koneru, M., O’Cearbhaill, R., Pendharkar, S., Spriggs, D.R., and Brentjens, R.J. (2015). A phase I clinical trial of adoptive T cell therapy using IL-12 secreting MUC-16ecto

directed chimeric antigen receptors for recurrent ovarian cancer. *J. Transl. Med.* *13*, 102.

Krammer, P.H. (2000). CD95's deadly mission in the immune system. *Nature* *407*, 789–795.

Krogsgaard, M., Li, Q., Sumen, C., Huppa, J.B., Huse, M., and Davis, M.M. (2005). Agonist/endogenous peptide–MHC heterodimers drive T cell activation and sensitivity. *Nature* *434*, 238–243.

Krug, C., Birkholz, K., Paulus, A., Schwenkert, M., Schmidt, P., Hoffmann, N., Hombach, A., Fey, G., Abken, H., Schuler, G., et al. (2015). Stability and activity of MCSP-specific chimeric antigen receptors (CARs) depend on the scFv antigen-binding domain and the protein backbone. *Cancer Immunol. Immunother.* *64*, 1623–1635.

Kügler, M., Stein, C., Schwenkert, M., Saul, D., Vockentanz, L., Huber, T., Wetzel, S.K., Scholz, O., Plückthun, A., Honegger, A., et al. (2009). Stabilization and humanization of a single-chain Fv antibody fragment specific for human lymphocyte antigen CD19 by designed point mutations and CDR-grafting onto a human framework. *Protein Eng. Des. Sel.* *22*, 135–147.

Kuhns, M.S., and Davis, M.M. (2007). Disruption of extracellular interactions impairs T cell receptor-CD3 complex stability and signaling. *Immunity* *26*, 357–369.

Kuhns, M.S., and Davis, M.M. (2012). TCR Signaling Emerges from the Sum of Many Parts. *Front. Immunol.* *3*, 159.

Kumar, R., Ferez, M., Swamy, M., Arechaga, I., Rejas, M.T., Valpuesta, J.M., Schamel, W.W.A., Alarcon, B., and van Santen, H.M. (2011). Increased sensitivity of antigen-experienced T cells through the enrichment of oligomeric T cell receptor complexes. *Immunity* *35*, 375–387.

Leahy, D.J., Axel, R., and Hendrickson, W.A. (1992). Crystal structure of a soluble form of the human T cell coreceptor CD8 at 2.6 Å resolution. *Cell* *68*, 1145–1162.

Legha, S.S. (1997). Durable complete responses in metastatic melanoma treated with interleukin-2 in combination with interferon alpha and chemotherapy. *Semin. Oncol.* *24*, S39-43.

Legha, S.S., Ring, S., Bedikian, A., Plager, C., Eton, O., Buzaid, A.C., and Papadopoulos, N. (1996). Treatment of metastatic melanoma with combined chemotherapy containing cisplatin, vinblastine and dacarbazine (CVD) and biotherapy using interleukin-2 and interferon-alpha. *Ann. Oncol. Off. J. Eur. Soc. Med. Oncol. ESMO* *7*, 827–835.

Lekmine, F., and Salti, G.I. (2008). Induction of Microphthalmia Transcription Factor (Mitf) by Forskolin and Stimulation of Melanin Release in UISO-Mel-6 Cells. *J. Surg. Res.* *149*, 27–30.

Lesley, J.F., Kettman, J.R., and Dutton, R.W. (1971). IMMUNOGLOBULINS ON THE SURFACE OF THYMUS-DERIVED CELLS ENGAGED IN THE INITIATION OF A HUMORAL IMMUNE RESPONSE. *J. Exp. Med.* *134*, 618–629.

Levy, J.A., Buell, D.N., Creech, C., Hirshaut, Y., and Silverberg, H. (1971). Further Characterization of the WI-L1 and WI-L2 Lymphoblastoid Lines. *J. Natl. Cancer Inst.* *46*, 647–654.

Lewis, K.D., Samlowski, W., Ward, J., Catlett, J., Cranmer, L., Kirkwood, J., Lawson, D., Whitman, E., and Gonzalez, R. (2011). A multi-center phase II evaluation of the small molecule survivin suppressor YM155 in patients with unresectable stage III or IV melanoma. *Invest. New Drugs* *29*, 161–166.

Lin, J., and Weiss, A. (2003). The tyrosine phosphatase CD148 is excluded from the immunologic synapse and down-regulates prolonged T cell signaling. *J. Cell Biol.* *162*, 673–682.

Lin, M., Zhang, B.-X., Zhang, C., Shen, N., Zhang, Y.-Y., Wang, A.-X., and Tu, C.-X. (2014). Ginsenosides Rb1 and Rg1 Stimulate Melanogenesis in Human Epidermal Melanocytes via PKA/CREB/MITF Signaling. *Evid.-Based Complement. Altern. Med. ECAM 2014*, 892073.

Liu, H., and May, K. (2012). Disulfide bond structures of IgG molecules. *mAbs* *4*, 17–23.

Liu, X., Jiang, S., Fang, C., Yang, S., Olalere, D., Pequignot, E.C., Cogdill, A.P., Li, N., Ramones, M., Granda, B., et al. (2015). Affinity-Tuned ErbB2 or EGFR Chimeric Antigen Receptor T Cells Exhibit an Increased Therapeutic Index against Tumors in Mice. *Cancer Res.* *75*, 3596–3607.

Lo, A.S.Y., Ma, Q., Liu, D.L., and Junghans, R.P. (2010). Anti-GD3 chimeric sFv-CD28/T-cell receptor zeta designer T cells for treatment of metastatic melanoma and other neuroectodermal tumors. *Clin. Cancer Res. Off. J. Am. Assoc. Cancer Res.* *16*, 2769–2780.

Loftus, S.K., Larson, D.M., Baxter, L.L., Antonellis, A., Chen, Y., Wu, X., Jiang, Y., Bittner, M., Hammer, J.A., and Pavan, W.J. (2002). Mutation of melanosome protein RAB38 in chocolate mice. *Proc. Natl. Acad. Sci.* *99*, 4471–4476.

Long, G.V., Menzies, A.M., Nagrial, A.M., Haydu, L.E., Hamilton, A.L., Mann, G.J., Hughes, T.M., Thompson, J.F., Scolyer, R.A., and Kefford, R.F. (2011). Prognostic and clinicopathologic associations of oncogenic BRAF in metastatic melanoma. *J. Clin. Oncol. Off. J. Am. Soc. Clin. Oncol.* *29*, 1239–1246.

Lotan, R., and Lotan, D. (1980). Stimulation of melanogenesis in a human melanoma cell line by retinoids. *Cancer Res.* *40*, 3345–3350.

Love, P.E., and Hayes, S.M. (2010). ITAM-mediated Signaling by the T-Cell Antigen Receptor. *Cold Spring Harb. Perspect. Biol.* *2*.

- Lu, B., Ebensperger, C., Dembic, Z., Wang, Y., Kvatyuk, M., Lu, T., Coffman, R.L., Pestka, S., and Rothman, P.B. (1998). Targeted disruption of the interferon-gamma receptor 2 gene results in severe immune defects in mice. *Proc. Natl. Acad. Sci. U. S. A.* *95*, 8233–8238.
- Ly, L.V., Sluijter, M., Burg, S.H. van der, Jager, M.J., and Hall, T. van (2013). Effective Cooperation of Monoclonal Antibody and Peptide Vaccine for the Treatment of Mouse Melanoma. *J. Immunol.* *190*, 489–496.
- Lynn, R.C., Feng, Y., Schutsky, K., Poussin, M., Kalota, A., Dimitrov, D.S., and Powell Jr, D.J. (2016). High-affinity FR $\beta$ -specific CAR T cells eradicate AML and normal myeloid lineage without HSC toxicity. *Leukemia*.
- Mackensen, A., Meidenbauer, N., Vogl, S., Laumer, M., Berger, J., and Andreesen, R. (2006). Phase I Study of Adoptive T-Cell Therapy Using Antigen-Specific CD8+ T Cells for the Treatment of Patients With Metastatic Melanoma. *J. Clin. Oncol.* *24*, 5060–5069.
- Maher, J., Brentjens, R.J., Gunset, G., Rivière, I., and Sadelain, M. (2002). Human T-lymphocyte cytotoxicity and proliferation directed by a single chimeric TCRzeta/CD28 receptor. *Nat. Biotechnol.* *20*, 70–75.
- Marks, M.S., and Seabra, M.C. (2001). The melanosome: membrane dynamics in black and white. *Nat. Rev. Mol. Cell Biol.* *2*, 738–748.
- Mason, H.S. (1948). The chemistry of melanin; mechanism of the oxidation of dihydroxyphenylalanine by tyrosinase. *J. Biol. Chem.* *172*, 83–99.
- Matsui, K., Boniface, J.J., Steffner, P., Reay, P.A., and Davis, M.M. (1994). Kinetics of T-cell receptor binding to peptide/I-Ek complexes: correlation of the dissociation rate with T-cell responsiveness. *Proc. Natl. Acad. Sci. U. S. A.* *91*, 12862–12866.
- Mattes, M.J., Thomson, T.M., Old, L.J., and Lloyd, K.O. (1983). A pigmentation-associated, differentiation antigen of human melanoma defined by a precipitating antibody in human serum. *Int. J. Cancer J. Int. Cancer* *32*, 717–721.
- Maul, G.G. (1969). Golgi-melanosome relationship in human melanoma in vitro. *J. Ultrastruct. Res.* *26*, 163–176.
- McCall, M.N., Shotton, D.M., and Barclay, A.N. (1992). Expression of soluble isoforms of rat CD45. Analysis by electron microscopy and use in epitope mapping of anti-CD45R monoclonal antibodies. *Immunology* *76*, 310–317.
- McNaughton, B.R., Gareiss, P.C., Jacobs, S.E., Fricke, A.F., Scott, G.A., and Miller, B.L. (2009). A Potent Activator of Melanogenesis Identified from Small Molecule Screening. *ChemMedChem* *4*, 1583–1589.

- van der Merwe, P.A., McNamee, P.N., Davies, E.A., Barclay, A.N., and Davis, S.J. (1995). Topology of the CD2-CD48 cell-adhesion molecule complex: implications for antigen recognition by T cells. *Curr. Biol.* **5**, 74–84.
- van der Merwe, P.A., Davis, S.J., Shaw, A.S., and Dustin, M.L. (2000). Cytoskeletal polarization and redistribution of cell-surface molecules during T cell antigen recognition. *Semin. Immunol.* **12**, 5–21.
- Michie, C.A., McLean, A., Alcock, C., and Beverley, P.C.L. (1992). Lifespan of human lymphocyte subsets defined by CD45 isoforms. *Nature* **360**, 264–265.
- Milone, M.C., Fish, J.D., Carpenito, C., Carroll, R.G., Binder, G.K., Teachey, D., Samanta, M., Lakhal, M., Gloss, B., Danet-Desnoyers, G., et al. (2009). Chimeric receptors containing CD137 signal transduction domains mediate enhanced survival of T cells and increased antileukemic efficacy in vivo. *Mol. Ther. J. Am. Soc. Gene Ther.* **17**, 1453–1464.
- Miyazaki, T., Liu, Z.-J., Kawahara, A., Minami, Y., Yamada, K., Tsujimoto, Y., Barsoumian, E.L., Perlmutter, R.M., and Taniguchi, T. (1995). Three distinct IL-2 signaling pathways mediated by bcl-2, c-myc, and lck cooperate in hematopoietic cell proliferation. *Cell* **81**, 223–231.
- Morgan, R.A., Yang, J.C., Kitano, M., Dudley, M.E., Laurencot, C.M., and Rosenberg, S.A. (2010). Case Report of a Serious Adverse Event Following the Administration of T Cells Transduced With a Chimeric Antigen Receptor Recognizing ERBB2. *Mol. Ther.* **18**, 843–851.
- Moritz, D., and Groner, B. (1995). A spacer region between the single chain antibody- and the CD3 zeta-chain domain of chimeric T cell receptor components is required for efficient ligand binding and signaling activity. *Gene Ther.* **2**, 539–546.
- Mumprecht, S., Schürch, C., Schwaller, J., Solenthaler, M., and Ochsenbein, A.F. (2009). Programmed death 1 signaling on chronic myeloid leukemia-specific T cells results in T-cell exhaustion and disease progression. *Blood* **114**, 1528–1536.
- Nakatsu, F., and Ohno, H. (2003). Adaptor protein complexes as the key regulators of protein sorting in the post-Golgi network. *Cell Struct. Funct.* **28**, 419–429.
- Naradikian, M.S., Hao, Y., and Cancro, M.P. (2016). Age-associated B cells: key mediators of both protective and autoreactive humoral responses. *Immunol. Rev.* **269**, 118–129.
- Naviaux, R.K., Costanzi, E., Haas, M., and Verma, I.M. (1996). The pCL vector system: rapid production of helper-free, high-titer, recombinant retroviruses. *J. Virol.* **70**, 5701–5705.
- Nicholson, I.C., Lenton, K.A., Little, D.J., Decorso, T., Lee, F.T., Scott, A.M., Zola, H., and Hohmann, A.W. (1997). Construction and characterisation of a functional CD19

specific single chain Fv fragment for immunotherapy of B lineage leukaemia and lymphoma. *Mol. Immunol.* *34*, 1157–1165.

Niesen, F.H., Berglund, H., and Vedadi, M. (2007). The use of differential scanning fluorimetry to detect ligand interactions that promote protein stability. *Nat. Protoc.* *2*, 2212–2221.

Nika, K., Soldani, C., Salek, M., Paster, W., Gray, A., Etzensperger, R., Fugger, L., Polzella, P., Cerundolo, V., Dushek, O., et al. (2010). Constitutively active Lck kinase in T cells drives antigen receptor signal transduction. *Immunity* *32*, 766–777.

O'Day, S., Gonzalez, R., Lawson, D., Weber, R., Hutchins, L., Anderson, C., Haddad, J., Kong, S., Williams, A., and Jacobson, E. (2009). Phase II, randomized, controlled, double-blinded trial of weekly elesclomol plus paclitaxel versus paclitaxel alone for stage IV metastatic melanoma. *J. Clin. Oncol. Off. J. Am. Soc. Clin. Oncol.* *27*, 5452–5458.

Oikawa, A., and Nakayasu, M. (1974). Stimulation of melanogenesis in cultured melanoma cells by calciferols. *FEBS Lett.* *42*, 32–35.

Okamoto, S., Mineno, J., Ikeda, H., Fujiwara, H., Yasukawa, M., Shiku, H., and Kato, I. (2009). Improved expression and reactivity of transduced tumor-specific TCRs in human lymphocytes by specific silencing of endogenous TCR. *Cancer Res.* *69*, 9003–9011.

Okazaki, T., and Honjo, T. (2007). PD-1 and PD-1 ligands: from discovery to clinical application. *Int. Immunol.* *19*, 813–824.

Orlow, S.J., Silvers, W.K., Zhou, B.-K., and Mintz, B. (1998). Comparative Decreases in Tyrosinase, TRP-1, TRP-2, and Pmel 17/Silver Antigenic Proteins from Melanotic to Amelanotic Stages of Syngeneic Mouse Cutaneous Melanomas and Metastases. *Cancer Res.* *58*, 1521–1523.

Ormö, M., Cubitt, A.B., Kallio, K., Gross, L.A., Tsien, R.Y., and Remington, S.J. (1996). Crystal structure of the *Aequorea victoria* green fluorescent protein. *Science* *273*, 1392–1395.

Ostman, A., Yang, Q., and Tonks, N.K. (1994). Expression of DEP-1, a receptor-like protein-tyrosine-phosphatase, is enhanced with increasing cell density. *Proc. Natl. Acad. Sci.* *91*, 9680–9684.

Palathinkal, D.M., Sharma, T.R., Koon, H.B., and Bordeaux, J.S. (2014). Current Systemic Therapies for Melanoma. *Dermatol. Surg. Off. Publ. Am. Soc. Dermatol. Surg. Al.*

Pardoll, D.M. (2012). The blockade of immune checkpoints in cancer immunotherapy. *Nat. Rev. Cancer* *12*, 252–264.

- Patching, S.G. (2014). Surface plasmon resonance spectroscopy for characterisation of membrane protein–ligand interactions and its potential for drug discovery. *Biochim. Biophys. Acta BBA - Biomembr.* *1838*, 43–55.
- Patel, D., Bassi, R., Hooper, A.T., Sun, H., Huber, J., Hicklin, D.J., and Kang, X. (2008). Enhanced Suppression of Melanoma Tumor Growth and Metastasis by Combined Therapy with Anti-VEGF Receptor and Anti-TYRP-1/gp75 Monoclonal Antibodies. *Anticancer Res.* *28*, 2679–2686.
- Patel, S.D., Moskalenko, M., Smith, D., Maske, B., Finer, M.H., and McArthur, J.G. (1999). Impact of chimeric immune receptor extracellular protein domains on T cell function. *Gene Ther.* *6*, 412–419.
- Pearl, R.A., Pacifico, M.D., Richman, P.I., Wilson, G.D., and Grover, R. (2008). Stratification of patients by melanoma cell adhesion molecule (MCAM) expression on the basis of risk: implications for sentinel lymph node biopsy. *J. Plast. Reconstr. Aesthet. Surg.* *61*, 265–271.
- Pilon-Thomas, S., Mackay, A., Vohra, N., and Mulé, J.J. (2010). Blockade of PD-L1 Enhances the Therapeutic Efficacy of Combination Immunotherapy Against Melanoma. *J. Immunol. Baltim. Md 1950* *184*, 3442–3449.
- Porter, D.L., Levine, B.L., Kalos, M., Bagg, A., and June, C.H. (2011). Chimeric Antigen Receptor–Modified T Cells in Chronic Lymphoid Leukemia. *N. Engl. J. Med.* *365*, 725–733.
- Poulsen, T.R., Meijer, P.-J., Jensen, A., Nielsen, L.S., and Andersen, P.S. (2007). Kinetic, Affinity, and Diversity Limits of Human Polyclonal Antibody Responses against Tetanus Toxoid. *J. Immunol.* *179*, 3841–3850.
- Poulsen, T.R., Jensen, A., Haurum, J.S., and Andersen, P.S. (2011). Limits for Antibody Affinity Maturation and Repertoire Diversification in Hypervaccinated Humans. *J. Immunol.* *187*, 4229–4235.
- Puiu, M., and Bala, C. (2016). SPR and SPR Imaging: Recent Trends in Developing Nanodevices for Detection and Real-Time Monitoring of Biomolecular Events. *Sensors* *16*.
- PULÉ, M., CORDOBA, S., ONUOHA, S., and Thomas, S. (2016). *Cell*.
- Pulè, M.A., Straathof, K.C., Dotti, G., Heslop, H.E., Rooney, C.M., and Brenner, M.K. (2005). A Chimeric T Cell Antigen Receptor that Augments Cytokine Release and Supports Clonal Expansion of Primary Human T Cells. *Mol. Ther.* *12*, 933–941.
- Pule, M.A., Savoldo, B., Myers, G.D., Rossig, C., Russell, H.V., Dotti, G., Huls, M.H., Liu, E., Gee, A.P., Mei, Z., et al. (2008). Virus-specific T cells engineered to coexpress tumor-specific receptors: persistence and antitumor activity in individuals with neuroblastoma. *Nat. Med.* *14*, 1264–1270.

Quatromoni, J.G., Morris, L.F., Donahue, T.R., Wang, Y., McBride, W., Chatila, T., and Economou, J.S. (2011). T cell receptor transgenic lymphocytes infiltrating murine tumors are not induced to express foxp3. *J. Hematol. Oncol.* *4*, 48.

Quatromoni, J.G., Wang, Y., Vo, D.D., Morris, L.F., Jazirehi, A.R., McBride, W., Chatila, T., Koya, R.C., and Economou, J.S. (2012). T cell receptor (TCR)-transgenic CD8 lymphocytes rendered insensitive to transforming growth factor beta (TGF $\beta$ ) signaling mediate superior tumor regression in an animal model of adoptive cell therapy. *J. Transl. Med.* *10*, 127.

Ramos, C.A., Savoldo, B., Torrano, V., Ballard, B., Zhang, H., Dakhova, O., Liu, E., Carrum, G., Kamble, R.T., Gee, A.P., et al. (2016). Clinical responses with T lymphocytes targeting malignancy-associated  $\kappa$  light chains. *J. Clin. Invest.* *126*, 2588–2596.

Raper, H.S. (1927). The Tyrosinase-tyrosine Reaction: Production from Tyrosine of 5: 6-Dihydroxyindole and 5: 6-Dihydroxyindole-2-carboxylic Acid-the Precursors of Melanin. *Biochem. J.* *21*, 89–96.

Raposo, G., Tenza, D., Murphy, D.M., Berson, J.F., and Marks, M.S. (2001). Distinct Protein Sorting and Localization to Premelanosomes, Melanosomes, and Lysosomes in Pigmented Melanocytic Cells. *J. Cell Biol.* *152*, 809–824.

Rattmann, I., Kleff, V., Feldmann, A., Ludwig, C., Sorg, U.R., Opalka, B., Moritz, T., and Flasshove, M. (2007). Reliable Generation of Stable High Titer Producer Cell Lines for Gene Therapy. *Intervirology* *50*, 197–203.

Raychaudhuri, S., Tonks, M., Carbone, F., Ryskamp, T., Morrow, W.J., and Hanna, N. (1992). Induction of antigen-specific class I-restricted cytotoxic T cells by soluble proteins in vivo. *Proc. Natl. Acad. Sci.* *89*, 8308–8312.

Reed, K.B., Brewer, J.D., Lohse, C.M., Bringe, K.E., Pruitt, C.N., and Gibson, L.E. (2012). Increasing incidence of melanoma among young adults: an epidemiological study in Olmsted County, Minnesota. *Mayo Clin. Proc.* *87*, 328–334.

Ridge, J.P., Di Rosa, F., and Matzinger, P. (1998). A conditioned dendritic cell can be a temporal bridge between a CD4<sup>+</sup> T-helper and a T-killer cell. *Nature* *393*, 474–478.

Rivière, I., Brose, K., and Mulligan, R.C. (1995). Effects of retroviral vector design on expression of human adenosine deaminase in murine bone marrow transplant recipients engrafted with genetically modified cells. *Proc. Natl. Acad. Sci.* *92*, 6733–6737.

Robbins, P.F., Morgan, R.A., Feldman, S.A., Yang, J.C., Sherry, R.M., Dudley, M.E., Wunderlich, J.R., Nahvi, A.V., Helman, L.J., Mackall, C.L., et al. (2011). Tumor regression in patients with metastatic synovial cell sarcoma and melanoma using genetically engineered lymphocytes reactive with NY-ESO-1. *J. Clin. Oncol. Off. J. Am. Soc. Clin. Oncol.* *29*, 917–924.

- Robert, C., Ribas, A., Wolchok, J.D., Hodi, F.S., Hamid, O., Kefford, R., Weber, J.S., Joshua, A.M., Hwu, W.-J., Gangadhar, T.C., et al. (2014). Anti-programmed-death-receptor-1 treatment with pembrolizumab in ipilimumab-refractory advanced melanoma: a randomised dose-comparison cohort of a phase 1 trial. *Lancet*.
- Rosenberg, S.A., Yannelli, J.R., Yang, J.C., Topalian, S.L., Schwartzentruber, D.J., Weber, J.S., Parkinson, D.R., Seipp, C.A., Einhorn, J.H., and White, D.E. (1994). Treatment of patients with metastatic melanoma with autologous tumor-infiltrating lymphocytes and interleukin 2. *J. Natl. Cancer Inst.* *86*, 1159–1166.
- Rózanowska, M., Sarna, T., Land, E.J., and Truscott, T.G. (1999). Free radical scavenging properties of melanin: Interaction of eu- and pheo-melanin models with reducing and oxidising radicals. *Free Radic. Biol. Med.* *26*, 518–525.
- Ryan, M.C., Hering, M., Peckham, D., McDonagh, C.F., Brown, L., Kim, K.M., Meyer, D.L., Zabinski, R.F., Grewal, I.S., and Carter, P.J. (2007). Antibody targeting of B-cell maturation antigen on malignant plasma cells. *Mol. Cancer Ther.* *6*, 3009–3018.
- Sakuishi, K., Apetoh, L., Sullivan, J.M., Blazar, B.R., Kuchroo, V.K., and Anderson, A.C. (2010). Targeting Tim-3 and PD-1 pathways to reverse T cell exhaustion and restore anti-tumor immunity. *J. Exp. Med.* *207*, 2187–2194.
- Sallusto, F., Lenig, D., Förster, R., Lipp, M., and Lanzavecchia, A. (1999). Two subsets of memory T lymphocytes with distinct homing potentials and effector functions. *Nature* *401*, 708–712.
- Sarkar, S., Teichgräber, V., Kalia, V., Polley, A., Masopust, D., Harrington, L.E., Ahmed, R., and Wherry, E.J. (2007). Strength of Stimulus and Clonal Competition Impact the Rate of Memory CD8 T Cell Differentiation. *J. Immunol.* *179*, 6704–6714.
- Schmid, D.A., Irving, M.B., Posevitz, V., Hebeisen, M., Posevitz-Fejfar, A., Sarria, J.-C.F., Gomez-Eerland, R., Thome, M., Schumacher, T.N.M., Romero, P., et al. (2010). Evidence for a TCR Affinity Threshold Delimiting Maximal CD8 T Cell Function. *J. Immunol.* *184*, 4936–4946.
- Schmidt, P., Kopecky, C., Hombach, A., Zigrino, P., Mauch, C., and Abken, H. (2011). Eradication of melanomas by targeted elimination of a minor subset of tumor cells. *Proc. Natl. Acad. Sci. U. S. A.* *108*, 2474–2479.
- Schodin, B.A., Tsomides, T.J., and Kranz, D.M. (1996). Correlation Between the Number of T Cell Receptors Required for T Cell Activation and TCR–Ligand Affinity. *Immunity* *5*, 137–146.
- Schreuder, G.M.T., Hurley, C.K., Marsh, S.G.E., Lau, M., Maiers, M., Kollman, C., and Noreen, H.J. (2001). The HLA dictionary 2001: a summary of HLA-A, -B, -C, -DRB1/3/4/5, -DQB1 alleles and their association with serologically defined HLA-A, -B, -C, -DR, and -DQ antigens. *Hum. Immunol.* *62*, 826–849.

Schroeder, H.W., and Cavacini, L. (2010). Structure and Function of Immunoglobulins. *J. Allergy Clin. Immunol.* *125*, S41–S52.

Schwartz, R.H. (1992). Costimulation of T lymphocytes: the role of CD28, CTLA-4, and B7/BB1 in interleukin-2 production and immunotherapy. *Cell* *71*, 1065–1068.

Seiji, M., Fitzpatrick, T.B., Simpson, R.T., and Birbeck, M.S.C. (1963). Chemical Composition and Terminology Of Specialized Organelles (Melanosomes and Melanin Granules) in Mammalian Melanocytes. *Nature* *197*, 1082–1084.

Senisterra, G.A., and Patrick J. Finerty, J. (2009). High throughput methods of assessing protein stability and aggregation. *Mol. Biosyst.* *5*, 217–223.

Sennikov, S.V., Alshevskaya, A.A., Shkaruba, N.S., Chumasova, O.A., Sizikov, A.E., and Lopatnikova, J.A. (2015). Expression of TNF $\alpha$  membrane-bound receptors in the peripheral blood mononuclear cells (PMBC) in rheumatoid arthritis patients. *Cytokine* *73*, 288–294.

Setty, S.R.G., Tenza, D., Truschel, S.T., Chou, E., Sviderskaya, E.V., Theos, A.C., Lamoreux, M.L., Pietro, S.M.D., Starcevic, M., Bennett, D.C., et al. (2007a). BLOC-1 Is Required for Cargo-specific Sorting from Vacuolar Early Endosomes toward Lysosome-related Organelles. *Mol. Biol. Cell* *18*, 768–780..

Sha, W.C., Nelson, C.A., Newberry, R.D., Kranz, D.M., Russell, J.H., and Loh, D.Y. (1988). Positive and negative selection of an antigen receptor on T cells in transgenic mice. *Nature* *336*, 73–76.

Shankaran, V., Ikeda, H., Bruce, A.T., White, J.M., Swanson, P.E., Old, L.J., and Schreiber, R.D. (2001). IFN $\gamma$  and lymphocytes prevent primary tumour development and shape tumour immunogenicity. *Nature* *410*, 1107–1111.

Shen, C.-J., Yang, Y.-X., Han, E.Q., Cao, N., Wang, Y.-F., Wang, Y., Zhao, Y.-Y., Zhao, L.-M., Cui, J., Gupta, P., et al. (2013). Chimeric antigen receptor containing ICOS signaling domain mediates specific and efficient antitumor effect of T cells against EGFRvIII expressing glioma. *J. Hematol. Oncol.* *J Hematol Oncol* *6*, 33.

Sieh, M., Bolen, J.B., and Weiss, A. (1993). CD45 specifically modulates binding of Lck to a phosphopeptide encompassing the negative regulatory tyrosine of Lck. *EMBO J.* *12*, 315–321.

Simeonov, A. (2013). Recent Developments in the Use of Differential Scanning Fluorometry in Protein and Small Molecule Discovery and Characterization. *Expert Opin. Drug Discov.* *8*, 1071–1082.

Smith-Garvin, J.E., Burns, J.C., Gohil, M., Zou, T., Kim, J.S., Maltzman, J.S., Wherry, E.J., Koretzky, G.A., and Jordan, M.S. (2010). T-cell receptor signals direct the composition and function of the memory CD8+ T-cell pool. *Blood* *116*, 5548–5559.

Soengas, M.S., and Lowe, S.W. (2003). Apoptosis and melanoma chemoresistance. *Oncogene* 22, 3138–3151.

Sosman, J.A., Kim, K.B., Schuchter, L., Gonzalez, R., Pavlick, A.C., Weber, J.S., McArthur, G.A., Hutson, T.E., Moschos, S.J., Flaherty, K.T., et al. (2012). Survival in BRAF V600–Mutant Advanced Melanoma Treated with Vemurafenib. *N. Engl. J. Med.* 366, 707–714.

Sotillo, E., Barrett, D.M., Black, K.L., Bagashev, A., Oldridge, D., Wu, G., Sussman, R., Lanauze, C., Ruella, M., Gazzara, M.R., et al. (2015). Convergence of Acquired Mutations and Alternative Splicing of CD19 Enables Resistance to CART-19 Immunotherapy. *Cancer Discov.* 5, 1282–1295.

Stone, J.D., Chervin, A.S., and Kranz, D.M. (2009). T-cell receptor binding affinities and kinetics: impact on T-cell activity and specificity. *Immunology* 126, 165–176.

Stone, J.D., Aggen, D.H., Schietinger, A., Schreiber, H., and Kranz, D.M. (2012). A sensitivity scale for targeting T cells with chimeric antigen receptors (CARs) and bispecific T-cell Engagers (BiTEs). *Oncoimmunology* 1, 863–873.

Szymczak, A.L., Workman, C.J., Gil, D., Dilioglou, S., Vignali, K.M., Palmer, E., and Vignali, D.A.A. (2005). The CD3epsilon proline-rich sequence, and its interaction with Nck, is not required for T cell development and function. *J. Immunol. Baltim. Md* 1950 175, 270–275.

T M Thomson, M.J.M., Roux, L., Lloyd, J.O., and Lloyd, K.O. (1985). Pigmentation-associated glycoprotein of human melanomas and melanocytes: definition with a mouse monoclonal antibody. *J. Invest. Dermatol.* 85, 169–174.

Tai, T., Eisinger, M., Ogata, S., and Lloyd, K.O. (1983). Glycoproteins as Differentiation Markers in Human Malignant Melanoma and Melanocytes. *Cancer Res.* 43, 2773–2779.

Taylor, P., Tsai, S., Shameli, A., Serra, P., Wang, J., Robbins, S., Nagata, M., Szymczak-Workman, A.L., Vignali, D.A.A., and Santamaria, P. (2008). The proline-rich sequence of CD3epsilon as an amplifier of low-avidity TCR signaling. *J. Immunol. Baltim. Md* 1950 181, 243–255.

Takechi, Y., Hara, I., Naftzger, C., Xu, Y., and Houghton, A.N. (1996). A melanosomal membrane protein is a cell surface target for melanoma therapy. *Clin. Cancer Res.* 2, 1837–1842.

Takeuchi, K., Yang, H., Ng, E., Park, S., Sun, Z.-Y.J., Reinherz, E.L., and Wagner, G. (2008). Structural and functional evidence that Nck interaction with CD3epsilon regulates T-cell receptor activity. *J. Mol. Biol.* 380, 704–716.

Tamma, S., Huang, X., Wong, M., Milone, M.C., Ma, L., Levine, B.L., June, C.H., Wagner, J.E., Blazar, B.R., and Zhou, X. (2010). 4-1BB and CD28 signaling plays a

synergistic role in redirecting umbilical cord blood T cells against B-cell malignancies. *Hum. Gene Ther.* *21*, 75–86.

Theos, A.C., Tenza, D., Martina, J.A., Hurbain, I., Peden, A.A., Sviderskaya, E.V., Stewart, A., Robinson, M.S., Bennett, D.C., Cutler, D.F., et al. (2005). Functions of adaptor protein (AP)-3 and AP-1 in tyrosinase sorting from endosomes to melanosomes. *Mol. Biol. Cell* *16*, 5356–5372.

Thomas, S., Xue, S.-A., Bangham, C.R.M., Jakobsen, B.K., Morris, E.C., and Stauss, H.J. (2011). Human T cells expressing affinity-matured TCR display accelerated responses but fail to recognize low density of MHC-peptide antigen. *Blood* *118*, 319–329.

Thomas, S., Straathof, K., Himoudi, N., Anderson, J., and Pule, M. (2016). An Optimized GD2-Targeting Retroviral Cassette for More Potent and Safer Cellular Therapy of Neuroblastoma and Other Cancers. *PLoS ONE* *11*.

Thomson, T.M., Real, F.X., Murakami, S., Cordon-Cardo, C., Old, L.J., and Houghton, A.N. (1988). Differentiation Antigens of Melanocytes and Melanoma: Analysis of Melanosome and Cell Surface Markers of Human Pigmented Cells With Monoclonal Antibodies. *J. Invest. Dermatol.* *90*, 459–466.

Tian, S., Maile, R., Collins, E.J., and Frelinger, J.A. (2007). CD8+ T Cell Activation Is Governed by TCR-Peptide/MHC Affinity, Not Dissociation Rate. *J. Immunol.* *179*, 2952–2960.

Tomita, Y., Fukushima, M., and Tagami, H. (1986). Stimulation of melanogenesis by cholecalciferol in cultured human melanocytes: a possible mechanism underlying pigmentation after ultraviolet irradiation. *Tohoku J. Exp. Med.* *149*, 451–452.

Toyofuku, K., Wada, I., Valencia, J.C., Kushimoto, T., Ferrans, V.J., and Hearing, V.J. (2001). Oculocutaneous albinism types 1 and 3 are ER retention diseases: mutation of tyrosinase or *Typr1* can affect the processing of both mutant and wild-type proteins. *FASEB J.* *15*, 2149–2161.

Trowbridge, I.S., Ostergaard, H.L., and Johnson, P. (1991). CD45: a leukocyte-specific member of the protein tyrosine phosphatase family. *Biochim. Biophys. Acta BBA - Mol. Cell Res.* *1095*, 46–56.

True, C.D. (2001). Preparation of an iodinated radioligand. *Curr. Protoc. Neurosci.* Editor. Board Jacqueline N Crawley *Appendix 3*, Appendix 3A.

Truschel, S.T., Simoes, S., Setty, S.R.G., Harper, D.C., Tenza, D., Thomas, P.C., Herman, K.E., Sackett, S.D., Cowan, D.C., Theos, A.C., et al. (2009). ESCRT-I function is required for *Typr1* transport from early endosomes to the melanosome limiting membrane. *Traffic Cph. Den.* *10*, 1318–1336.

Tsai, J., Lee, J.T., Wang, W., Zhang, J., Cho, H., Mamo, S., Bremer, R., Gillette, S., Kong, J., Haass, N.K., et al. (2008). Discovery of a selective inhibitor of oncogenic B-Raf kinase with potent antimelanoma activity. *Proc. Natl. Acad. Sci.* *105*, 3041–3046.

- Tsukamoto, K., Jackson, I.J., Urabe, K., Montague, P.M., and Hearing, V.J. (1992). A second tyrosinase-related protein, TRP-2, is a melanogenic enzyme termed DOPAchrome tautomerase. *EMBO J.* *11*, 519–526.
- Turatti, F., Figini, M., Balladore, E., Alberti, P., Casalini, P., Marks, J.D., Canevari, S., and Mezzanzanica, D. (2007). Redirected activity of human antitumor chimeric immune receptors is governed by antigen and receptor expression levels and affinity of interaction. *J. Immunother. Hagerstown Md* *1997* *30*, 684–693.
- Turtle, C.J., Hanafi, L.-A., Berger, C., Gooley, T.A., Cherian, S., Hudecek, M., Sommermeyer, D., Melville, K., Pender, B., Budiarto, T.M., et al. (2016). CD19 CAR–T cells of defined CD4+:CD8+ composition in adult B cell ALL patients. *J. Clin. Invest.* *126*, 2123–2138.
- Uslu, U., Schuler, G., Dörrie, J., and Schaft, N. (2016). Combining a chimeric antigen receptor and a conventional T-cell receptor to generate T cells expressing two additional receptors (TETARs) for a multi-hit immunotherapy of melanoma. *Exp. Dermatol.*
- Vajdos, F.F., Adams, C.W., Breece, T.N., Presta, L.G., de Vos, A.M., and Sidhu, S.S. (2002). Comprehensive Functional Maps of the Antigen-binding Site of an Anti-ErbB2 Antibody Obtained with Shotgun Scanning Mutagenesis. *J. Mol. Biol.* *320*, 415–428.
- Valencia, J.C., Watabe, H., Chi, A., Rouzaud, F., Chen, K.G., Vieira, W.D., Takahashi, K., Yamaguchi, Y., Berens, W., Nagashima, K., et al. (2006). Sorting of Pmel17 to melanosomes through the plasma membrane by AP1 and AP2: evidence for the polarized nature of melanocytes. *J. Cell Sci.* *119*, 1080–1091.
- Valitutti, S., Müller, S., Cella, M., Padovan, E., and Lanzavecchia, A. (1995a). Serial triggering of many T-cell receptors by a few peptide–MHC complexes. *Nature* *375*, 148–151.
- Vijayasaradhi, S., Xu, Y., Bouchard, B., and Houghton, A.N. (1995). Intracellular sorting and targeting of melanosomal membrane proteins: identification of signals for sorting of the human brown locus protein, gp75. *J. Cell Biol.* *130*, 807–820.
- Viola, A., and Lanzavecchia, A. (1996). T cell activation determined by T cell receptor number and tunable thresholds. *Science* *273*, 104–106.
- Virador, V., Matsunaga, N., Matsunaga, J., Valencia, J., Oldham, R.J., Kameyama, K., Peck, G.L., Ferrans, V.J., Vieira, W.D., Abdel-Malek, Z.A., et al. (2001). Production of Melanocyte-Specific Antibodies to Human Melanosomal Proteins: Expression Patterns in Normal Human Skin and in Cutaneous Pigmented Lesions. *Pigment Cell Res.* *14*, 289–297.
- Virgin, H.W., Wherry, E.J., and Ahmed, R. (2009). Redefining Chronic Viral Infection. *Cell* *138*, 30–50.

de Vries, T.J., Trancikova, D., Ruiter, D.J., and van Muijen, G.N. (1998). High expression of immunotherapy candidate proteins gp100, MART-1, tyrosinase and TRP-1 in uveal melanoma. *Br. J. Cancer* *78*, 1156–1161.

Wang, D.-S., and Fan, S.-K. (2016). Microfluidic Surface Plasmon Resonance Sensors: From Principles to Point-of-Care Applications. *Sensors* *16*.

Wang, K., Wei, G., and Liu, D. (2012). CD19: a biomarker for B cell development, lymphoma diagnosis and therapy. *Exp. Hematol. Oncol.* *1*, 36.

Wang, Y., Liu, Y., Han, R., Li, Q., Yao, Z., Niu, W., Yuan, Y., Tang, Z., Zhu, Z., and Shen, Z. (2010). Monitoring of CD95 and CD38 expression in peripheral blood T lymphocytes during active human cytomegalovirus infection after orthotopic liver transplantation. *J. Gastroenterol. Hepatol.* *25*, 138–142.

Wasmeier, C., Romao, M., Plowright, L., Bennett, D.C., Raposo, G., and Seabra, M.C. (2006). Rab38 and Rab32 control post-Golgi trafficking of melanogenic enzymes. *J. Cell Biol.* *175*, 271–281.

Watabe, H., Valencia, J.C., Yasumoto, K., Kushimoto, T., Ando, H., Muller, J., Vieira, W.D., Mizoguchi, M., Appella, E., and Hearing, V.J. (2004). Regulation of Tyrosinase Processing and Trafficking by Organellar pH and by Proteasome Activity. *J. Biol. Chem.* *279*, 7971–7981.

Watanabe, K., Terakura, S., Martens, A.C., Meerten, T. van, Uchiyama, S., Imai, M., Sakemura, R., Goto, T., Hanajiri, R., Imahashi, N., et al. (2015). Target Antigen Density Governs the Efficacy of Anti-CD20-CD28-CD3  $\zeta$  Chimeric Antigen Receptor-Modified Effector CD8+ T Cells. *J. Immunol.* *194*, 911–920.

Weijtens, M.E., Hart, E.H., and Bolhuis, R.L. (2000). Functional balance between T cell chimeric receptor density and tumor associated antigen density: CTL mediated cytolysis and lymphokine production. *Gene Ther.* *7*, 35–42.

Weiss, A., and Littman, D.R. (1994). Signal transduction by lymphocyte antigen receptors. *Cell* *76*, 263–274.

Wels, W., Beerli, R., Hellmann, P., Schmidt, M., Marte, B.M., Kornilova, E.S., Hekele, A., Mendelsohn, J., Groner, B., and Hynes, N.E. (1995). EGF receptor and p185erbB-2-specific single-chain antibody toxins differ in their cell-killing activity on tumor cells expressing both receptor proteins. *Int. J. Cancer J. Int. Cancer* *60*, 137–144.

Welt, S., Mattes, M.J., Grando, R., Thomson, T.M., Leonard, R.W., Zanzonico, P.B., Bigler, R.E., Yeh, S., Oettgen, H.F., and Old, L.J. (1987). Monoclonal antibody to an intracellular antigen images human melanoma transplants in nu/nu mice. *Proc. Natl. Acad. Sci.* *84*, 4200–4204.

Wiedenmann, J., Ivanchenko, S., Oswald, F., Schmitt, F., Röcker, C., Salih, A., Spindler, K.-D., and Nienhaus, G.U. (2004). EosFP, a fluorescent marker protein with UV-

inducible green-to-red fluorescence conversion. *Proc. Natl. Acad. Sci. U. S. A.* *101*, 15905–15910.

Wild, M.K., Cambiaggi, A., Brown, M.H., Davies, E.A., Ohno, H., Saito, T., and van der Merwe, P.A. (1999). Dependence of T cell antigen recognition on the dimensions of an accessory receptor-ligand complex. *J. Exp. Med.* *190*, 31–41.

Wilkie, S., Picco, G., Foster, J., Davies, D.M., Julien, S., Cooper, L., Arif, S., Mather, S.J., Taylor-Papadimitriou, J., Burchell, J.M., et al. (2008). Retargeting of Human T Cells to Tumor-Associated MUC1: The Evolution of a Chimeric Antigen Receptor. *J. Immunol.* *180*, 4901–4909.

Willcox, B.E., Gao, G.F., Wyer, J.R., Ladbury, J.E., Bell, J.I., Jakobsen, B.K., and van der Merwe, P.A. (1999). TCR Binding to Peptide-MHC Stabilizes a Flexible Recognition Interface. *Immunity* *10*, 357–365.

Williams, M.A., and Bevan, M.J. (2007). Effector and memory CTL differentiation. *Annu. Rev. Immunol.* *25*, 171–192.

Williams, C.B., Engle, D.L., Kersh, G.J., Michael White, J., and Allen, P.M. (1999). A Kinetic Threshold between Negative and Positive Selection Based on the Longevity of the T Cell Receptor–Ligand Complex. *J. Exp. Med.* *189*, 1531–1544.

Wooldridge, L., van den Berg, H.A., Glick, M., Gostick, E., Laugel, B., Hutchinson, S.L., Milicic, A., Brenchley, J.M., Douek, D.C., Price, D.A., et al. (2005). Interaction between the CD8 coreceptor and major histocompatibility complex class I stabilizes T cell receptor-antigen complexes at the cell surface. *J. Biol. Chem.* *280*, 27491–27501.

Wu, L.C., Tuot, D.S., Lyons, D.S., Garcia, K.C., and Davis, M.M. (2002). Two-step binding mechanism for T-cell receptor recognition of peptide–MHC. *Nature* *418*, 552–556.

Wyer, J.R., Willcox, B.E., Gao, G.F., Gerth, U.C., Davis, S.J., Bell, J.I., Merwe, P.A. van der, and Jakobsen, B.K. (1999). T Cell Receptor and Coreceptor CD8 $\alpha$  Bind Peptide-MHC Independently and with Distinct Kinetics. *Immunity* *10*, 219–225.

Xie, Y., Akpinarli, A., Maris, C., Hipkiss, E.L., Lane, M., Kwon, E.-K.M., Muranski, P., Restifo, N.P., and Antony, P.A. (2010). Naive tumor-specific CD4<sup>+</sup> T cells differentiated in vivo eradicate established melanoma. *J. Exp. Med.* *207*, 651–667.

Yamaguchi, Y., Brenner, M., and Hearing, V.J. (2007). The Regulation of Skin Pigmentation. *J. Biol. Chem.* *282*, 27557–27561.

Yang, F., Moss, L.G., and Phillips, G.N. (1996). The molecular structure of green fluorescent protein. *Nat. Biotechnol.* *14*, 1246–1251.

Yiqing Xu, Setaluri, V., Takechi, Y., and Houghton, A.N. (1997). Sorting and Secretion of a Melanosome Membrane Protein, gp75/TRP1. *J. Invest. Dermatol.* *109*, 788–795.

- Yvon, E., Del Vecchio, M., Savoldo, B., Hoyos, V., Dutour, A., Anichini, A., Dotti, G., and Brenner, M.K. (2009). Immunotherapy of metastatic melanoma using genetically engineered GD2-specific T cells. *Clin. Cancer Res. Off. J. Am. Assoc. Cancer Res.* *15*, 5852–5860.
- Zajac, A.J., Blattman, J.N., Murali-Krishna, K., Sourdive, D.J., Suresh, M., Altman, J.D., and Ahmed, R. (1998). Viral immune evasion due to persistence of activated T cells without effector function. *J. Exp. Med.* *188*, 2205–2213.
- Zhang, L., Yu, K., Robert, K.W., DeBolt, K.M., Hong, N., Tao, J.-Q., Fukuda, M., Fisher, A.B., and Huang, S. (2011). Rab38 targets to lamellar bodies and normalizes their sizes in lung alveolar type II epithelial cells. *Am. J. Physiol. - Lung Cell. Mol. Physiol.* *301*, L461–L477.
- Zhang, M., Chang, H., Zhang, Y., Yu, J., Wu, L., Ji, W., Chen, J., Liu, B., Lu, J., Liu, Y., et al. (2012). Rational design of true monomeric and bright photoactivatable fluorescent proteins. *Nat. Methods* *9*, 727–729.
- Zhao, Q., Ahmed, M., Tassev, D.V., Hasan, A., Kuo, T.-Y., Guo, H., O'Reilly, R.J., and Cheung, N.-K.V. (2015). Affinity maturation of T-cell receptor-like antibodies for Wilms tumor 1 peptide greatly enhances therapeutic potential. *Leukemia* *29*, 2238–2247.
- Zhao, Y., Bennett, A.D., Zheng, Z., Wang, Q.J., Robbins, P.F., Yu, L.Y.L., Li, Y., Molloy, P.E., Dunn, S.M., Jakobsen, B.K., et al. (2007). High-Affinity TCRs Generated by Phage Display Provide CD4+ T Cells with the Ability to Recognize and Kill Tumor Cell Lines. *J. Immunol.* *179*, 5845–5854.
- Zheng, Z., Chinnasamy, N., and Morgan, R.A. (2012). Protein L: a novel reagent for the detection of chimeric antigen receptor (CAR) expression by flow cytometry. *J. Transl. Med.* *10*, 29.
- Zhong, S., Malecek, K., Johnson, L.A., Yu, Z., Miera, E.V.-S. de, Darvishian, F., McGary, K., Huang, K., Boyer, J., Corse, E., et al. (2013). T-cell receptor affinity and avidity defines antitumor response and autoimmunity in T-cell immunotherapy. *Proc. Natl. Acad. Sci.* *110*, 6973–6978.
- Zhu, J.W., Brdicka, T., Katsumoto, T.R., Lin, J., and Weiss, A. (2008). Structurally distinct phosphatases CD45 and CD148 both regulate B cell and macrophage immunoreceptor signaling. *Immunity* *28*, 183–196.